

**SYNTHESIS OF COMPLEX INORGANIC COLLOIDAL
HOLLOW NANOSCALED ARCHITECTURES AND ITS
APPLICATIONS**

CHRISTOPHER YEC

(B.Sc. Chemistry, University of Santo Tomas, Philippines)

A THESIS SUBMITTED

FOR THE DEGREE OF DOCTOR OF PHILOSOPHY

**NUS GRADUATE SCHOOL FOR INTEGRATIVE
SCIENCES AND ENGINEERING**

NATIONAL UNIVERSITY OF SINGAPORE

2016

Declaration

I hereby declare that this thesis is my original work, and it has been written by me in its entirety. I have duly acknowledged all the sources of information that have been used in the thesis.

This thesis has also not been submitted for any degree in any university previously.



Christopher C. Yec

17th July 2016

Acknowledgement

In completing this dissertation, I would like to acknowledge several persons for making it possible to complete this work. First and foremost, I thank the National University of Singapore Graduate School for Integrative Sciences and Engineering for giving me the opportunity to pursue my Ph.D.

I thank my supervisor Prof. Zeng Hua Chun for his research guidance and support since my first year. He has enlightened me on the right research direction and has given me some creative research ideas. I would also like to thank the Chemical and Biomolecular Engineering department for allowing me to conduct my research and experiments in their department

I have been blessed to work with several colleagues that helped me for the past four years. I give my regards and thanks to Dr. Pang Maolin, Dr. Xiong Shenglin, Dr. Xi Baojuan, Dr. Wang Danping, Ms. Chng Ting Ting, Dr. Li Chengchao, Dr. Li Zheng, Dr. Dou Jian, Dr. Liu Minghui, Mr. Sheng Yuan, Ms. Zhou Yao, Mr. Zhan Guowu, Mdm. Khoh Leng Khim, Sandy, Mr. Mao Ning, Mr. Chia Phai Ann, Mr. Liu Zhicheng, Mr. Ng Kimpoi, Mr. Alistair Chan and Mr. Suppiah Rajamohan.

Last but not least, I thank my family and friends for their support and patience during my Ph.D. studies.

Table of Contents

Declaration.....	i
Acknowledgement	ii
Table of Contents	iii
Summary.....	vi
List of Figures and Schemes	viii
List of Tables	xi
CHAPTER 1. INTRODUCTION.....	1
1.1. Background on Colloidal Inorganic Hollow Structures	1
1.2. Objectives and Scope	2
1.3 Purpose of study and Significance.....	3
1.4 Scopes and Limitations.....	4
References	4
CHAPTER 2. LITERATURE REVIEW.....	6
2.1 Template Based Approaches.....	6
2.2 Chemical Transformation.....	7
2.2.1 Cation/Anion Exchange Reaction	8
2.2.2 Galvanic Exchange Reaction.....	9
2.3 Ostwald Ripening	9
2.3.1 Ostwald ripening on random crystallite aggregates	10
2.3.2 Ostwald ripening on ordered crystallite aggregates	12
2.3.3 Ostwald ripening in Core-shell and Yolk-shell Structure	14
2.3.4 Ostwald ripening in Multi-layered Hollow Structures.....	18
2.3.5 The ubiquity of Ostwald ripening as a hollowing method.....	19
References	22
CHAPTER 3. SYNTHETIC ARCHITECTURE OF MULTIPLE CORE-SHELL AND YOLK-SHELL STRUCTURES OF (Cu₂O@)_nCu₂O (n = 1-4) WITH CENTRICITY AND ECCENTRICITY	30
3.1 Introduction	31

3.2 Experimental Section	34
3.3 Results and Discussion	38
3.3.1. Synthetic Chemistry and Strategies	38
3.3.2. Controlling Factors and Ripening Mechanisms	45
3.3.3. Centricity and Eccentricity of Structures	57
3.3.4. Structures and Optical Properties	59
3.3.5. Electrochemical Applications	61
3.4 Conclusion	68
References	70
CHAPTER 4. TRANSFORMATIVE SYNTHESSES OF COMPLEX COPPER-BASED NANOSTRUCTURES FROM PRECURSORS WITH PREDESIGNED ARCHITECTURE AND REACTIVITY	78
4.1 Introduction	78
4.2 Experimental Section	81
4.3 Results and Discussion	86
4.3.1 Reduction-complexation of CSPAR	86
4.3.2 Galvanic exchange-reduction of CSPAR	89
4.3.3 Electrochemical reduction of CSPAR	90
4.3.4 Ambient recrystallization and gas interfacial reactions	91
4.3.5 Anion exchange reactions	92
4.3.6 Reactions of passivated Cu ₂ O CSPAR	94
4.3.7 Correlation of Structure and Property	99
4.4 Conclusion	101
Reference	102
CHAPTER 5. SEED-MEDIATED SYNTHESIS OF M@Cu₂O@Zn(OH)₂ (M = Au, Ag, Au/Ag, Pd) and M@Cu CORE-SHELL STRUCTURES	107
5.1 Introduction	107
5.2 Experimental Section	108
5.3 Results and Discussion	112
5.3.1 Seed-Mediated Synthesis of M@Cu ₂ O and M@Cu ₂ O@Zn(OH) ₂ Core-Shell Structure	112
5.3.2 Thermal Treatment of M@Cu ₂ O@Zn(OH) ₂ Core-Shell Structure	122
5.3.3 Reduction of 4-Nitrophenol Using M@Cu ₂ O and M@Cu ₂ O@Zn(OH) ₂ Core-Shell	125
5.3.4 Photocatalytic Degradation of Methyl Orange using M@Cu ₂ O and M@Cu ₂ O@Zn(OH) ₂ Core-Shell	127

5.4 Conclusion	131
Reference	131
CHAPTER 6. NANOBUBBLES ON A MICROBUBBLE: SYNTHESIS AND SELF-ASSEMBLY OF HOLLOW MANGANESE SILICATE AND ITS METAL-DOPED DERIVATIVES	133
6.1 Introduction	133
6.2 Experimental Section	136
6.3 Results and Discussion	140
6.3.1 Manganese Silicate Nanobubbles	140
6.3.2 Doped Manganese Silicate Nanobubbles	144
6.3.3 Synthetic Mechanism of Manganese Silicate Nanobubbles	149
6.3.4 Catalytic Applications of Manganese Silicate Nanobubbles	157
6.4 Conclusion	159
Reference	160
CHAPTER 7. CONCLUSIONS AND RECOMMENDATIONS.....	164
7.1 Conclusions	164
7.2 Recommendations for Future Work.....	167
APPENDIX 1	169
APPENDIX 2	188
APPENDIX 3.....	231
APPENDIX 4.....	240
PUBLICATIONS ARISING FROM THIS THESIS	282

Summary

In recent years, significant attention has been given on the synthesis and property of nanostructured materials. Among these materials, hollow nanostructured materials represent a class of material that possess unique property compared with their solid counterparts. These materials are useful in the fields of catalysis, energy, and drug delivery. Although the syntheses of hollow structures have been widely reported, the approach relies on trial and error and the addition of structural complexity for hollow structures has remained elusive.

This dissertation focuses on the development of several synthetic methods for complex hollow structures and the elucidation of their formation mechanism. In addition to their preparation, we correlated the relation between the material's complex architecture with respect to its functional property. Several complex nano-architectures and their formation mechanism were determined. These structures include a multi-shelled Cu_2O core-shell, Cu hollow spheres, $\text{Cu}_2\text{O}@ZnO$ core-shell, Cu_2O nanoparticle embedded on ZnO hollow spheres, $M@Cu_2O@ZnO$ (M = noble metal) core-shell, and a hollow spherical assembly of nanobubbles of manganese silicate. These synthetic structures possess a potential for applications in catalysis, electrochemical sensing, and electrocatalysis.

Chapter 3 presents a combined seed-mediated and Ostwald ripening synthetic approach for multi-shelled Cu_2O core-shell with up to four shells. These core-shell structures demonstrated electrochemical sensing property for non-enzymatic amperometric glucose detection.

In Chapter 4, the chemical reactivity and structural transformation of Cu_2O homogeneous core-shell were determined. This core-shell structure is unique due to

the presence of a reactivity gradient within the structure and can be termed as a “*core-shell with predesigned architecture and reactivity*” (CSPAR). These CSPAR and its Zn(OH)₂ passivated structures were subjected to reduction-complexation reactions, electrochemical reduction, galvanic replacement reactions, anion exchange, recrystallization, and thermal treatment. The resulting products for reduction-complexation reactions displayed a structure and functional property correlation in the photocatalytic degradation of methyl orange.

In Chapter 5, the seed-mediated synthetic approach was extended for a noble metal core. M@Cu₂O (where M = Au, Ag, AuAg and Pd) and M@Cu₂O@Zn(OH)₂ core-shell structures were synthesized using this approach. In addition to their preparation, the chemical and structural transformation of these core-shell structures were also determined. The effect of a noble metal core on the photocatalytic activity towards methyl orange degradation was studied. Compared with structures prepared in Chapter 4, the photocatalytic activity of these structures was lower. These are explained through slower diffusion and enhanced exciton recombination rates.

In Chapter 6, the formation and mechanism of hollow spherical assembly (200 nm) of manganese silicate nanobubbles (7 nm) during hydrothermal conditions are presented. This formation can be attributed to CO₂ gas bubble templating during hydrothermal conditions, where the SiO₂ template acted as a catalysis for CO₂ formation. The assembled structure showed excellent catalytic activity for advanced oxidation process (AOP) of methylene blue. In addition, the assembled structure can also serve as a precursor for other transformative synthesis.

List of Figures and Schemes

Figure 2.1 Schematic illustration detailing all major steps involved in the formation of Au-Ag nanocages with well controlled pores at the corners.	8
Figure 2.2 The formation process of anatase TiO ₂ hollow spheres via Ostwald ripening	11
Figure 2.3 Schematic illustration of oriented attachment and its combination with Ostwald ripening to generate non-spherical hollow structures	13
Figure 2.4 Schematic illustrations of different modes of Ostwald ripening to generate an interior void	15
Figure 2.5 A combined seed-mediated and Ostwald ripening approach to generate heterogeneous hollow core-shell structures.....	17
Figure 2.6 The process of successive phases of Ostwald ripening to form multi-shelled structures and corresponding TEM images of the samples.....	19
Figure 2.7 A schematic illustration of Ostwald ripening to generate interior voids for mesoporous SiO ₂ spheres.	20
Figure 2.8 Structural features (TEM images) of mesoporous SiO ₂ hollow spheres generated via Ostwald ripening using various growth conditions.	21
Figure 3.1 Illustrations of synthetic strategies of (Cu ₂ O@) _n Cu ₂ O (<i>n</i> = 1 to 4) core-shell and yolk-shell structures.	39
Figure 3.2 Schematic illustrations of (Cu ₂ O@) _n Cu ₂ O formation processes	40
Figure 3.3 Schematic illustration of eight possible triple-shelled (Cu ₂ O@) ₃ Cu ₂ O structures and their related TEM images.....	41
Figure 3.4 Representative TEM images of various (Cu ₂ O@) _n Cu ₂ O (<i>n</i> = 1 to 4) products.....	43
Figure 3.5 Powder X-ray diffraction patterns of pristine Cu ₂ O cubes and different types of complex (Cu ₂ O@) _n Cu ₂ O structures.....	44
Figure 3.6 Effect of ripening time on the growth of the 1 st shell (<i>n</i> = 1)	46
Figure 3.7 Effect of ripening time on the growth of the 2 nd shell (<i>n</i> = 2)	47
Figure 3.8 Effect of ripening time on the growth of the 3 rd shell (<i>n</i> = 3).....	48
Figure 3.9 Effect of ripening time on the growth of the 4 th shell (<i>n</i> = 4).....	49
Figure 3.10 Hollowing kinetics as a function of nominal stirring rate.	50
Figure 3.11 Effect of stirring conditions on the growth of the 1 st shell	52
Figure 3.12 Effect of stirring conditions on the growth of the 2 nd shell	53
Figure 3.13 Asymmetric Ostwald ripening	54
Figure 3.14 Triple-shelled bean pod structures synthesized with a small amount of "double-shelled seeds"	56

Figure 3.15 Extinction spectra of pristine Cu ₂ O cubes and different types of complex (Cu ₂ O@) _n Cu ₂ O structures.....	60
Figure 3.16 Cyclic voltammograms of different Cu ₂ O/Nf/GCEs with different amount of glucose.....	63
Figure 3.17 Chronoamperometric responses of various Cu ₂ O/Nf/GCEs upon successive addition of 10 μM glucose.	67
Figure 4.1 Schematic diagram for transformation of Cu ₂ O CSPAR.....	81
Figure 4.2 Resulting morphology and phase of Cu ₂ O CSPAR at different reactions.	87
Figure 4.3 Resulting morphology and phase of Zn(OH) ₂ passivated Cu ₂ O core-shell at different reactions.....	95
Figure 4.4 Photocatalytic applications of Cu ₂ O@ZnO core-shell and Cu ₂ O nanoparticles embedded on ZnO hollow shell.....	100
Figure 5.1 Representative TEM images of M@Cu ₂ O, and M@Cu ₂ O@Zn(OH) ₂	113
Figure 5.2 Effect of reaction duration on M@Cu ₂ O synthesis	114
Figure 5.3 Effect of NH ₄ NO ₃ on M@Cu ₂ O Growth.	115
Figure 5.4 Effect of PVP on M@Cu ₂ O Growth.....	117
Figure 5.5 XRD pattern for different M@Cu ₂ O core-shell structure.....	118
Figure 5.6 Reduction of the as-synthesized M@Cu ₂ O Core-Shell structure with various amount of NaBH ₄ solution.	119
Figure 5.7 Reduction of the as-synthesized M@Cu ₂ O@Zn(OH) ₂ with 1 mL of NaBH ₄ solution at various concentrations.	120
Figure 5.8 Reduction of redispersed M@Cu ₂ O@Zn(OH) ₂ with 1 mL of NaBH ₄ solution at various concentration.....	121
Figure 5.9 Thermal treatment of M@Cu ₂ O@Zn(OH) ₂ at various temperature under flowed Argon condition.	123
Figure 5.10 Corresponding XRD pattern of M@Cu ₂ O@Zn(OH) ₂ after thermal treatment in Argon conditions.....	124
Figure 5.11 Catalytic reduction of 4-nitrophenol with various M@Cu ₂ O, M@Cu, and M@Cu ₂ O@ZnO core-shell catalyst).	126
Figure 5.12 Concentration profile of 4-Nitrophenol during reduction with NaBH ₄ at various types of catalyst	127
Figure 5.13 Concentration profile of Methyl Orange during photocatalytic degradation at various types of catalyst.....	128
Figure 5.14 Energy level diagram of different M@Cu ₂ O@ZnO core-shell structures.....	130
Scheme 6.1 Schematic illustration of surface-catalyzed dual templating process.....	136

Figure 6.1 Representative TEM images: SiO ₂ precursor beads; and spherically assembled nanobubbles of manganese silicate.....	141
Figure 6.2 X-ray diffraction patterns of nanobubbles of manganese silicate synthesized with different kinds of carboxylate anions.....	142
Figure 6.3 Representative TEM images of spherically assembled nanobubbles of manganese silicate doped with the first row transition metal elements	144
Figure 6.4 Representative TEM images of spherically assembled nanobubbles of manganese silicate doped with rare earth elements.....	145
Figure 6.5 Representative TEM images of manganese silicate doped with other elements	146
Figure 6.6 X-ray diffraction patterns of transition metal doped manganese silicate.	147
Figure 6.7 X-ray diffraction patterns of rare earth doped manganese silicate	148
Figure 6.8 Comparison of FTIR spectra of different samples.	150
Figure 6.9 Spherically assembled nanobubbles of manganese silicate prepared with different carboxylate ions.....	151
Figure 6.10 Hollow spheres of metal silicates synthesized using 50 mg of SiO ₂ spheres, 5 mmol of NaCH ₃ COO, and 20 mL of H ₂ O under hydrothermal conditions (180°C).....	153
Figure 6.11 Hydrothermal treatment of SiO ₂ with different metal sulfate salts.	154
Figure 6.12 Concentration profiles of methylene blue, rhodamine 6G, and methyl orange during catalytic decomposition	158

List of Tables

Table 1.1 Anodic Peak Potential and Current of Different Cu ₂ O Structures	66
Table 6.1 Summary of BET Analysis and BJH Desorption Analysis for Manganese Silicate Samples	143
Table A-1 Excess ascorbate and nitrate anions present in the reaction solution.	169
Table A-2 Excess ascorbate and nitrate anions present in the reaction solution.	172
Table A-3 Comparison of the Actual Atomic Ratio between Manganese and Dopant Material	256
Table A-4 List of Emission Energy during Analysis of Doped Manganese Silicate Structure	256
Table A-5 Summary of Particle Size and Shell Thickness of Manganese Silicate Samples	266
Table A-6 Stability Constants (K) of Metal Carboxylates	267

Chapter 1. Introduction

1.1. Background on Colloidal Inorganic Hollow Structures

Colloidal particles are solids that possess sizes less than 1 micron and are dispersed in another phase. These suspensions have a variety of technological applications and are playing significant roles in our lives. Several typical examples of colloidal particles include blood, milk, detergents and paints. In many cases, the properties of colloidal particles are heavily influenced by its particle size, morphology, density, size-morphology distribution and its chemical composition. For example, the presence of interior voids in the colloidal particle allows it to function as a carrier of several biomolecules and drugs within an organism. In addition to its storage property, these cavities allow the modification of the structure's optical property due to scattering effects. These colloidal particles with an interior void are technically termed as "hollow colloidal structures".

Hollow colloidal structures possess several important characteristics such as low density, large surface to volume ratio, and a low coefficient of thermal expansion. In addition to these properties, the presence of an interior cavity allows the structure to be a carrier for both material and energy as mentioned previously. It should be noted that these materials have already demonstrated several potential applications in the field of catalysis, sensing, energy storage, and environmental remediation¹⁻⁴.

In recent years, numerous methods have been developed for the preparation of hollow colloidal structure since nanoscale sciences and technology were the research trend for the past decade⁵⁻⁷. For this chapter, we would only introduce several synthetic methods on hollow colloidal structures, and more details would be given in

the next chapter. Hollow colloidal particles are usually synthesized using a template structure. This template can serve as a site for heterogeneous nucleation and growth of solid particles. Therefore, the exterior morphology of the particle relies on the template's morphology. In addition, these templates can be either classified as hard or soft template. The former refers to solid particulates dispersed in a solution while the latter refers to non-solid templates such as vesicles, micelles, gas bubbles, *etc.*^{8,9}. Among these templates, polystyrene and colloidal silica spheres are commonly used due to their availability and ease of use. After the growth of solid particles on the template, post-synthetic treatments are required to generate the interior cavity of the structure. For instance, thermal calcination is performed for polystyrene templates; while hydrolysis is conducted for silica templates^{5,10}. Besides these hard/soft-templating approaches, the preparation of colloidal hollow particles using self-template approach is also possible. In this approach, the colloidal particle would transform into a hollow structure at longer reaction duration due to a chemical potential gradient between the interior and exterior of the particle. This phenomenon is called "Ostwald ripening" or coarsening in the field of material sciences⁷. Aside from the use of chemical potential gradient, diffusion gradients between two materials are also used to fabricate hollow structures. This phenomenon is called Kirkendall diffusion between two materials⁶.

1.2. Objectives and Scope

In the light of these problems, this thesis aims to study the synthesis and applications of complex hollow structures. Chapter 2 presents a literature review on several synthetic approaches towards hollow structured materials. These are divided into template-based, chemical transformation, and Ostwald ripening approaches. In

Chapter 3, a seed-mediated synthesis of multi-shelled Cu₂O hollow core-shell structure and its application in glucose sensing are presented. This chapter gives a foundation for the subsequent chapters since the methodology and results in this chapter is also used in subsequent chapters. Chapter 4 presents a study on the structural transformation of Cu₂O core-shell with predesigned architecture and reactivity and its passivized form upon chemical reactions. On the other hand, Chapter 5 presents a seed-mediated synthetic approach for an M@Cu₂O core-shell (M = Au, Ag, Au/Ag, Pd) structures and a correlation of different core-material with respect to its catalytic property. Chapter 6 describes the mechanism and the synthetic preparation of self-assembled manganese silicate hollow nanosphere and its metal doped analogues. Finally, Chapter 7 concludes the thesis and provides recommendations on future research work.

1.3 Purpose of study and Significance

Although studies regarding the synthesis of inorganic hollow structures had been conducted for several decades, the preparation of these materials remains a challenge. This difficulty is due to the lack of a theoretical model that can predict an optimal synthetic parameter for generating monodisperse and homogeneous hollow materials for different types of material. As a result of this limitation, research on hollow material synthesis has been done based on “trial and error” approach rather than a classical scientific method. Moreover, proposed synthetic mechanisms are not confirmed *in-situ*, and their computational simulations are understudied.^[11,12] In addition to this problem, the technological application of this hollow structure is still at its early stage of research and commercialization of these technologies has not been implemented. Therefore, this dissertation aims to develop several synthetic

approaches that enables composition, structural and symmetric control of nanostructures, and to demonstrate the correlation of structural features with respect to its improved property on certain applications like photocatalysis, catalysis, and electrochemistry.

1.4 Scopes and Limitations

This dissertation would only focus on the synthesis and applications of inorganic metal-oxides and silicate hollow structures. Organic materials are not included in this study. Moreover, theoretical and molecular simulations of Ostwald ripening will not be considered in this dissertation due to technical constraints. Finally, the preparation and application of non-spherical hollow structures are also not considered in this study.

References

1. Kim, S.-W.; *et al.* Fabrication of Hollow Palladium Spheres and Their Successful Application to the Recyclable Heterogeneous Catalyst for Suzuki Coupling Reactions. *J. Am. Chem. Soc.* **2002**, *124*, 7642-7643.
2. Zhang, H.; *et al.* One-pot Synthesis and Hierarchical Assembly of Hollow Cu₂O Microspheres with Nanocrystals-composed Porous Multishell and Their Gas-Sensing Properties. *Adv. Funct. Mater.* **2007**, *17*, 2766-2771.
3. Zhou, L.; Zhao, D.; Lou, X. LiNi_{0.5}Mn_{1.5}O₄ Hollow Structures as High-Performance Cathodes for Lithium-Ion Batteries. *Angew. Chem. Int. Ed.* **2012**, *51*, 239-241.

4. Wang, Y.; *et al.* Chemical-Template Synthesis of Micro/Nanoscale Magnesium Silicate Hollow Spheres for Waste-Water Treatment. *Chem. Eur. J.* **2010**, *16*, 3497-3503.
5. Caruso, F.; Caruso, R.A.; Möhwald, H. Nanoengineering of Inorganic and Hybrid Hollow Spheres by Colloidal Templating. *Science* **1998**, *282*, 1111-1114.
6. Yin, Y.D.; *et al.* Formation of Hollow Nanocrystals Through the Nanoscale Kirkendall Effect. *Science* **2004**, *304*, 711-714.
7. Yang, H.G.; Zeng, H.C. Preparation of Hollow Anatase TiO₂ Nanospheres *via* Ostwald Ripening. *J. Phys. Chem. B* **2004**, *108*, 3492-3495.
8. Peng, Q.; Dong, Y.; Li, Y. ZnSe Semiconductor Hollow Microspheres. *Angew. Chem. Int. Ed.* **2003**, *42*, 3027-3030.
9. Wang, W.Z.; *et al.* Synthesis of PbTe Nanoboxes Using a Solvothermal Technique. *Adv. Mater.* **2005**, *17*, 2110-2114.
10. Wong, Y.J.; *et al.* Revisiting the Stober Method: Inhomogeneity in Silica Shells. *J. Am. Chem. Soc.* **2011**, *133*, 11422-11425.
11. Belova, I.V.; Murch, G.E. Analysis of the Formation of Hollow Nanocrystals: Theory and Monte Carlo Simulation. *J. Phase Equilib. Diffus.* **2005**, *26*, 430-434.
12. Evteev, A.V.; *et al.* Shrinking Kinetics by Vacancy Diffusion of a Pure Element Hollow Nanosphere. *Philos. Mag.* **2007**, *87*, 3787-3796.

Chapter 2. Literature Review

In this chapter, we will review several synthetic strategies on colloidal hollow structures. These strategies are template-based approach, chemical transformations, and Ostwald ripening. A brief description of template-based approaches and chemical transformations would be given. Ostwald ripening would be discussed in details.

2.1 Template Based Approaches

Template-based approaches require the use of existing nanomaterial wherein heterogeneous nucleation of other particles can occur¹. Subsequently these templates are removed through either physical or chemical treatments¹. These treatments include chemical etching² and decomposition³. These methods offer the advantage of preparing hollow nanomaterials with monodisperse size distribution due to inhibition of homogeneous nucleation in the solution. The template can be classified into hard or soft-templates. Hard templating methods require the use of solid phase materials as a substrate for particle growth⁴. On the other hand, soft template methods use either surfactants, micelles, vesicles, coordination polymers or gas bubbles as the substrate for the formation of the hollow nanoparticle^{3,5-9}. It should be noted that the size of hollow nanostructures prepared through template-based methods is always larger than their template particles. In addition, the final shape of the particle does not always follow their template's morphology, which depends on the growth kinetics of deposited materials. For example, at a greater supersaturation, the growth particle may ignore the presence of the template, and homogeneous nucleation can occur¹⁰. In addition, branching of the growth particle can occur due to a supersaturation driven crystallographic mismatch effect^{10,11}.

2.2 Chemical Transformation

In addition to template methods, chemical conversion of nanomaterial can result in hollow nanomaterials with different composition. This hollowing approach requires the conversion of the precursor to another hollow structure with different composition. Compared with the transformation of bulk materials, chemical transformation of nanomaterials occurs more rapidly due to its larger surface to volume ratio, which reduces the diffusion barrier during chemical reactions¹². Currently, most reported chemical transformation approaches that result in hollow structures are classified as ion exchange, galvanic exchange, or chemical dissolution. The formation of interior hollow regions is usually attributed to Kirkendall diffusion^{13,14}. Kirkendall diffusion is a phenomenon where vacancy regions are generated due to the difference in diffusion rate between two atomic components of the particle.

The kinetics and selectivity of chemical transformation of nanostructures also depend on the surface structure of the precursor. It has been established that different surface orientations or facets have various surface energy¹⁵. This property determines the selectivity and sequence of a particle reaction¹⁵. For example, the Xia group demonstrated this concept by conducting a facet selective galvanic exchange of silver truncated nanocube with HAuCl_4 (Figure 2.1)¹⁶. The Ag nanocube (100) facets were passivated with polyvinylpyrrolidone (PVP). During its galvanic replacement, they observed the dissolution of (111) facet of Ag and the formation of a cage like structure¹⁶. Their result implied that surface passivation can also affect the architecture of the product after chemical reactions.

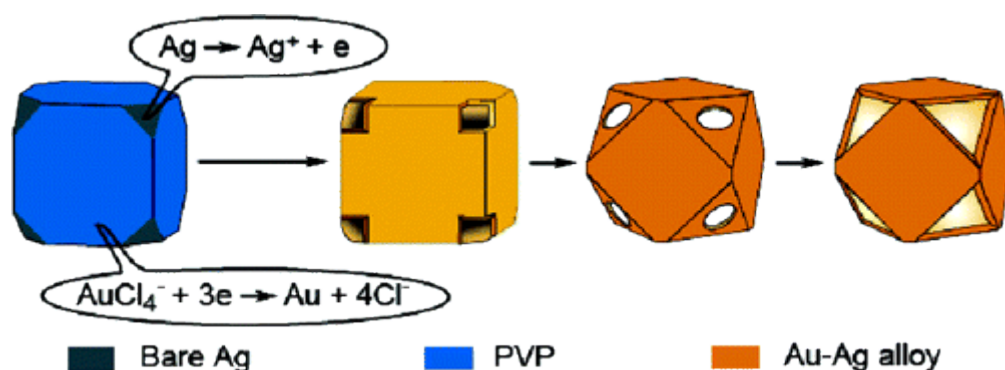


Figure 2.1 Schematic illustration detailing all major steps involved in the formation of Au-Ag nanocages with well-controlled pores at the corners. The success of this synthesis relies on the use of Ag nanocubes bearing truncated corners at (111) facets to react with aqueous HAuCl₄. The pore size is mainly determined by the molar ratio of HAuCl₄ to Ag. Reprinted with permission from the American Chemical Society (J. Am. Chem. Soc., 2006, 128, 14776–14777).

2.2.1 Cation/Anion Exchange Reaction

Most inorganic semiconductor nanostructures are ionic compounds. One feature of ionic compounds is that these compounds possess ionic bonds, which permits an exchange of cations or anions with other constituent elements in ionic form. Cation exchange of semiconductor is achieved with mutual diffusion with other cations. This process enables the maintenance of structural features after reaction since the structural framework of a semiconductor depends on its anions. As a result, cation exchange reactions do not result in hollow structure formation^{12,17,18}.

On the other hand, anion exchange reactions of inorganic nanostructure can result in hollow structures¹⁹⁻²⁵. The driving force of these reactions is the stability difference between reactant and product. For anion exchange in solutions, the difference in solubility between the reactant and product is the driving force²³. Since the diffusion rate of anions is lower compared with cations, the anion exchange

usually occurs at higher temperature. The solubility for metal chalcogenide decreases as the anion radius increase; therefore O^{2-} will be displaced by S^{2-} and S^{2-} will be displaced by Se^{2-} .

2.2.2 Galvanic Exchange Reaction

The galvanic replacement reaction of nanomaterials has been widely used to prepare hollow metallic nanostructures^{14,26,27}. This reaction is thermodynamically driven by the difference in the standard reduction potential between the reactant and the dissolved metal ion in the solution. The hollow region are generated through oxidation of the reactant structure and its subsequent dissolution. The variation in temperature, pH, and concentration can affect the value of the reduction potential. As a result, some replacement reactions are reversible Although the method has been widely reported to prepare hollow metallic structure^{14,26-28}, this reaction has been recently demonstrated to be applicable for oxide materials²⁹.

2.3 Ostwald Ripening

In 1900, Wilhelm Ostwald systematically investigated the influence of the size of crystals on their solubility, and he observed that smaller crystals have higher solubility compared with larger crystals³⁰. This phenomenon, which bears his name “Ostwald ripening”, often refers to the coarsening and recrystallization process in a nearly saturated solution and according to its definition recommended by IUPAC in 2007, this phenomenon refers to the “dissolution of small crystals or sol particles and the redeposition of the dissolved species on the surfaces of larger crystals or sol particles”³¹. Moreover, the driving force for this phenomenon can be attributed to the fact that smaller particles possess higher interfacial energy; hence, their total Gibbs

energy is greater compared with larger particles. Though it had been known for six decades, the phenomenon was not understood fully until Lifshitz, Slyozov, and Wagner proposed a theoretical model in 1961^{32,33}. Moreover, it also took more than a century to apply this phenomenon for the general synthesis of hollow structures when emerging research interests towards the preparation of complex nanostructured materials became intense after 2000^{13,34,35}.

2.3.1 Ostwald ripening on random crystallite aggregates

In 2004, Yang and Zeng showed that the Ostwald ripening phenomenon could be used as a template-free approach to synthesizing hollow spheres of TiO₂³⁴. Moreover, this pioneering work has paved the way for synthesizing hollow structures without the use of the template. Figure 2.1 shows a schematic illustration and TEM images of this ripening mechanism. During this process, the TiO₂ phase is first obtained through the hydrolysis of TiF₄ precursor under hydrothermal conditions that produced primary TiO₂ crystallites. Subsequently, random aggregation of these crystallites minimize total interfacial energy, leading to a spherical structure (Fig. 2.1B). As the supersaturation of the solution reached near equilibrium, the central part of the spheres started to evacuate through dissolution and generated an internal cavity. Upon the formation of interior space (i.e., dissolution of inner crystallites), crystallites located at the shell showed better crystallinity, which indicates that Ostwald ripening is the underlying mechanism. Later, similar works have demonstrated that the Ostwald ripening is a general mechanism in making hollow structures for many other metal oxides and sulfides after longer reaction durations^{36,37}. Although the Ostwald ripening hollowing mechanism proposed by Yang and Zeng is an important discovery, their methodology cannot observe the in-situ particle transformation. In addition, the

primary assumption of this theory is that particles in the central region are more energetic compared with those on the particle exterior, which is still difficult to verify.

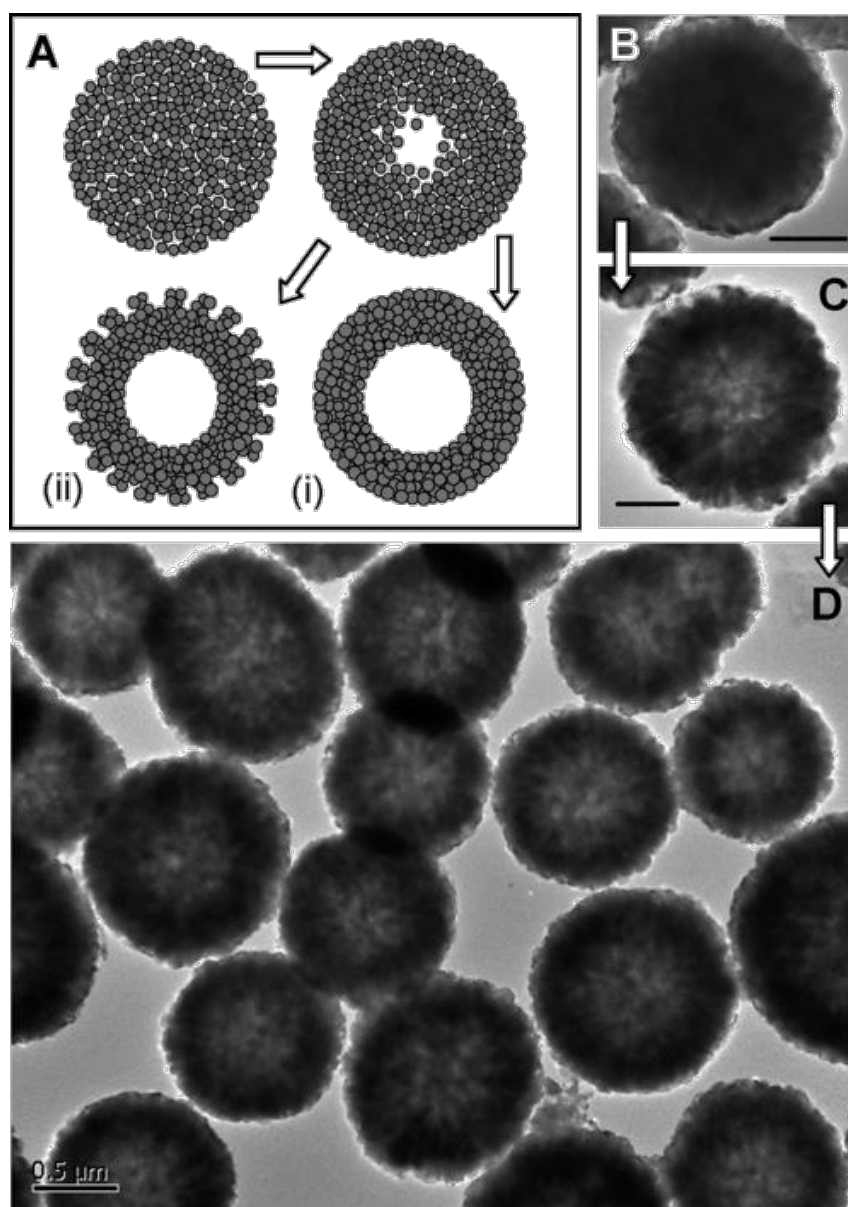


Figure 2.2 The formation process (a) of anatase TiO_2 hollow spheres via Ostwald ripening - the random aggregation of primary crystallites to generate a sphere and its subsequent evacuation. Two synthetic routes can be further devised: (i) formation of a hollow sphere, and (ii) formation of a hollow sphere with additional surface fine structures. TEM images (b–d) illustrate the evolution of TiO_2 spheres synthesized with 30 mL of TiF_4 (1.33 mM) at 180 °C with different reaction times: 2 h (b; scale bar = 200 nm), 20 h (c; scale bar = 200 nm), and 50 h (d; scale bar = 500 nm). Reprinted with permission from the American Chemical Society (*J. Phys. Chem. B*, 2004, 108, 3492–3495).

Therefore, in-situ mechanism studies are required to verify the mechanism. In addition to generating hollow interiors, Ostwald ripening enables modification of the structure's physical properties by simply varying the ripening time³⁶. Several reports demonstrated the unique optical and electronic band gap properties of Cu₂O hollow spheres obtained through Ostwald ripening^{36,38}.

2.3.2 Ostwald ripening on ordered crystallite aggregates

Deviating from the classical crystal growth models, Penn and Banfield have proposed that individual crystallites can merge directly with their neighbouring crystallites possessing same crystallographic orientation to minimize its interfacial energy³⁹. This model of crystal growth is termed as oriented attachment³⁹. Moreover, crystallographic interfaces among the attached crystalline units could either be correctly aligned or slightly misoriented which may result in dislocations and other defects in the resultant crystal structure^{39,40}. Since crystalline materials possess a certain degree of surface anisotropy, the product morphology is expected to be non-spherical or only quasi-spherical.

For the attachment process, initial small crystallites serve as “building-blocks” to construct a bulk product whose final shape in many cases is quite similar to that of its primary crystallites. In this regard, the attachment process can be further combined with the Ostwald ripening to produce non-spherical (faceted) hollow structures⁴¹. This combined approach has enabled the synthesis of non-spherical hollow structures without the use of the template, and it is shown in Figure 2.3. Based on the figure, primary crystallites may either randomly aggregate to form a solid spherical precursor (Fig. 2.2a) or completely follow an oriented attachment mechanism to form a non-spherical precursor, depending on their growth conditions (Fig. 2.3a). Once the solid

precursor is formed, Ostwald ripening of interior crystallites occurs to generate respective hollow structures. This method was first demonstrated for the hollowing of Cu_2O cubes, as shown in Figure 2.3. Since oriented attachment growth typically leads to formation of mesocrystals, dislocations and crystal defects among the attached crystallites are anticipated owing to misorientation and non-faceted primary crystallites. In addition, the crystallites located in the central part are small, and their packing density is low. For this reason, solvothermal preparation of cubic crystals of Cu_2O under

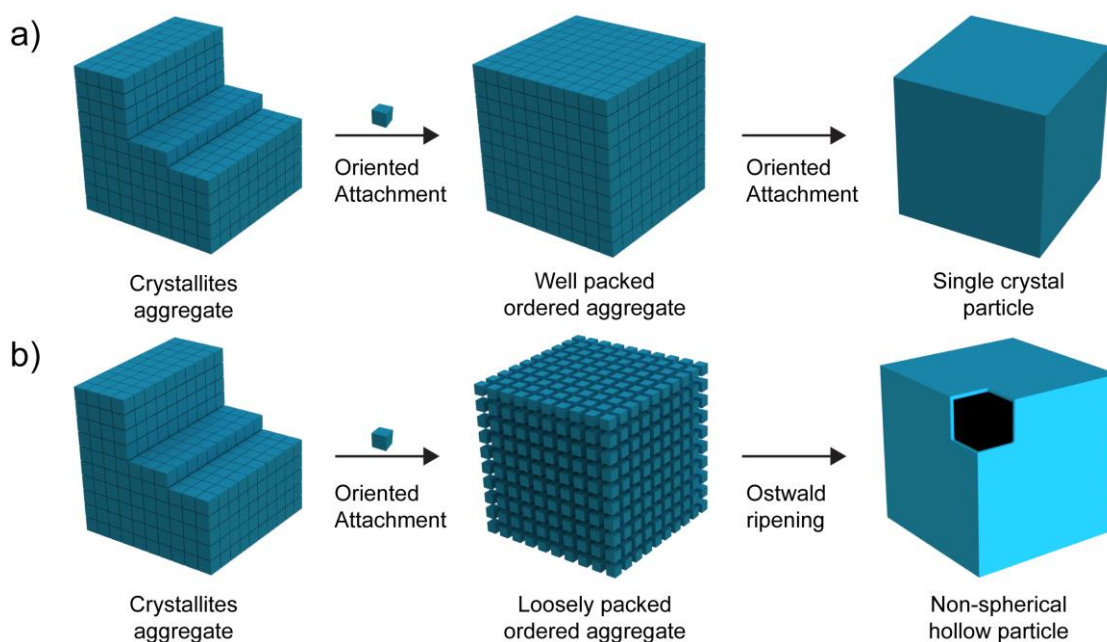


Figure 2.3 Schematic illustration of oriented attachment and its combination with Ostwald ripening to generate non-spherical hollow structures. (a) Oriented attachment of well packed ordered crystallite aggregate and (b) oriented attachment coupled with Ostwald ripening for a loosely packed aggregate to generate non-spherical hollow particles.

synthesis condition with a low water content results in a loose ordered aggregate (Fig. 2.3b)⁴¹. Therefore, longer reaction durations for this system generate central voids for the Cu_2O crystals *via* Ostwald ripening. Later, the above combined concept of oriented attachment with Ostwald ripening was adopted widely in explaining the

formation of hollow interiors observed in many non-spherical inorganic solids such as CaTiO_3 , CeO_2 , CoFe_2O_4 , In_2O_3 , NiO , PbSe , SnO_2 , SrZrO_3 , ZnO , and $\text{K}_{0.22}\text{Co}_{0.58}\text{Fe}_{2.2}(\text{CN})_6$ ⁴²⁻⁵².

2.3.3 Ostwald ripening in Core-shell and Yolk-shell Structure

Depending on the aggregation patterns of primary crystallites or particles, using Ostwald ripening to generate a void space is not limited to only the central region. In fact, the simple concept of Ostwald ripening for a central space creation can be further extended; it can be better classified as symmetric and asymmetric Ostwald ripening⁵³. The two ripening mechanisms can also be used to create homogeneous core-shell, yolk-shell, or basketlike hollow structures. Figure 2.4a gives some typical hollowing modes of Ostwald ripening to generate cavities within a crystallite aggregate with increasing structural complexity. The type of symmetric or asymmetric ripening can be further assigned to them, namely, central hollowing (scheme i, symmetric), the formation of core-shell or yolk-shell (scheme ii, symmetric), and the formation of an off-centre core or yolk (scheme iii, asymmetric). In addition, the basic hollowing schemes can be combined in order to prepare even more complex hollow structures. For instance, an oscillating assemblage of primary crystallites with different sizes or packing densities may lead to the formation of multiple-shelled hollow structures, in which different hollowing modes could occur simultaneously (e.g., scheme iv, a combined scheme of schemes i and iii)⁵³. Figure 2.4b depicts the process for creating an additional interior space between the core and shell in schemes ii to iv, where surface crystallites are smaller or less compact. Due to the presence of Ostwald ripening, surface crystallites are grown at the expense of the underneath ones,

resulting in a more condensed surface shell and a concentric vacant space. If this process continues, the surface shell

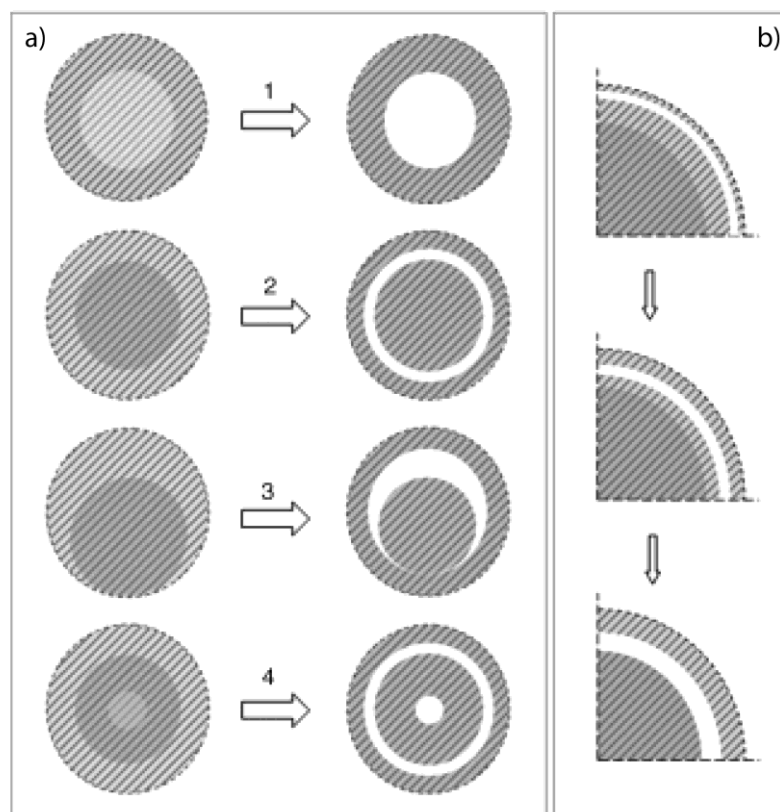


Figure 2.4 Schematic illustrations of different modes of Ostwald ripening to generate an interior void: (a) interior hollowing (i), symmetric Ostwald ripening for the core-shell structure (ii), asymmetric Ostwald ripening for the core-shell structure (iii), and symmetric Ostwald ripening for double shells (iv), and (b) symmetric Ostwald ripening for the core-shell structure, where the interior crystallites near the surface region would first dissolve and recrystallise. Reprinted with permission from WILEY-VCH Verlag GmbH & Co. KGaA, Weinheim (Small, 2005, 1, 566–57)

gets thicker, while the vacant space moves towards the centre of the sphere. Whether the hollowing process is related to the symmetric or asymmetric Ostwald ripening depends on the initial packing style and aggregative density of crystallites. In addition, the ripening conditions could also be critical. To a hollowing structure, for example, the degree of the supersaturation, concentration gradient of solute, convection pattern of liquid, temperature fluctuation, and incidental experimental disturbance might determine the actual ripening processes.

Subsequent investigations on a series of homogeneous core-/yolk-shell structures have further affirmed the above hollowing mechanisms⁵⁴⁻⁷⁷. Concerning these ripening processes, however, some general points should be taken into account. Inside a ripening medium, for example, more complex structures are likely to be less stable, because a continuous matter-relocation proceeds from the central portion to the external surfaces that have lower surface energies. Another important observation is that a longer ripening process could turn a complicated structure into a simpler one which often has a larger interior. In some extreme cases, even the simplest hollow structures may not be observable at all because they might have collapsed entirely and transformed into large pieces of crystal if one does not monitor the solid intermediates during the structural evolution. Although they can be structurally complex, the core/yolk and shell products of Figure 2.4 are made of the same material (i.e., the so-called homogeneous core-/yolk-shell structures). It can be easily recognized that the Ostwald ripening is not only applicable for making such complex monophasic structural products, but is also extendable to the preparation of composite nanomaterials (i.e., so-called heterogeneous core-/yolk-shell structures) once additional material phases are included in the solid precursors prior to Ostwald ripening. Indeed, this idea was first tested in our preparation of Au-TiO₂ core-/yolk-shell “nanoreactors”⁷⁸. Figure 2.5 shows a schematic diagram of two synthetic routes developed in that study. The gold nanoparticles serve as a hard template for the deposition of TiO₂ crystallites (steps i and ii). After a longer process time, Ostwald ripening initiates preferably at the interface between the core and the shell due to structural strains of the different materials. As a result, heterogeneous hollow core-shell structures of Au-TiO₂ are formed (step iii). Quite intriguingly, the TiO₂ shell in

the resultant Au–TiO₂ composite is permeable and therefore the Au–TiO₂ core–shell can be treated as a membrane reactor. It can be modified further by allowing an overgrowth on its core phase for size-tuning (steps iv and v),^{79,80} or allowing the inclusion of molecular species to the surfaces of the core and/or the shell (step vi). Generally speaking, this approach is suitable for synthesizing inorganic heterogeneous hollow core–shell structures provided that the shell material can grow or deposit onto

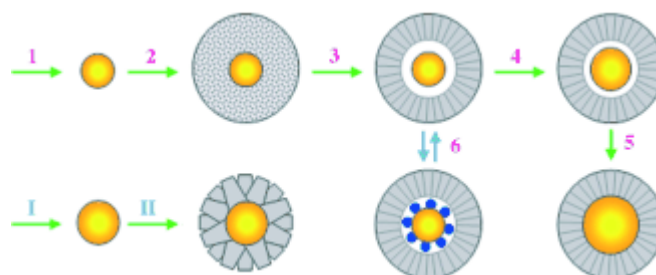


Figure 2.5 A combined seed-mediated and Ostwald ripening approach to generate heterogeneous hollow core–shell structures: (i) forming a metallic core, (ii) aggregating primary (shell) particles on the core, (iii) Ostwald ripening at the core–shell interface, (iv and v) tuning the core size through an interior growth, and (vi) modifying a core surface through the adsorption of inorganic ions or organic molecules. Reprinted with permission from WILEY-VCH Verlag GmbH & Co. KGaA, Weinheim (*Angew. Chem., Int. Ed.*, 2005, 44, 4342–4345).

the core template and the core material is more stable or less soluble. Because noble metals are relatively inert in solution compared to their transition metal oxide counterparts, the above hollowing scheme has been adopted primarily for the synthesis of hollow core–shell structures with the inclusion of noble metals and transition-metal-oxides, though it is also applicable for the preparation of heterogeneous hollow core–shell structures of metal-oxide composites. For example, a broad array of such core–shell structures (e.g., Au–Cu₂O⁸¹, Ag–Cu₂O⁸¹, Ag–Fe₃O₄⁸², Pd–Fe₃O₄⁸², Pt–CeO₂⁸³, and Fe₂O₃–SnO₂⁸⁴, etc.) has been synthesized in recent years.

2.3.4 Ostwald ripening in Multi-layered Hollow Structures

Even in the early stage of process development, the high versatility of Ostwald ripening for structural and morphological engineering was recognized. For example, the possibility of modifying a hollowed structure was elucidated by refilling the previously evacuated central void (by a “two-pot” or “multi-pot” solution method) and re-engineering surface structures (Fig. 2.2a)³⁴. On the other hand, as discussed earlier, Ostwald ripening can generate multi-shelled hollow structures (Fig. 2.4a, scheme iv) in a “one-pot” manner. However, though it is simple, this single-step method depends on the size variation and packing density of the initial crystallites of precursors but these intrinsic structural parameters are difficult to control deliberately. Recently, successive solid deposition and Ostwald ripening have been proven to be an efficient process for preparing complex hollow structures⁸⁵. Using this new solution approach, multi-shelled hollow structures of Cu₂O have been synthesized successfully with control of the shell number and morphology as demonstrated in Figure 2.6. The above multiple addition processes involves deposition of new crystallites to a hollow sphere generated at a previous stage via Ostwald ripening. Since they are freshly formed, the new crystallite aggregates are more prone to Ostwald ripening. As a result, an inter-shell space is created between the new and old ones, in addition to an existing central void. Quite interestingly, the dimension of the inner shell (which is “older”) would not seem to be changed because it is better crystallised due to a longer ripening time. Furthermore, the deposition-then-ripening process can be repeated for several cycles to have multiple interior shells by continuously adding reactants into the growth solution, thereby gradually decreasing the shell thickness as the number of shells increases.

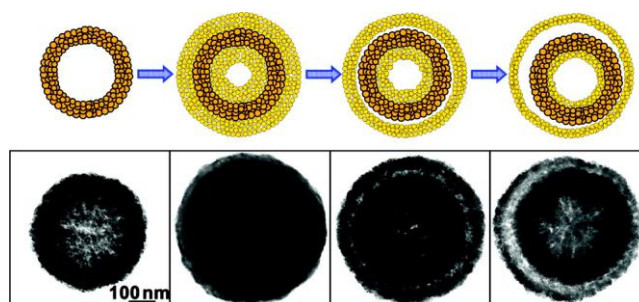


Figure 2.6 The process of successive phases of Ostwald ripening to form multi-shelled structures and corresponding TEM images of the samples. Reprinted with permission from the American Chemical Society (*J. Phys. Chem. C*, 2011, 115, 18479–18485).

2.3.5 The ubiquity of Ostwald ripening as a hollowing method

In most reported cases, Ostwald ripening is adopted as a hollowing approach for stoichiometric compounds. However, it should be pointed out that this mechanism can also be operative to create a hollow space for non-stoichiometric solid compounds, such as doped materials⁸⁶. The applicability was first elucidated for a Sn-doped TiO₂ system⁸⁶, and was later extended to many other doped materials^{63,74,87-89}. Compared to pure substances, doped materials may offer novel functionalities and advantages. For instance, doping in semiconductors results in the modification of their energy band structures and thus changes their performances over an extensive range of applications⁹⁰.

According to the IUPAC definition, the phenomenon of Ostwald ripening is not entirely limited to crystalline materials³¹. In a wider sense, this phenomenon only involves the minimization of the total Gibbs energy of crystallites/particles through dissolution and subsequent regrowth. Recently, we found that the above Ostwald ripening approach was also workable to create interior space for mesoporous SiO₂ spheres, despite the material being a non-crystalline solid⁹¹. By prolonging the reaction time at solvothermal conditions, a central void space was created within the

SiO₂ spheres while the mesopores of the shell were well preserved. Figure 2.7 depicts three such synthetic schemes. In this ripening process, it is assumed that primary SiO₂ particles (or oligomers), which were generated through the hydrolysis and condensation of silicon alkoxides (e.g., tetraethyl orthosilicate), randomly aggregate to form a spherical structure. Since aggregated primary particles also possess size distribution (as discussed earlier, the central particles are typically smaller due to rapid reaction and particle aggregation), Ostwald ripening would take place and generate a void in the central region of the spheres (Fig. 2.7a). This evolutionary process can be seen in Figure 2.8, together with the results of materials characterization. The surface of the initial sphere is composed of mesopores (Fig. 2.8a and b); increasing the reaction temperature results in the formation of irregular threadlike voids (Fig. 2.8c and d) which propagate at longer reaction durations (Fig. 2.8e,f). At a higher temperature, the rate of mass transport in solution increases, and a complete evacuation of interior SiO₂ via Ostwald ripening can be

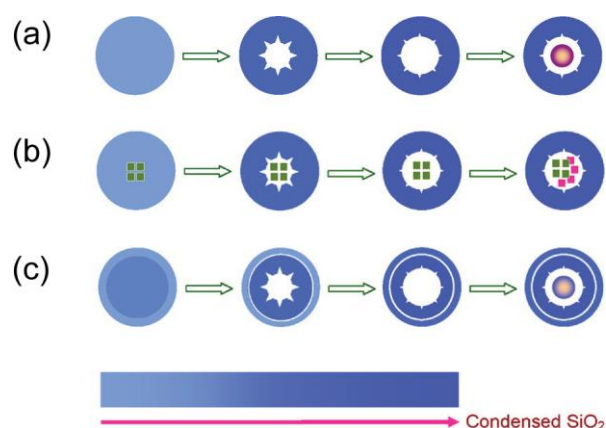


Figure 2.7 A schematic illustration of Ostwald ripening to generate interior voids for mesoporous SiO₂ spheres: (a) core-hollowing of mesoporous SiO₂, (b) encapsulation of nanoparticles into the mesoporous SiO₂ followed by Ostwald ripening, and (c) creation of a less dense surface region and formation of a double-shelled structure of SiO₂. The degree of SiO₂ densification is represented by a range of blue colours; a deeper colour indicates a more condensed SiO₂ phase. Note that additional material phases (in different colours) can also be included in the central cavity through an interior growth in all of the cases. Reprinted with permission from the American Chemical Society (Chem. Mater., 2011, 23, 4886–4899).

achieved (Fig. 2.8g and h). Moreover, nanoparticles can be preinstalled inside a solid sphere of SiO₂ and then an interior space is created (Fig. 2.7b). Inside this new space, different nanoparticles can also be grown directly in the central cavity (Fig. 2.7b). Similar to scheme iv of Figure 2.4a, by controlling the reaction parameters in synthesis, simultaneous Ostwald ripening could take place in both the central region and the interface region, producing double-shelled mesoporous SiO₂ spheres (Fig. 2.7c). In addition to the silica and conventional inorganic materials, the possibility of using Ostwald ripening to create hollow structures has also been proven to be workable for new types of functional materials, such as metal–organic frameworks or coordination polymers. In particular, this mechanism has been adopted to explain the creation of interior space and shell porosity for inorganic–polymer hybrids, such as iron-based and cobalt-based ferrocenyl coordination polymer microspheres^{92,93}.

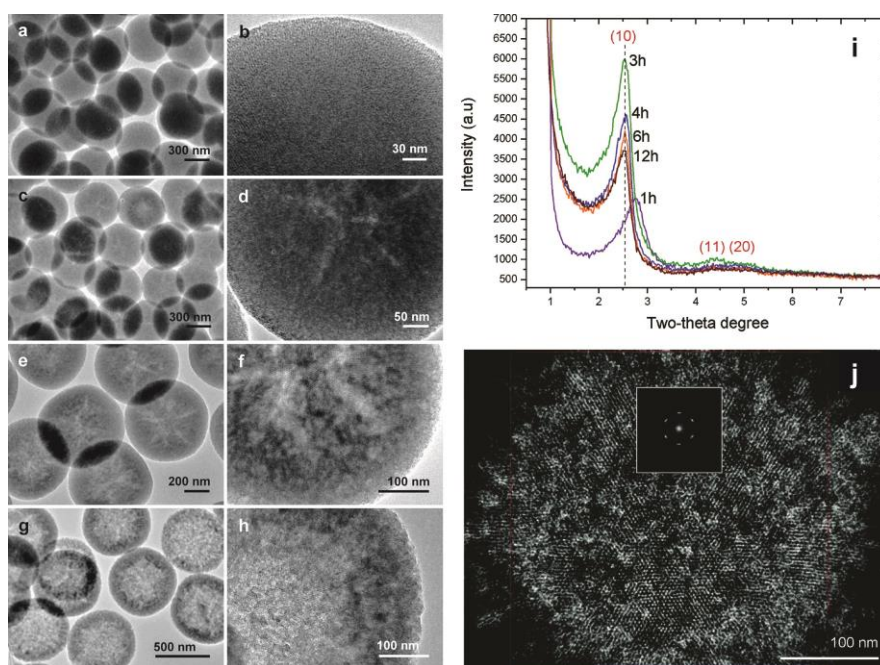


Figure 2.8 Structural features (TEM images) of mesoporous SiO₂ hollow spheres generated via Ostwald ripening using various growth conditions: (a and b) 100 °C for 3 h, (c and d) 120 °C for 2.3 h, (e and f) 120 °C for 4 h, and (g and h) 180 °C for 4 h, X-ray diffraction pattern of hollow mesoporous SiO₂ at various reaction times (i), and a HRTEM image (j) and its related FFT pattern (inset) of a mesoporous hollow sphere of SiO₂. Reprinted with permission from the American Chemical Society (Chem. Mater., 2011, 23, 4886–4899).

References

- 1 Caruso, F., Caruso, R. A. & Mohwald, H. Nanoengineering of inorganic and hybrid hollow spheres by colloidal templating. *Science* **282**, 1111-1114, doi:10.1126/science.282.5391.1111 (1998).
- 2 Wang, Z., Wang, Z., Wu, H. & Lou, X. W. Mesoporous Single-crystal CoSn(OH)₆ Hollow Structures with Multilevel Interiors. *Sci. Rep.* **3**, doi:<http://www.nature.com/srep/2013/130306/srep01391/abs/srep01391.html#supplementary-information> (2013).
- 3 Zhang, G., Yu, L., Wu, H. B., Hoster, H. E. & Lou, X. W. Formation of ZnMn₂O₄ Ball-in-Ball Hollow Microspheres as a High-Performance Anode for Lithium-Ion Batteries. *Adv. Mater.* **24**, 4609-4613, doi:10.1002/adma.201201779 (2012).
- 4 Zheng, M. *et al.* Simple Shape-Controlled Synthesis of Carbon Hollow Structures. *Inorg Chem* **49**, 8674-8683, doi:10.1021/ic9024316 (2010).
- 5 Peng, Q., Dong, Y. & Li, Y. ZnSe semiconductor hollow microspheres. *Angew. Chem. Int. Ed.* **42**, 3027-3030, doi:10.1002/anie.200250695 (2003).
- 6 Gu, F., Li, C. Z., Wang, S. F. & Lü, M. K. Solution-Phase Synthesis of Spherical Zinc Sulfide Nanostructures. *Langmuir* **22**, 1329-1332, doi:10.1021/la052539m (2005).
- 7 Liu, B. & Zeng, H. C. Hollow ZnO Microspheres with Complex Nanobuilding Units. *Chem. Mater.* **19**, 5824-5826, doi:10.1021/cm702121v (2007).
- 8 Yu, M., Wang, H., Zhou, X., Yuan, P. & Yu, C. One Template Synthesis of Raspberry-like Hierarchical Siliceous Hollow Spheres. *J Am Chem Soc* **129**, 14576-14577, doi:10.1021/ja077110r (2007).
- 9 Cho, W., Lee, Y. H., Lee, H. J. & Oh, M. Multi Ball-In-Ball Hybrid Metal Oxides. *Adv. Mater.* **23**, 1720-+, doi:10.1002/adma.201004493 (2011).
- 10 Liu, X. Y. & Lim, S. W. Templating and supersaturation-driven anti-templating: Principles of biomineral architecture. *J Am Chem Soc* **125**, 888-895, doi:10.1021/ja020355d (2003).
- 11 Yang, H. G. & Zeng, H. C. Lattice strain directed synthesis of anatase TiO₂ single-crystal microplatelet arrays on alpha-MoO₃ (010) template. *J Phys Chem B* **108**, 819-823, doi:10.1021/jp036760o (2004).
- 12 Son, D. H., Hughes, S. M., Yin, Y. & Paul Alivisatos, A. Cation Exchange Reactions in Ionic Nanocrystals. *Science* **306**, 1009-1012, doi:10.1126/science.1103755 (2004).

- 13 Yin, Y. D. *et al.* Formation of hollow nanocrystals through the nanoscale Kirkendall Effect. *Science* **304**, 711-714, doi:10.1126/science.1096566 (2004).
- 14 Gonzalez, E., Arbiol, J. & Puntès, V. F. Carving at the Nanoscale: Sequential Galvanic Exchange and Kirkendall Growth at Room Temperature. *Science* **334**, 1377-1380, doi:10.1126/science.1212822 (2011).
- 15 Vitos, L., Ruban, A. V., Skriver, H. L. & Kollár, J. The surface energy of metals. *Surf Sci* **411**, 186-202, doi:[http://dx.doi.org/10.1016/S0039-6028\(98\)00363-X](http://dx.doi.org/10.1016/S0039-6028(98)00363-X) (1998).
- 16 Chen, J. *et al.* Facile Synthesis of Gold–Silver Nanocages with Controllable Pores on the Surface. *J Am Chem Soc* **128**, 14776-14777, doi:10.1021/ja066023g (2006).
- 17 Feng, S. & Xu, R. New Materials in Hydrothermal Synthesis. *Accounts Chem Res* **34**, 239-247, doi:10.1021/ar0000105 (2000).
- 18 Sadtler, B. *et al.* Selective Facet Reactivity during Cation Exchange in Cadmium Sulfide Nanorods. *J Am Chem Soc* **131**, 5285-5293, doi:10.1021/ja809854q (2009).
- 19 Xiong, S. L. & Zeng, H. C. Serial Ionic Exchange for the Synthesis of Multishelled Copper Sulfide Hollow Spheres. *Angew Chem Int Edit* **51**, 949-952, doi:10.1002/anie.201106826 (2012).
- 20 Park, J., Zheng, H., Jun, Y.-w. & Alivisatos, A. P. Hetero-Epitaxial Anion Exchange Yields Single-Crystalline Hollow Nanoparticles. *J Am Chem Soc* **131**, 13943-13945, doi:10.1021/ja905732q (2009).
- 21 Feldman, Y. *et al.* Bulk Synthesis of Inorganic Fullerene-like MS₂ (M = Mo, W) from the Respective Trioxides and the Reaction Mechanism. *J Am Chem Soc* **118**, 5362-5367, doi:10.1021/ja9602408 (1996).
- 22 Xie, Y. *et al.* CdS/CdSe core/sheath nanostructures obtained from CdS nanowires. *Chem Commun*, 1969-1970, doi:10.1039/A905669F (1999).
- 23 Pang, M. L. & Zeng, H. C. Highly Ordered Self-Assemblies of Submicrometer Cu₂O Spheres and Their Hollow Chalcogenide Derivatives. *Langmuir* **26**, 5963-5970, doi:10.1021/la904292t (2010).
- 24 Pang, M. L., Hu, J. Y. & Zeng, H. C. Synthesis, Morphological Control, and Antibacterial Properties of Hollow/Solid Ag₂S/Ag Heterodimers. *J Am Chem Soc* **132**, 10771-10785, doi:10.1021/Ja102105q (2010).
- 25 Shim, H.-S. *et al.* Diameter-Tunable CdSe Nanotubes from Facile Solution-Based Selenization of Cd(OH)₂ Nanowire Bundles for Photoelectrochemical Cells. *Chem. Mater.* **21**, 1875-1883, doi:10.1021/cm8034483 (2009).

- 26 Sun, Y. G. & Xia, Y. N. Shape-controlled synthesis of gold and silver nanoparticles. *Science* **298**, 2176-2179, doi:10.1126/science.1077229 (2002).
- 27 Lu, X. *et al.* Mechanistic Studies on the Galvanic Replacement Reaction between Multiply Twinned Particles of Ag and H₂AuCl₄ in an Organic Medium. *J Am Chem Soc* **129**, 1733-1742, doi:10.1021/ja067800f (2007).
- 28 Zhang, H. *et al.* Facile Synthesis of Pd–Pt Alloy Nanocages and Their Enhanced Performance for Preferential Oxidation of CO in Excess Hydrogen. *Acs Nano* **5**, 8212-8222, doi:10.1021/nn202896q (2011).
- 29 Oh, M. H. *et al.* Galvanic Replacement Reactions in Metal Oxide Nanocrystals. *Science* **340**, 964-968, doi:10.1126/science.1234751 (2013).
- 30 Ostwald, W. On the assumed isomerism of red and yellow mercury oxide and the surface-tension of solid bodies. *Zeitschrift Fur Physikalische Chemie--Stoichiometrie Und Verwandtschaftslehre* **34**, 495-503 (1900).
- 31 Aleman, J. *et al.* Definitions of terms relating to the structure and processing of sols, gels, networks, and inorganic-organic hybrid materials (IUPAC Recommendations 2007). *Pure Appl Chem* **79**, 1801-1827, doi:10.1351/pac200779101801 (2007).
- 32 Lifshitz, I. M. & Slyozov, V. V. THE KINETICS OF PRECIPITATION FROM SUPERSATURATED SOLID SOLUTIONS. *J Phys Chem Solids* **19**, 35-50, doi:10.1016/0022-3697(61)90054-3 (1961).
- 33 Wagner, C. THEORIE DER ALTERUNG VON NIEDERSCHLAGEN DURCH UMLOSEN (OSTWALD-REIFUNG). *Zeitschrift Fur Elektrochemie* **65**, 581-591 (1961).
- 34 Yang, H. G. & Zeng, H. C. Preparation of hollow anatase TiO₂ nanospheres via Ostwald ripening. *J Phys Chem B* **108**, 3492-3495, doi:10.1021/jp0377782 (2004).
- 35 Sun, Y. & Xia, Y. Shape-Controlled Synthesis of Gold and Silver Nanoparticles. *Science* **298**, 2176-2179, doi:10.1126/science.1077229 (2002).
- 36 Chang, Y., Teo, J. J. & Zeng, H. C. Formation of colloidal CuO nanocrystallites and their spherical aggregation and reductive transformation to hollow Cu₂O nanospheres. *Langmuir* **21**, 1074-1079, doi:10.1021/la0476711 (2005).
- 37 Cheng, Y., Wang, Y. S., Jia, C. & Bao, F. MnS hierarchical hollow spheres with novel shell structure. *J Phys Chem B* **110**, 24399-24402, doi:10.1021/jp063698x (2006).

- 38 Zhang, L. & Wang, H. Cuprous Oxide Nanoshells with Geometrically Tunable Optical Properties. *Acs Nano* **5**, 3257-3267, doi:10.1021/nn200386n (2011).
- 39 Penn, R. L. & Banfield, J. F. Imperfect oriented attachment: Dislocation generation in defect-free nanocrystals. *Science* **281**, 969-971, doi:10.1126/science.281.5379.969 (1998).
- 40 Pacholski, C., Kornowski, A. & Weller, H. Self-assembly of ZnO: From nanodots, to nanorods. *Angew Chem Int Edit* **41**, 1188+, doi:10.1002/1521-3773(20020402)41:7<1188::aid-anie1188>3.0.co;2-5 (2002).
- 41 Teo, J. J., Chang, Y. & Zeng, H. C. Fabrications of hollow nanocubes of Cu₂O and Cu via reductive self-assembly of CuO nanocrystals. *Langmuir* **22**, 7369-7377, doi:10.1021/la060439q (2006).
- 42 Yang, X. F. *et al.* Perovskite hollow cubes: morphological control, three-dimensional twinning and intensely enhanced photoluminescence. *J Mater Chem* **18**, 3543-3546, doi:10.1039/b808396g (2008).
- 43 Yang, X. F. *et al.* Formation Mechanism of CaTiO₃ Hollow Crystals with Different Microstructures. *J Am Chem Soc* **132**, 14279-14287, doi:10.1021/ja106461u (2010).
- 44 Chen, G. Z. *et al.* Template-free Synthesis of Single-Crystalline-like CeO₂ Hollow Nanocubes. *Cryst Growth Des* **8**, 4449-4453, doi:10.1021/cg800288x (2008).
- 45 Chen, G. Z., Zhu, F. F., Sun, X. A., Sun, S. X. & Chen, R. P. Benign synthesis of ceria hollow nanocrystals by a template-free method. *Crystengcomm* **13**, 2904-2908, doi:10.1039/c0ce00758g (2011).
- 46 Zhang, H., Zhai, C. X., Wu, J. B., Ma, X. Y. & Yang, D. R. Cobalt ferrite nanorings: Ostwald ripening dictated synthesis and magnetic properties. *Chem Commun*, 5648-5650, doi:10.1039/b812752b (2008).
- 47 Yang, H. X., Wang, S. P. & Yang, Y. Z. Zn-doped In₂O₃ nanostructures: preparation, structure and gas-sensing properties. *Crystengcomm* **14**, 1135-1142, doi:10.1039/c1ce06143g (2012).
- 48 Zhao, J. B., Wu, L. L. & Zou, K. Fabrication of hollow mesoporous NiO hexagonal microspheres via hydrothermal process in ionic liquid. *Mater Res Bull* **46**, 2427-2432, doi:10.1016/j.materresbull.2011.08.026 (2011).
- 49 Ye, T. N. *et al.* Controllable fabrication of perovskite SrZrO₃ hollow cuboidal nanoshells. *Crystengcomm* **13**, 3842-3847, doi:10.1039/c1ce05206c (2011).
- 50 Yao, K. X. & Zeng, H. C. Asymmetric ZnO nanostructures with an interior cavity. *J Phys Chem B* **110**, 14736-14743, doi:Doi 10.1021/Jp062751e (2006).

- 51 Yao, K. X. & Zeng, H. C. ZnO/PVP nanocomposite spheres with two hemispheres. *J Phys Chem C* **111**, 13301-13308, doi:10.1021/Jp072550q (2007).
- 52 Zhai, C. X., Du, N., Zhang, H. & Yang, D. R. Cobalt-iron cyanide hollow cubes: Three-dimensional self-assembly and magnetic properties. *J Alloy Compd* **509**, 8382-8386, doi:10.1016/j.jallcom.2011.05.073 (2011).
- 53 Liu, B. & Zeng, H. C. Symmetric and asymmetric Ostwald ripening in the fabrication of homogeneous core-shell semiconductors. *Small* **1**, 566-571, doi:10.1002/sml.200500020 (2005).
- 54 Lou, X. W., Wang, Y., Yuan, C., Lee, J. Y. & Archer, L. A. Template-free synthesis of SnO₂ hollow nanostructures with high lithium storage capacity. *Adv. Mater.* **18**, 2325-+, doi:10.1002/adma.200600733 (2006).
- 55 Zheng, Y. H. *et al.* Metastable gamma-MnS hierarchical architectures: Synthesis, characterization, and growth mechanism. *J Phys Chem B* **110**, 8284-8288, doi:10.1021/jp060351l (2006).
- 56 Wang, W.-S., Zhen, L., Xu, C.-Y., Zhang, B.-Y. & Shao, W.-Z. Room temperature synthesis of hollow CdMoO₄ microspheres by a surfactant-free aqueous solution route. *J Phys Chem B* **110**, 23154-23158, doi:10.1021/jp064162e (2006).
- 57 Wang, W.-S., Zhen, L., Xu, C.-Y. & Shao, W.-Z. Aqueous solution synthesis of Cd(OH)₂ hollow microspheres via Ostwald ripening and their conversion to CdO hollow microspheres. *J Phys Chem C* **112**, 14360-14366, doi:10.1021/jp8046483 (2008).
- 58 Qi, Y., Tang, K., Zeng, S. & Zhou, W. Template-free one-step fabrication of porous CuInS₂ hollow microspheres. *Micropor Mesopor Mat* **114**, 395-400, doi:10.1016/j.micromeso.2008.01.027 (2008).
- 59 Guan, M., Tao, F., Sun, J. & Xu, Z. Facile preparation method for rare earth phosphate hollow spheres and their photoluminescence properties. *Langmuir* **24**, 8280-8283, doi:10.1021/la800789x (2008).
- 60 Tian, X., Li, J., Chen, K., Han, J. & Pan, S. Template-Free and Scalable Synthesis of Core-Shell and Hollow BaTiO₃ Particles: Using Molten Hydrated Salt as a Solvent. *Cryst Growth Des* **9**, 4927-4932, doi:10.1021/cg900700u (2009).
- 61 Qiao, R., Zhang, X. L., Qiu, R., Kim, J. C. & Kang, Y. S. Morphological Transformation of Co(OH)₂ Microspheres from Solid to Flowerlike Hollow Core-Shell Structures. *Chem-Eur J* **15**, 1886-1892, doi:10.1002/chem.200800803 (2009).

- 62 Zhou, Y.-X. *et al.* Hierarchical Hollow Co₉S₈ Microspheres: Solvothermal Synthesis, Magnetic, Electrochemical, and Electrocatalytic Properties. *Chem-Eur J* **16**, 12000-12007, doi:10.1002/chem.200903263 (2010).
- 63 Zhao, J. *et al.* A Facile Approach to Fabrication of Hexagonal-Phase NaYF₄:Yb³⁺, Er³⁺ Hollow Nanospheres: Formation Mechanism and Upconversion Luminescence. *Eur J Inorg Chem*, 1813-1819, doi:10.1002/ejic.200901119 (2010).
- 64 Cheng, W., Tang, K., Qi, Y., Sheng, J. & Liu, Z. One-step synthesis of superparamagnetic monodisperse porous Fe₃O₄ hollow and core-shell spheres. *J Mater Chem* **20**, 1799-1805, doi:10.1039/b919164j (2010).
- 65 Yang, Z. *et al.* Mesoporous CeO₂ Hollow Spheres Prepared by Ostwald Ripening and Their Environmental Applications. *Eur J Inorg Chem*, 3354-3359, doi:10.1002/ejic.201000030 (2010).
- 66 Zheng, C., Zheng, X., Hong, Z., Ding, X. & Wei, M. Template-free synthesis of SnO₂ nanostructural hollow spheres covered by nanorods. *Mater Lett* **65**, 1645-1647, doi:10.1016/j.matlet.2011.02.061 (2011).
- 67 Ye, T. *et al.* Controllable Synthesis and Photoluminescence of Single-Crystalline BaHfO₃ Hollow Micro- and Nanospheres. *Langmuir* **27**, 8878-8884, doi:10.1021/la201749z (2011).
- 68 Wang, Y., Zhu, Q. & Tao, L. Fabrication and growth mechanism of hierarchical porous Fe₃O₄ hollow sub-microspheres and their magnetic properties. *Crystengcomm* **13**, 4652-4657, doi:10.1039/c1ce05119a (2011).
- 69 Dong, Z. *et al.* Perovskite BaZrO₃ hollow micro- and nanospheres: controllable fabrication, photoluminescence and adsorption of reactive dyes. *J Mater Chem* **21**, 5978-5984, doi:10.1039/c0jm04534a (2011).
- 70 Shang, S., Jiao, X. & Chen, D. Template-Free Fabrication of TiO₂ Hollow Spheres and Their Photocatalytic Properties. *Acs Appl Mater Inter* **4**, 860-865, doi:10.1021/am201535u (2012).
- 71 Geng, B., Liu, J., Zhao, Y. & Wang, C. A room-temperature chemical route to homogeneous core-shell Cu₂O structures and their application in biosensors. *Crystengcomm* **13**, 697-701, doi:10.1039/c0ce00372g (2011).
- 72 Li, Q., Chen, W., Ju, M., Liu, L. & Wang, E. ZnO-based hollow microspheres with mesoporous shells: Polyoxometalate-assisted fabrication, growth mechanism and photocatalytic properties. *J Solid State Chem* **184**, 1373-1380, doi:10.1016/j.jssc.2011.04.006 (2011).

- 73 Lei, Y., Hu, J., Liu, H. & Li, J. Template-free synthesis of hollow core-shell MoO₂ microspheres with high lithium-ion storage capacity. *Mater Lett* **68**, 82-85, doi:10.1016/j.matlet.2011.10.043 (2012).
- 74 Shi, J. W. *et al.* Facile one-pot synthesis of Eu, N-codoped mesoporous titania microspheres with yolk-shell structure and high visible-light induced photocatalytic performance. *Appl Catal a-Gen* **435**, 86-92, doi:10.1016/j.apcata.2012.05.044 (2012).
- 75 Kong, F. Y. *et al.* Template-free hydrothermal synthesis of VO₂ hollow microspheres. *Crystengcomm* **14**, 3858-3861, doi:10.1039/c2ce25199j (2012).
- 76 Zhong, J., Cao, C., Liu, H., Ding, Y. & Yang, J. Fabrication of Hollow and Yolk-Shell Structured eta-Fe₂O₃ Nanoparticles with Versatile Configurations. *Ind Eng Chem Res* **52**, 1303-1308, doi:10.1021/ie302652b (2013).
- 77 Li, S. *et al.* One-pot synthesis of ZnS hollow spheres via a low-temperature, template-free hydrothermal route. *Crystengcomm* **15**, 1571-1577, doi:10.1039/c2ce26769a (2013).
- 78 Li, J. & Zeng, H. C. Nanoreactors - Size tuning, functionalization, and reactivation of Au in TiO₂ nanoreactors. *Angew Chem Int Edit* **44**, 4342-4345, doi:DOI 10.1002/anie.200500394 (2005).
- 79 Jana, N. R., Wang, Z. L., Sau, T. K. & Pal, T. Seed-mediated growth method to prepare cubic copper nanoparticles. *Current Science* **79**, 1367-1370 (2000).
- 80 Yu, H., Gibbons, P. C., Kelton, K. F. & Buhro, W. E. Heterogeneous seeded growth: A potentially general synthesis of monodisperse metallic nanoparticles. *J Am Chem Soc* **123**, 9198-9199, doi:10.1021/ja016529t (2001).
- 81 Zhang, L., Blom, D. A. & Wang, H. Au-Cu₂O Core-Shell Nanoparticles: A Hybrid Metal-Semiconductor Heteronanostructure with Geometrically Tunable Optical Properties. *Chem. Mater.* **23**, 4587-4598, doi:10.1021/cm202078t (2011).
- 82 Xuan, S. *et al.* One step method to encapsulate nanocatalysts within Fe₃O₄ nanoreactors. *J Mater Chem* **21**, 15398-15404, doi:10.1039/c1jm12798e (2011).
- 83 Zhang, N., Fu, X. & Xu, Y.-J. A facile and green approach to synthesize Pt@CeO₂ nanocomposite with tunable core-shell and yolk-shell structure and its application as a visible light photocatalyst. *J Mater Chem* **21**, 8152-8158, doi:10.1039/c1jm10100e (2011).
- 84 Chen, J. S. *et al.* One-pot formation of SnO₂ hollow nanospheres and alpha-Fe₂O₃@SnO₂ nanorattles with large void space and their lithium storage properties. *Nanoscale* **1**, 280-285, doi:10.1039/b9nr00102f (2009).

- 85 Zhang, L. & Wang, H. Interior Structural Tailoring of Cu₂O Shell-in-Shell Nanostructures through Multistep Ostwald Ripening. *J Phys Chem C* **115**, 18479-18485, doi:10.1021/jp2059613 (2011).
- 86 Li, J. & Zeng, H. C. Hollowing Sn-doped TiO₂ nanospheres via Ostwald ripening. *J Am Chem Soc* **129**, 15839-15847, doi:Doi 10.1021/Ja073521w (2007).
- 87 Yang, X., Zhou, Y., Yu, X., Demir, H. V. & Sun, X. W. Bifunctional highly fluorescent hollow porous microspheres made of BaMoO₄:Pr³⁺ nanocrystals via a template-free synthesis. *J Mater Chem* **21**, 9009-9013, doi:10.1039/c1jm10458f (2011).
- 88 Zhou, J. K. *et al.* Synthesis of self-organized polycrystalline F-doped TiO₂ hollow microspheres and their photocatalytic activity under visible light. *J Phys Chem C* **112**, 5316-5321, doi:10.1021/jp709615x (2008).
- 89 Xiao, Y. *et al.* Nano-sized Y₂O₃:Eu³⁺ hollow spheres with enhanced photoluminescence properties. *J Alloy Compd* **509**, 5755-5760, doi:10.1016/j.jallcom.2010.12.132 (2011).
- 90 Asahi, R., Morikawa, T., Ohwaki, T., Aoki, K. & Taga, Y. Visible-light photocatalysis in nitrogen-doped titanium oxides. *Science* **293**, 269-271, doi:10.1126/science.1061051 (2001).
- 91 Wang, D. P. & Zeng, H. C. Creation of Interior Space, Architecture of Shell Structure, and Encapsulation of Functional Materials for Mesoporous SiO₂ Spheres. *Chem. Mater.* **23**, 4886-4899, doi:Doi 10.1021/Cm201631m (2011).
- 92 Huo, J. *et al.* Hollow Ferrocenyl Coordination Polymer Microspheres with Micropores in Shells Prepared by Ostwald Ripening. *Angew Chem Int Edit* **49**, 9237-9241, doi:10.1002/anie.201004745 (2010).
- 93 Huo, J. *et al.* Synthesis, characterization and magnetic properties of hollow microspheres with micro-mesoporous shells assembled from cobalt-based ferrocenyl coordination polymers. *J Colloid Interf Sci* **367**, 92-100, doi:10.1016/j.jcis.2011.07.099 (2012).

Chapter 3. Synthetic Architecture of Multiple Core-Shell and Yolk-Shell Structures of $(\text{Cu}_2\text{O})_n\text{Cu}_2\text{O}$ ($n = 1-4$) with Centricity and Eccentricity

Abstract

In this work, we describe a seed-mediated approach with successive Ostwald ripening to synthesize various multiple-shell core-shell and yolk-shell structures of $(\text{Cu}_2\text{O})_n\text{-Cu}_2\text{O}$ ($n = 1-4$). In particular, the structure formed in the previous step can serve as a newer-generation seed for a subsequent shell growth; a total of 20 representative structures have been thus synthesized in a sequential manner. With an increase in shell number n , in principle, 2^n shelled products can be fabricated, taking into account the centricity and eccentricity in their geometric symmetry. Synthetic chemistry and functions of chemical additives have also been investigated to explain the formation mechanism and to ensure the uniformity of the product. We found that symmetric or asymmetric Ostwald ripening during the hollowing process can be manipulated by controlling stirring conditions. Furthermore, optical properties of the resultant samples are related to structural aspects of the products, such as the overall size, the thickness of shells, the number of shells, and, the centricity and eccentricity in the final products. To test their applicability, we have also studied the electrocatalytic properties of these complex structures in nonenzymatic glucose sensing. Quite encouragingly, $(\text{Cu}_2\text{O})_n\text{Cu}_2\text{O}$ samples have shown an improved sensitivity as the number of thin shells increased.

3.1 Introduction

Development of nanoscience and nanotechnology crucially depends on our ability to design and synthesize advanced nanomaterials to obtain or to tune their physicochemical properties arising from quantum confinement, quantum coherence, and synergistic surface and interface effects^{1,2}. Over the past decade, solution-based preparation of inorganic nanostructures has attracted significant research interest because of the possibility of mass-scale production at a low cost. Furthermore, these chemical methods allow facile control over size, shape, crystal facet, polymorph, and overall product morphology as well as assembly for desired functional materials³⁻⁵. Numerous nanoscale structures and configurations of inorganic materials can be fabricated in solution phase rather routinely today. For instance, nanocubes⁶⁻¹⁰, nanorods^{11, 12}, nanowires^{13,14}, nanorings¹⁵, nanosprings¹⁶, polyhedrons¹⁷⁻¹⁹, core-shell structures^{20,21}, yolk-shell structures²²⁻²⁴, hollow sphere structures²⁵⁻³², heterostructures (including Janus particles)³³⁻³⁵, high-Miller-index-faceted crystals³⁶⁻³⁹, etc., have been published extensively in recent years. Among these research endeavors, in particular, the synthesis of multishell nanostructures or so-called nanomatrashkas⁴⁰⁻⁴² has also received tremendous attention because of their potential applications in chemical sensing^{43, 44}, drug delivery^{41,45}, medical imaging⁴⁵, and energy storage^{46,47}. In general, the novel nanostructures mentioned above are prepared by utilizing one of the following strategies: conventional hard-templating methods followed by a postchemical process such as chemical etching^{42,46} and calcination^{44,45}, template-free methods such as Ostwald ripening^{43,46,48,49} and ionic exchange⁵⁰, and soft-templating methods^{41,47,51,52}. However, it is quite difficult for these methods to achieve control of the size distribution and clarity of the shell structures. Very recently, synthesis of

polycrystalline multishell Cu_2O hollow spheres through a multiple-Ostwald ripening solution route has been reported⁵³; hollow spheres of Cu_2O with up to four shells have been successfully fabricated in a step-by-step manner. The multiple shells in these hollow spheres are mostly concentric in nature and possess a high centricity in the context of structural geometry. Fundamentally, nevertheless, making even more uniform and complex hollow structures to exploit the new synthetic capacity of solution-based preparation of nanomaterials remains a grand challenge. For example, adding a movable core or yolk into such multishell hollow spheres is equivalent to introducing a potential asymmetric element into existing highly symmetric systems, which allows the effective control of the overall structural symmetry. For instance, an off-central arrangement of core or yolk inside the hollow interior of a sphere could break its centricity, and, therefore, an overall eccentricity for the same sphere can be created. It is believed that such eccentricity may alter the course of light absorption and scattering. From the angle of reaction applications, on the other hand, such a movable core or yolk would enhance chemical mixing and mass transport within the hollow interiors and their external environments⁴⁸. Along with the control of centricity or eccentricity, there are also plenty of alternatives for introducing an initial core or yolk into the central interior. For example, the chemical composition of the core or yolk could be different from that of shells, or it could be simply kept the same; different selections would lead to the formation of heterostructures or homostructures. In addition, even if they have an identical chemical phase, the core or yolk does not necessarily have the same crystallographic polymorph as the shells. Similarly, monocrystallinity or polycrystallinity poses as another possible combination for modifying complicated multishell core- or yolk-shell homostructures. More

importantly, the concept of a core or yolk is no longer limited to a simple solid form; it could be just another resultant multishell core- or yolk-shell structure. In such cases, if the final eccentricity is further targeted, more intershell space is then required to form a detached (movable) or attached complex core or yolk in a newly generated shell of a spherical product. With these new research challenges and opportunities in mind, in this work, we report our recent efforts aimed at the synthetic architecture of several multishell core- or yolk-shell Cu_2O structures [i.e., $(\text{Cu}_2\text{O}@)_n\text{Cu}_2\text{O}$, where n is the number of Cu_2O shells (Appendix 1-1A)] with precise control over the size and product morphology through multiple-step seed-mediated growth and successive Ostwald ripening treatment at room temperature. We have further classified the product structures according to our designed combinations of cores and shells and overall product centricity or eccentricity. It has been found that with n shells, there will be 2^n possible final structures (Appendix 1-1A). In addition to single-sphere configurations, multishell peanut and bean-pod structures have also been fabricated. Along with these fundamental synthetic studies, we have also investigated the optical properties of these types of structures and explored their potential applications as nonenzymatic amperometric sensors of glucose. Quite encouragingly, an improvement in the detection sensitivity of glucose has been revealed using these multishell $(\text{Cu}_2\text{O}@)_n\text{Cu}_2\text{O}$ structures.

3.2 Experimental Section

Chemicals and Reagents. The following reagents were used in this work: copper(II) chloride dihydrate ($\text{CuCl}_2 \cdot 2\text{H}_2\text{O}$, >99%, Sigma-Aldrich), polyvinylpyrrolidone (PVP K30, MW = 40000, Fluka), sodium hydroxide (NaOH, >99%, Merck), L-ascorbic acid (AA, $\text{C}_6\text{H}_8\text{O}_6$, >99%, Sigma-Aldrich), copper(II) nitrate trihydrate [$\text{Cu}(\text{NO}_3)_2 \cdot 3\text{H}_2\text{O}$, 99.5%, Merck], ammonium nitrate (NH_4NO_3 , >99%, Acros), D-(+)-glucose ($\text{C}_6\text{H}_{12}\text{O}_6$, 99%, Alfa Aesar), perfluorosulfonic acid-PTFE copolymer [Nafion, 5% (w/w) solution, Alfa Aesar], ethanol ($\text{CH}_3\text{CH}_2\text{OH}$, 99%, Merck), and deionized water. All experiments were conducted at room temperature. Unless otherwise specified, the synthetic solutions were stirred with a 30 mm (length) \times 6mm (diameter) magnetic stirring bar at a nominal speed setting of 880 rpm (CAT model M 16.5).

Synthesis of Cu_2O -Truncated Cubes. In a typical synthesis, $\text{CuCl}_2 \cdot 2\text{H}_2\text{O}$ (0.10 mmol) and PVP (0.10 g) were dissolved in 50.0 mL of deionized water, followed by the dropwise addition (1 drop/s) of 2.0 mL of 0.2 M NaOH; the solution was stirred magnetically for 5 min. Finally, 2.0 mL of 0.10 M ascorbic acid was added dropwise (1 drop/3 s), and the solution was further stirred for 5 min.

Synthesis of $\text{Cu}_2\text{O}@ \text{Cu}_2\text{O}$ Core-Shell Structure. After the synthesis described above, 5.0 mL of the Cu_2O -truncated nanocube suspension was transferred to a solution mixture of $\text{Cu}(\text{NO}_3)_2 \cdot 3\text{H}_2\text{O}$ (0.1186 mmol) and NH_4NO_3 (0.8744 mmol) in 45.0 mL of deionized water. The solution was stirred magnetically for 1 min, followed by the dropwise addition (1 drop/s) of 2.0 mL of 0.20 M NaOH; the solution was

stirred for an additional 1 min. Finally, 3.5 mL of 0.10 M ascorbic acid was added dropwise (1 drop/3 s), and the solution was further stirred for 5 min.

Synthesis of $\text{Cu}_2\text{O}@ \text{Cu}_2\text{O}$ Yolk–Shell Structure. This procedure is similar to the $\text{Cu}_2\text{O}@ \text{Cu}_2\text{O}$ core–shell synthesis, but the magnetic stir bar is placed such that the stirring disturbance is heard (e.g., near the wall of the beaker or convex base of the glassware). After the addition of ascorbic acid, the solution was stirred for 22–28 min.

Synthesis of $(\text{Cu}_2\text{O}@)_2\text{Cu}_2\text{O}$ Structure. After the synthesis of the $\text{Cu}_2\text{O}@ \text{Cu}_2\text{O}$ core–shell or yolk–shell structure, 10.0–30.0 mL of the resultant solution was transferred to a solution mixture of $\text{Cu}(\text{NO}_3)_2 \cdot 3\text{H}_2\text{O}$ (0.1186 mmol) and NH_4NO_3 (0.8744 mmol) in 20.0–40.0 mL of deionized water. The solution was stirred magnetically for 1 min, followed by the dropwise addition (1 drop/s) of 1.0 mL of 0.20 M NaOH; the solution was stirred for an additional 1 min. Finally, 1.5 mL of 0.10 M ascorbic acid was added dropwise (1 drop/3 s), and the solution was stirred for 9–12 min.

Synthesis of $(\text{Cu}_2\text{O}@)_3\text{Cu}_2\text{O}$ Structure. As in the previous procedure, 40.0 mL of the resultant $(\text{Cu}_2\text{O}@)_2\text{Cu}_2\text{O}$ suspension was transferred to a solution of $\text{Cu}(\text{NO}_3)_2 \cdot 3\text{H}_2\text{O}$ (0.1186 mmol) and NH_4NO_3 (0.8744 mmol) in 10.0 mL of deionized water. The solution was stirred magnetically for 1 min, followed by the dropwise addition (1 drop/s) of 1.0 mL of 0.20 M NaOH; the solution was stirred for an additional 1 min. Finally, 1.5 mL of 0.10 M ascorbic acid was added dropwise (1 drop/3 s), and the solution was stirred for 12 min.

Synthesis of $(\text{Cu}_2\text{O}@)_4\text{Cu}_2\text{O}$ Structure. After the synthesis of the $(\text{Cu}_2\text{O}@)_3\text{Cu}_2\text{O}$ structure, 45.0 mL of the solution was transferred to a solution of $\text{Cu}(\text{NO}_3)_2 \cdot 3\text{H}_2\text{O}$ (0.1186 mmol) and NH_4NO_3 (0.8744 mmol) in 5.0 mL of deionized water. The solution was stirred for 1 min. After the dropwise addition (1 drop/s) of 1.0 mL of 0.20 M NaOH, the solution was stirred for an additional 1 min. Finally, 1.5 mL of 0.10 M ascorbic acid was added dropwise (1 drop/3 s), and the solution was stirred for 16 min.

Characterization of Materials. The crystallographic information about the Cu_2O seeds and $(\text{Cu}_2\text{O}@)_n\text{Cu}_2\text{O}$ samples was obtained by powder X-ray diffraction (XRD, Shimadzu, model XRD-6000, Cu $K\alpha$ radiation at 1.5406 Å). Morphological and structural investigations were conducted via transmission electron microscopy (TEM, JEM-2010, 200 kV) and high-resolution transmission electron microscopy with selected area electron diffraction (HRTEM/SAED, JEM-2100F, 200 kV). The extinction spectrum for each sample was measured through a UV-vis spectrophotometer (Shimadzu model UV-2450). Chemical information about Cu_2O seeds and $(\text{Cu}_2\text{O}@)_n\text{Cu}_2\text{O}$ yolk-shell or core-shell samples was established via Fourier transform infrared spectroscopy (FTIR, KBr pellet method, Bio-Rad model FTS 135).

Electrochemical Measurements. Prior to the modification, the glassy carbon electrode (GCE, 3 mm diameter) was polished with 1.0 and 0.05 μm alumina slurries on chamois leather. The electrodes were rinsed with deionized water and washed with $\text{H}_2\text{O}/\text{HNO}_3$ mixture (1:1), an ethanol/ H_2O mixture (1:1), and deionized water in an ultrasonic bath after each polishing step. Next, 10.0 mg of different $(\text{Cu}_2\text{O}@)_n\text{Cu}_2\text{O}$

structures was dispersed in 1.0 mL of ethanol, and 5.0 μL of the solution was cast on the surface of GCE and dried in a refrigerator (7 $^\circ\text{C}$) for 1 h. Finally, 3.0 μL of 0.35% Nafion was cast on the surface. Electrochemical measurements were recorded using a computer-controlled potentiostat (Autolab, PGSTAT 302N) with a standard three-electrode configuration. Pt gauze and Ag/AgCl/saturated KCl act as the counter and reference electrodes, respectively. Prior to the measurements, a 0.10 M NaOH solution was sparged with nitrogen for 20 min. Cyclic voltammetry (CV) measurements with different $(\text{Cu}_2\text{O}@)_n\text{Cu}_2\text{O}$ modified electrodes (i.e., $\text{Cu}_2\text{O}/\text{Nf}/\text{GCEs}$) were taken in the potential range of -0.1 to 0.7 V (vs Ag/AgCl) with a scan rate of 50 mV/s in a 0.10 M nitrogen-saturated NaOH solution at glucose concentrations of 0.0, 5.0, and 10.0 mM. Chronoamperometric measurements for different $\text{Cu}_2\text{O}/\text{Nf}/\text{GCE}$ electrodes were recorded at a constant applied potential of 0.50 V (vs. Ag/AgCl) in a 0.10 M nitrogen-saturated NaOH solution while the samples were being mildly magnetically stirred. The amperometric signal was allowed to reach a steady-state current before the successive addition of 10.0 μM glucose to the solution.

3.3 Results and Discussion

3.3.1. Synthetic Chemistry and Strategies

The structure of the Cu_2O seed used in this work is a truncated cube with 6 $\{100\}$ planes on its main surface, 12 $\{110\}$ facets on its edges, and 8 $\{111\}$ facets on its corners (i.e., rhombicuboctahedron). In view of its high degree of structural symmetry, the truncated cube can be considered a good approximation of a sphere. Herein, a single crystal Cu_2O core is preferred, because it would be more able to withstand multiple-Ostwald ripening processes involved in this work, compared to those polycrystalline Cu_2O spheres³⁰. Figure 3.1 summarizes the structures synthesized in this work. (refer to Appendix 1-1A for more structural details). It also illustrates the general synthetic strategies toward $(\text{Cu}_2\text{O}@)_n\text{Cu}_2\text{O}$ complex through seed-mediated growth processes followed by Ostwald ripening. As depicted in Figure 3.2, nanocrystallites of $\text{Cu}(\text{OH})_2$ are first formed upon addition of NaOH (eq 1), and subsequently, these crystallites aggregate on the surfaces of Cu_2O seeds. Moreover, the rapid growth of the $\text{Cu}(\text{OH})_2$ phase is inhibited by the presence of NH_4NO_3 salt, which is able to reverse $\text{Cu}(\text{OH})_2$ to $[\text{Cu}(\text{H}_2\text{O})_6]^{2+}$ (see eq 2), therefore, initial clusters and/or crystallites of $\text{Cu}(\text{OH})_2$ are solely deposited on the Cu_2O seeds instead of spontaneous unseeded crystal growth occurring. Afterward, the reduction of $\text{Cu}(\text{OH})_2$ to Cu_2O proceeds with addition of ascorbic acid ($\text{C}_6\text{H}_8\text{O}_6$, eq 3). Symmetric or asymmetric Ostwald ripening then follows, producing either core-shell or yolk-shell structures⁴⁸. Interestingly, the thus grown core-shell or yolk-shell products can be further used as new “structured seeds” to form even more complex configurations or architectures. The shell addition process can be expressed in eq 4.

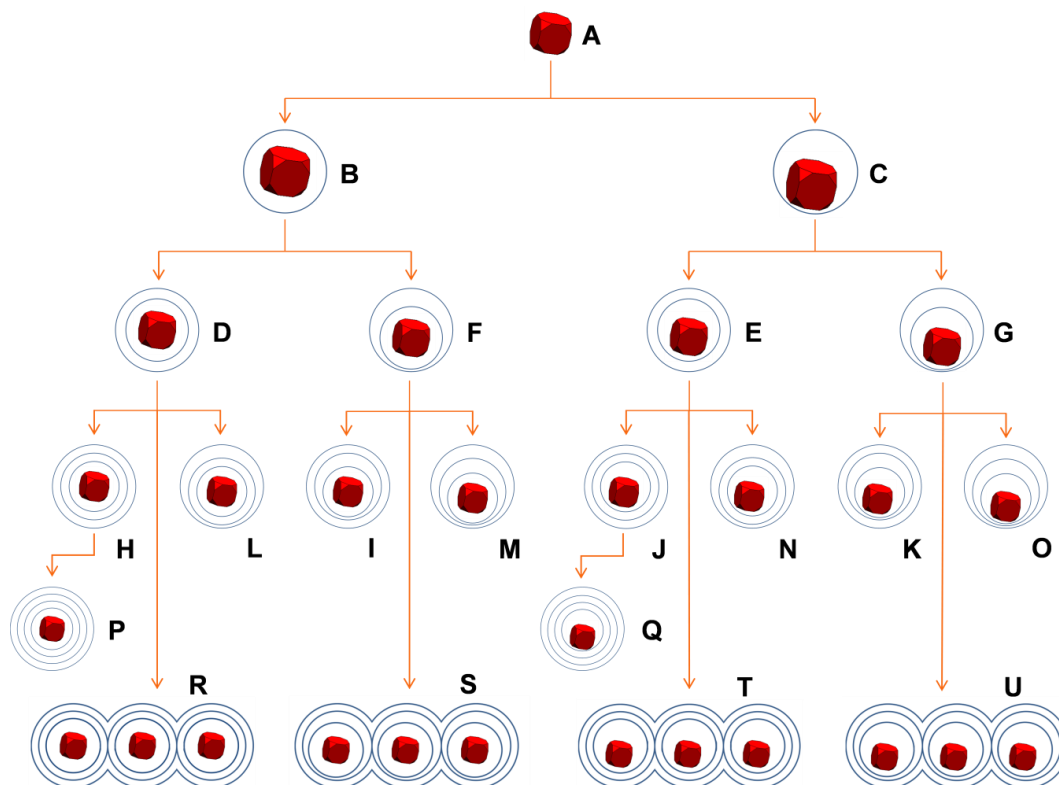
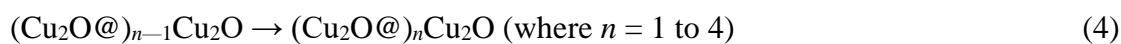
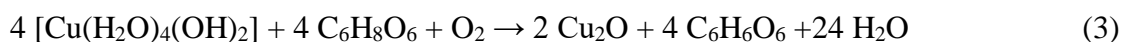
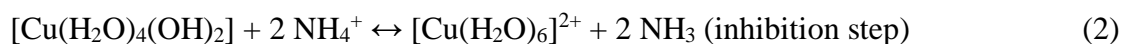
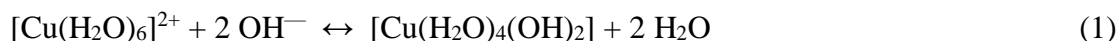


Figure 3.1 Illustrations of synthetic strategies of $(\text{Cu}_2\text{O}@)_n\text{Cu}_2\text{O}$ ($n = 1$ to 4) core-shell and yolk-shell structures. An earlier formed structure serves as a seed for a newer generation structure. Red cubes: single-crystal Cu_2O seeds and blue cycles: polycrystalline Cu_2O shells. See A-1 for more structural explanations.



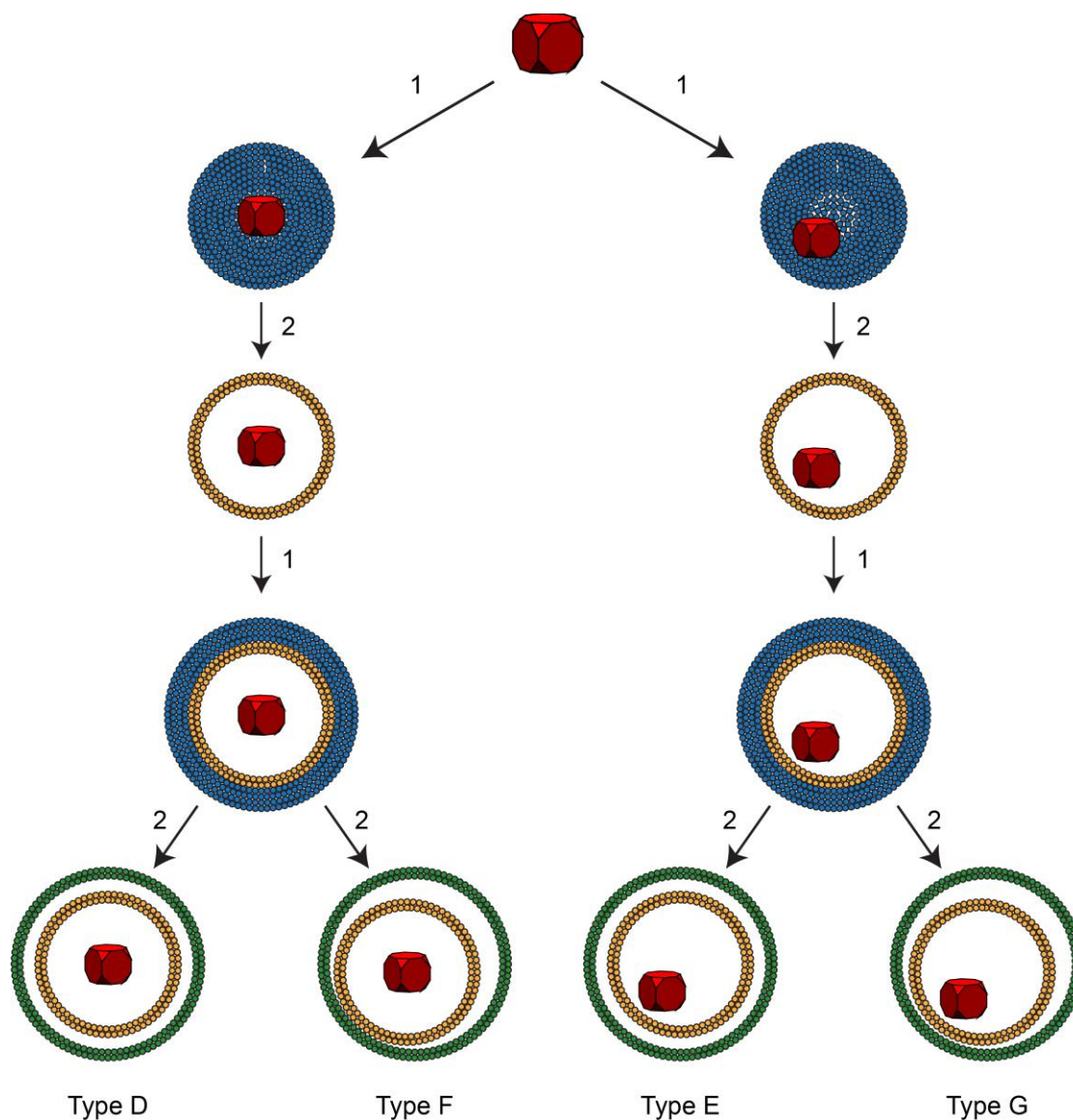


Figure 3.2 Schematic illustrations of $(\text{Cu}_2\text{O}@)_n\text{Cu}_2\text{O}$ formation processes. A seed-mediated approach in fabricating the 4 types of double-shelled structures (types D, F, E and G, Figure 3.1); where: (1) $\text{Cu}(\text{OH})_2$ formation, (2) formation of Cu_2O by ascorbic acid and its subsequent symmetric/asymmetric Ostwald ripening.

By repeating seeded growth n times, as illustrated in the family tree of Figure 1, we can fabricate various structurally hierarchical core–shell or yolk–shell products. With the addition of n shells, in principle, 2^n structural configurations can be made by using

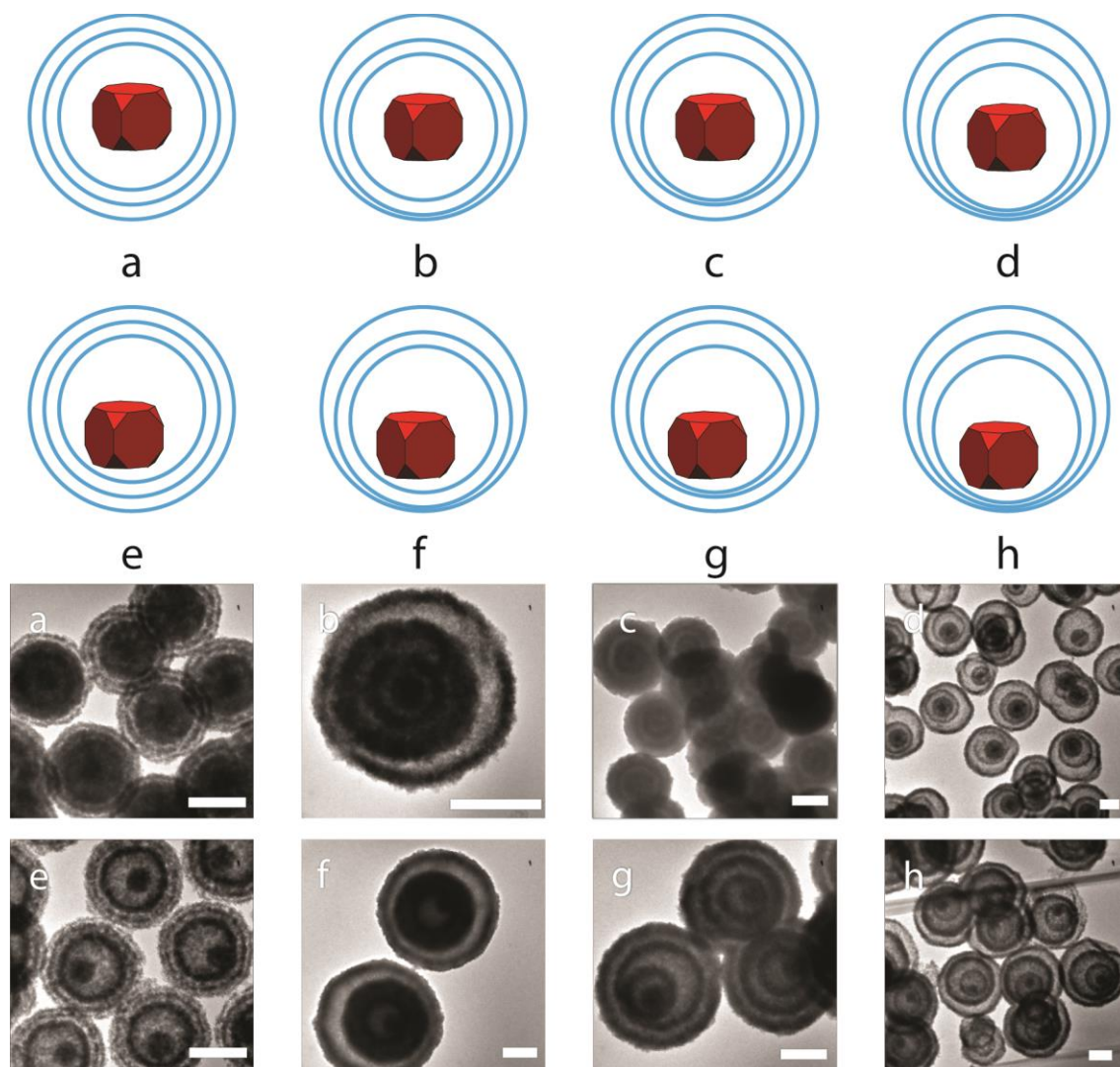


Figure 3.3 Schematic illustration of eight possible triple-shelled $(\text{Cu}_2\text{O}@)_3\text{Cu}_2\text{O}$ structures (a to h) and their related TEM images (a to h); they are in the sequence of H, L, I, M, J, N, K and O types of structures, as described in Figure 3.1. Scale bar: 200 nm.

different types of seeds and varying synthetic parameters (refer to Figure 3.1). For instance, there are four possible configurations for double-shell structures ($n = 2$) that were obtained from types D–G, while for triple-shell structures ($n = 3$), eight possible configurations were observed from type H to type O as shown in Figure 3.3. The structural complexity therein corresponds to various combinations of centricity or eccentricity between the core and the shell when n is increasing; actual synthetic

schemes of the eight structures can be found in Appendix 1-1B. The monodisperse seed of Cu_2O employed in this work was first synthesized via a similar literature method⁶, followed by a subsequent transfer to another reaction vessel thereby facilitating shell growth. Repeating such a process would yield monodisperse multishell core-shell or yolk-shell structures. To prepare type C yolk-shell structures, we deliberately placed the magnetic stirring bar near the wall of the reaction container, and the sound of the magnetic stirring bar hitting the wall of the glass container was heard. Compared with the normal concentric stirring (used in type B synthesis), this off-central stirring created fluctuation of the stirring speed and disrupted normal fluidic convections, and thus, it affected the hollowing mechanism and kinetics that will be discussed below. Figure 3.4 shows some representative samples synthesized according to the schemes summarized in Figure 3.1 (see section Appendix 1-1B for experimental details).

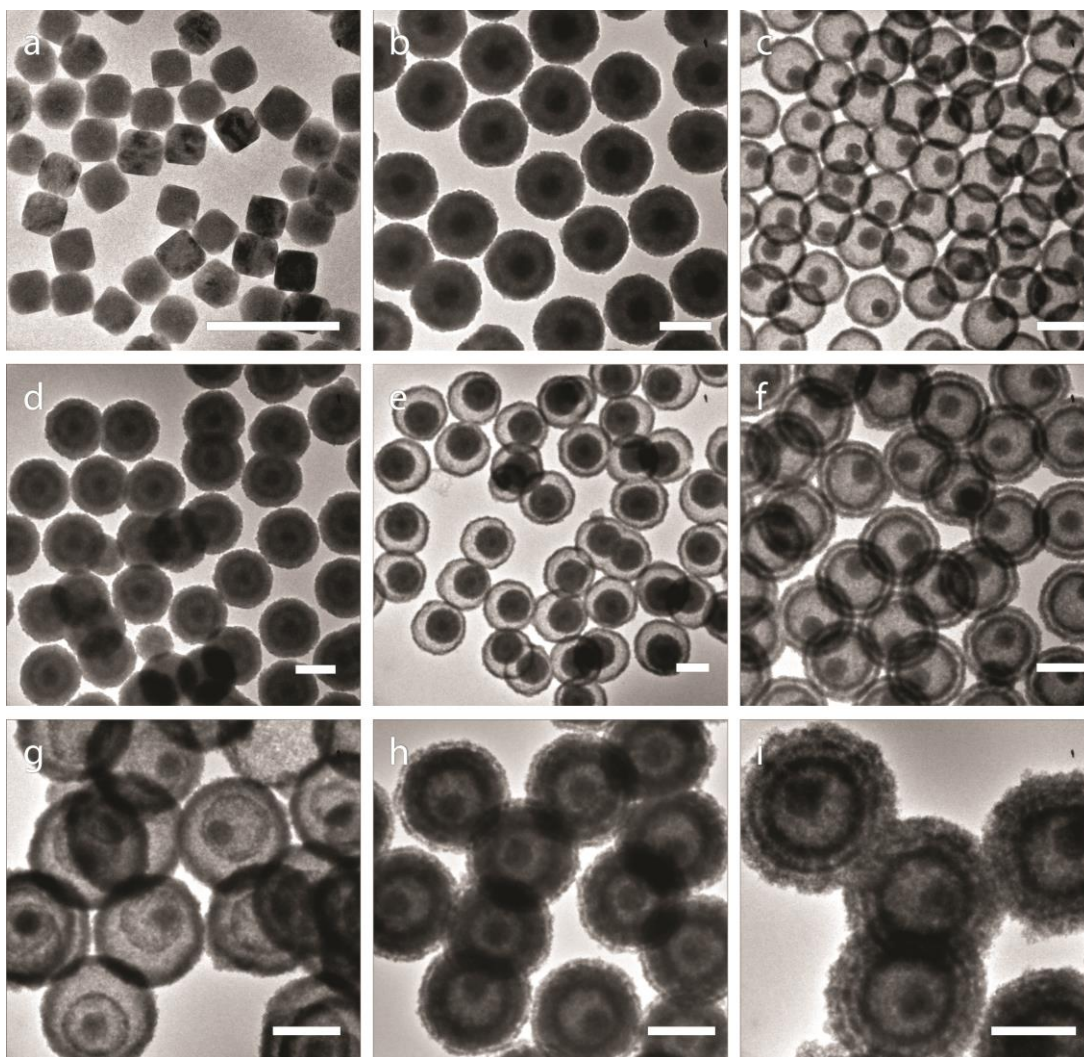


Figure 3.4 Representative TEM images of various $(\text{Cu}_2\text{O}@)_n\text{Cu}_2\text{O}$ ($n = 1$ to 4) products: (a) truncated cube (starting seed), type A, (b) core-shell, type B, (c) yolk-shell, type C, (d) concentric double-shelled core-shell, type D, (e) non-concentric double-shelled core-shell, type F, (f) concentric double-shelled yolk-shell with a movable core, type E, (g) non-concentric double-shelled yolk-shell with a movable core, type G, (h) concentric triple-shelled yolk-shell with a movable core, type J, and (i) concentric quadruple-shelled yolk-shell with a movable core, type Q. Scale bar: 200 nm. Refer to Appendix 1-1A and 3-1B for further structural and experimental details.

From Figure 3.4a–3.4i, the average edge length of pristine Cu_2O cubes (i.e., the starting seeds) or the average diameter of the resultant spherical structures increases in the following sequence: 60, 260, 210, 300, 320, 300, 340, 340, and 400 nm, corresponding to sizes of types A, B, C, D, F, E, G, J, and Q structures, respectively.

Our HRTEM investigation reveals that the shell consists of tiny crystallites with sizes ranging from 5 to 6 nm (Appendix 1-2A). In addition, our study with selected area electron diffraction [SAED (Appendix 1-2B)] indicates that the starting Cu_2O cubes (seeds, type A) are single-crystalline forms, whereas the grown Cu_2O shells are polycrystalline in all the product structures. In addition to the HRTEM/SAED study, Figure 3.5a displays the X-ray diffraction patterns of different structural products investigated in this work.

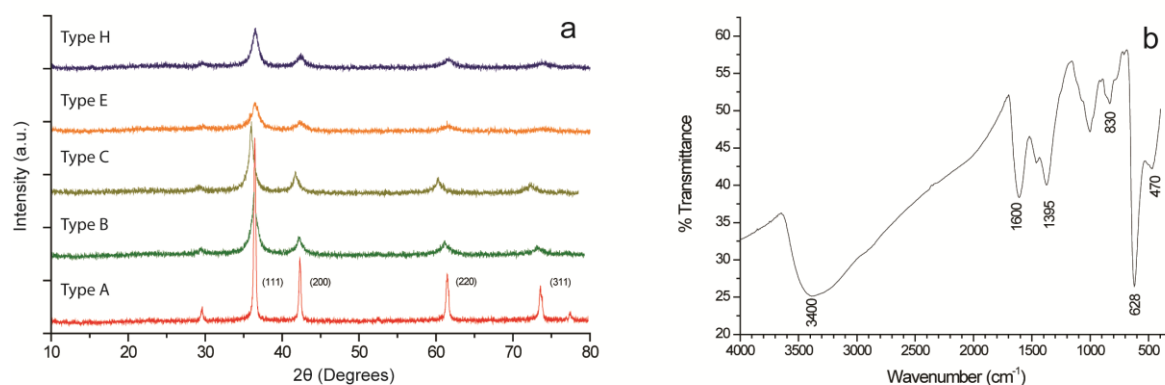


Figure 3.5 (a) Powder X-ray diffraction patterns of pristine Cu_2O cubes and different types of complex $(\text{Cu}_2\text{O}@)_n\text{Cu}_2\text{O}$ structures: seed (type A), core-shell (type B), yolk-shell (type C), double-shelled core-shell (type E), and triple-shelled core-shell (type H), and (b) A representative FTIR spectrum of $(\text{Cu}_2\text{O}@)_n\text{Cu}_2\text{O}$ sample (type B structure).

Diffraction peaks of CuO or metallic Cu were absent in all these patterns, and the patterns can be assigned perfectly to cubic cuprous oxide (JCPDS Card 77-0199), confirming the formation of phase pure Cu_2O . In comparison, stronger diffraction peaks of the Cu_2O seed were attributed to its larger crystal size and monocrystallinity, whereas those of shelled structures were broader and the intensities lower because of their smaller crystallite size and polycrystallinity (Appendix 1-2A and 3-2B). Using Scherrer's equation, the crystallite size of the shells was estimated to be 5–6 nm,

which is in good agreement with the HRTEM result of the shells. To understand the chemical bonding situation in these products, we also applied the FTIR spectroscopic method. Figure 3.5b shows the infrared spectrum of a typical $\text{Cu}_2\text{O}@Cu_2\text{O}$ core-shell structure. In particular, the peaks at 628 and 470 cm^{-1} are assigned to Cu-O bond stretching and bending modes of Cu_2O , while the large band around 3400 cm^{-1} is due to surface hydroxylation (Cu-O-H) on the core-shell structure. Other peaks correspond to the stretching and bending modes of NO_3^- , because of the surface adsorption of nitrate ions, denoting the fact that FTIR is extremely sensitive to the detection of this anion.

3.3.2. Controlling Factors and Ripening Mechanisms

In our synthesis, the size of Cu_2O seeds did not decrease noticeably upon a subsequent shell growth and ripening, because these single crystal seeds were more stable compared to depositing nanocrystallites that are more prone to mass relocation and Ostwald ripening starting at the interface between the seed and its crystallite aggregates⁵⁴. Figure 3.6 details the effect of reaction-cum-ripening time on the growth of the first shell ($n = 1$).

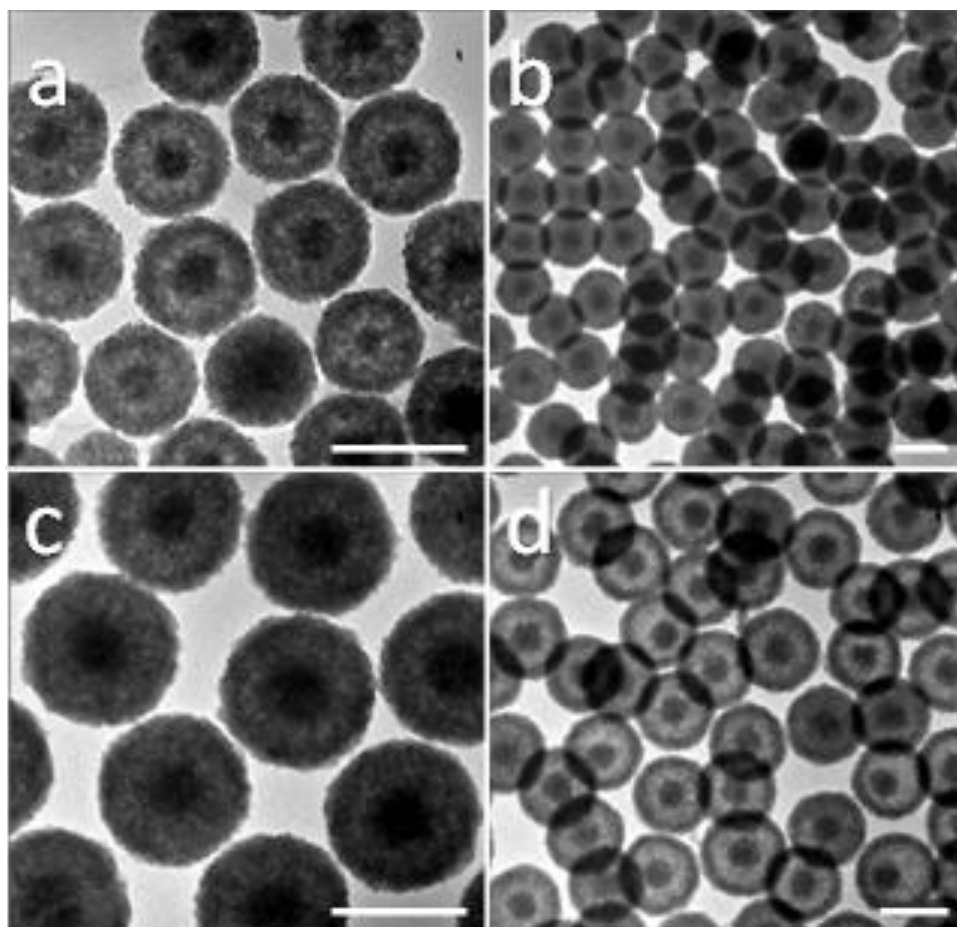


Figure 3.6 Effect of ripening time on the growth of the 1st shell ($n = 1$): (a) 1 min (average diameter 170 nm), (b) 10 min (200 nm), (c) 30 min (240 nm), and (d) 42 min (240 nm). Scale bar: 200 nm.

Clearly, a longer process time would yield a larger core-shell structure because smaller interior crystallites were relocated onto the sphere surface, thus increasing the overall size of the structure. Associated with this mass relocation, a hollow space between the core and shell was developed, following so-called symmetric Ostwald ripening (Figure 3.6d)⁴⁸. Moreover, complete detachment of the core from the shell could also be observed, which gave rise to a yolk-shell structure upon ripening. A similar process analysis can also be applied to multishell core-shell structures ($n = 2, 3,$ and 4) displayed in Figure 3.7–3.9, though it is noted that for the multishell

core-shell synthesis, the hollowing kinetics proceeds at a rate faster than that of single-shell core-shell and yolk-shell growths.

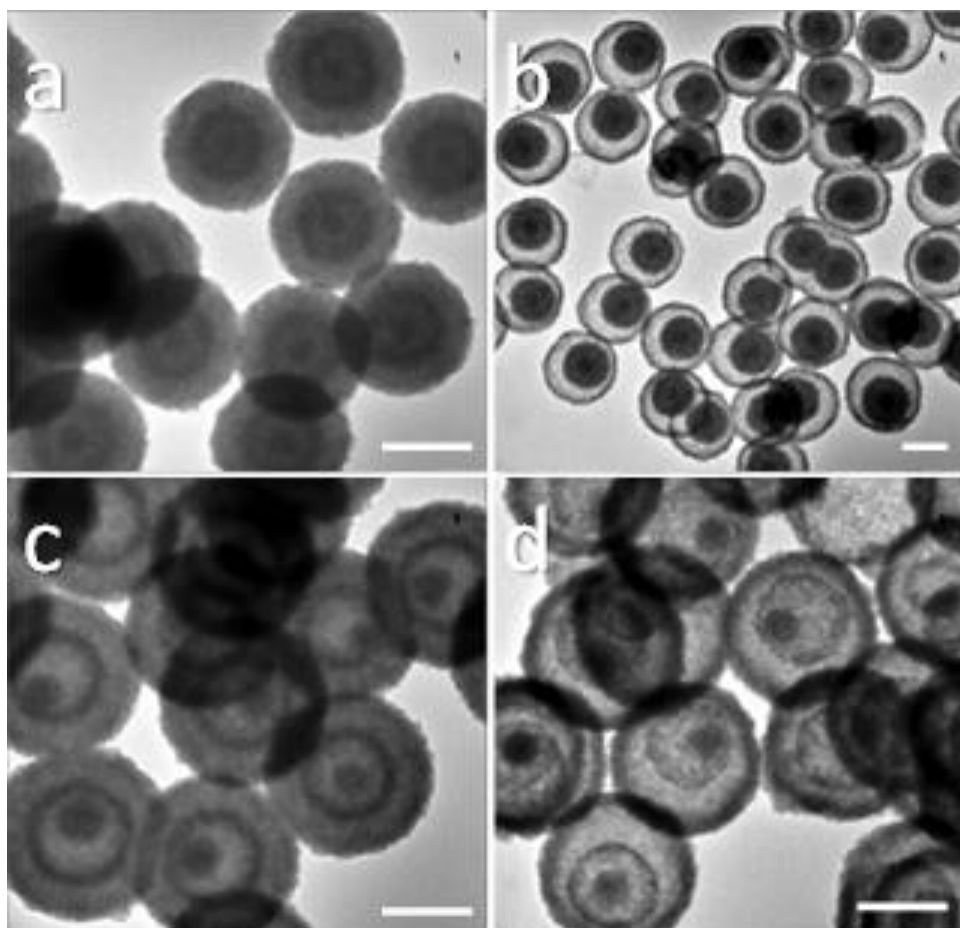


Figure 3.7 Effect of ripening time on the growth of the 2nd shell ($n = 2$): (a) 7 min, (b) 10 min, (c) 7 min, and (d) 9 min. All synthetic experiments were started with 10 mL of core-shell (a and b) or yolk-shell (c and d) seeds (see Experimental Section). Scale bar: 200 nm.

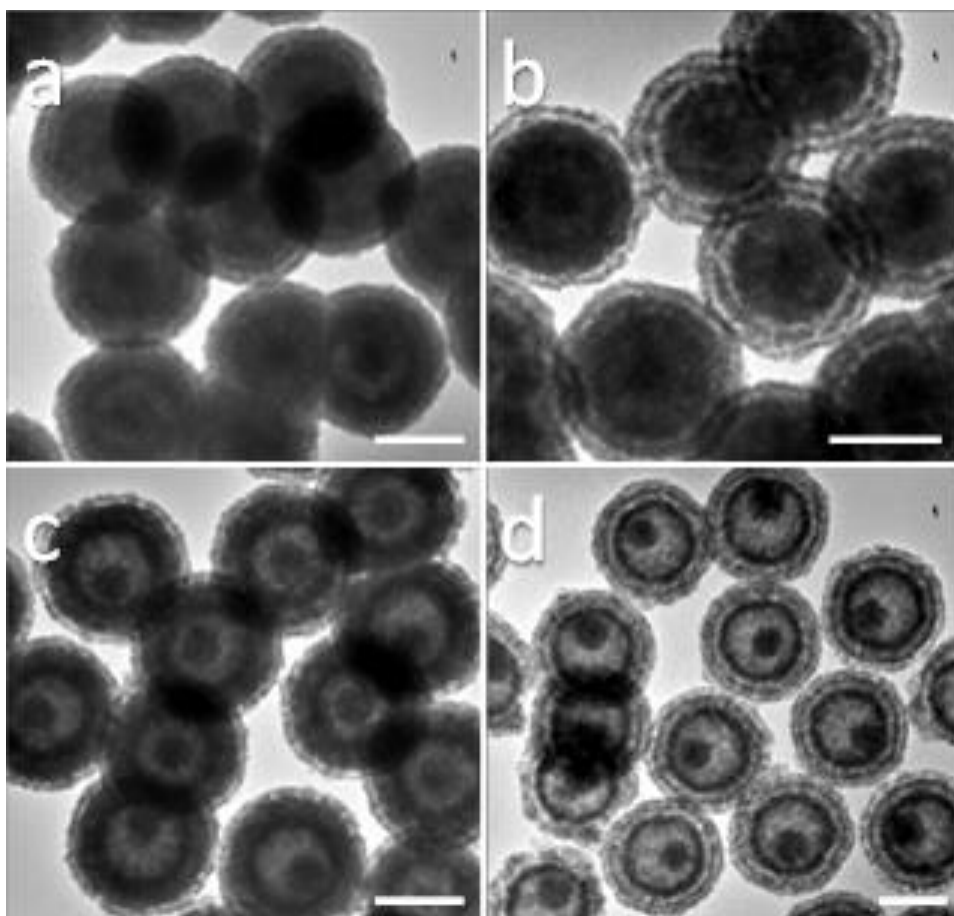


Figure 3.8 Effect of ripening time on the growth of the 3rd shell ($n = 3$): (a) 18 min, (b) 25 min, (c) 12 min, and (d) 12.5 min. All synthetic experiments were started with 40 mL of double-shelled core-shell (a and b) and yolk-shell (c and d) seeds. Scale bar: 200 nm.

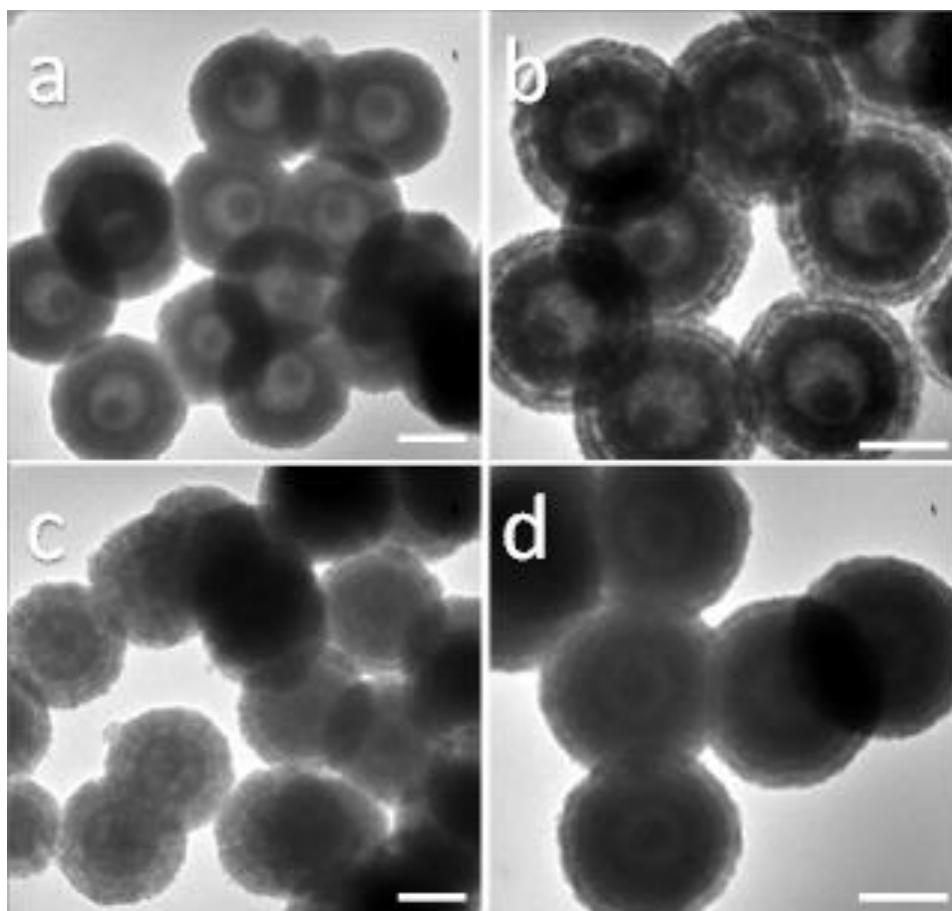


Figure 3.9 Effect of ripening time on the growth of the 4th shell ($n = 4$): (a) 10 min, (b) 22 min, (c) 24 min, (d) 27 min. Note that 30 mL of seeds were used for the growth of the 2nd shell, 40 mL of seeds were used for the growth of the 3rd shell, and 45 mL of seeds were used for the growth of the 4th shell. Refer to Experimental Section and A-2 for further details. Scale bar: 200 nm.

Furthermore, inconsistency in hollowing kinetics is attributed to the stirring condition (i.e., stirring rate and fluctuation and disturbance mentioned earlier). The effect of stirring rate on the hollowing kinetics has also been investigated. As shown in Figure 3.10, the system demonstrated an optimal stirring rate to maintain the homogeneity of both size and structure.

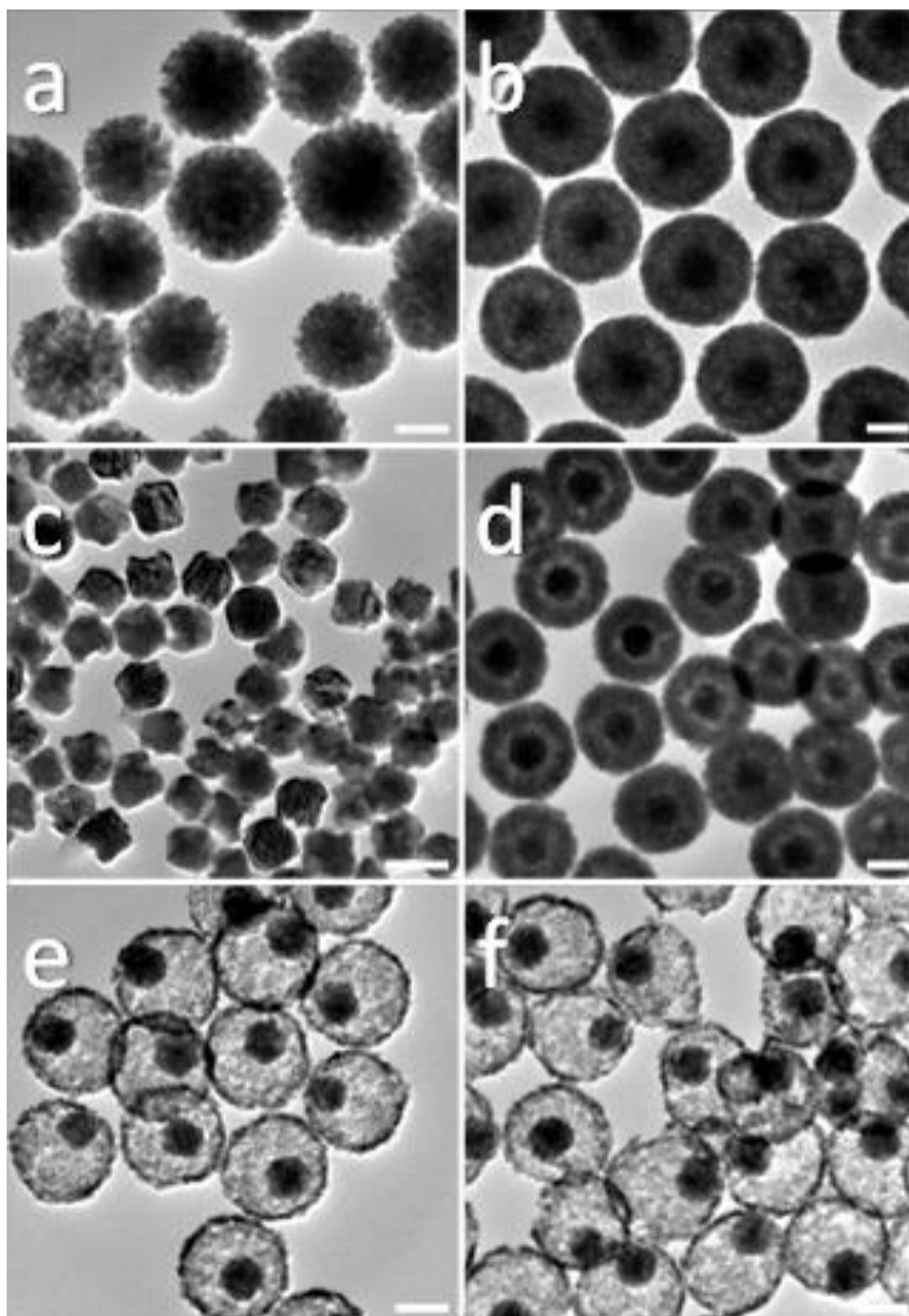


Figure 3.2 Hollowing kinetics as a function of nominal stirring rate: (a) 600 rpm, 10 min, (b) 880 rpm, 10 min, (c) 1500 rpm, 3 min, (d) 1100 rpm, 10 min, (e) 1100 rpm, 12 min, and (f) 1100 rpm, 15 min. Scale bar: 100 nm.

It is known that mechanical agitation has two opposite effects toward aggregation of particles⁵⁵⁻⁵⁷. First, stirring can enhance the rate of collisions between particles with respect to Brownian motion, thus increasing the possibility of nucleation and growth⁵⁵⁻⁵⁷. On the other hand, mechanical shear can destroy aggregated particulates by weakening the effective attractive interaction between neighboring particles because of mechanical stress and thus maintain particles in a well-dispersed state⁵⁵⁻⁵⁷. At a slow stirring speed of 600 rpm (Figure 3.10a), aggregation of nanocrystallites was observed and the size distribution was poor, while increasing the stirring speed to 880 rpm yielded particles with a good size distribution and well-defined structure (Figure 3.10b). In contrast, with a vigorous stirring speed of 1500 rpm (Figure 3.10c), granular seed particles with an increased size and surface roughness were obtained and no core-shell structure formation was observed, which can be ascribed to the second effect. It is also known that mechanical agitation can enhance mass transfer in-situ⁵⁵⁻⁵⁷. Hence, when the stirring rate was increased from 880 to 1100 rpm, the hollowing mechanism not only follows a symmetric Ostwald ripening but also proceeds at a faster rate (Figure 3.10d–3.10f). In Figure 3.11, the effect of the stirring nature on first-shell growth is elucidated.

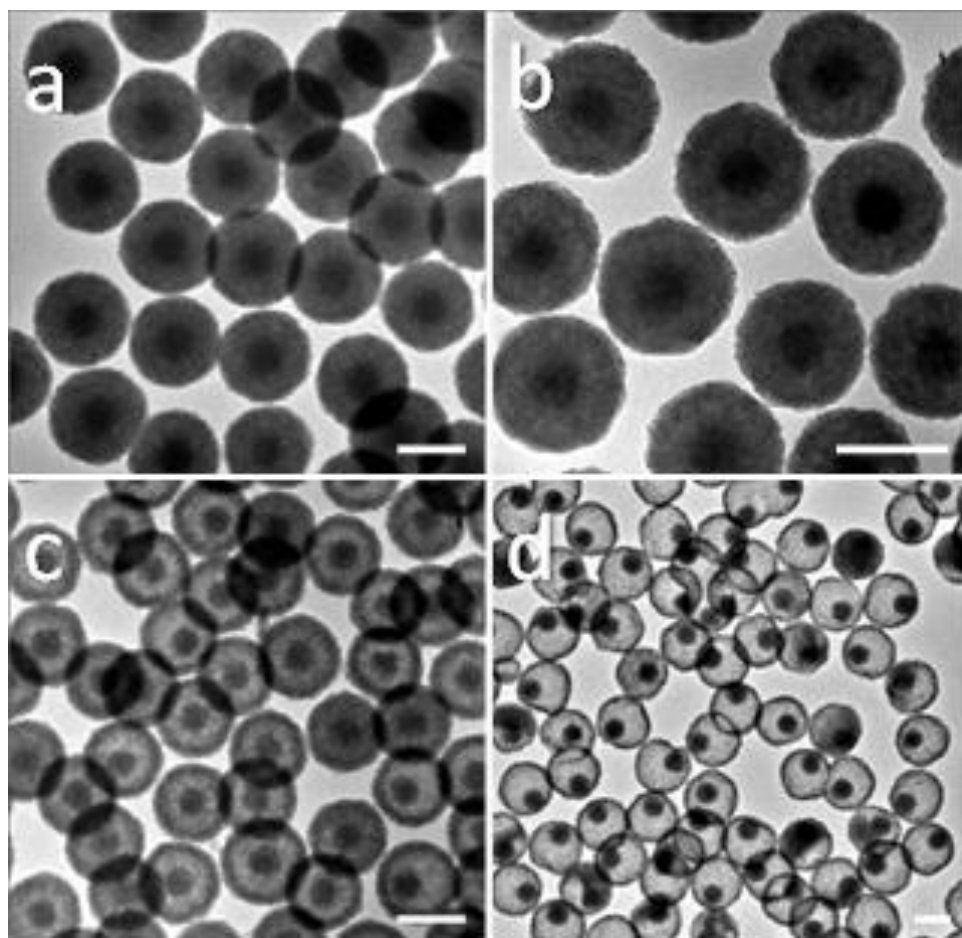


Figure 3.3 Effect of stirring conditions on the growth of the 1st shell: (a) center-stirring, 29 min of reaction, (b) center-stirring, 31 min of reaction, (c) center-stirring, 42 min of reaction, and (d) off-center-stirring with disturbance, 22 min of reaction. Refer to Experimental Section and A-2 for further details. Scale bar: 200 nm.

As shown therein, if the solution was stirred without any random solid solution disturbance (i.e., absence of a stirring bar hitting the glass containers), tiny Cu_2O crystallites would symmetrically deposit on the seeds; therefore, symmetric Ostwald ripening is the mechanism of the hollowing process, and the kinetics proceeds at a slower rate (Figure 3.11a–3.11c). In contrast, when the solution was stirred with a random disturbance (that is fluctuation in stirring speeds; the sound of the stirring bar hitting the glass was heard), the Cu_2O crystallites would land less symmetrically on

the seeds; therefore, asymmetric Ostwald ripening becomes the hollowing mechanism, and the kinetics proceeds at a faster rate (Figure 3.11d)⁴⁸. As additional evidence, Figure 3.11 shows the effect of the stirring condition on the growth of the second shell.

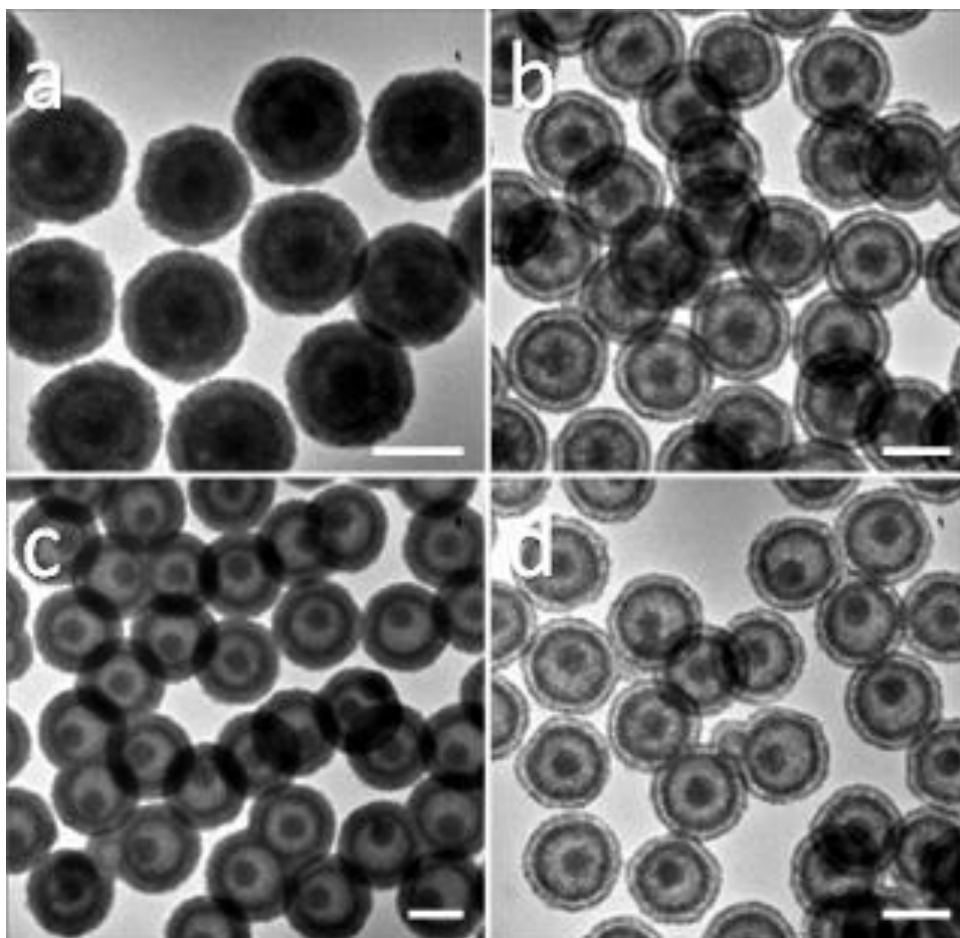


Figure 3.4 Effect of stirring conditions on the growth of the 2nd shell: (a) center-stirring, 11 min of reaction, (b) off-center-stirring with disturbance, 9 min of reaction, (c) center-stirring, 12 min of reaction, and (d) off-center-stirring with disturbance, 11 min of reaction. All synthetic experiments were started with 30 mL of core-shell (a and b) or yolk-shell (c and d) seeds. Refer to Experimental Section and A-2 for further details. Scale bar: 200 nm.

Similar to Figure 3.11, when the solution was stirred smoothly (without any drastic disturbance), hollowing kinetics proceeds at a slower rate, as opposed to that of the

sample stirred with a “unstable stir bar” (Figure 3.12b,3.12d). More TEM images of asymmetric Ostwald ripening are also provided in Figure 3.13.

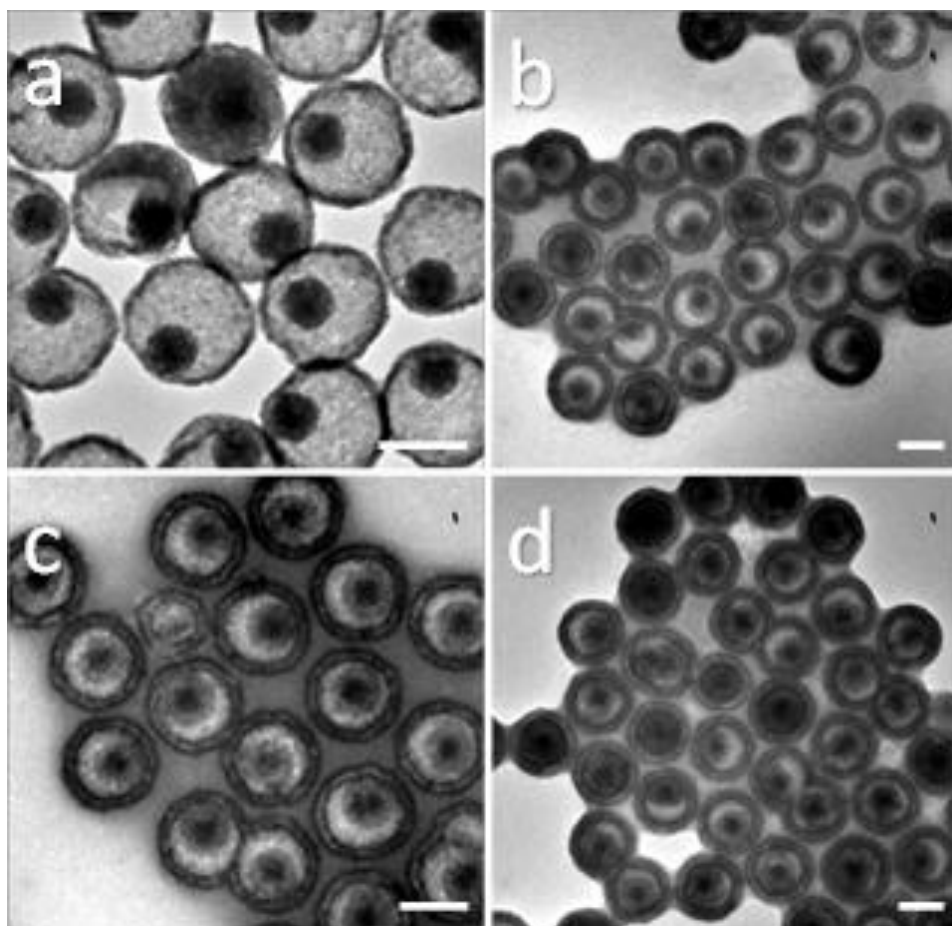


Figure 3.5 Asymmetric Ostwald ripening: (a) $\text{Cu}_2\text{O}@Cu_2\text{O}$ yolk–shells with incomplete hollowing, and (b to d) $\text{Cu}_2\text{O}@Cu_2\text{O}$ partial yolk–shell synthesized under 26 min then used as a seed for subsequent shell growth (i.e., to form $(\text{Cu}_2\text{O}@)_2\text{Cu}_2\text{O}$). Scale bar: 200 nm

In such cases, the solid evacuation can be described as an asymmetric mass relocation wherein the direction starts from one side of the sphere toward the core, which will be addressed more thoroughly below. Via variation of the amount of seed used in a subsequent growth, the size of $(\text{Cu}_2\text{O}@)_n\text{Cu}_2\text{O}$ structures can be tuned because of the associated control over the solid evacuation and shell thickness (Appendix 1-3A). With a smaller quantity of seeds, the size increase due to addition of a subsequent

shell is going to be larger, compared to those supplied with abundant seeds, because limited seeds are available for the same amount of growth units to be added. On the other hand, if the system is introduced with a larger number of seeds, the scarcity of the growth units would become an issue. As a result, fewer depositing crystallites could be available, and an increase in product size would be accordingly smaller. In addition to the amount of seeds used, concentrations of ascorbate and nitrate anions present for the synthesis also influence the aggregative and thus dispersive states of the spheres, because of the electrostatic effects of these ions. For example, when their concentrations are lower, quite interestingly, it is possible to encapsulate two or more cores with a newly formed shell. Corresponding to types R–U of Figure 3.1, peanut-like or bean-pod structures could be further generated in this way, as reported in Figure 3.14; a comparison of the concentrations of ascorbate and nitrate ions under various preparative conditions is given in Appendix 1-1B.

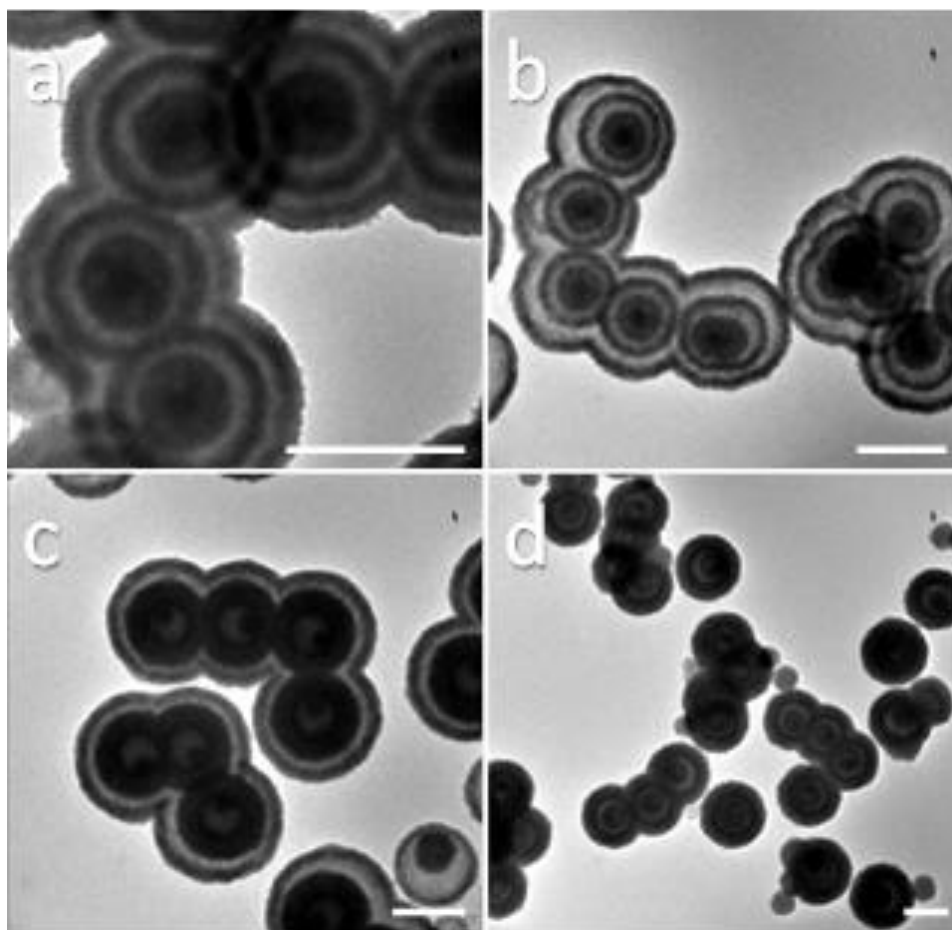


Figure 3.6 Triple-shelled bean pod structures synthesized with a small amount of "double-shelled seeds": (a) type R structure, (b) type S structure, (c) type T structure, and (d) type U structure. Refer to Figure 3.1 and A-1 for structural details. Scale bar: 400 nm.

Similar to those of single spheres, the following mechanism of formation of these complex structures could be proposed. First, type D–G structures of $(\text{Cu}_2\text{O}@)_2\text{Cu}_2\text{O}$ interconnect themselves upon transfer to the new reaction vessel. Second, $\text{Cu}(\text{OH})_2$ nanocrystallites are deposited on the external surface of the existing aggregates. Third, the deposited $\text{Cu}(\text{OH})_2$ phase was converted to Cu_2O through reduction. Finally, hollowing of the structure proceeds via Ostwald ripening, which creates the final peanut or bean-pod structures [types R–U, Appendix 1-1A]. It should also be mentioned that the morphological yield of each type of product listed in Figure 3.1 is

close to 100% in each batch of synthesis, which can be seen from the panoramic views of all our TEM images. For example, one might question whether the type G structure is due to a side view of type D spheres. If it were; however, one would have seen a mixture of both type G and type D structures in Figure 3.4d. However, across an entire copper grid, we can see only type D structure in all the spheres of this sample. According to eq 2, it is also important to determine the role of ammonium nitrate (NH_4NO_3) in shell formation. Via our synthetic experiments (section A-4 of the Appendix), we found that if ammonium nitrate is absent in the growth solution, no shell formation was observed. Instead, spontaneous nucleation and other growth events took place, which led to the formation of large polydisperse Cu_2O particles. As the concentration of NH_4NO_3 increases, however, small Cu_2O crystallites can form (Appendix 1-3B), which was due to inhibition of the rapid growth of $\text{Cu}(\text{OH})_2$ (eq 2) as mentioned earlier. To further strengthen the argument, the effects of different monovalent inorganic salts such as KNO_3 and NH_4Cl were also investigated in this work. We found that the growth with KNO_3 did not allow the formation of a shell on the Cu_2O seeds but promoted spontaneous nucleation and other growth events (Appendix 1-3B). On the other hand, the growth with NH_4Cl could allow the formation of spherical structures, but at a higher concentration of NH_4Cl , partially hollow spheres were seen because of the conversion of Cu_2O seeds to $\text{Cu}_2\text{Cl}(\text{OH})_3$ or its hydrated forms with an excess of Cl^- .^[19] Rather than their counter anions NO_3^- , therefore, the NH_4^+ cations are essential for shell formation.

3.3.3. Centricity and Eccentricity of Structures

With smooth central stirring, as mentioned earlier, tiny crystallites of Cu_2O can be formed on the provided seeds, forming concentric core-shell structures (e.g.,

Figure 3.11a, 3.11b). Even if Ostwald ripening becomes operative in these cases with a longer process time, the hollowing proceeds in a symmetric manner (Figure 3.11c), which can be described as a so-called symmetric Ostwald ripening.^[48] The $(\text{Cu}_2\text{O}@)_n\text{Cu}_2\text{O}$ products synthesized under such conditions can maintain high centricity before complete detachment of the core or yolk from the shell. In Figure 3.11c, the thin Cu_2O treads (or “bridges”) are still connecting Cu_2O cubes and the newly formed shell. In this hollowing process, the central Cu_2O crystallites are gradually relocated to the shells while the single-crystal Cu_2O seeds remain largely intact. It is interesting to note that the sample reported in Figure 3.11c is still a highly centric solid intermediate falling between core-shell and yolk-shell structures, because plenty of intercrystallite spaces have been created between the cores and shells but the single-crystal Cu_2O cubes are still located in the center. In addition to these single-shell spheres, many multishell core-shell products possessing centricity have also been prepared in this work. In Figure 3.1, samples with type B, D, H, and P structures belong to this class of materials, and their respective product morphologies can be found from the TEM images listed in Appendix 1-1A. From a structural viewpoint, any detached core or yolk (it does not matter whether it is in a simple or complex form) in a hollow sphere would lead to an overall eccentricity for the structure, because the separate core or yolk would roll freely over the internal surface of the shell because of the gravity or influence of any external forces or fields. In a liquid phase, however, the core or yolk could move to a central location of the hollow space because of dynamical motion and/or convection of the fluid, but such a centricity should be considered only momentary as it requires a simultaneous balance of all possible forces exerted on the core or yolk. Though it is difficult, nevertheless,

the temporary centricity of yolk-shell structures does exist in dynamic systems in which liquid fluids are flowing in and out of the cavity space. On the other hand, to produce highly eccentric multishell yolk-shell structures, a sufficiently large intershell space must be ensured. For example, compare type E with type G structure (Figure 3.1). Apparently, a larger space between the first and second shells is required for the formation of a movable $\text{Cu}_2\text{O}@_n\text{Cu}_2\text{O}$ yolk [Figure 3.3g (type G) vs. Figure 3.4f (type E)]. In this synthesis, another kind of eccentricity, permanent eccentricity, can also be obtained in our $(\text{Cu}_2\text{O}@)_n\text{Cu}_2\text{O}$ products. As shown in Figure 3.11d, the yolk-shell structures formed in disrupted solid solution systems would undergo asymmetric Ostwald ripening during their hollowing process. It is noted that the pristine Cu_2O cube (seed) and the remaining Cu_2O mass (crystallites) in the central area are brought together toward shell walls (for example, some of this solid intermediate can be clearly seen in Figures 3.10a and 3.11a), resulting in direct attachment of the seeds to the walls, resulting in permanent eccentricity for the final products. In addition to single-shell off-central yolk-shell structures, multishell yolk-shell products with permanent eccentricity can also be prepared when asymmetric Ostwald ripening is conducted (e.g., Figure 3.13b–3.13d) in creating interior spaces.

3.3.4. Structures and Optical Properties

Concerning the applications of this class of complex materials, the effect of the structural configuration on their optical property has been further investigated. As the first step in this effort, in particular, extinction spectra at 300–800 nm of several $(\text{Cu}_2\text{O})_n\text{Cu}_2\text{O}$ samples were measured in this work. Apart from the chemical nature of the material, it should be recognized that a number of factors would also determine fingerprint features of extinction spectra, including the sizes of our pristine cubes and

crystallites of shells, the number and thickness of shells, core- or yolk- shell and shell-shell distances, and overall centricity and eccentricity of product spheres. In Figure 3.15, a spectral comparison among structural types A-E, H, and P is made, using type A cubic seeds as a reference. Interestingly, both type B and C structures exhibit a blue shift in their extinction peaks, while type D, E, H, and P structures indicate a red shift.

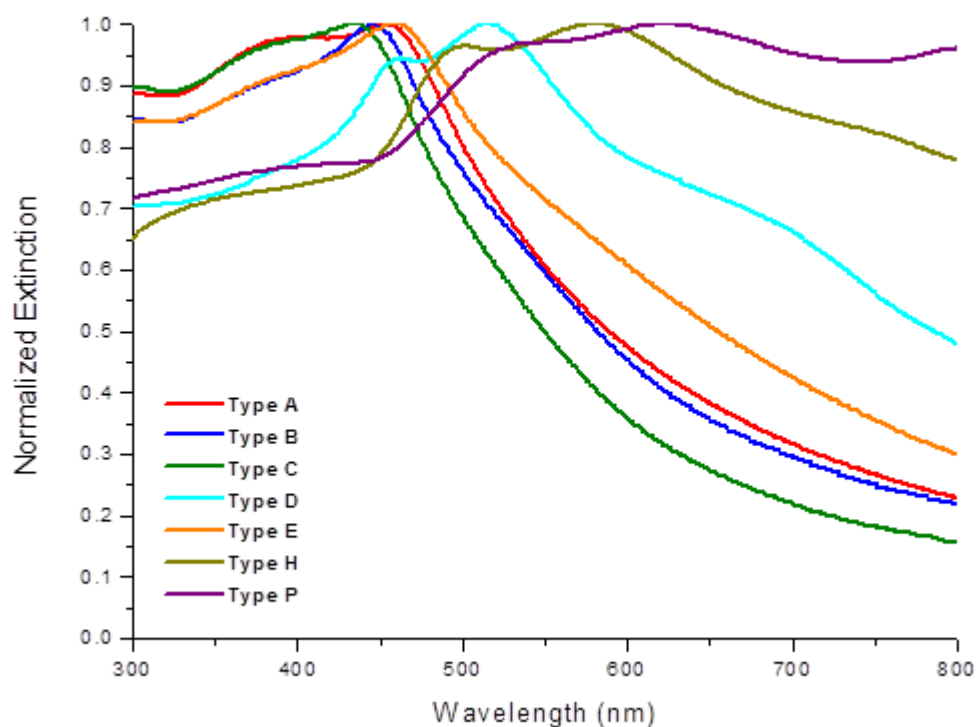


Figure 3.7. Extinction spectra of pristine Cu_2O cubes and different types of complex $(\text{Cu}_2\text{O}@)_n\text{Cu}_2\text{O}$ structures. Refer to Figure 3. 1 and A-1 for structural details.

The observed blue shifts in the extinction peak for single-shell structures may be attributable to the contribution of absorption of the polycrystalline shell to the extinction, and thus, the extinction peak would be blue-shifted compared to that of

type A. On the other hand, the redshifts in the extinction peak are likely due to the overall increase in the sphere size and scattering contribution to the extinction from more and thicker shells⁵³. A detailed correlation between the resultant optical property and a given amount of shells is also presented with more such $(\text{Cu}_2\text{O}@)_n\text{Cu}_2\text{O}$ samples (Appendix 1-4A). On the basis of this comparative study, several interesting observations can be made. First, two extinction peaks are better resolved starting from double-shell type D structure onward to subsequent multishell structures. The multiple peak features have been attributed to the appearance of higher-order modes at Mie scattering resonances because of phase retardation effects when the sphere size is comparable to the wavelength of incident light.^[40,53] Second, structures with thinner shells exhibit a blue shift of the extinction peak that may be ascribed to the dominant contribution of absorption to the extinction at a thin-shell regime³². Third, the presence of a movable yolk would enhance the eccentricity of the structure and display essentially a single extinction peak (e.g., type E in Figure 3.15, and other examples in Appendix 1-4A). In this regard, signatory extinction behaviors of nonconcentric configurations are however complicated, and a complete description for them would require extensive theoretical development with a drastic departure from the scattering model using concentric spheres⁵⁸.

3.3.5. Electrochemical Applications

To study the electrochemical properties of the structures described above, the oxidation of glucose by Cu_2O in an alkaline solution was chosen, because this reaction system can be used as a nonenzymatic amperometric sensor of glucose⁵⁹⁻⁶³. Cyclic voltammetry (CV) measurements were thus performed using $(\text{Cu}_2\text{O}@)_n\text{Cu}_2\text{O}$ /Nafion-modified GCEs (i.e., $\text{Cu}_2\text{O}/\text{Nf}/\text{GCEs}$) in 0.1 M nitrogen-saturated NaOH containing

different concentrations of glucose (0.0, 5.0, and 10.0 mM) at a scan rate of 50 mV/s. Associated with these tests, Nafion-modified GCE (i.e., Nf/GCE) was also prepared for comparison (Appendix 1-4B), which shows a capacitive charging response with an oxidative wave as the applied potential increase, and the signal may be attributed to the initialization of water electrolysis at 0.60 V⁶². In addition, no redox peaks were observed upon addition of glucose, and signals show only a small increase in current. Figure 3.16 details the cyclic voltammograms of our $\text{Cu}_2\text{O}/\text{Nf}/\text{GCEs}$ at different glucose concentrations.

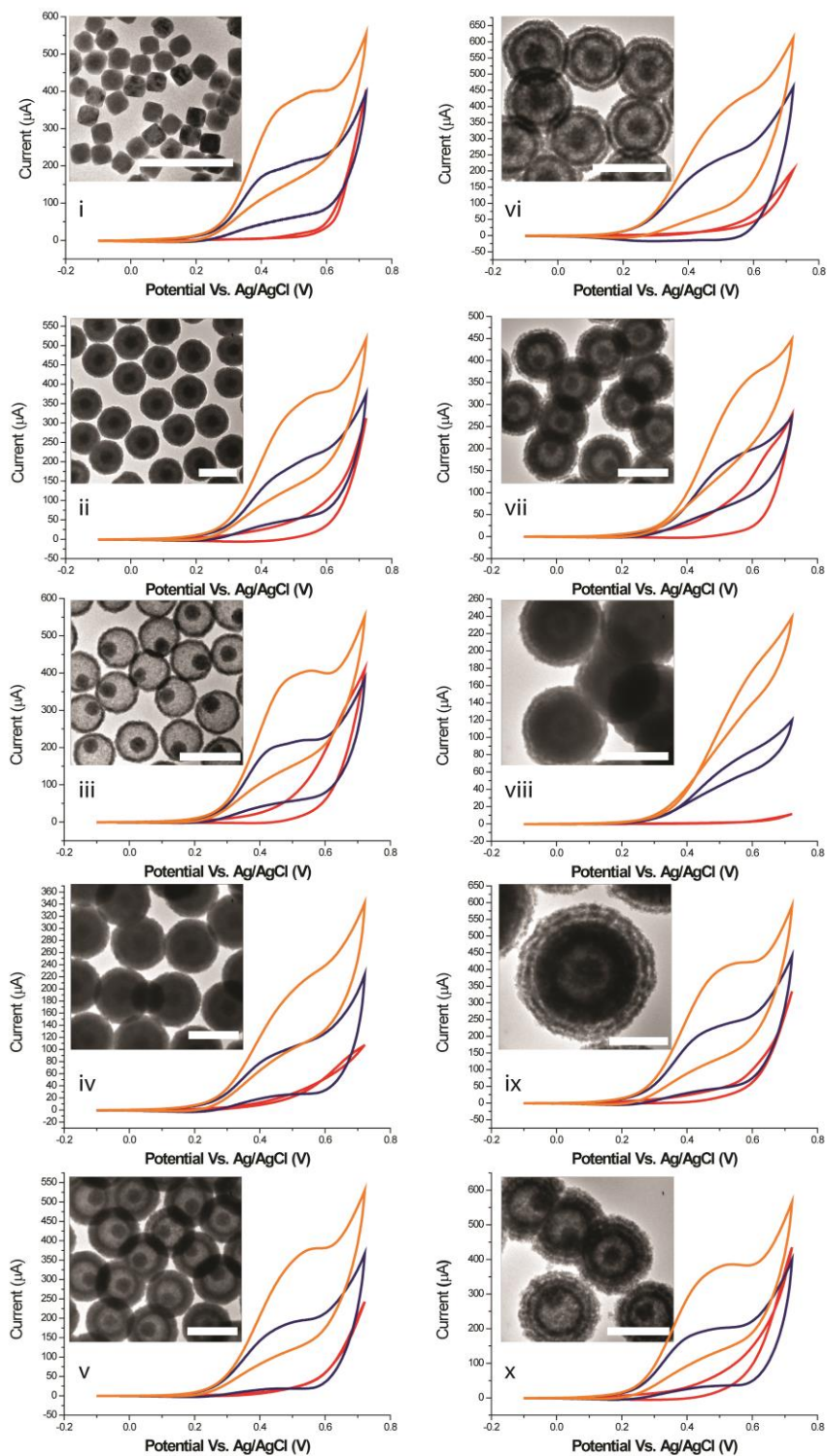


Figure 3.8 Cyclic voltammograms of different $\text{Cu}_2\text{O}/\text{Nf}/\text{GCEs}$ with 0.0 (red, after 5 cycles), 5.0 (blue, after 30 cycles) and 10.0 (orange, after 30 cycles) mM glucose in 0.10 M nitrogen-saturated NaOH: (i) type A, (ii) type B, (iii) type C, (iv) type D with thick shells, (v) type E, (vi) type D with thin shells, (vii) type H, (viii) type P with thick shells, (ix) type P with thin

shells, and (x) type Q with thin shells. Scan rate: 50 mVs^{-1} . Synthetic details can be found in Experimental Section and Appendix 1-1B. Insets: corresponding TEM images of the $(\text{Cu}_2\text{O}@)_n\text{Cu}_2\text{O}$ structures. Scale bar: 300 nm.

Similar to the Nf/GCE, the $\text{Cu}_2\text{O}/\text{Nf}/\text{GCEs}$ show only a large oxidative tail, and no redox peaks were observed without glucose. With an increase in the glucose concentration to 5.0 mM, a single forward anodic wave, which corresponds to the irreversible glucose oxidation reaction, was observed for each structure type, and the increases in the anodic currents for most structures were recorded at around 0.20 V (vs Ag/AgCl), indicating the start of glucose oxidation. The currents continued to increase until a potential of 0.60 V (vs Ag/AgCl) was achieved, and this oxidative peak (or wave) can also be attributed to the involvement of copper(II) and copper(III) surface species in glucose oxidation according to the literature⁶³⁻⁶⁵. Table 1 summarizes the anodic peak potential and current of $\text{Cu}_2\text{O}/\text{Nf}/\text{GCEs}$ at different glucose concentrations. There are several findings that can be drawn from both Figure 3.16 and Table 1. First, the anodic peak potential is shifted to a more positive side as the number of shell increases. For instance, the anodic potential of the type A structure at 5.0 mM glucose is 0.412 V, and that of a thick shell type P structure at the same concentration is 0.507 V. This is understandable, because slower diffusion of the analyte toward the inner parts of structure is expected when the number of shells increases, and accordingly, the anodic peak potential in the latter case has to be increased. Second, structures with thinner shells show a lower anodic peak potential and a higher anodic peak current. For example, thick- and thin-shell type P structures at 5.0 mM glucose give anodic peak potentials of 0.507 and 0.431 V and anodic peak currents of 60 and 200 μA , respectively (Table 1). Similar to the first observation, a

thicker shell would likely exert greater diffusion barrier for the analyte to overcome, resulting in a larger portion of Cu_2O that is not in contact with the analyte. In this connection, we have also examined the cyclic voltammogram of thick-shell type P structure from 1 to 30 cycles. As shown in Appendix 1-4B, the anodic peak current of this sample starts to appear after ten cycles and increases until 30 cycles, which also shows that the thicker shell can limit the diffusion of an analyte. Third, the pristine seed nanocubes exhibit a higher current and a lower peak potential, compared to those of some of the structures. This may be attributed to their small mean size and the truncated cube morphology. In such a shell-free case, diffusion through a shell barrier is not an issue, and the Cu_2O can be largely used in the sensing reaction, although the average cube size is not very small. Furthermore, the contribution of specific crystal facets (such as the $\{110\}$ and $\{111\}$ facets mentioned earlier) of these truncated cubes to the oxidation activity may also be identifiable. Because of the high intrinsic complexity of shell structures, no definite trends were observed for the effect of shell number on the magnitude of the anodic current. However, as a general finding, structures with thinner shells have higher anodic peak currents, compared to those of their thicker-shell counterparts. Moreover, type C and type P (thin-shell) structures show the highest anodic peak currents, both with a magnitude of $370 \mu\text{A}$ at 10 mM glucose (Table 1).

Table 1.1. Anodic Peak Potential and Current of Different Cu_2O Structures (Figure 3.15)

Structure	Glucose Concentration (mM)	Anodic Peak Potential (V)	Anodic Peak Current (μA)	Structure	Glucose Concentration (mM)	Anodic Peak Potential (V)	Anodic Peak Current (μA)
Type A	5	+0.412	170	Type D, thin shells	5	+0.426	190
	10	+0.446	340		10	+0.470	350
Type B	5	+0.441	160	Type H	5	+0.497	160
	10	+0.473	310		10	+0.546	320
Type C	5	+0.426	190	Type P, thick shells	5	+0.507	60
	10	+0.470	370		10	+0.570	160
Type D, thick shells	5	+0.424	80	Type P, thin shells	5	+0.431	200
	10	+0.470	180		10	+0.470	370
Type E	5	+0.429	160	Type Q	5	+0.400	170
	10	+0.483	330		10	+0.441	350

The glucose sensing performance of various $\text{Cu}_2\text{O}/\text{Nf}/\text{GCEs}$ was evaluated by chronoamperometric measurements in 0.10 M nitrogen-saturated NaOH at an applied constant potential of 0.5 V (vs. Ag/AgCl). Figure 3.17 reports the amperometric responses of these electrodes.

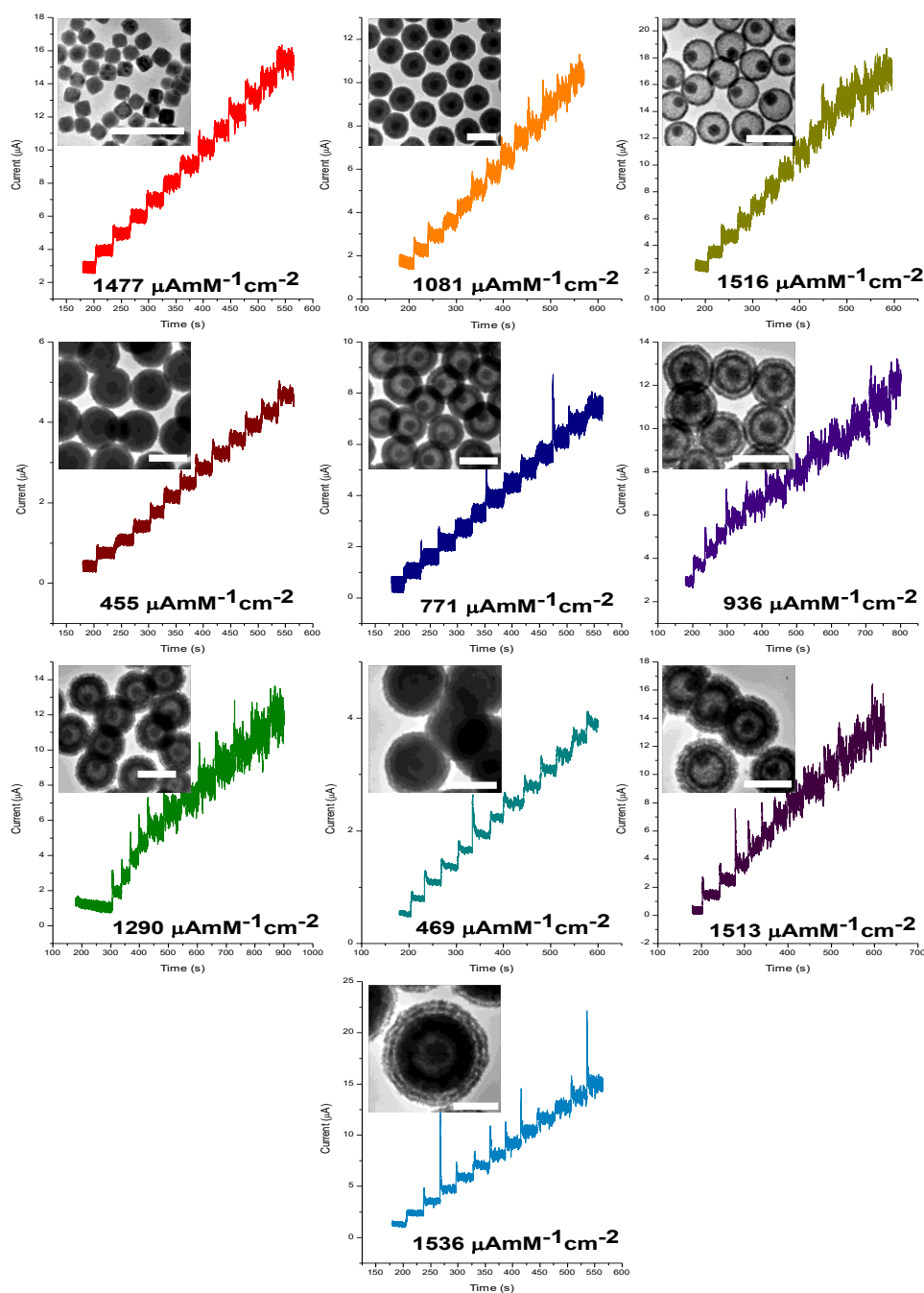


Figure 3.9 Chronoamperometric responses of various $\text{Cu}_2\text{O}/\text{Nf}/\text{GCEs}$ upon successive addition of $10 \mu\text{M}$ glucose into a gently stirred 0.10 M nitrogen saturated NaOH at 0.50 V (vs. Ag/AgCl electrode): (i) type A, (ii) type B, (iii) type C, (iv) type D with thick shells, (v) type E, (vi) type D with thin shells, (vii) type H, (viii) type P with thick shells, (ix) type P with thin shells, and (x) type Q with thin shells. Insets: corresponding TEM images of the $(\text{Cu}_2\text{O}@)_n\text{Cu}_2\text{O}$ structures and sensitivities of the electrodes. Scale bar: 300 nm .

As one can see, type P (thin shell) structure gives the highest sensitivity toward glucose at $1536 \mu\text{A mM}^{-1} \text{cm}^{-2}$, while the sensitivities of other structures are ordered as follows: type P (thin shells, $1536 \mu\text{A mM}^{-1} \text{cm}^{-2}$) > type C ($1516 \mu\text{A mM}^{-1} \text{cm}^{-2}$) > type Q (thin shells, $1513 \mu\text{A mM}^{-1} \text{cm}^{-2}$) > type A ($1477 \mu\text{A mM}^{-1} \text{cm}^{-2}$) > type J ($1290 \mu\text{A mM}^{-1} \text{cm}^{-2}$) > type B ($1081 \mu\text{A mM}^{-1} \text{cm}^{-2}$) > type D (thin shells, $936 \mu\text{A mM}^{-1} \text{cm}^{-2}$) > type E (thick shells, $771 \mu\text{A mM}^{-1} \text{cm}^{-2}$) > type P (thick shells, $469 \mu\text{A mM}^{-1} \text{cm}^{-2}$) > type D (thick shells, $455 \mu\text{A mM}^{-1} \text{cm}^{-2}$). It can be inferred from this sequence that an overall thinner-shell structure would give greater sensitivity toward glucose oxidation because of the ease of diffusion and charge transfer of the analyte. More importantly, there are several factors that contribute to the sensitivity of the structures such as the shell thickness, the surface area, and the amount of shell. Although the thin-shell type P and type Q structures are larger than the other structures, their sensitivities are higher for the following reasons. First, the structures are composed of multiple thin shells that would facilitate easier diffusion of analytes toward the interior of the structure. Second, each shell consists of crystallites that can act as a sensing material for glucose, and thus, the total active Cu_2O for sensing would be more tremendous. Interestingly, type A structure also shows a high sensitivity toward glucose with a value of $1477 \mu\text{A mM}^{-1} \text{cm}^{-2}$. As mentioned earlier, this can be attributed to easy diffusion and fast charge transfer of analytes with these truncated nanocubes. Compared to some thick-shell structures (such as types D and P), the type A sample can be treated as a smaller shell-free structure having an immediately accessible electroactive surface.

3.4 Conclusion

In summary, a family of multishell core-shell and yolk-shell spherical structures, $(\text{Cu}_2\text{O}@)_n\text{Cu}_2\text{O}$, has been synthesized using a seed-mediated growth approach followed by Ostwald ripening. With this multiple-step solution-based approach, the structure formed in the previous step can serve as a newer generation seed for subsequent shell growth. Therefore, by varying the types of seed, we can determine the overall spherical centricity or eccentricity; such combined growths lead to the generation of 2^n structures (where n is the number of shells). It has been found that the inhibition of rapid growth of $\text{Cu}(\text{OH})_2$ through addition of NH_4NO_3 is essential for the formation of the polycrystalline shell. Symmetric or asymmetric Ostwald ripening for hollowing can be further controlled by smooth stirring or introducing fluctuation and/or disturbance to the solid solution systems. The thickness of the shell and the overall size and morphology of the spheres can be tuned facilely by changing the amount of seed added and the reaction and/or ripening time. Furthermore, simultaneous encapsulation of two or more cores also possible at lower concentrations of ascorbate and nitrate anions; peanut-like and bean-pod-like structures have been thus produced. Nevertheless, additional investigation is needed to achieve more precise control of the number of seeds encapsulated and the size uniformity of final hierarchical structures. The optical characterization reveals certain relationships between the size or structure of spheres and the observed extinction spectra in the visible wavelength regime. The multishell spheres with thinner shells show improved sensing sensitivity and activity for nonenzymatic glucose sensing application. This solution-based approach is a simple, but effective method for fabricating various very complex multishell structures without compromising the ability to control the size monodispersity and morphological yield. At present, the

synthesis of multishell $(\text{Cu}_2\text{O}@)_n\text{Cu}_2\text{O}$ spheres with a larger n value ($n > 4$) may remain a technical challenge, especially with large intershell spaces for the creation of structural eccentricity. Such synthetic architectures require further research efforts.

References

1. Alivisatos, A. P. Semiconductor Clusters, Nanocrystals, and Quantum Dots. *Science* **1996**, *271*, 933-937.
2. Choi, C. L.; Alivisatos, A. P. From Artificial Atoms to Nanocrystal Molecules: Preparation and Properties of More Complex Nanostructures, *Annu. Rev. Phys. Chem.* **2010**, *61*, 369-389.
3. Habas, S. E.; *et al.* Shaping Binary Metal Nanocrystals Through Epitaxial Seeded Growth. *Nat. Mater.* **2007**, *6*, 692-697.
4. Peng, X. G.; *et al.* Shape Control of CdSe Nanocrystals. *Nature* **2000**, *404*, 59-61.
5. Punties, V. F.; Krishnan, K. M.; Alivisatos, A. P. Colloidal Nanocrystal Shape and Size Control: The Case of Cobalt. *Science* **2001**, *291*, 2115-2117.
6. Kuo, C. H.; Chen, C. H.; Huang, M. H. Seed-Mediated Synthesis of Monodispersed Cu_2O Nanocubes with Five Different Size Ranges from 40 to 420 nm. *Adv. Funct. Mater.* **2007**, *17*, 3773-3780.
7. Gou, L.; Murphy, C. J. Solution-Phase Synthesis of Cu_2O Nanocubes. *Nano Lett.* **2002**, *3*, 231-234.
8. Park, J.C.; *et al.* Gram-Scale Synthesis of Cu_2O Nanocubes and Subsequent Oxidation to CuO Hollow Nanostructures for Lithium-Ion Battery Anode Materials. *Adv. Mater.* **2009**, *21*, 803.

9. Zhang, Q.; *et al.* Seed-Mediated Synthesis of Ag Nanocubes with Controllable Edge Lengths in the Range of 30-200 nm and Comparison of Their Optical Properties. *J. Am. Chem. Soc.* **2010**, *132*, 11372-11378.
10. Yao, K. X.; *et al.* Synthesis, Self-Assembly, Disassembly, and Reassembly of Two Types of Cu_2O Nanocrystals Unifaceted with {001} or {110} Planes. *J. Am. Chem. Soc.* **2010**, *132*, 6131-6144.
11. Liu, B.; Zeng, H. C. Hydrothermal Synthesis of ZnO Nanorods in the Diameter Regime of 50 nm. *J. Am. Chem. Soc.* **2003**, *125*, 4430-4431.
12. Liu, B.; Zeng, H. C. Room Temperature Solution Synthesis of Monodispersed Single-Crystalline ZnO Nanorods and Derived Hierarchical Nanostructures. *Langmuir* **2004**, *20*, 4196-4204.
13. Huang, M. H.; *et al.* Room-Temperature Ultraviolet Nanowire Nanolasers. *Science* **2001**, *292*, 1897-1899.
14. Huang, M.H.; *et al.* Catalytic Growth of Zinc Oxide Nanowires by Vapor Transport. *Adv. Mater.* **2001**, *13*, 113-116.
15. Liu, B.; Zeng, H. C. Semiconductor Rings Fabricated by Self-Assembly of Nanocrystals. *J. Am. Chem. Soc.* **2005**, *127*, 18262-18268.
16. Xu, J.; *et al.* Mechanical Nanosprings: Induced Coiling and Uncoiling of Ultrathin Au Nanowires. *J. Am. Chem. Soc.* **2010**, *132*, 11920-11922.
17. Siegfried, M. J.; Choi, K. S. Directing the Architecture of Cuprous Oxide Crystals During Electrochemical Growth. *Angew. Chem. Int. Ed.* **2005**, *44*, 3218-3223.
18. Siegfried, M. J.; Choi, K. S. Electrochemical Crystallization of Cuprous Oxide with Systematic Shape Evolution. *Adv. Mater.* **2004**, *16*, 1743.

19. Siegfried, M. J.; Choi, K. S. Elucidating the Effect of Additives on the Growth and Stability of Cu_2O Surfaces via Shape Transformation of Pre-grown Crystals. *J. Am. Chem. Soc.* **2006**, *128*, 10356-10357.
20. Liz-Marzan, L.M.; Giersig, M.; Mulvaney, P. Synthesis of Nanosized Gold-Silica Core-shell Particles. *Langmuir* **1996**, *12*, 4329-4335.
21. Lauhon, L.J.; *et al.* Epitaxial Core-shell and Core-multishell Nanowire Heterostructures. *Nature* **2002**, *420*, 57-61.
22. Zhang, T.; *et al.* Formation of Hollow Silica Colloids through a Spontaneous Dissolution-regrowth Process. *Angew. Chem. Int. Ed.* **2008**, *47*, 5806-5811.
23. Fang, Q.; *et al.* Yolk-like Micro/Nanoparticles with Superparamagnetic Iron Oxide Cores and Hierarchical Nickel Silicate Shells. *Adv. Funct. Mater.* **2011**, *21*, 1902-1909.
24. Li, J.; Zeng, H. C. Nanoreactors - Size tuning, Functionalization, and Reactivation of Au in TiO_2 Nanoreactors. *Angew. Chem. Int. Ed.* **2005**, *44*, 4342-4345.
25. Yin, Y. D.; *et al.* Formation of Hollow Nanocrystals through the Nanoscale Kirkendall Effect. *Science*, **2004**, *304*, 711-714.
26. Yang, H. G.; Zeng, H.C. Preparation of Hollow Anatase TiO_2 Nanospheres via Ostwald Ripening. *J. Phys. Chem. B* **2004**, *108*, 3492-3495.
27. Chang, Y.; Teo, J. J.; Zeng, H. C. Formation of Colloidal CuO Nanocrystallites and their Spherical Aggregation and Reductive Transformation to Hollow Cu_2O Nanospheres. *Langmuir* **2005**, *21*, 1074-1079.

28. Teo, J. J.; Chang, Y.; Zeng, H. C. Fabrications of Hollow Nanocubes of Cu_2O and Cu via Reductive Self-assembly of CuO Nanocrystals. *Langmuir* **2006**, *22*, 7369-7377.
29. Lou, X.W.; *et al.* Template-free Synthesis of SnO_2 Hollow Nanostructures with High Lithium Storage Capacity. *Adv. Mater.* **2006**, *18*, 2325.
30. Pang, M. L.; Zeng, H. C. Highly Ordered Self-Assemblies of Submicrometer Cu_2O Spheres and Their Hollow Chalcogenide Derivatives. *Langmuir* **2010**, *26*, 5963-5970.
31. Ding, S.; *et al.* Formation of SnO_2 Hollow Nanospheres inside Mesoporous Silica Nanoreactors. *J. Am. Chem. Soc.*, **2011**, *133*, 21-23.
32. Zhang, L.; Wang, H. Cuprous Oxide Nanoshells with Geometrically Tunable Optical Properties. *ACS Nano*, **2011**, *5*, 3257-3267.
33. Cozzoli, P. D.; Pellegrino, T.; Manna, L. Synthesis, Properties and Perspectives of Hybrid Nanocrystal Structures. *Chem. Soc. Rev.* **2006**, *35*, 1195-1208.
34. Casavola, M.; *et al.* Colloidal Strategies for Preparing Oxide-based Hybrid Nanocrystals. *Eur. J. Inorg. Chem.* **2008**, 837-854.
35. Pang, M. L.; Hu, J. Y.; Zeng, H.C. Synthesis, Morphological Control, and Antibacterial Properties of Hollow/Solid $\text{Ag}_2\text{S}/\text{Ag}$ Heterodimers. *J. Am. Chem. Soc.* **2010**, *132*, 10771-10785.
36. Tian, N.; *et al.*, Synthesis of Tetrahedral Platinum Nanocrystals with High-index Facets and High Electro-oxidation Activity. *Science* **2007**, *316*, 732-735.

37. Ma, Y.; *et al.*, Synthesis of Trisoctahedral Gold Nanocrystals with Exposed High-Index Facets by a Facile Chemical Method. *Angew. Chem. Int. Ed.* **2008**, *47*, 8901-8904.
38. Ming, T.; *et al.*, Growth of Tetrahedral Gold Nanocrystals with High-index Facets. *J. Am. Chem. Soc.* **2009**, *131*, 16350.
39. Leng, M.; *et al.*, Polyhedral 50-Facet Cu_2O Microcrystals Partially Enclosed by $\{311\}$ High-Index Planes: Synthesis and Enhanced Catalytic CO Oxidation Activity. *J. Am. Chem. Soc.* **2010**, *132*, 17084-17087.
40. Bardhan, R., *et al.*, Nanosphere-in-a-Nanoshell: A Simple Nanomatryushka. *J. Phys. Chem. C.* **2010**, *114*, 7378-7383.
41. Liu, J., *et al.*, A Facile Vesicle Template Route to Multi-shelled Mesoporous Silica Hollow Nanospheres. *J. Mater. Chem.* **2010**, *20*, 4595-4601.
42. Wong, Y.J.; *et al.*, Revisiting the Stober Method: Inhomogeneity in Silica Shells. *J. Am. Chem. Soc.* **2011**, *133*, 11422-11425.
43. Zhang, H.; *et al.*, One-pot Synthesis and Hierarchical Assembly of Hollow Cu_2O Microspheres with Nanocrystals-composed Porous Multishell and their Gas-sensing Properties. *Adv. Funct. Mater.* **2007**, *17*, 2766-2771.
44. Lai, X.; *et al.*, General Synthesis and Gas-Sensing Properties of Multiple-Shell Metal Oxide Hollow Microspheres. *Angew. Chem. Int. Ed.* **2011**, *50*, 2738-2741.
45. Wu, H.; *et al.*, A Hollow-Core, Magnetic, and Mesoporous Double-Shell Nanostructure: In Situ Decomposition/Reduction Synthesis, Bioimaging, and Drug-Delivery Properties. *Adv. Funct. Mater.* **2011**, *21*, 1850-1862.

46. Lou, X. W.; Yuan, C.; Archer, L. A. Shell-by-shell Synthesis of Tin Oxide Hollow Colloids with Nanoarchitected Walls: Cavity Size Tuning and Functionalization. *Small* **2007**, *3*, 261-265.
47. Wang, X.; *et al.*, Synthesis and Lithium Storage Properties of Co_3O_4 Nanosheet-Assembled Multishelled Hollow Spheres. *Adv. Funct. Mater.* **2010**, *20*, 1680-1686.
48. Liu, B.; Zeng, H. C. Symmetric and Asymmetric Ostwald Ripening in the Fabrication of Homogeneous Core-shell Semiconductors. *Small* **2005**, *1*, 566-571.
49. Lou, X. W.; Yuan, C.; Archer, L. A. Double-walled SnO_2 Nano-cocoons with Movable Magnetic Cores. *Adv. Mater.* **2007**, *19*, 3328.
50. Xiong, S.; Zeng, H. C. Serial Ionic Exchange for the Synthesis of Multishelled Copper Sulfide Hollow Spheres. *Angew. Chem. Int. Ed.* **2012**, *51*, 949-952.
51. Xu, H.; Wang, W. Template Synthesis of Multishelled Cu_2O Hollow Spheres with a Single-Crystalline Shell Wall. *Angew. Chem. Int. Ed.*, **2007**, *46*, 1489-1492.
52. Cho, W.; *et al.*, Multi Ball-In-Ball Hybrid Metal Oxides. *Adv. Mater.* **2011**, *23*, 1720.
53. Zhang, L.; Wang, H. Interior Structural Tailoring of Cu_2O Shell-in-Shell Nanostructures through Multistep Ostwald Ripening. *J. Phys. Chem. C* **2011**, *115*, 18479-18485.
54. Zeng, H. C. Ostwald Ripening: A Synthetic Approach for Hollow Nanomaterials. *Current Nanoscience* **2007**, *3*, 177-181.

55. Li, D.; Kaner, R. B. Shape and Aggregation Control of Nanoparticles: Not Shaken, Not Stirred. *J. Am. Chem. Soc.* **2006**, *128*, 968-975.
56. Cerda, J.J.; *et al.*, Shear Effects on Crystal Nucleation in Colloidal Suspensions. *Phys. Rev. E*, **2008**. *78*, 031403.
57. Oles, V., Shear-induced Aggregation and Breakup of Polystyrene Latex-particles. *J. Colloid Interface Sci.* **1992**, *154*, 351-358.
58. Aden, A. L.; Kerker, M. Scattering of Electromagnetic Waves from 2 Concentric Spheres. *J. Appl. Phys.* **1951**, *22*, 1242-1246.
59. Zhang, L.; *et al.*, Porous Cuprous Oxide Microcubes for Non-enzymatic Amperometric Hydrogen Peroxide and Glucose Sensing. *Electrochem. Commun.* **2009**, *11*, 812-815.
60. Batchelor-McAuley, C.; *et al.*, The Use of Copper(II) Oxide Nanorod Bundles for the Non-enzymatic Voltammetric Sensing of Carbohydrates and Hydrogen Peroxide. *Sens. Actuators, B* **2008**, *135*, 230-235.
61. Zhang, X.; *et al.*, Fixure-reduce Method for the Synthesis of $\text{Cu}_2\text{O}/\text{MWCNTs}$ Nanocomposites and its Application as Enzyme-free Glucose Sensor. *Biosens. Bioelectron.* **2009**, *24*, 3395-3398.
62. Jiang, L. C.; Zhang, W. D. A Highly Sensitive Nonenzymatic Glucose Sensor Based on CuO Nanoparticles-modified Carbon Nanotube Electrode. *Biosens. Bioelectron.* **2010**, *25*, 1402-1407.
63. Zhuang, Z.; *et al.*, An Improved Sensitivity Non-enzymatic Glucose Sensor Based on a CuO Nanowire Modified Cu Electrode. *Analyst* **2008**, *133*, 126-132.

64. Farrell, S. T.; Breslin, C. B. Oxidation and Photo-induced Oxidation of Glucose at a Polyaniline Film Modified by Copper Particles. *Electrochim. Acta* **2004**, *49*, 4497-4503.
65. Marioli, J. M.; Kuwana, T. Electrochemical Characterization of Carbohydrate Oxidation at Copper Electrodes. *Electrochim. Acta* **1992**, *37*, 1187-1197.

Chapter 4. Transformative Syntheses of Complex Copper-Based Nanostructures from Precursors with Predesigned Architecture and Reactivity

Abstract

Chemical transformation of nanomaterial coupled with kinetic control provides a versatile route to engineer a variety of complex nanostructures from a single precursor. Here we present an architecture-dependent reactivity-based kinetic control to manipulate both structure and composition of nanomaterials under all possible types of transformative processes. The key is to use a solid precursor with predesigned variations in crystallinity and grain size, thus enabling multiple regions of reactivity along the structure. This reactivity gradient allows additional kinetic control of various transformative processes that result in unique nanostructures. These unique structures demonstrate structure-property correlations that lead to better understanding of the design of photocatalytic and solar cell nanodevices. This comprehensive study represents an advancement in structural control of complex nanomaterials under different types of transformative processes and opens up possibilities for the exploration of size- and shape-scaling laws.

4.1 Introduction

The reactivity of materials depends not only on their composition, but also on their ability to form an interface with other components which is determined by its size, crystallinity and architecture. It has been established that nanomaterials are in general more reactive than their bulk counterparts due to their small sizes and thus large

surface to volume ratio. This feature enables efficient reduction of the activation barrier for diffusion and the significant contribution of surface energy during a phase transition or chemical transformation. As a result of their size and shape effects, nanomaterials demonstrate unique size-driven physicochemical properties that deviate from classical thermodynamics^{1,2}. Among these deviations, the chemistry of nanomaterials has been explored due to its significance in predicting the property and stability for the technological applications of nanomaterials^{3,4}.

In recent years, chemical transformation has become a prevailing approach to prepare nanomaterials whose desired shapes and sizes are difficult to achieve using more easily available solid precursors. Recent findings demonstrated that complex inorganic nanostructures can be synthesized through simple manipulation of reaction kinetics⁵⁻⁷. These conventional kinetic manipulations allow the precise engineering of nanostructures through several experimental parameters such as reaction temperature, turbulence of solution, rate of change in supersaturation, and precursor and surfactant concentration. In the same way as total synthesis in organic chemistry, these findings reported the conversion of simple solid precursors to more complex structures through chemical reactions and well-known physical processes such as self-assembly, galvanic replacement, Kirkendall diffusion, Ostwald ripening, and etc⁸⁻¹⁵. In addition, there have been several reports addressing chemical reactivity on surface facets to engineer complex nanostructures¹⁶⁻²². Although significant progress in the understanding of nanomaterials chemistry developed in recent years, the precise engineering of nanostructures during transformative synthesis has not been deliberately explored. In particular, most reports on transformative

kinetic control of nanostructures emphasized the use of a single class of transformative process for a single type of precursor. Furthermore, the chemical reactivity within the bulk phase of a solid precursor and its effect on the controlled synthesis and transformation of nanostructures has been overlooked. As a result, these gaps contribute to an incomplete comprehension and control on the precise engineering of nanomaterials during a chemical transformation. Thus, a comprehensive approach that enables a higher degree of kinetic control based on the interior reactivity and architecture under all possible classes of transformative routes should prove advantageous in tailoring unique nanostructures.

Herein we report a combined strategy to demonstrate a structurally tiered- and reactivity-gradient-based kinetic control to produce a wide variety of products with high-level chemical and structural complexity under all possible classes of transformative process (Figure 4.1). For the illustrative purpose, in this work, we focus on the chemical and structural transformations of $\text{Cu}_2\text{O}@\text{Cu}_2\text{O}$ homogeneous core-shell with a monocrystalline cubic core and polycrystalline spherical shell(s), that is termed as *core-shell with pre-designated architecture and reactivity* (CSPAR). Furthermore, such transformative processes have also been investigated with encapsulated CSPAR ($\text{CSPAR}@\text{Zn}(\text{OH})_2$). Because they are functionally gradient materials (FGM)²³⁻²⁵, chemical reactivity of these designed precursors varies along a radial direction, due to different crystallinity, grain size, and constituent among their core and shell(s). We also show that complex architectures obtained from these reactions exhibit structurally dependent properties that make final products attractive for photocatalytic applications.

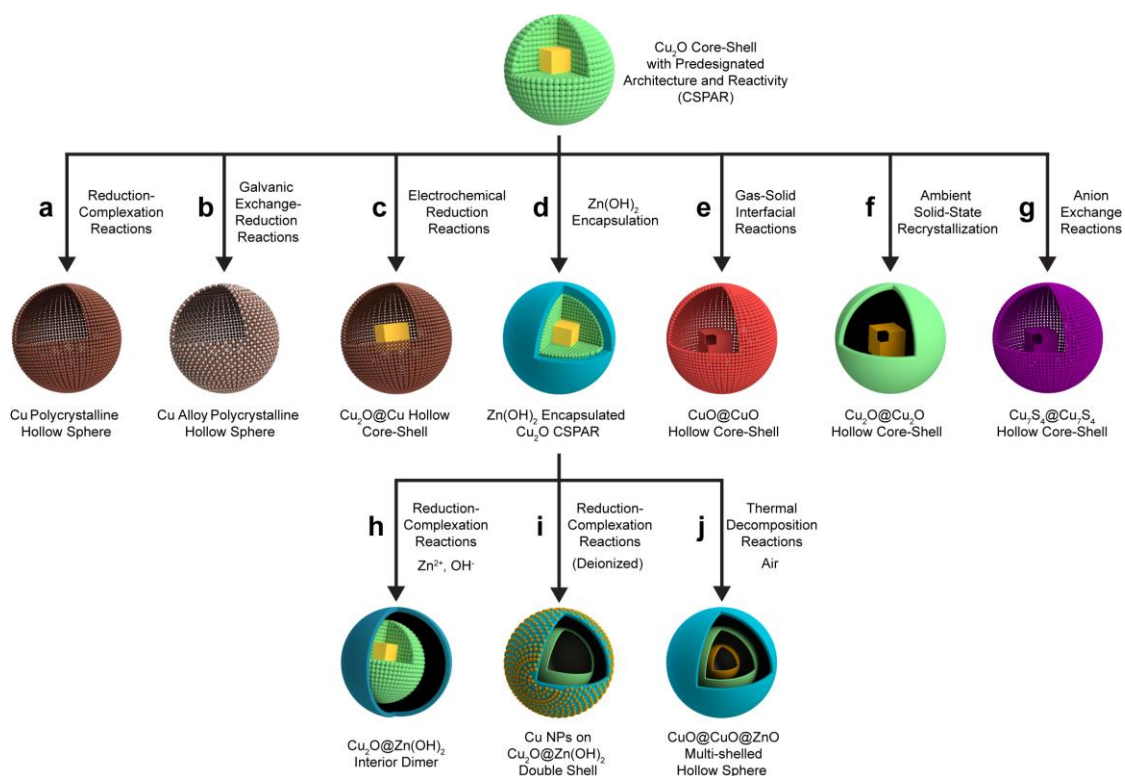


Figure 4.1 Schematic diagram for transformation of Cu_2O CSPAR. (a) Reduction-complexation, (b) galvanic exchange-reduction, (c) electrochemical reduction on an electrode, (d) $\text{Zn}(\text{OH})_2$ encapsulation, (e) gas-solid interfacial reaction, (f) solid-state recrystallization, (g) anion exchange reaction, (h) reduction-complexation of $\text{Zn}(\text{OH})_2$ encapsulated Cu_2O CSPAR, (i) reduction-complexation of $\text{Zn}(\text{OH})_2$ encapsulated Cu_2O CSPAR at low ion concentration, and (j) thermal decomposition of $\text{Zn}(\text{OH})_2$ under aerobic conditions.

4.2 Experimental Section

All reagents used in this work are the following: copper (II) chloride dihydrate ($\text{CuCl}_2 \cdot 2\text{H}_2\text{O}$, 99+%, Sigma-Aldrich), polyvinylpyrrolidone (PVP K30, MW = 40,000, Fluka), sodium hydroxide (NaOH , 99+%, Merck), L-ascorbic acid ($\text{C}_6\text{H}_8\text{O}_6$, >99%, Sigma-Aldrich), copper (II) nitrate trihydrate ($\text{Cu}(\text{NO}_3)_2 \cdot 3\text{H}_2\text{O}$, 99 - 104%, Sigma-Aldrich), ammonium nitrate (NH_4NO_3 , 99+%, Acros), ammonium sulfide solution ($(\text{NH}_4)_2\text{S}$, 20% in water, Sigma-Aldrich), zinc (II) acetate dihydrate ($\text{Zn}(\text{CH}_3\text{COO})_2 \cdot 2\text{H}_2\text{O}$, EMSURE, Merck), sodium borohydride (NaBH_4 , 99.99%,

Sigma-Aldrich), gold (III) chloride trihydrate ($\text{HAuCl}_4 \cdot 3\text{H}_2\text{O}$, 99.9+%, Sigma-Aldrich), palladium (II) chloride (PdCl_2 , anhydrous 60% Pd, Aldrich), hydrogen hexachloroplatinate (IV) hydrate ($\text{H}_2\text{PtCl}_6 \cdot x\text{H}_2\text{O}$, 99.9+%, Aldrich), potassium bicarbonate (KHCO_3 , 99.7%, Sigma-Aldrich), methyl orange (C.I. 13025, Merck, ACS), ethanol ($\text{CH}_3\text{CH}_2\text{OH}$, Merck, 99%) and deionized water. All synthetic experiments were conducted under room temperatures. Unless otherwise specified, the synthetic solutions were prepared in a 70 mm x 42 mm (height x diameter) in glass vessel and were stirred using a 30 mm \times 6 mm (length \times diameter) magnetic stirring bar at a nominal speed setting of 900 rpm (Brand: Corning PC-420D). In addition, all products were centrifuged (3800g, 7 min) and washed with water and ethanol.

Synthesis of $\text{Cu}_2\text{O}@\text{Cu}_2\text{O}$ Core-Shell Precursor. The core-shell precursor was synthesized using a seed-mediated approach, as previously reported²¹. Briefly, 0.1 mmol of $\text{CuCl}_2 \cdot 2\text{H}_2\text{O}$ and 0.1 g PVP K30 was dissolved in 50 mL deionized H_2O . Followed by the dropwise addition (0.0286 mL/s) of 0.2 M NaOH (2.0 mL) and the solution was stirred for 5 minutes. Afterwards, 0.1 M of ascorbic acid (2.0 mL) was added into the solution dropwise (0.0286 mL/s), and the solution was further stirred for 5 minutes. Immediately, 5.0 mL of the as-synthesized Cu_2O core suspension was transferred to a solution mixture of $\text{Cu}(\text{NO}_3)_2 \cdot 3\text{H}_2\text{O}$ (0.1186 mmol) and NH_4NO_3 (0.8744 mmol) in 45.0 mL deionized water. The solution was stirred magnetically for 1 min, followed by the dropwise addition (0.0286 mL/s) of 2.0 mL of 0.2 M NaOH; the solution was stirred for another 1 min. Finally, 3.5 mL of 0.10 M ascorbic acid was added drop wise (0.0269 mL/3s) and the solution was further stirred for 5 min.

Passivation of Cu₂O@Cu₂O Core-Shell Precursor. After the synthesis of Cu₂O core-shell, 30.0 mL of the core-shell suspension was transferred to a solution of Zn(CH₃COO)₂ (0.1 mmol) in 20.0 mL deionized water. The solution was stirred magnetically for 1 minute, followed by the dropwise addition (0.0286 mL/s) of 2.0 mL of 1.0 M NaOH; the solution was further stirred for 25 minutes.

Transformations in Solution with Reduction-Complexation Reactions. An alkaline solution of NaBH₄ was prepared by dissolving 20 mg NaBH₄ in 1 mL of 50 mM NaOH before the synthesis of the Cu₂O precursor. After the synthesis of Cu₂O core-shell, 0.50 mL of NaBH₄ solution was added into the as-synthesized core-shell suspension and was stirred for 7 min. The solution turned from yellow to black after the addition of NaBH₄ solution.

Transformations in Solution with Electrochemical Process. Before the reaction, a 3 x 2 cm copper plate was electrochemically polished by partially submerging (2 x 2 cm) it in 85 % phosphoric acid solution. An applied potential of 3.2 V vs. Pt was used for 3 minutes, afterwards, the copper plate was washed using deionized water and dried under room temperature. Subsequently, 0.4 mL of Cu₂O core-shell suspension (2 mg/mL, in ethanol) was casted onto the surface of the polished substrate. The film was allowed to dry slowly at room temperature. After drying, the electrode was used as the working electrode in a 3-electrode cell, where Ag/AgCl/KCl (3.0 M) and Pt gauze act as the reference and counter electrode, respectively. Various potentials were applied onto the cell under room temperature in a CO₂ saturated 0.5 M KHCO₃ (pH = 7.6) electrolyte for 1 minute.

Transformations in Solution with Galvanic Exchange-Reduction Reactions.

Before the reaction, aqueous stock solutions (20 mM) of Au, Pt, and Pd were prepared by dissolving either HAuCl_4 , H_2PtCl_6 or PdCl_2 in water. Note that the dissolution of PdCl_2 required HCl to form $[\text{PdCl}_4]^{2-}$. Briefly, one mmol of PdCl_2 was first dissolved in 2 mL of 1 M HCl before diluting the solution to 50 mL.

After the synthesis of Cu_2O core-shell, 1 mL of either Au or Pt solution or 2 mL Pd solution was added into the core-shell suspension, and the solution was allowed to be stirred for 5 minutes. Afterwards, 1 mL of an alkaline NaBH_4 solution (100 mg/mL) was added into the solution, and the solution was further stirred for another 5 minutes.

Ambient Solid-State Recrystallization. After the synthesis of Cu_2O core-shell, the suspension was washed with deionized water and ethanol and was separated from its supernatant by centrifugation. The solid-product was allowed dry at 40 mBar for 1 hour. Subsequently, the solid product was placed and heated in a tube furnace under argon flow (50 mL/min) for 12 hours.

Gas-Solid Interfacial Reactions. A 200 μL suspension of Cu_2O core-shell (4 mg/mL) in ethanol was casted onto an electropolished copper plate (2 x 2 cm) as mentioned above. The film was dried in ambient room temperature. Afterwards, the film was placed in an electric furnace and was heated at 180 – 500 $^\circ\text{C}$ under ambient conditions for various durations.

Anion Exchange Reactions. After the synthesis of Cu_2O core-shell, 1 mL of 80 mM $(\text{NH}_4)_2\text{S}$ solution was added dropwise (0.0286 mL/s) into the solution. The solution was magnetically stirred for 10 minutes.

Reduction-complexation of as-synthesized Zn(OH)₂ passivated Cu₂O CSPAR.

After the synthesis of Zn(OH)₂ passivated Cu₂O CSPAR, 1 mL of 200 mg/mL NaBH₄ in 50 mM NaOH was added into the solution. The solution was magnetically stirred for another 15 minutes.

Preparation of Cu nanoparticle-embedded Cu₂O@Zn(OH)₂ hollow sphere.

After the synthesis of Zn(OH)₂ passivated Cu₂O CSPAR, the suspension was centrifuged and washed with 30 mL deionized water. The obtained solid was dispersed in 50 mL H₂O and was transferred to a reaction vessel. The suspension was stirred for 1 minute at 900 rpm, followed by the addition of 1 mL of 150 mg/mL NaBH₄ solution in 50 mM NaOH. The suspension was stirred for another 30 minutes. The transparent orange solution was centrifuged at 3800g for 5 minutes, then the product was washed with deionized water followed by ethanol. It should be noted that if the solid residue is black after centrifugation, copper nanoparticle/branch aggregation occurred, whereas non-aggregated particles forms an orange film.

Thermal decomposition of Zn(OH)₂ passivated Cu₂O CSPAR. Zn(OH)₂ passivated Cu₂O CSPAR powders were heated inside a tube furnace at 300 °C for 4 hours under ambient atmosphere. After heating, the powders were slowly cooled to room temperature.

Material Characterization. Crystallographic information for all synthetic structures was determined by X-ray diffraction (Bruker D8 Advanced, Cu K α radiation at 1.5406 Å). Morphological and structural investigations were done via transmission electron microscopy (TEM, JEM-2010, accelerating voltage = 200 kV) and high-resolution

transmission electron microscopy (HRTEM, JEM-2100F, accelerating voltage = 200 kV). Compositional analysis of all synthetic structures was determined by an energy dispersive X-ray spectroscopy.

Photocatalytic Degradation of Methyl Orange. Cu nanoparticle embedded on Zn(OH)₂, and Cu₂O@Zn(OH)₂ CSPAR were heated under argon flow (50 mL/min) at 150 °C for 2 hours to decompose the Zn(OH)₂ to ZnO. The catalysts (4.5 mg) was dispersed in 100 mL of aqueous Methyl orange solution (15 mg/L) through ultrasonication. Afterwards, the suspension was stirred in dark conditions at room temperature for 30 minutes to reach adsorption equilibrium. The suspension was illuminated using a high-pressure Hg lamp (125 W, Phillips) with a long-pass filter (cut on wavelength: 360 nm). For every 10 minutes interval, 4 mL of the suspension was collected and centrifuged at 4000 g for 1 minute. The supernatant was transferred to a quartz cuvette using an optical path length of 10 mm and its absorption spectrum from 300 – 600 nm was acquired through a UV-Vis spectrophotometer (Shimadzu UV-2450). Sampling and measurement were continued for 240 minutes.

4.3 Results and Discussion

4.3.1 Reduction-complexation of CSPAR

We adopted a combination of single-crystalline Cu₂O and polycrystalline Cu₂O (*i.e.*, Cu₂O@Cu₂O core-shell)²⁶ to serve as a starting base for this study. Transmission electron micrograph (TEM) of the Cu₂O CSPAR (Appendix 2-2A(b)) reveals that such samples indeed comprise a single-crystalline cubic core with an edge length of

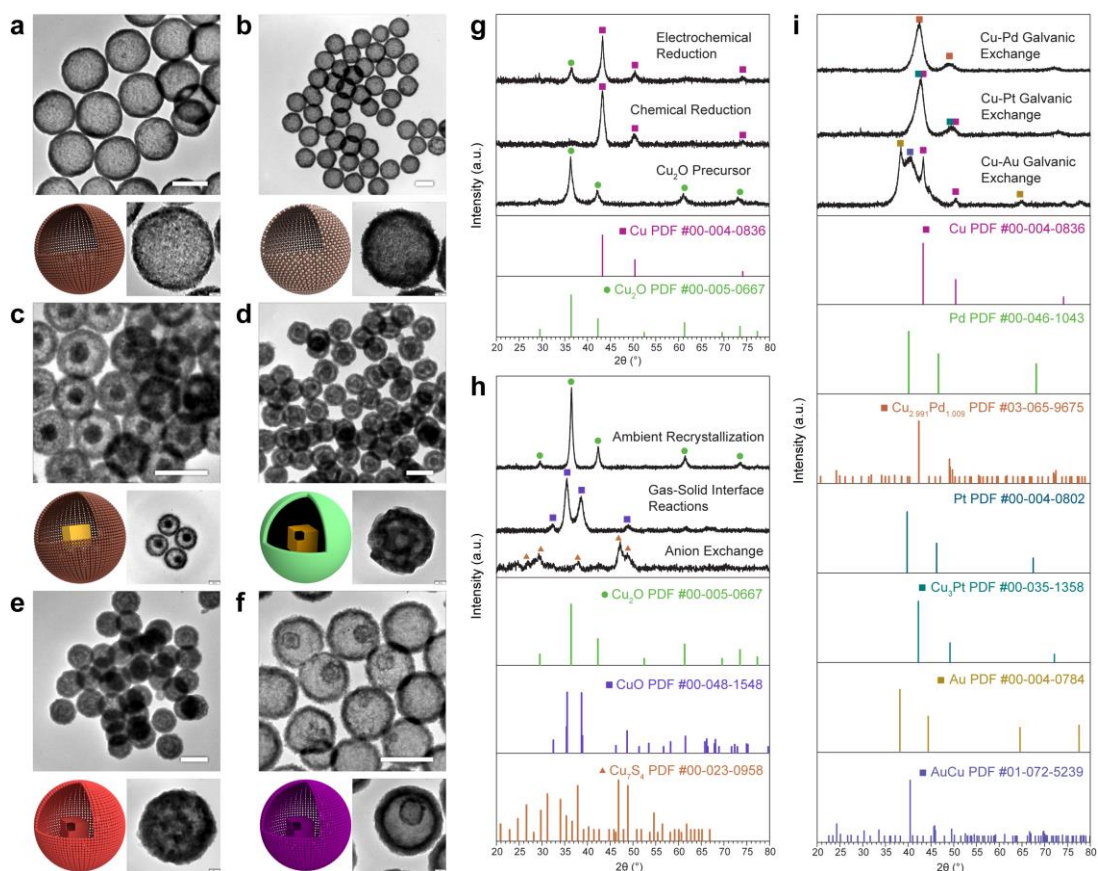


Figure 4.2 Resulting morphology and phase of Cu₂O CSPAR at different reactions. (a) Reduction-complexation, (b) galvanic exchange-reduction, (c) electrochemical reactions, (d) ambient recrystallization, (e) gas-solid interface reaction, (f) anion exchange, (g-i) X-ray diffractograms of reaction products with corresponding standards. (All scale bars are 200 nm) conditions²². The formation mechanism was determined by reacting re-dispersed

60 nm and a polycrystalline shell with a diameter of 220 nm. Structural and chemical transformations of such CSPAR were investigated under various reaction conditions that include reduction-complexation, galvanic replacement, electrochemical reduction, solid-state recrystallization, and gas-solid interfacial reaction (Figures 4.1a to 4.1g). In addition, structural and chemical transformations of the CSPAR under a confined space (underneath Zn(OH)₂) were also conducted (Figures 4.1h to 4.1j).

During reduction-complexation reaction of CSPAR, the evolution of hollow sphere with a diameter of 265 nm (Figure 4.2a, and Appendix 2-2A(f)) was examined by reacting the CSPAR with varying amounts of NaBH₄ (Supplementary Fig. 1). When less NaBH₄ was used, the interior polycrystalline shell dissolved while leaving the single-crystal core intact (Appendix 2-2A(c-e)). As the concentration of NaBH₄ increased, hollow polycrystalline spheres were observed (Appendix 2-2A(f)), and their phase was determined to be Cu through XRD (Figure 4.2g). High-resolution TEM (HRTEM) image of these hollow spheres shows that the crystallites possess {200} planes of metallic Cu (Appendix 2-2B). EDX analysis reveals that the hollow spheres are composed of 96.8% Cu, indicating partial oxidation of Cu hollow spheres during storage (Appendix 2-2C). This observation is rather expected since Cu nanoparticles have a high propensity to oxidize under ambient conditions²⁷. The formation mechanism was determined by reacting re-dispersed aqueous suspensions of CSPAR in the presence of one or more participating ions (Appendix 2-2D). Cu hollow spheres were only observed when both Cu²⁺ and NH₄⁺ were present in the solution (Appendix 2-2D(d)). This transformation can be described as a reduction-complexation or reductive dissolution (Appendix 2-2E). The reduction reaction is driven by the difference in the standard reduction potentials of Cu²⁺/Cu (0.10 V) and Cu₂O/Cu (-0.365 V) with BO₂⁻/BH₄⁻ (-1.24 V) pairs, in which Cu²⁺ and Cu₂O are both reduced to Cu. The large potential differences prevent back reaction from Cu to Cu₂O. Upon the formation of exterior Cu layer, NH₄⁺/NH₃ would selectively dissolve the interior Cu₂O since copper dissolution using NH₃ requires the formation of an oxide film to proceed²⁸. The reductive-dissolution would continue until the interior core is completely dissolved. In the same way, this transformation concept can be

extended to double-shelled Cu₂O CSPAR that results in double-shelled hollow spheres (Appendix 2-2F).

4.3.2 Galvanic exchange-reduction of CSPAR

When the Cu₂O CSPAR was mixed with noble metal (NM = Au, Pt, and Pd) ion prior to reduction-complexation reaction, hollow spheres of Cu- NM alloy were obtained (Figure 4.2b and Appendix 2-3A). In the case of Pd, the framework of the cubic core was retained after the reaction (Appendix 2-3(b)). XRD measurement of these products confirmed the formation of Cu-NM alloys (Figure 4.2i), since diffraction peaks located between pure Cu and pure NM were observed. In addition, EDX elemental maps of these products showed that Cu and included NMs are homogeneously distributed in the structure (Appendix 2-3B to 2-3E). Atomic ratios of Cu to Au, Pd, and Pt are *ca* 9:1, 2:1, and 9:1, respectively (Appendix 2-3B to 2-3E). As reported in the literature, the formation of hollow alloy particles can be described as a galvanic exchange process^{5,8,29,30}. The reaction is driven by the difference in the standard reduction potential of CuO/Cu₂O (−0.22 V) with AuCl₄[−]/Au (1.00 V), PdCl₄^{2−}/Pd (0.62 V), or PtCl₆^{2−}/Pt (0.74 V). However, the presence of NaBH₄ (BO₂[−]/BH₄[−], −1.24 V) not only prevents the oxidation of Cu₂O CSPAR, but also reduces the Cu₂O into Cu phase.

4.3.3 Electrochemical reduction of CSPAR

Similar to reduction-complexation reaction, electrochemical reduction of CSPAR also resulted in structural hollowing (Figure 4.2c). To explore the mechanism of this transformation, the CSPAR was subjected to different applied electrical potentials and resultant morphologies were examined under TEM (Appendix 2-4A). We found that the dissolution of interior Cu_2O crystallites increases with the applied potential and the transformation of single-crystalline core occurs at a higher applied potential (Appendix 2-4A). Compared with reduction-complexation reactions, the shell thickness of the product during the electrochemical reduction was found to be larger (*ca* 40 nm, Appendix 2-4A). Voltammetry measurement of Cu_2O CSPAR showed a cathodic peak at -0.2 V *vs.* RHE (Appendix 2-4B(a)), which indicates the reduction of Cu_2O CSPAR. On the other hand, a cathodic tail was only observed for the Cu hollow spheres obtained from reduction-complexation reaction of CSPAR (Appendix 2-4B(b)). Such electrochemically reduced product exhibited XRD patterns of both Cu and Cu_2O (Figure 4.2g). This result suggests that the electrochemical reduction of CSPAR only occurred at the polycrystalline shell, and the single crystalline core was not affected. The structural transformation of CSPAR during the electrochemical process can be attributed to Ostwald ripening under applied electric potential³¹ since thicker shells were observed after the process.

4.3.4 Ambient recrystallization and gas interfacial reactions

When the Cu₂O CSPAR was heated under an Ar flow, hollow interior regions were found in both the polycrystalline shell and the single-crystalline core (Figure 4.2d). XRD characterization of the product revealed sharper and stronger diffraction peaks of Cu₂O (Figure 4.2h, Appendix 2-5A(a)) compared with its CSPAR precursor. This result indicates that the Cu₂O CSPAR had undergone recrystallization or Ostwald ripening during its thermal treatment under the Ar atmosphere¹⁰. To determine the effect of temperature on the recrystallization, pristine CSPAR sample was subjected to different temperature treatments under constant Ar flow (Appendix 2-5B). We found that the size of crystallites, composing the exterior shell, gradually increased with the reaction temperature (Appendix 2-5B(a-c)); however, the exterior shell was gone entirely for the CSPAR after heated at 400°C (Appendix 2-5B(d)).

Unlike the recrystallization of CSPAR under the Ar stream, double-shelled hollow structures were observed after thermal oxidation of Cu₂O CSPAR (Figure 4.2e) in laboratory air. XRD characterization of the double-shelled hollow product reveals the presence of only CuO (Figure 4.2h), indicating a complete oxidation of CSPAR. The evolution of the double-shelled hollow structure was further examined at different conversion durations (Appendix 2-5C). We found the formation of interior hollow region occurred before the transformation of the single-crystalline core at longer reactions (Appendix 2-5C(a & d)). In addition, the reaction temperature affects the rate of transformation of Cu₂O CSPAR (Appendix 2-5D). In the same way, this transformation can be extended to double-shelled Cu₂O CSPAR that results in the formation of triple-shelled hollow structure (Appendix 2-5E and 2-5F). XRD

characterization of the triple-shelled hollow structure shows both Cu_2O and CuO phases for samples heated at 180°C ; while CuO phase was observed for samples heated at 200°C (Appendix 2-5A). This result indicates that the transformation consists of two pathways: Ostwald ripening and oxidative reaction. Formations of hollow interior region and triple-shelled structure were readily observed at 180°C with minimal phase changes (Appendix 2-5A(b) and Appendix 2-5E), indicating the occurrence of Ostwald ripening. Similarly, multishelled hollow structures were also produced when the calcination temperature was increased to 200°C ; however, the product phase was found to be only CuO (Appendix 2-5A(b) and Appendix 2-5F). Furthermore, the rate and degree of transformation of double-shelled Cu_2O CSPAR depend on its particle density for a given area (Appendix 2-5G). When the particle density of double-shelled Cu_2O CSPAR deposited on the substrate is 0.2 mg/cm^2 , only core hollowing were observed during its thermal treatment (Appendix 2-5G(b)). On the other hand, the cubic core remained intact when the particle density was doubled (Appendix 2-5G(d)).

4.3.5 Anion exchange reactions

To examine the chemical and structural transformation of Cu_2O CSPAR during its anion exchange reaction, the pristine Cu_2O CSPAR was reacted with S^{2-} . Unlike other previous findings of anion exchange reactions^{6,32-36}, our precursor possessed a designated architecture and a reactivity gradient, aiming at a higher degree of synthetic manipulation. Despite ionic exchange, we observed the formation of double-shelled hollow structure with this sulfidation (Figure 4.2f). XRD of the product shows

the generation of Cu_7S_4 phase (Figure 4.2h) after complete ion exchange between O^{2-} and S^{2-} anions. The formation process of Cu_7S_4 hollow structure was examined through reacting CSPAR with different amounts of S^{2-} anions (Appendix 2-6A). Similar with other reactions, we noted that the transformation followed a sequential pattern and can be described as 3 stages: (i) formation of a hollow region on the polycrystalline shell (Appendix 2-6A(b & c)), (ii) conversion of the single-crystalline core (Appendix 2-6A(d)), and (iii) dissolution of the single-crystalline core (Appendix 2-6A(e,f)). These stages were also found in the sulfidation of double-shelled Cu_2O CSPAR (Appendix 2-6B). At an optimal amount of S^{2-} , double-shelled core-shell structures were observed (Appendix 2-6B(b)). EDX line scan analysis of the product reveals that the interior shell and core are composed of oxygen while the exterior shell is composed of sulphur (Appendix 2-6C(a)). Both Cu_2O and Cu_7S_4 phases were identified by XRD technique (Appendix 2-6C(b)). These results indicate the ionic exchange is feasible for engineering complex multiple phase structures with multishelled CSPAR precursors since ionic exchange is limited by the diffusion process.

4.3.6 Reactions of passivated Cu₂O CSPAR

Further manipulation of chemical reactivity can be achieved by adding a capsulating shell which in turn becomes a part of product structure. Herein such encapsulating effects on the structural and chemical transformation of Cu₂O CSPAR was examined by growing a shell of Zn(OH)₂ on the surface of Cu₂O CSPAR (Figure 4.1d). The thickness of Zn(OH)₂ shell could be tuned (10 to 20 nm; Figure 4.3a) depending on the alkalinity of reaction solution and reaction duration. For example, the shell thickness increased to 40 nm when a small amount of NaOH was used in synthesis (Appendix 2-7A(a-b)), while a thinner shell was obtained with more NaOH (Appendix 2-7A(c-d)). This result is attributed to the formation of soluble zincate ions [Zn(OH)₄]²⁻ at higher alkaline conditions. In addition, prolonged reaction results in an increase of Zn(OH)₂ thickness (Appendix 2-7B). Note that the Zn(OH)₂ shell was found to expand under prolonged electron beam exposure (Appendix 2-7C). Moreover, thermal treatment of the encapsulated structure in Ar or laboratory air stabilizes the structure in the TEM measurement. These results are attributed to the electron-induced and/or thermal decomposition of Zn(OH)₂ to ZnO.

As anticipated, the Zn(OH)₂ shell is stable during reduction reactions, since its standard reduction potential of Zn(OH)₂/Zn (-1.25 V) is lower than that of BO₂⁻/BH₄⁻ (-1.24 V). During the chemical reduction of the as-prepared encapsulated CSPAR, an

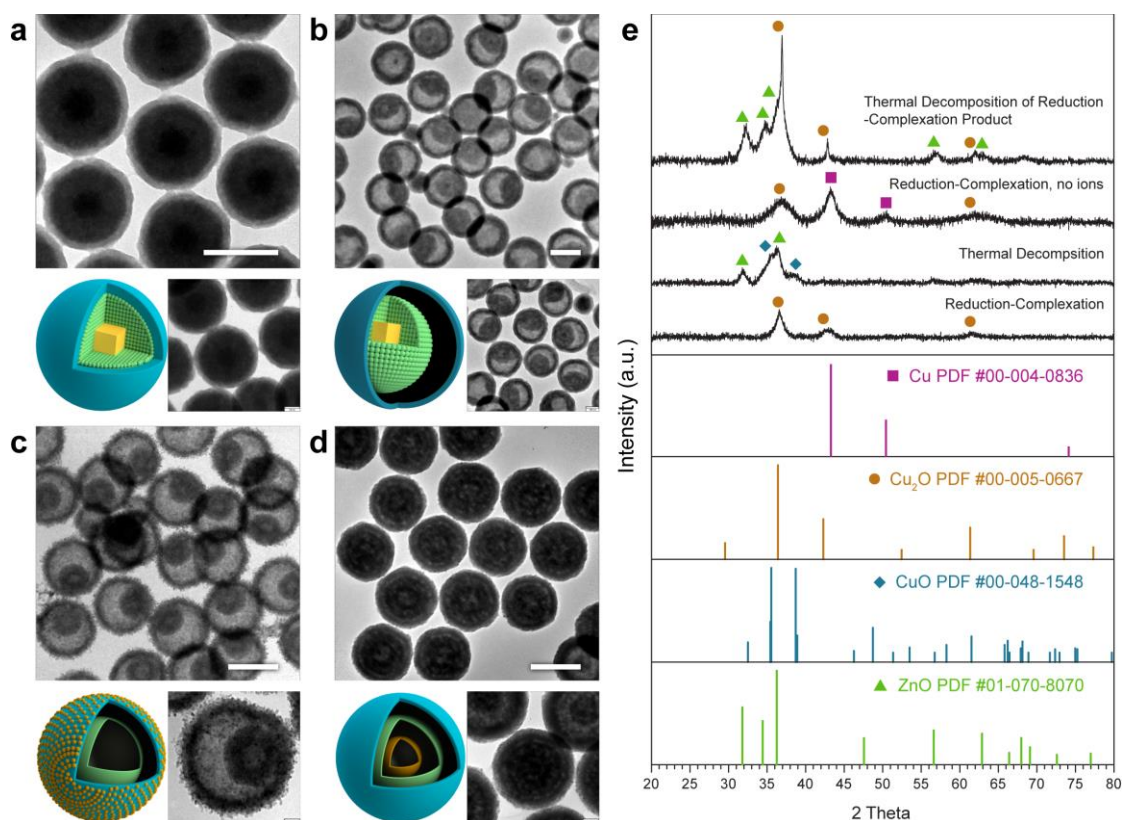


Figure 4.3 Resulting morphology and phase of Zn(OH)_2 passivated Cu_2O core-shell at different reactions. (a) Formation of Zn(OH)_2 passivated Cu_2O CSPAR, (b) reduction-complexation reaction, (c) reduction-complexation reaction under low ion concentration, (d) solid state thermal decomposition, and (e) X-ray diffractograms of reaction products with corresponding standards. (All scale bars are 200 nm).

asymmetric core-shell (Figure 4.3b), where the core is attached on the shell, was formed. This transformation was investigated by reacting the encapsulated CSPAR with increasing amounts of NaBH_4 (Appendix 2-8A(a-b) and 2-8B). In addition to the formation of asymmetric core-shell (Figure 4.3b), several complex structures such as $\text{Cu}_2\text{O}@Zn(\text{OH})_2$ yolk-shell and $\text{Cu}_2\text{O}@Zn(\text{OH})_2$ hollow sphere were also made with more significant amounts of NaBH_4 . These results suggest that the encapsulation of CSPAR slows down the hollowing process and allows the formation of asymmetric core-shell products due to incomplete reactions. In addition, these asymmetric core-

shell structures may appear as concentric structures (Appendix 2-8C), but after rotation under TEM, the concentric structures also appear as asymmetric (Appendix 2-8C). This result reveals that the interior core is permanently attached on the Zn(OH)_2 inner wall. EDX elemental maps of the asymmetric structure show that the interior core is composed of Cu, Zn, and O (Appendix 2-8D(a)). In addition, line scan analysis (Appendix 2-8D(b)) confirms the component of the shell to be Zn(OH)_2 since the diameter of the Cu map is smaller than the Zn map. Because of permanent eccentricity and compositional difference between the core and shell, such an asymmetric structure can be termed as an “*interior dimer*”. XRD investigation of the interior dimer only shows a sole phase of Cu_2O (Figure 4.3e). When the interior diameter of the encapsulated CSPAR was increased from 220 to 260 nm, multishelled hollow structures could be made (Appendix 2-8E). This result shows that larger $\text{Cu}_2\text{O}@Zn(OH)_2$ CSPAR precursors have slower reaction kinetics, which allows recrystallization of its interior components.

To our surprise, when the Zn(OH)_2 encapsulated CSPAR was washed and re-dispersed in deionized water prior to reduction, nanoparticles embedded on a $\text{Cu}_2\text{O}@Zn(OH)_2$ double shells were seen (Figure 4.3c). Both the embedded nanoparticles and hollow substrates were measured to be 4.6 and 230 nm, respectively (Appendix 2-8F and 2-8G(e-f)). The embedded nanoparticles (NPs) possess metallic Cu(200) planes under high-resolution TEM (Appendix 2-8H). In this agreement, only Cu and Cu_2O phases were found with XRD method (Figure 4.3e). This result indicates that a reduction of Cu_2O CSPAR occurred. EDX elemental maps confirm that $\text{Cu}_2\text{O}@Zn(OH)_2$ double-shell is the substrate for Cu nanoparticles embedded on the

surface, since the diameter of the Cu map is larger than Zn and O maps (Appendix 2-8I(a)). The formation of embedded Cu NPs/ Zn(OH)₂ hollow sphere was examined by varying the reaction duration and the amount of NaBH₄ used (Appendix 2-8F and 2-8G). Cu branches embedded on Cu₂O@Zn(OH)₂ hollow spheres were observed at shorter reaction durations (Appendix 2-8F(a)). At longer durations, the frequency of the branches decreased (Appendix 2-8F(c)) due to ripening and further increasing the duration results in complete dissolution of interior Cu₂O (Appendix 2-8F(e-f)). On the other hand, the rate of dissolution of interior Cu₂O was not affected when more considerable amount of NaBH₄ was used to prepare the Cu NPs embedded structures (Appendix 2-8I(c-d)). This result suggests that the embedded Cu NPs further inhibits mass transport between the interior region of the structure and the solution.

Based on these results, we proposed a transformation mechanism for the reduction-complexation of Zn(OH)₂ encapsulated Cu₂O CSPAR (Appendix 2-8J). The reduction-complexation of Zn(OH)₂-encapsulated Cu₂O with NaBH₄ and NaOH are localized due to unequal Zn(OH)₂ shell thickness. This feature allows the BH₄⁻ and OH⁻ to preferentially diffuse in particular regions of the particle, which would lead to an anisotropic conversion of interior Cu₂O crystallites. Consequently, an asymmetric *interior dimer* can be obtained after the reduction-complexation reactions. This process would continue until the interior Cu₂O CSPAR is completely reacted. On the one hand, dissolved copper ions from the interior are reduced to Cu, which are deposited on the Zn(OH)₂ interior surface. On the other hand, when the reduction-complexation reaction occurred under low ionic concentrations, the alkalinity of the solution is lower. This condition possesses slower rate of precipitation and formation

of $\text{Cu}(\text{OH})_2$ and $[\text{Cu}(\text{OH})_4]^{2-}$, which enables the reduction of dissolved copper ions on the exterior $\text{Zn}(\text{OH})_2$ surface. Consequently, Cu NPs are formed on the double-shelled structure of $\text{Cu}_2\text{O}@\text{Zn}(\text{OH})_2$. The deposited Cu NPs on $\text{Zn}(\text{OH})_2$ surface slows down the rate of material transport between the interior region of $\text{Zn}(\text{OH})_2$ particle and the exterior solution. This inhibition explains the presence of interior Cu_2O shell during the early stage of reduction-complexation. The reduction-complexation process would continue until the interior Cu_2O hollow sphere is completely dissolved. In addition, the preparation and chemical reduction of $\text{Zn}(\text{OH})_2$ encapsulated Cu_2O CSPAR can also be scaled up to three-fold (Appendix 2-8K).

Thermal decomposition of $\text{Zn}(\text{OH})_2$ encapsulated Cu_2O CSPAR under aerobic conditions resulted in the formation of multishelled hollow structure (Figure 4.3d). We observed XRD patterns of both ZnO and CuO phases in the product (Figure 4.3e). This result indicates that the simultaneous occurrence of decomposition of $\text{Zn}(\text{OH})_2$ shell and the oxidation of Cu_2O CSPAR. To examine the formation of multishelled hollow structure during thermal decomposition, the $\text{Zn}(\text{OH})_2$ -encapsulated precursor was heated at various temperatures and durations, and its resultant morphology was examined under TEM (Appendix 2-9A). At a lower temperature (200 °C), multishelled hollow structure was not observed, but a hollow core-shell structure (Appendix 2-9A(a-c)). On the other hand, when heating temperature was increased to 300 °C, multishelled hollow structures were found at longer reaction times (Appendix 2-9A(e-f)). In addition to TEM analysis, XRD measurements for the heated products at different temperatures and durations were made (Appendix 2-9B). We observed Cu_2O and ZnO diffraction patterns for the structure obtained at 200 °C, whereas

diffraction peaks for both CuO and ZnO were observed for the multishelled hollow structure formed at 300 °C. These results indicate that Ostwald ripening occurred for samples calcined at 200 °C to form hollow core-shell structure since the interior Cu₂O CSPAR did not change its phase. EDX elemental mapping and line scan analysis of the multishelled hollow structure confirm that the interior shells are composed of Cu while the exterior shell is composed of Zn (Appendix 2-9C).

4.3.7 Correlation of Structure and Property

Semiconductor metal-oxide materials such as *p*-Cu₂O and *n*-ZnO are promising materials for photocatalysis. Specifically, their heterojunction can introduce a built-in potential that efficiently separates photogenerated holes and electrons³⁷. These photogenerated holes can directly oxidize organic molecules, or react with water to generate hydroxyl radical (OH•), which is a potent oxidizing agent³⁸. To demonstrate the correlation between material architecture and their property, we examined the photocatalytic activity towards dye degradation of two structures with different configurations, namely ZnO encapsulated Cu₂O CSPAR (Structure A, Figure 4.4g) and Cu₂O NPs embedded on Cu₂O@ZnO hollow sphere (Structure B, Figure 4.4h). In addition, the photocatalytic activity of the two structures was compared with Cu₂O CSPAR. For Structure A, the ZnO (*n*-type) shell would create an interface with the solution, whereas, for Structure B, the Cu₂O (*p*-type) could form an interface with the solution. These features determine the band gap configuration of the *p-n* heterojunction (Figures 4.4a and 4.4b) and have a significant effect towards their photocatalytic property. Excitation of heterojunction results in separation of charge

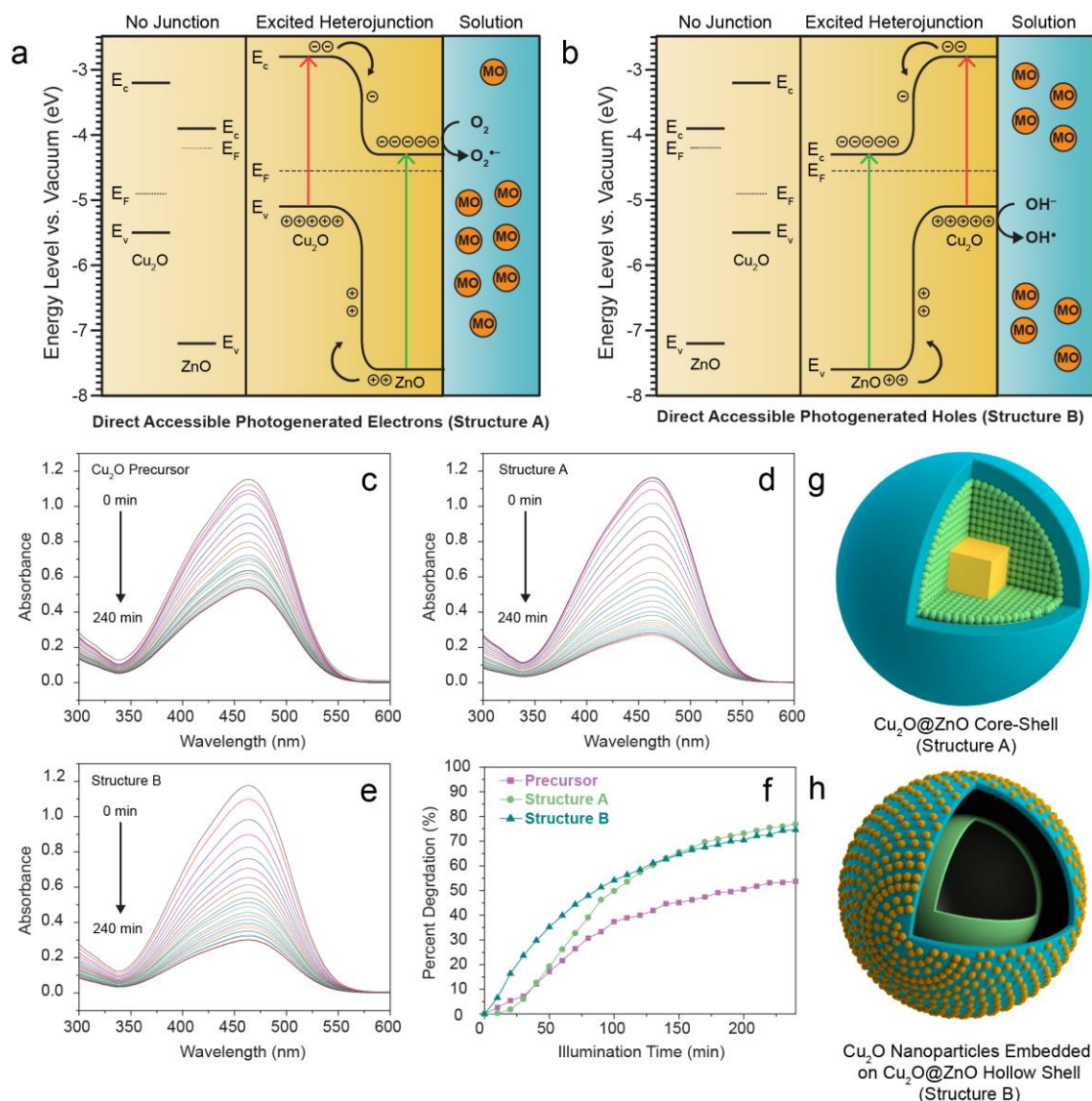


Figure 4.4 Photocatalytic applications of Cu₂O@ZnO core-shell and Cu₂O nanoparticle embedded on ZnO hollow shell. (a,b) energy level diagram illustrating two different configurations for hole generation, (c-e) UV-vis absorption spectrum of methyl orange (15 mg/L) during photocatalysis with an interval of 10 minutes, (f) comparison of total methyl orange degradation using Cu₂O precursor, structure A, and B, (g-h) schematic illustration of Structure A and Structure B. (Appendix 2-10 displays the E_F , E_g , E_c and E_v values)

carriers for both Cu₂O and ZnO due to an induced potential barrier³⁹. During the degradation reaction, both Structures A and B degraded more than 70% of methyl orange within 4 hours, whereas, the Cu₂O CSPAR only degraded 50% (Figures. 4.4c-4.4f). In addition, we found that Structure B demonstrated faster degradation rate

compared to Structure A during the first 100 minutes; afterwards, the rates for both structures were observed to be similar (Figure 4.4f). This result suggests that the diffusion rate of methyl orange and water are slower in Structure A compared with Structure B; thus hydroxyl radical and photogenerated holes are more accessible in Structure B (Figure 4.4b).

4.4 Conclusion

Our results demonstrate that transformations of solid precursors with predesignated architecture and reactivity can significantly ease the synthesis of complex functional materials. The unique transformations of this type are due to an existing reactivity gradient across a precursor that promises further kinetic control during the chemical and physical transformations. Such synthetic strategy not only allows to precise structural engineering of high-quality complex nanostructures but also enables a variety of compositional tailoring *via* other possible chemical reactions. The availability of the new materials arising from this combined strategy will stimulate new fundamental and applied researches, ranging from its extension to other inorganic precursors to the determination of structure-property correlations. For example, this work demonstrates how spatial configuration of a staggered Type II *p-n* semiconductor junction ($\text{Cu}_2\text{O}/\text{ZnO}$) can affect its charge carrier transport during excitation, which is curcially important to photocatalysis and solar cell devices³⁹⁻⁴¹. Configurations with photoexcited hole–solution interface demonstrate enhanced rate of photoinduced oxidative degradation of the organic dye molecules. While, the opposite configuration may find its use in photoinduced reduction applications. Thus,

this finding provides a guideline for the evaluation and design of photocatalysis and devices. On the other hand, several complex Cu architectures can serve as a starting point for catalytic research. For instance, the electrocatalytic evaluation of Cu polycrystalline hollow sphere (Figure 4.2a) on the selective reduction of CO₂ and CO to hydrocarbons,⁴²⁻⁴⁴ and the catalytic evaluation of Cu NPs embedded on Zn(OH)₂ (Figure 4.3c) on the selective hydrogenation of syngas^{45,46}.

In summary, our work demonstrates a new type of structure- and reactivity gradient-based kinetic control to synthesize complex nanostructures. In particular, this strategy differentiates the solid precursor with designated crystallinity and configuration. When coupled with different conversion processes, better structural and compositional manipulation for the products can be further attained. Therefore, a large compendium of new complex nanostructures with varying architecture, composition, and functionality has been fabricated in this work. We believe that other complex nanomaterials with desired physicochemical properties can be further developed with inherent architecture and reactivity for their respective solid precursors.

Reference

- 1 Navrotsky, A., Ma, C. C., Lilova, K. & Birkner, N. Nanophase transition metal oxides show large thermodynamically driven shifts in oxidation-reduction equilibria. *Science* 330, 199-201, doi:10.1126/science.1195875 (2010).
- 2 Buffat, P. & Borel, J. P. Size effect on melting temperature of gold particles. *Phys. Rev. A* 13, 2287-2298, doi:10.1103/PhysRevA.13.2287 (1976).
- 3 Dou, J. & Zeng, H. C. Targeted synthesis of silicomolybdic acid (Keggin acid) inside mesoporous silica hollow spheres for Friedel-Crafts alkylation. *J. Am. Chem. Soc.* 134, 16235-16246, doi: 10.1021/Ja3055723 (2012).

- 4 Pang, M. L., Hu, J. Y. & Zeng, H. C. Synthesis, morphological control, and antibacterial properties of hollow/solid Ag₂S/Ag heterodimers. *J. Am. Chem. Soc.* 132, 10771-10785, doi:10.1021/Ja102105q (2010).
- 5 Gonzalez, E., Arbiol, J. & Puntès, V. F. Carving at the nanoscale: sequential galvanic exchange and Kirkendall growth at room temperature. *Science* 334, 1377-1380, doi:10.1126/science.1212822 (2011).
- 6 Xiong, S. L. & Zeng, H. C. Serial ionic exchange for the synthesis of multishelled copper sulfide hollow spheres. *Angew. Chem. Int. Ed.* 51, 949-952, doi:10.1002/anie.201106826 (2012).
- 7 Yu, Y., Zhang, Q., Xie, J. & Lee, J. Y. Engineering the architectural diversity of heterogeneous metallic nanocrystals. *Nat. Commun.* 4, 1454, doi:10.1038/ncomms2474 (2013).
- 8 Sun, Y. & Xia, Y. Shape-controlled synthesis of gold and silver nanoparticles. *Science* 298, 2176-2179, doi:10.1126/science.1077229 (2002).
- 9 Yin, Y. D. *et al.* Formation of hollow nanocrystals through the nanoscale Kirkendall effect. *Science* 304, 711-714, doi:10.1126/science.1096566 (2004).
- 10 Yang, H. G. & Zeng, H. C. Preparation of hollow anatase TiO₂ nanospheres via Ostwald ripening. *J. Phys. Chem. B* 108, 3492-3495, doi:10.1021/jp0377782 (2004).
- 11 Son, D. H., Hughes, S. M., Yin, Y. & Paul Alivisatos, A. Cation exchange reactions in ionic nanocrystals. *Science* 306, 1009-1012, doi:10.1126/science.1103755 (2004).
- 12 Buck, M. R., Bondi, J. F. & Schaak, R. E. A total-synthesis framework for the construction of high-order colloidal hybrid nanoparticles. *Nat Chem* 4, 37-44, doi:10.1038/nchem.1195 (2012).
- 13 Zhou, Y. & Zeng, H. C. Simultaneous synthesis and assembly of noble metal nanoclusters with variable micellar templates. *J. Am. Chem. Soc.* 136, 13805-13817, doi:10.1021/ja506905j (2014).
- 14 Yao, K. X., Yin, X. M., Wang, T. H. & Zeng, H. C. Synthesis, self-assembly, disassembly, and reassembly of two types of Cu₂O nanocrystals uniaxially with {001} or {110} planes. *J. Am. Chem. Soc.* 132, 6131-6144, doi:10.1021/Ja100151f (2010).
- 15 Yec, C. C. & Zeng, H. C. Nanobubbles within a microbubble: synthesis and self-assembly of hollow manganese silicate and its metal-doped derivatives. *ACS Nano*, doi:10.1021/nn501948h (2014).
- 16 Chen, C. *et al.* Highly crystalline multimetallic nanoframes with three-dimensional electrocatalytic surfaces. *Science* 343, 1339-1343, doi:10.1126/science.1249061 (2014).

- 17 Kuo, C.-H. & Huang, M. H. Fabrication of truncated rhombic dodecahedral Cu₂O nanocages and nanoframes by particle aggregation and acidic etching. *J. Am. Chem. Soc.* 130, 12815-12820, doi:10.1021/ja804625s (2008).
- 18 Lu, X. *et al.* Mechanistic studies on the galvanic replacement reaction between multiply twinned particles of Ag and HAuCl₄ in an organic medium. *J. Am. Chem. Soc.* 129, 1733-1742, doi:10.1021/ja067800f (2007).
- 19 Yin, Y., Erdonmez, C., Aloni, S. & Alivisatos, A. P. Faceting of nanocrystals during chemical transformation: from solid silver spheres to hollow gold octahedra. *J. Am. Chem. Soc.* 128, 12671-12673, doi:10.1021/ja0646038 (2006).
- 20 Xie, S. *et al.* Synthesis of Pd-Rh core-frame concave nanocubes and their conversion to Rh cubic nanoframes by selective etching of the Pd Cores. *Angew. Chem. Int. Ed.* 51, 10266-10270, doi:10.1002/anie.201206044 (2012).
- 21 Sadtler, B. *et al.* Selective facet reactivity during cation exchange in cadmium sulfide nanorods. *J. Am. Chem. Soc.* 131, 5285-5293, doi:10.1021/ja809854q (2009).
- 22 Wang, D.-Y. *et al.* Chemical transformation from FePt to Fe_{1-x}PtM_x (M = Ru, Ni, Sn) nanocrystals by a cation redox reaction: X-ray absorption spectroscopic studies. *J. Am. Chem. Soc.* 129, 1538-1540, doi:10.1021/ja0675671 (2007).
- 23 Markworth, A. J., Ramesh, K. S. & Parks, W. P., Jr. Modelling studies applied to functionally graded materials. *J. Mater. Sci.* 30, 2183-2193, doi:10.1007/BF01184560 (1995).
- 24 Suresh, S. Graded materials for resistance to contact deformation and damage. *Science* 292, 2447-2451, doi:10.1126/science.1059716 (2001).
- 25 Birman, V. & Byrd, L. W. Modeling and analysis of functionally graded materials and structures. *Appl. Mech. Rev.* 60, 195-216, doi:10.1115/1.2777164 (2007).
- 26 Yec, C. C. & Zeng, H. C. Synthetic architecture of multiple core-shell and yolk-shell structures of (Cu₂O@)_nCu₂O (n=1-4) with centricity and eccentricity. *Chem. Mater.* 24, 1917-1929, doi:10.1021/cm300672r (2012).
- 27 Hung, L. I., Tsung, C. K., Huang, W. Y. & Yang, P. D. Room-temperature formation of hollow Cu₂O nanoparticles. *Adv. Mater.* 22, 1910-1914, doi:10.1002/adma.200903947 (2010).
- 28 Halpern, J. Kinetics of the dissolution of copper in aqueous ammonia. *J. Electrochem. Soc.* 100, 421-428, doi:10.1149/1.2780873 (1953).
- 29 Oh, M. H. *et al.* Galvanic replacement reactions in metal oxide nanocrystals. *Science* 340, 964-968, doi:10.1126/science.1234751 (2013).

- 30 Sun, Y. & Xia, Y. Alloying and dealloying processes involved in the preparation of metal nanoshells through a galvanic replacement reaction. *Nano Lett* 3, 1569-1572, doi:10.1021/nl034765r (2003).
- 31 Redmond, P. L., Hallock, A. J. & Brus, L. E. Electrochemical Ostwald ripening of colloidal Ag particles on conductive substrates. *Nano Lett* 5, 131-135, doi:10.1021/nl048204r (2005).
- 32 Pang, M. & Zeng, H. C. Highly ordered self-assemblies of submicrometer Cu₂O spheres and their hollow chalcogenide derivatives. *Langmuir* 26, 5963-5970, doi:10.1021/la904292t (2010).
- 33 Zhang, D. F., Zhang, H., Shang, Y. & Guo, L. Stoichiometry-controlled fabrication of Cu_xS hollow structures with Cu₂O as sacrificial templates. *Cryst Growth Des* 11, 3748-3753, doi:10.1021/cg101283w (2011).
- 34 Kuo, C.-H., Chu, Y.-T., Song, Y.-F. & Huang, M. H. Cu₂O nanocrystal-templated growth of Cu₂S nanocages with encapsulated Au nanoparticles and in-situ transmission X-ray microscopy study. *Adv. Funct. Mater.* 21, 792-797, doi:10.1002/adfm.201002108 (2011).
- 35 Park, J., Zheng, H., Jun, Y.-w. & Alivisatos, A. P. Hetero-epitaxial anion exchange yields single-crystalline hollow nanoparticles. *J. Am. Chem. Soc.* 131, 13943-13945, doi:10.1021/ja905732q (2009).
- 36 Jiao, S., Xu, L., Jiang, K. & Xu, D. Well-defined non-spherical copper sulfide mesocages with single-crystalline shells by shape-controlled Cu₂O crystal templating. *Adv. Mater.* 18, 1174-1177, doi:10.1002/adma.200502386 (2006).
- 37 Nozik, A. J. & Memming, R. Physical chemistry of semiconductor-liquid interfaces. *J. Phys. Chem.* 100, 13061-13078, doi:10.1021/jp953720e (1996).
- 38 Konstantinou, I. K. & Albanis, T. A. TiO₂-assisted photocatalytic degradation of azo dyes in aqueous solution: kinetic and mechanistic investigations - A review. *Appl. Catal., B* 49, 1-14, doi:10.1016/j.apcatb.2003.11.010 (2004).
- 39 Jiang, T. F., Xie, T. F., Chen, L. P., Fu, Z. W. & Wang, D. J. Carrier concentration-dependent electron transfer in Cu₂O/ZnO nanorod arrays and their photocatalytic performance. *Nanoscale* 5, 2938-2944, doi:10.1039/c3nr34219k (2013).
- 40 Wilson, S. S. *et al.* Interface stoichiometry control to improve device voltage and modify band alignment in ZnO/Cu₂O heterojunction solar cells. *Energy Environ. Sci.* 7, 3606-3610, doi:10.1039/C4EE01956C (2014).
- 41 Paracchino, A., Laporte, V., Sivula, K., Grätzel, M. & Thimsen, E. Highly active oxide photocathode for photoelectrochemical water reduction. *Nat. Mater.* 10, 456-461, doi:10.1038/nmat3017 (2011).
- 42 Hori, Y., Murata, A. & Takahashi, R. Formation of hydrocarbons in the electrochemical reduction of carbon dioxide at a copper electrode in aqueous

- solution. *J. Chem. Soc., Farad. T 1* 85, 2309-2326, doi:10.1039/F19898502309 (1989).
- 43 Li, C. W. & Kanan, M. W. CO₂ reduction at low overpotential on Cu electrodes resulting from the reduction of thick Cu₂O films. *J. Am. Chem. Soc.* 134, 7231-7234, doi:10.1021/ja3010978 (2012).
- 44 Li, C. W., Ciston, J. & Kanan, M. W. Electroreduction of carbon monoxide to liquid fuel on oxide-derived nanocrystalline copper. *Nature* 508, 504-507, doi:10.1038/nature13249 (2014).
- 45 Behrens, M. *et al.* The active site of methanol synthesis over Cu/ZnO/Al₂O₃ industrial catalysts. *Science* 336, 893-897, doi:10.1126/science.1219831 (2012).
- 46 Graciani, J. *et al.* Highly active copper-ceria and copper-ceria-titania catalysts for methanol synthesis from CO₂. *Science* 345, 546-550, doi:10.1126/science.1253057 (2014).

Chapter 5. Seed-Mediated Synthesis of $M@Cu_2O@Zn(OH)_2$ ($M = Au, Ag, Au/Ag, Pd$) and $M@Cu$ Core-Shell Structures

Abstract

In this study, we present a room temperature seed-mediated approach for the preparation of $M@Cu_2O@Zn(OH)_2$ ($M = Au, Ag, Au/Ag, Pd$) and $M@Cu_2O$ core-shell structures. This approach enables the formation of high quality metal-semiconductor core-shell structures. Similar with Chapter 4, the chemical reactivity and structural transformation of $M@Cu_2O@Zn(OH)_2$ and $M@Cu_2O$ core-shell were also tested. To test the applicability of these structures, we have demonstrated its catalytic activity towards 4-nitrophenol degradation. In addition, the photocatalytic properties towards methyl orange of $M@Cu_2O@ZnO$ were determined and were compared with $Cu_2O@ZnO$ CSPAR and Cu_2O nanoparticles embedded on ZnO hollow spheres.

5.1 Introduction

Compared with their individual component, metal-semiconductor hybrid heterostructures represent an interesting class of materials due to their unique optical and electronic properties. These properties are attributed to the synergistic effect between the metal and semiconductor.¹ Specifically, metal-semiconductor hybrid structures allow charge separation of photogenerated holes and electrons that are beneficial for photoelectrochemical reactions.¹ Among metal-semiconductor hybrid structures, the nanostructured core-shell configuration has received numerous research

interest due to its large surface to volume ratio that further improves its synergistic property.²⁻⁷

Herein, we report a seed-mediated synthetic approach for a $M@Cu_2O@Zn(OH)_2$ (where $M = Au, Ag, Au/Ag,$ and Pd) multishelled core-shell nanostructures. This layer-by-layer approach allows the synthesis monodispersed of core-shell structure. Similar to Chapter 4, we have also determined the transformation of these core-shell structures under different physical and chemical conditions. Under reduction conditions, $M@Cu$ hollow core-shell structures were obtained. In addition to their syntheses, $M@Cu_2O@ZnO$, and $M@Cu_2O$ core-shell structures were used as a catalyst for the photodegradation of methyl orange and the reduction of 4-nitrophenol.

5.2 Experimental Section

All reagents used in this work are the following: copper (II) chloride dihydrate ($CuCl_2 \cdot 2H_2O$, 99+%, Sigma–Aldrich), polyvinylpyrrolidone (PVP K30, MW = 40,000, Fluka), sodium hydroxide ($NaOH$, 99+%, Merck), L–ascorbic acid ($C_6H_8O_6$, >99%, Sigma–Aldrich), (+)-sodium L-ascorbate ($C_6H_7NaO_6$, $\geq 99.0\%$, Sigma), copper (II) nitrate trihydrate ($Cu(NO_3)_2 \cdot 3H_2O$, 99 - 104%, Sigma-Aldrich), ammonium nitrate (NH_4NO_3 , 99+%, Acros), zinc (II) acetate dihydrate ($Zn(CH_3COO)_2 \cdot 2H_2O$, EMSURE, Merck), sodium citrate tribasic dihydrate ($\geq 99.0\%$, Sigma-Aldrich), gold (III) chloride trihydrate ($HAuCl_4 \cdot 3H_2O$, $\geq 99.0\%$, Sigma-Aldrich), silver nitrate ($AgNO_3$, Merck), palladium (II) chloride ($PdCl_2$, 60% Pd basis, Sigma-Aldrich), perfluorosulfonic acid–PTFE copolymer (Nafion, 5% w/w solution, Alfa Aesar),

potassium bicarbonate ($KHCO_3$, 99.7%, Sigma-Aldrich), ethanol (CH_3CH_2OH , Merck, 99%) and deionized water. All synthetic experiments were conducted under room temperatures. Unless otherwise specified, the synthetic solutions were prepared in a 70 mm x 42 mm (height x diameter) in glass vessel and were stirred using a 30 mm x 6 mm (length x diameter) magnetic stirring bar at a nominal speed setting of 900 rpm (Brand: Corning PC-420D). In addition, all products were centrifuged (3800g, 7 min) and washed twice with ethanol.

Preparation of Pd Stock Solution. A 0.0495 g of $PdCl_2$ was dissolved in 2 mL of 1 M HCl. After dissolution, the solution was diluted to 50 mL with deionized water.

Synthesis of Au Core Nanocrystal. A 50 mL of 0.25 mM $HAuCl_4$ aqueous solution was stirred at 900 rpm and was heated to 100 °C. Subsequently, 1.7 mL of a freshly prepared 0.2 M sodium citrate was added to the boiling solution. The solution was allowed to be stirred for 5 minutes. Finally, the red solution was cooled at room temperature.

Synthesis of Ag Core Nanocrystal. A 50 mL of 0.25 mM $AgNO_3$ solution was stirred at 900 rpm and was heated to 100 °C. Subsequently, 1.7 mL of 0.2 M sodium citrate and 0.6 mL of 0.1 M ascorbic acid solution were added simultaneously to the boiling solution. The solution was allowed to be stirred for 5 minutes. Finally, the yellow solution was cooled at room temperature.

Synthesis of AuAg Core Nanocrystal. A 50 mL of 0.125 mM $HAuCl_4$ solution was heated to 100 °C. Subsequently, a 0.5 mL of 12.5 mM $AgNO_3$ was added into the boiling solution. Immediately, 1.7 mL of 0.2 M sodium citrate was added into the

solution, and the solution was stirred for another 5 minutes. Finally, the yellow-orange solution was cooled at room temperature.

Synthesis of Pd Core Nanocrystal. A 3.32 mL of Pd solution and 1.7 mL of sodium citrate were both mixed and diluted to 50 mL. The solution was heated to 100 °C. Subsequently, a 0.6 mL of 0.1 M ascorbic acid solution was added into the solution and was stirred for 20 minutes. Finally, the yellow-brown solution was cooled at room temperature.

Synthesis of $M@Cu_2O$ Core-Shell ($M = Au, Ag, Au/Ag, Pd$). After the synthesis of either Au, Au, Au/Ag, Pd nanocrystals, 5.0 mL of the core suspension was immediately transferred to a solution of NH_4NO_3 (0.125 mmol) in 45.0 mL deionized water. Afterwards, 2.0 mL of 0.2 M NaOH was added into the solution and was magnetically stirred for 1 minute. Subsequently, a 1.0 mL of 2.72% $Cu(NO_3)_2$ solution was added dropwise (0.0143 mL/s); the solution was stirred for another 1 minute. Finally, 3.0 mL of 0.10 M ascorbic acid was added dropwise (0.0269 mL/3s) and the solution was further stirred for 10 minutes.

Synthesis of $M@Cu_2O@Zn(OH)_2$ Core-Shell ($M = Au, Ag, Au/Ag, Pd$). Similar with Chapter 5, a 30.0 mL of the as-synthesized $M@Cu_2O$ core-shell suspension was transferred to a solution of $Zn(CH_3COO)_2$ (0.1 mmol) in 20.0 mL deionized water. The solution was stirred magnetically for 1 minute, followed by the dropwise addition (0.0286 mL/s) of 2.0 mL of 1.0 M NaOH; the solution was stirred for 25 minutes.

Material Characterization. Crystallographic information for all synthetic structures was determined by X-ray diffraction (Bruker D8 Advanced, Cu $K\alpha$ radiation at 1.5406

Å). Morphological and structural investigations were done via transmission electron microscopy (TEM, JEM-2010, accelerating voltage = 200 kV) and high-resolution transmission electron microscopy (HRTEM, JEM-2100F, accelerating voltage = 200 kV). Compositional analysis of all synthetic structures was determined by an energy dispersive X-ray spectroscopy.

Thermal Treatment of M@Cu₂O@Zn(OH)₂ Multiple Core-Shell under flowed Argon.

After the synthesis of M@Cu₂O@Zn(OH)₂ multiple core-shell, the suspensions were washed using ethanol. The solids were dried in an oven at 60 °C for 10 minutes. After drying, these solids were placed in a furnace and heated at 200 – 400 °C under ambient conditions or flowed Argon gas (50 mL/min) for 12 hours.

Catalytic Reduction of 4-Nitrophenol. The reduction of 4-nitrophenol was conducted using a modified procedure. In a typical reaction, an aqueous solution of 4-nitrophenol (0.03 mL, 0.010 M) was added to 3 mL deionized water. An aqueous solution of NaBH₄ (0.12 mL, 0.10 M in 50 mM NaOH) was added into the 4-nitrophenol solution. Subsequently, an aqueous solution of the synthesized structure (0.05 mL, 1 mg/mL) was added to the reaction system. The mixture was transferred into a quartz cuvette with an optical path length of 1.0 cm. The UV/Vis absorption were monitored for 1 hour with a sampling interval of 1 minute.

Photocatalytic Degradation of Methyl Orange. Similar with Chapter 4, the photocatalytic degradation of Methyl orange by heating the catalysts under argon flow (50 mL/min) at 200 °C for 12 hours to decompose the Zn(OH)₂ to ZnO. The catalysts (4.5 mg) was dispersed in 100 mL of aqueous Methyl orange solution (15 mg/L) through ultrasonication. Afterwards, the suspension was stirred in dark conditions at room temperature for 30 minutes to reach adsorption equilibrium. The suspension was illuminated using a high-pressure Hg lamp (125 W, Phillips) with a long-pass filter (cut on wavelength: 360 nm). For every 10 minutes

interval, 4 mL of the suspension was collected and centrifuged at 4000 g for 1 minute. The supernatant was transferred to a quartz cuvette using an optical path length of 10 mm and its absorption spectrum from 300 – 600 nm was acquired through a UV-Vis spectrophotometer (Shimadzu UV-2450). Sampling and measurement were continued for 240 minutes.

5.3 Results and Discussion

5.3.1 Seed-Mediated Synthesis of $M@Cu_2O$ and $M@Cu_2O@Zn(OH)_2$ Core-Shell Structure

Similar with Chapter 3 and 4, a seed-mediated growth was used to synthesize $M@Cu_2O@Zn(OH)_2$ core-shell structure. Figure 5.1 shows the structure of $M@Cu_2O$ and $M@Cu_2O@Zn(OH)_2$ core-shell structure. Due to the difference in electrical conductivity between the metal core, Cu_2O , and $Zn(OH)_2$ shells, a contrast between these materials can be seen. The size of the $M@Cu_2O$ (Figure 5.1a) was measured to be 90 nm; while $M@Cu_2O@Zn(OH)_2$ core-shell (Figure 5.1b) was measured to be 120 nm. However, prolonged electron beam exposure of $M@Cu_2O@Zn(OH)_2$ resulted to the detachment of $Zn(OH)_2$ layer with respect to the Cu_2O layer. As a result, the size of the $M@Cu_2O@Zn(OH)_2$ core-shell (Figure 5.1c) was observed to further increased. In addition to $M@Cu_2O$ core-shell structures, it is also possible to grow a $Zn(OH)_2$ layer on $M@Cu_2O$ yolk-shell structures as shown in Figure 5.1d.

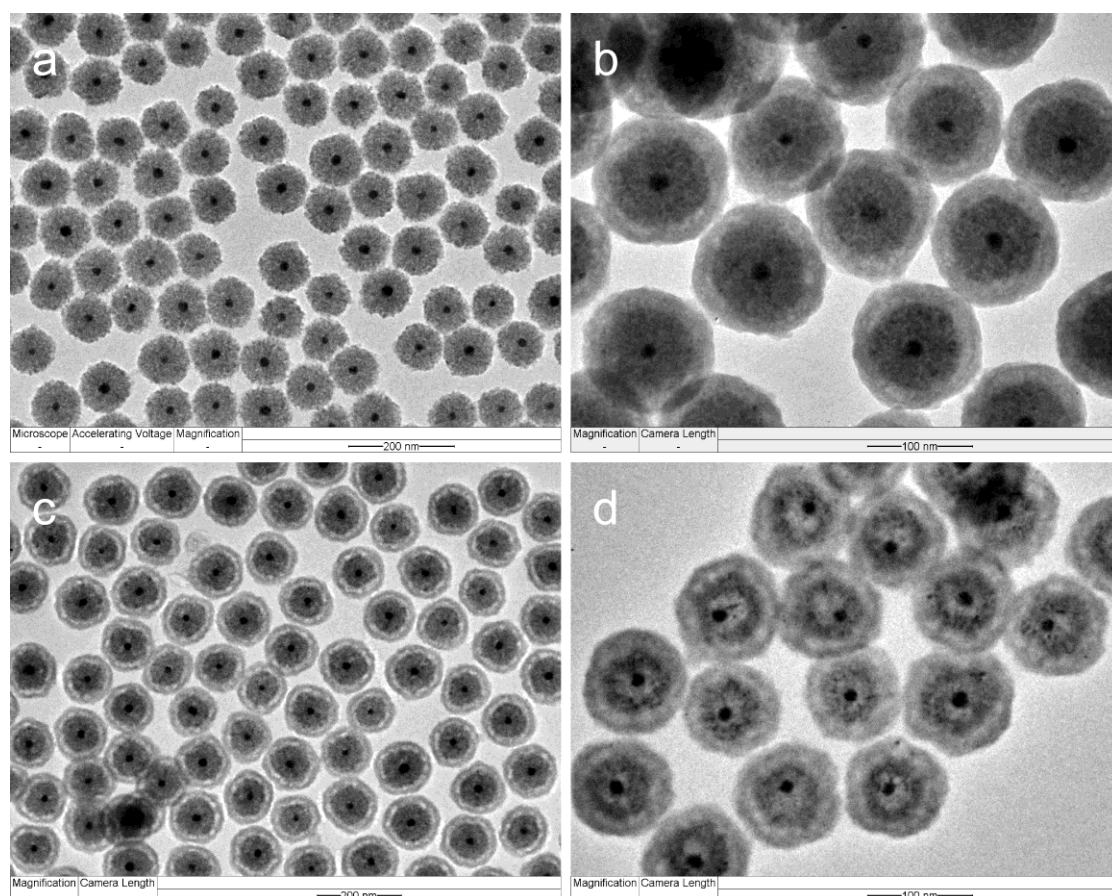


Figure 5.1 Representative TEM images of (a) $M@Cu_2O$, (b) $M@Cu_2O@Zn(OH)_2$, (c) Low magnification image of $M@Cu_2O@Zn(OH)_2$, and (d) $M@Cu_2O@Zn(OH)_2$ Yolk-Shell Structure.

Prolonged reactions result in the formation $M@Cu_2O$ yolk-shell structures which can be attributed to Ostwald ripening of Cu_2O interior crystallites.^{6,8,9} Figure 5.2 shows the Ostwald ripening process for a $M@Cu_2O$ core-shell structure. At longer reaction durations, void interior regions can be seen in the $M@Cu_2O$ core-shell structure thus forming a movable metal core. In contrast with the ripening process for homogeneous Cu_2O core-shell structure (Chapter 3), the occurrence of Ostwald ripening for $M@Cu_2O$ can be readily observed in the bulk solution; since the solution's color changed from green to brown for the transition of $Au@Cu_2O$ core-shell to $Au@Cu_2O$ yolk-shell structure.

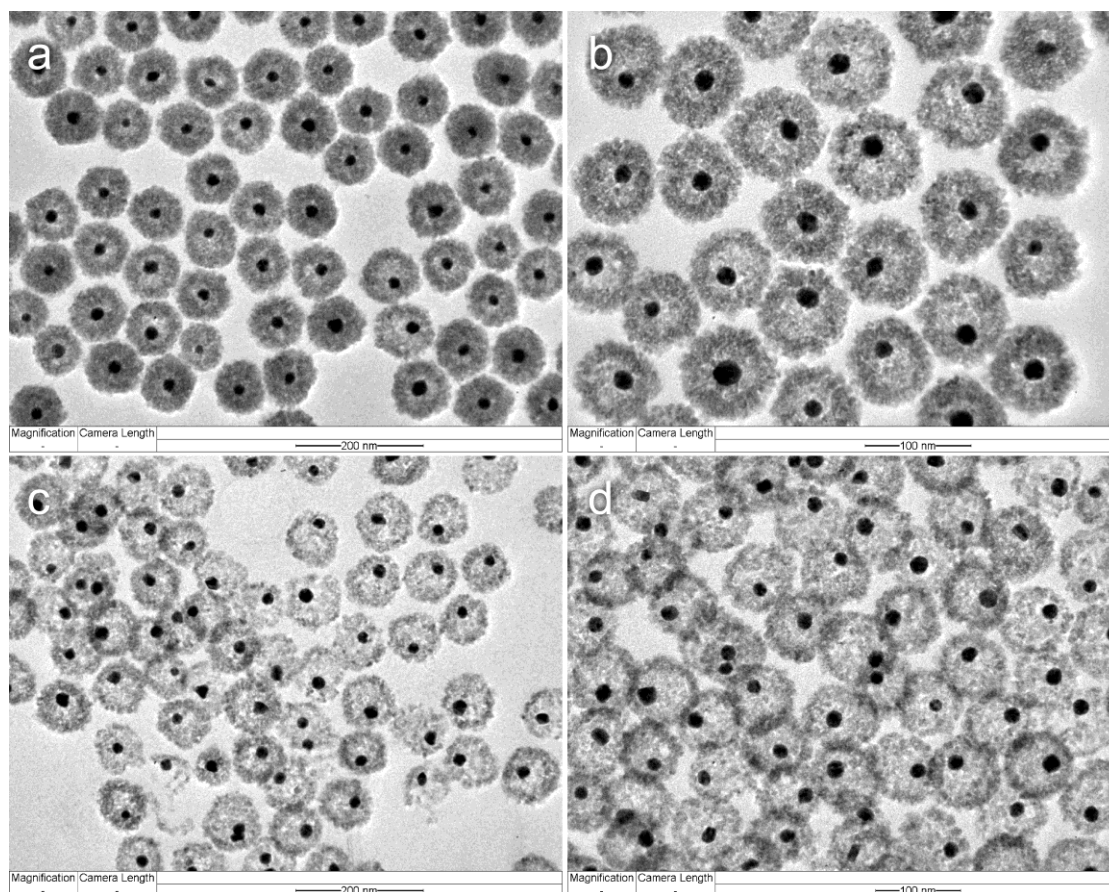


Figure 5.2 Effect of reaction duration on $M@Cu_2O$ synthesis: (a) 16 min, (b) 17 min, (c) 19 min, (d) 22 min

Aside from reaction duration, we also determined the individual effect of both NH_4NO_3 and PVP on $M@Cu_2O$ growth. In the absence of NH_4NO_3 , single crystal Cu_2O shells are formed rather than polycrystalline shells (Figure 5.3a). Furthermore, $M@Cu_2O$ dimers were found when the seed amount was further increased (Figure 5.3b). This formation can be attributed to partial Cu_2O growth due to scarcity of growth units. On the other hand, the presence of NH_4NO_3 in the solution results in polycrystalline Cu_2O shells (Figure 5.3c).

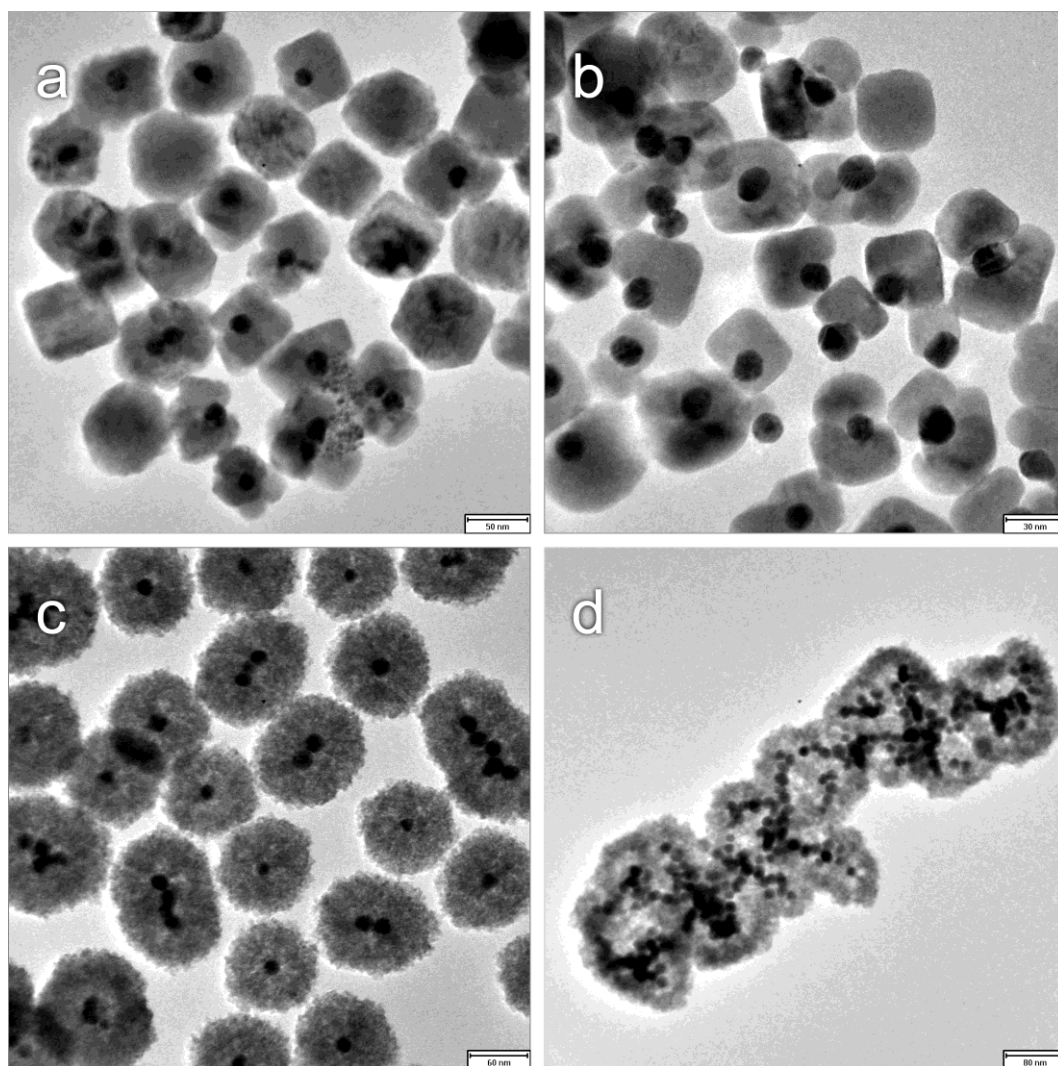


Figure 5.3 Effect of NH_4NO_3 on $M@Cu_2O$ Growth: (a) 5 mL Au seed, No NH_4NO_3 , (b) 10 mL Au seed, No NH_4NO_3 , (c) 0.042 g NH_4NO_3 , and (d) 0.068 g NH_4NO_3 . (The synthetic solution does not contain PVP).

Similar with Chapter 3, the formation of Cu_2O polycrystallites are attributed to the inhibition of $Cu(OH)_2$ with NH_4^+ . In addition to polycrystallites formation, it was also found that multiple cores aggregate to form an elongated *bean pod-like* structure when NH_4NO_3 is present in the solution (Figure 5.3c and 5.3d). This result is attributed to destabilization effect of salts on the electrical double layer of colloids, which results in aggregation. This result suggests that the inhibition of $Cu(OH)_2$ growth with NH_4NO_3

during Cu_2O will result to polycrystallites; while smooth single crystal when no growth additives are present. In order to circumvent the aggregation of cores during Cu_2O growth, the addition of surfactants in the growth solution may enhance the stability and separation of metallic cores. In this study, the effect of PVP on the metallic core aggregation and the morphology of $M@Cu_2O$ core-shell were determined (Figure 5.4). As expected, a single $M@Cu_2O$ particle with single crystal structure was observed when PVP was included during the Cu_2O growth (Figure 5.4a); however, the single $M@Cu_2O$ particle with single crystal structure was also observed in the absence of PVP (Figure 5.4b) using sodium ascorbate as the reducing agent. This result suggests that a relatively acidic solution destabilizes the metallic core during synthesis. On the other hand, an irregular shaped and quasi-spherical $M@Cu_2O$ core-shell structure was observed when ascorbic acid was used as the reducing agent (Figure 5.4c and 5.4d).

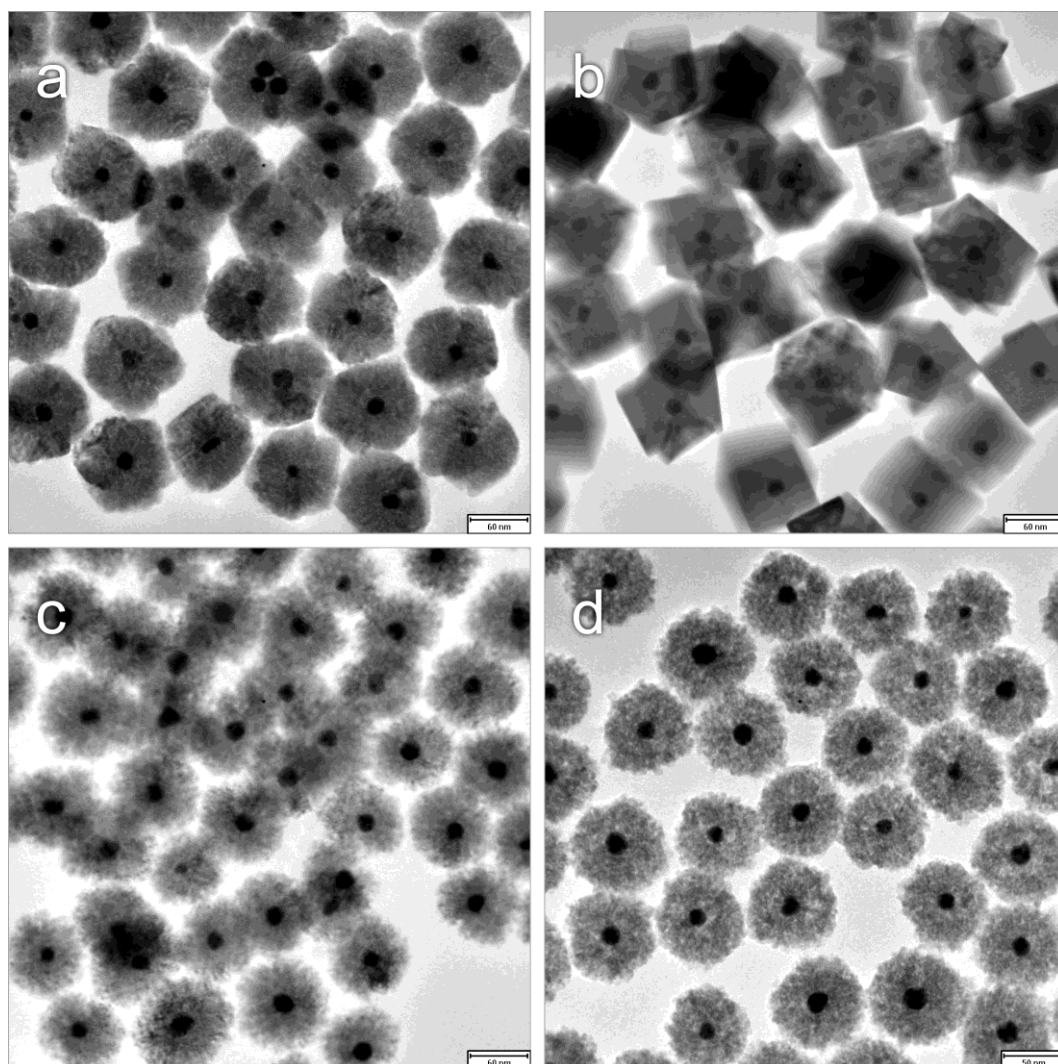


Figure 5.4 Effect of PVP on $M@Cu_2O$ Growth: (a) 2 g PVP, (b) No PVP, (c) 2 g PVP, and (d) 2 g PVP with 0.01 g NH_4NO_3 (For a and b, the reducing agent used was sodium ascorbate).

In addition to TEM characterization, XRD measurement of various $M@Cu_2O$ confirmed the presence of each respective metallic core (Au, Ag, and Pd) and Cu_2O shells (Figure 5.5). Scherrer's analysis of the diffraction patterns revealed that the crystallite size is 5 nm. This result confirmed that the Cu_2O shell is polycrystalline. Furthermore, EDX elemental mapping of $M@Cu_2O@Zn(OH)_2$ verify the presence of metallic PVP and $Zn(OH)_2$ passivation as shown in Appendix 5-1A and 5-1B.

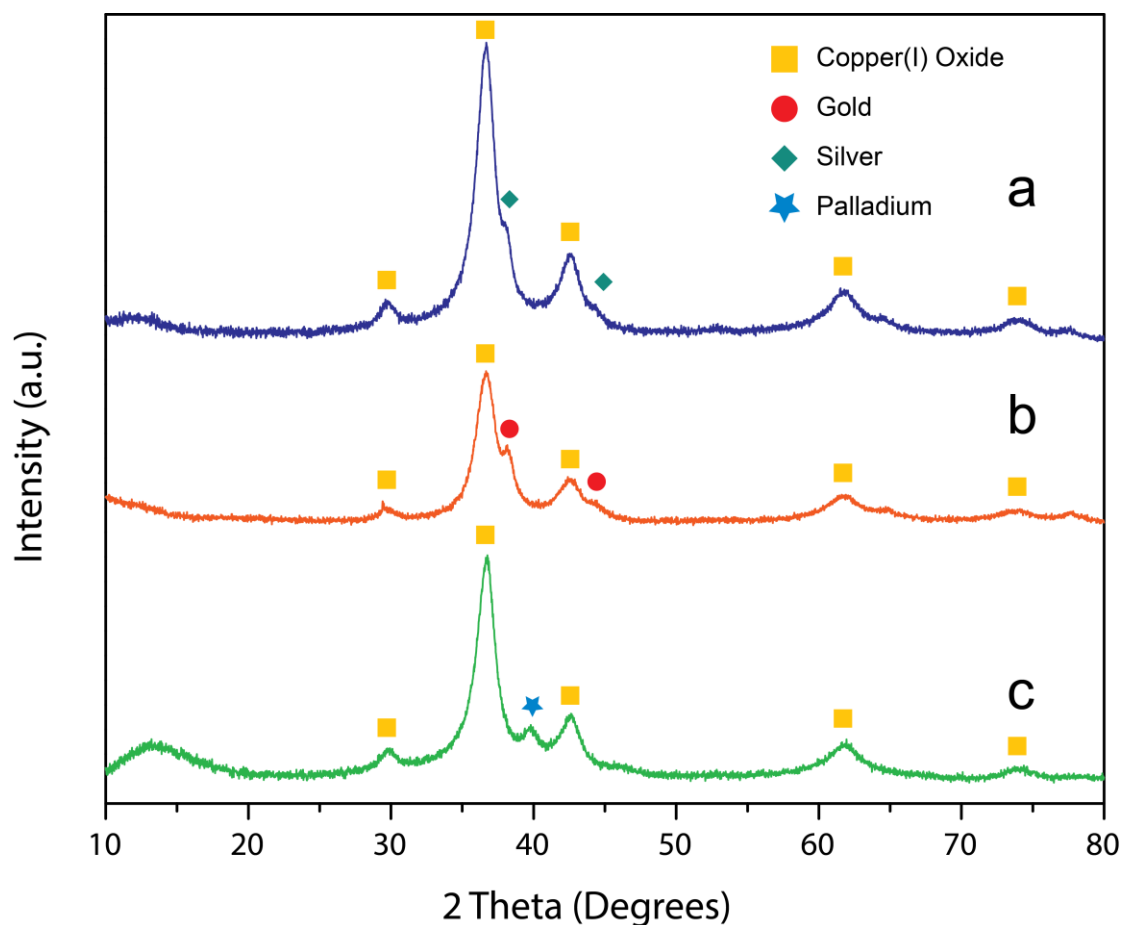


Figure 5.5 XRD pattern for different $M@Cu_2O$ core-shell structure: (a) $Ag@Cu_2O$, (b) $Au@Cu_2O$, and (c) $Pd@Cu_2O$.

Similar with Chapter 4, the reactivity and the associated structural transformation of $M@Cu_2O$ and $M@Cu_2O@Zn(OH)_2$ core-shell with $NaBH_4$ were also studied. Figure 5.6 shows the structural transformation of $M@Cu_2O$ core-shell after reaction with $NaBH_4$. Similar with the reduction of Cu_2O homogeneous core-shell, the formation of polycrystalline hollow shells occurred after the addition of $NaBH_4$ into the as-synthesized $M@Cu_2O$ core-shell. However, the prerequisite amount of reducing agent significantly decreased compared with the reduction of Cu_2O homogeneous core-shell. This decrease can be attributed to a decrease in Cu_2O shell size. The formation of hollow core-shell structure can be attributed to a reduction-dissolution mechanism, as had been discussed in Chapter 4.

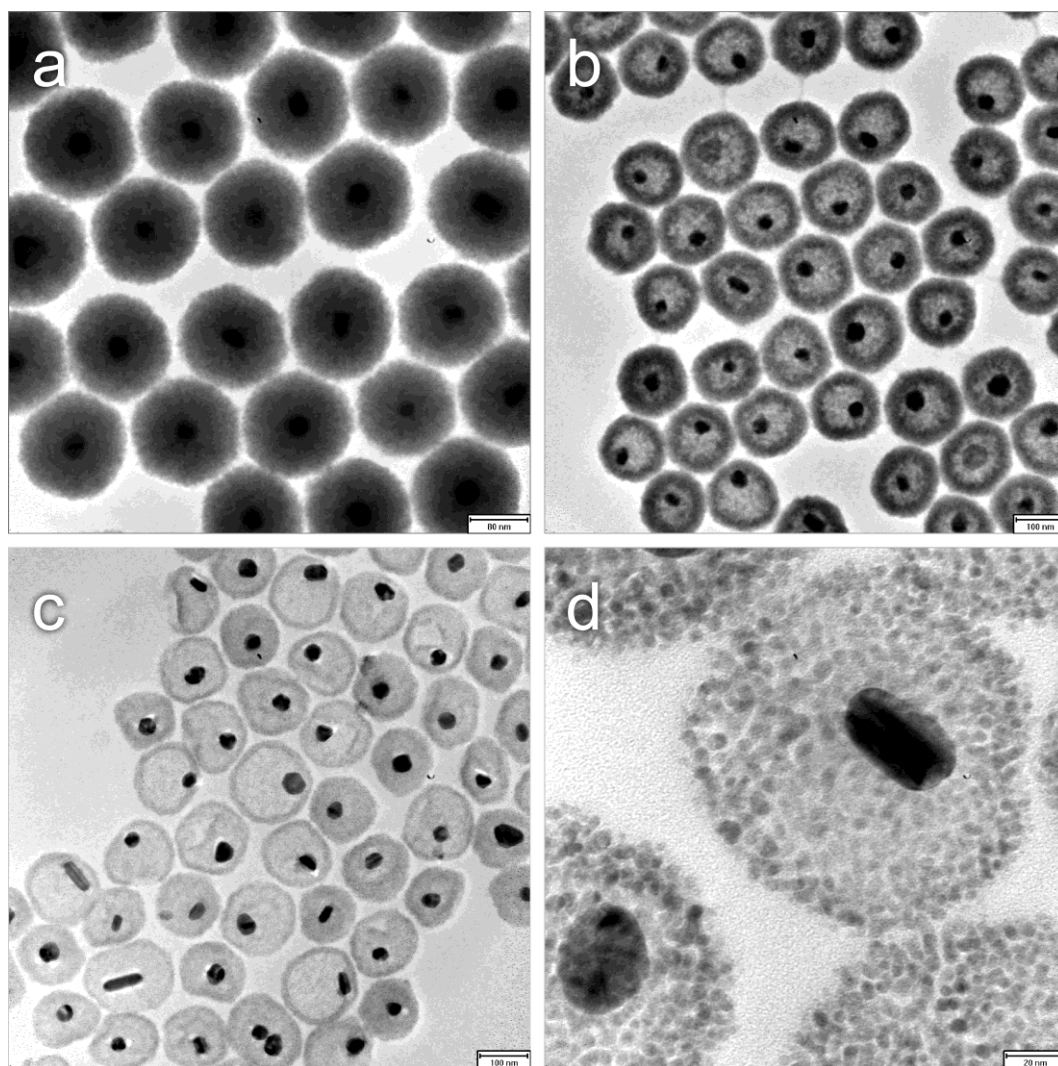


Figure 5.6 Reduction of the as-synthesized $M@Cu_2O$ Core-Shell structure with various amount of $NaBH_4$ solution (10 mg/mL): (a) 0, (b) 50, (c) 100, and (d) 150 μL .

In addition to $M@Cu_2O$ core-shell, the reduction and structural transformation of the as-synthesized $M@Cu_2O@Zn(OH)_2$ were also determined. Figure 5.7 shows the structure of $M@Cu_2O@Zn(OH)_2$. In contrast with the reduction of Cu_2O , $Zn(OH)_2$ passivated Cu_2O , and $M@Cu_2O$ core-shells, there were no observed structural changes for $M@Cu_2O@Zn(OH)_2$ after the addition of $NaBH_4$ solution (Figure 5.7). This is attributed to the presence of both the $Zn(OH)_2$ layer and excess PVP in the solution. The $Zn(OH)_2$ allows the inhibition of mass transfer $NaBH_4$ into the particle.

On the other hand, the excess PVP in the solution can react with $NaBH_4$ to form its amine structure.

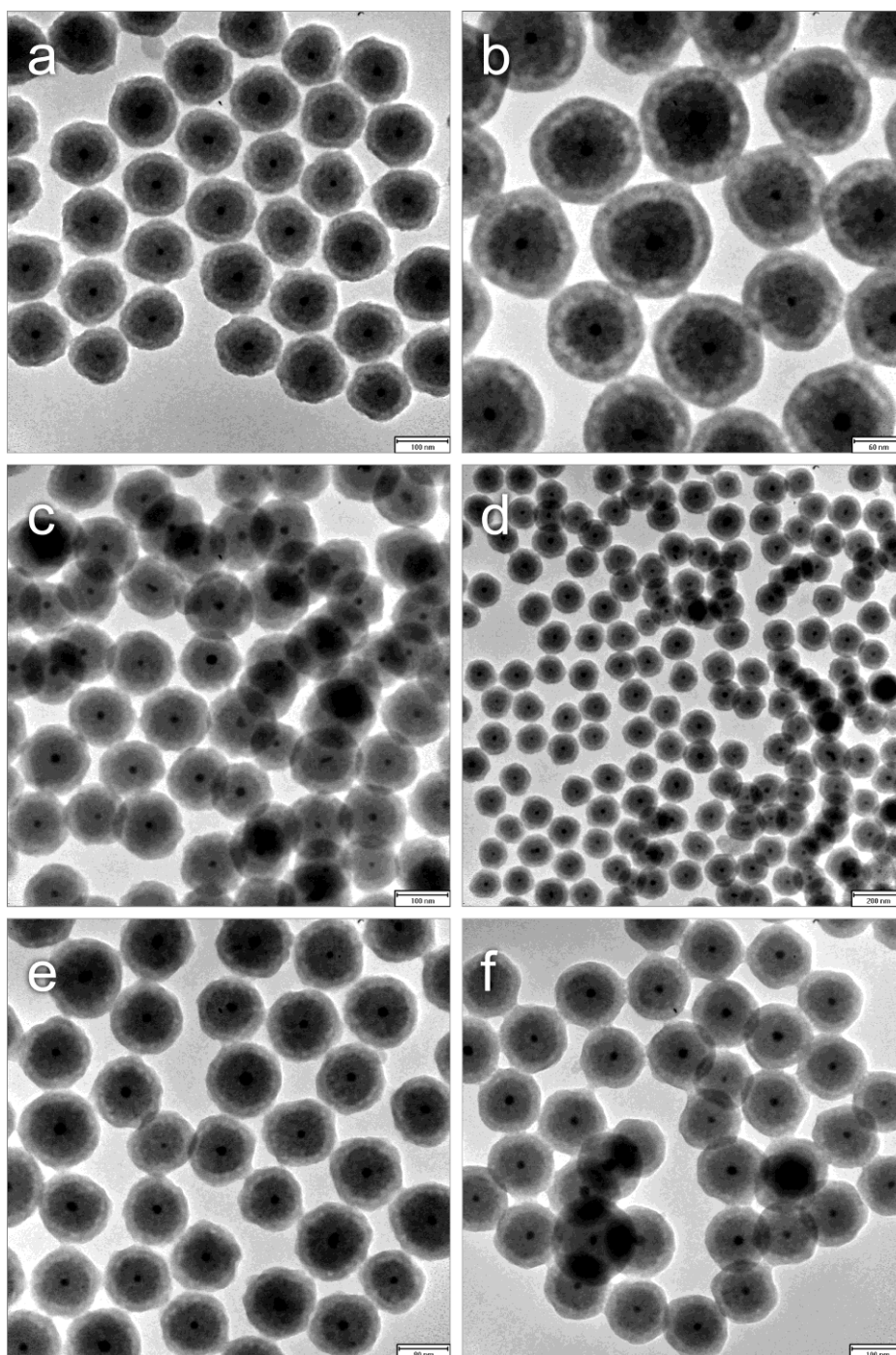


Figure 5.7 Reduction of the as-synthesized $M@Cu_2O@Zn(OH)_2$ with 1 mL of $NaBH_4$ solution at various concentrations: (a) 50, (b) 100, (c) 150, (d) 200, (e) 350, and (f) 400 mg/mL.

As a result, there is a decreased in the effect amount of $NaBH_4$. Therefore, we also determined the structural transformation of $M@Cu_2O@Zn(OH)_2$ after washing twice with ethanol solution. As shown in Figure 5.8, the structural transformation of $M@Cu_2O@Zn(OH)_2$ was finally observed after washing with ethanol.

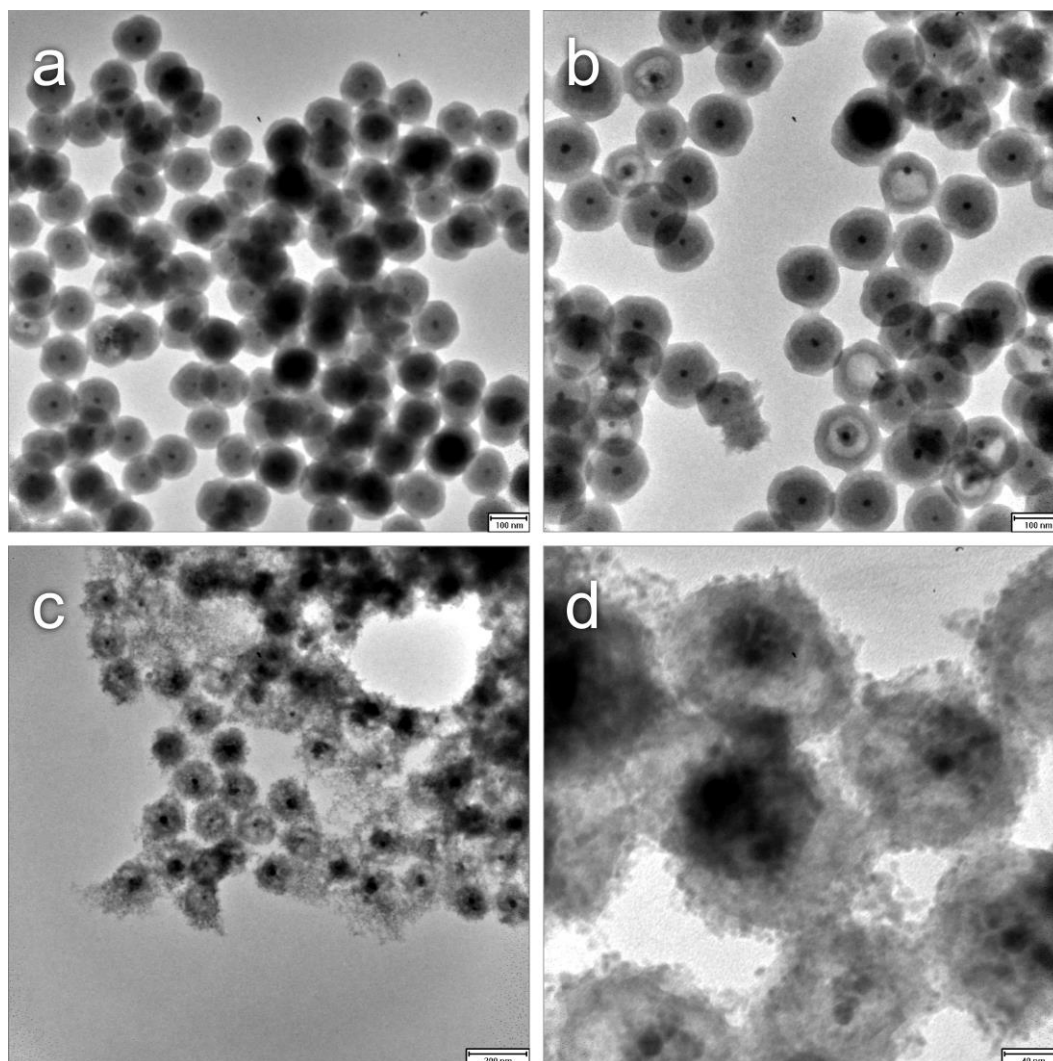


Figure 5.8 Reduction of redispersed $M@Cu_2O@Zn(OH)_2$ with 1 mL of $NaBH_4$ solution at various concentration, after washing twice with 25 mL ethanol: (a) 100, (b) 200, (c) 300, and (d) 400 mg/mL

Similar with that of a $Zn(OH)_2$ passivized Cu_2O core-shell, the transformation can be described as a “*surface to core*” void region formation (Figure 5.8b). However, the

homogeneity of the particle's morphology is widely distributed, not all M@Cu₂O@Zn(OH)₂ underwent structural changes. This result may indicate that PVP is still adsorbed on the particle. In addition, at higher amount of reducing agent, the spherical structure collapsed, and polycrystalline shells were observed (Figure 5.8c and 5.8d).

5.3.2 Thermal Treatment of M@Cu₂O@Zn(OH)₂ Core-Shell Structure

In addition to determining the chemical reactivity and structural transformation of M@Cu₂O@Zn(OH)₂ with NaBH₄, we also determined its structural transformation during thermal treatment. Figure 5.9 shows the structural transformation of M@Cu₂O@Zn(OH)₂ during thermal treatment under flowed Argon conditions. At a relatively low temperature (200 °C), there were no observed structural changes on the core-shell structure (Figure 5.9a). Further increasing the temperature (250 °C), the formation of interior hollow regions were observed (Figure 5.9b); however, the metallic core can still be distinguished from its shell structure. At even higher temperature (300 °C), a mixture of two distinct structures, in which both the metallic core and Cu₂O cannot be distinguished, was observed (Figure 5.9c). The first structure is a semi-concentric hollow structure of Cu₂O and ZnO; while the second structure is a hollow core-shell structure, where the Cu₂O layer merged with the metallic core. Finally at 400 °C, only the second structure was observed (Figure 5.9d).

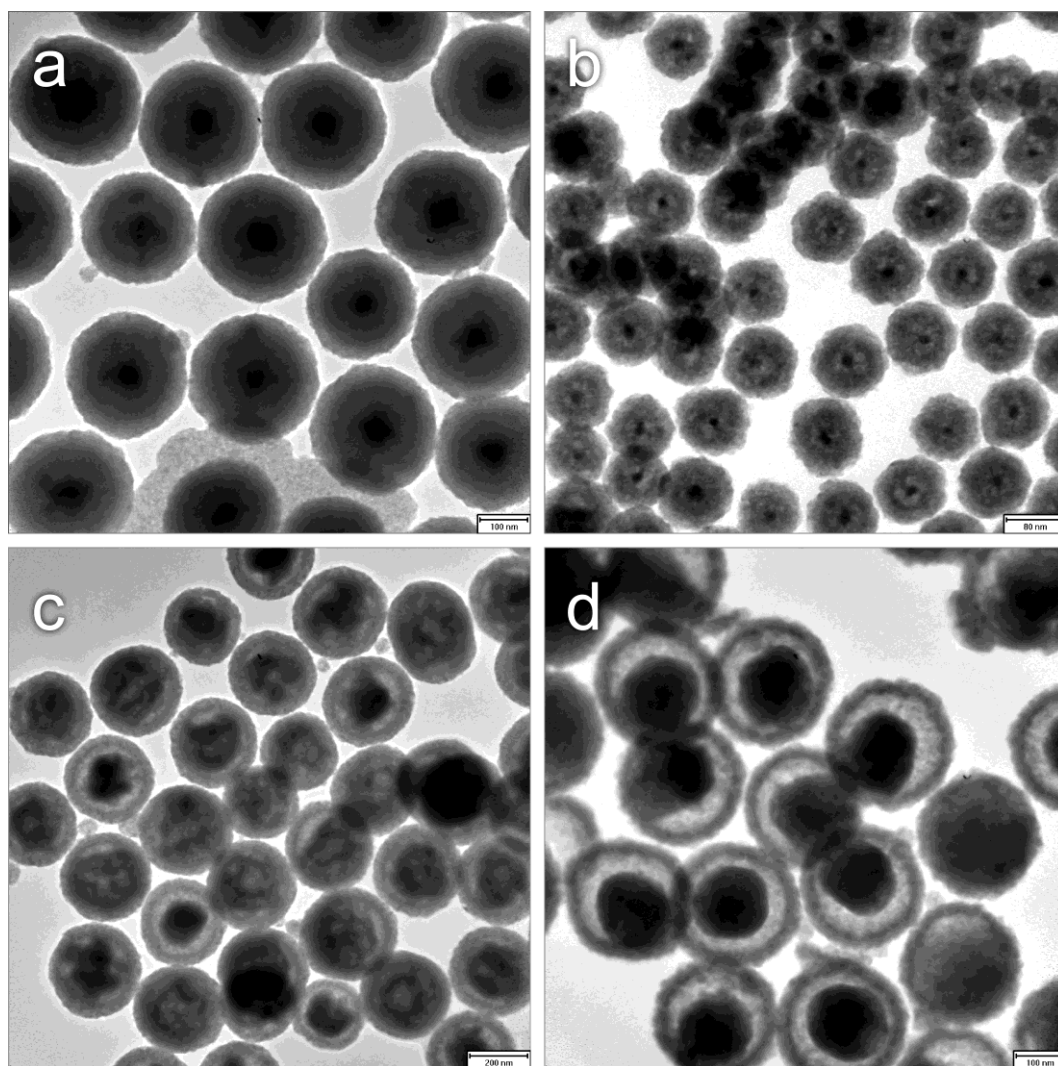


Figure 5.9 Thermal treatment of $M@Cu_2O@Zn(OH)_2$ at various temperature under flowed Argon condition for 12 hours: (a) 200, (b) 250, (c) 300, and (d) 400 °C.

In addition to TEM characterization, XRD characterization of the thermally treated $M@Cu_2O@Zn(OH)_2$ revealed the formation of several phases (Figure 5.10). Diffraction peaks for Cu_2O , ZnO , Cu , and Ag were observed for samples heated at 200 °C (Figure 5.10c), whereas, CuO peak were observed for samples heated at 300 °C and 400 °C (Figure 5.10b). In addition, samples heated at higher temperature have sharper diffraction peaks. The result suggests several implications. First, the crystallinity of $M@Cu_2O@Zn(OH)_2$ improves during thermal treatment since the diffraction peaks

become sharper as the annealing temperature increases. Second, the interior Cu_2O underwent disproportionate reaction to form CuO and Cu phase as previously reported. Third, the observation of ZnO phase after heating indicates that the initial third layer can be attributed to $Zn(OH)_2$. Finally, the XRD result suggests that the transformation of $M@Cu_2O@Zn(OH)_2$ while thermal treatment can be attributed to Ostwald ripening, which is the same explanation presented in Chapter 4. This explanation is supported by the presence of Cu_2O phase even after heating at $400\text{ }^\circ\text{C}$ and an improvement in crystallinity of the structure.

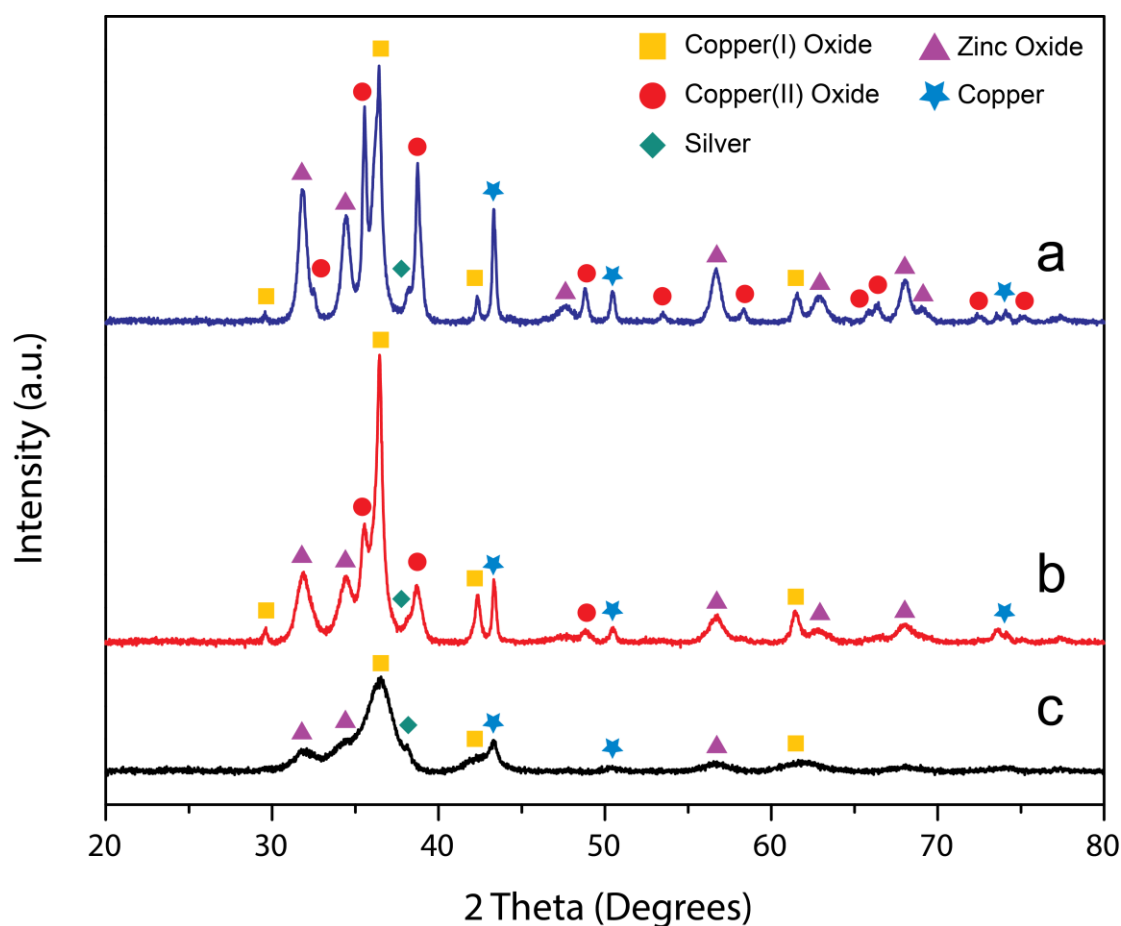


Figure 5.10 Corresponding XRD pattern of $M@Cu_2O@Zn(OH)_2$ after thermal treatment in Argon conditions: (a) $400\text{ }^\circ\text{C}$, (b) $300\text{ }^\circ\text{C}$, and (c) $200\text{ }^\circ\text{C}$.

5.3.3 Reduction of 4-Nitrophenol Using $M@Cu_2O$ and $M@Cu_2O@Zn(OH)_2$ Core-Shell

In order to test the applicability of $M@Cu_2O$ and $M@Cu_2O@Zn(OH)_2$ core-shell structures, the catalytic reduction of 4-nitrophenol was chosen as a model reaction.¹⁰ Figure 5.11 shows the absorption spectrum of the reduction of 4-nitrophenol under different catalysts. The concentration of 4-nitrophenol was determined by measuring absorption at 400 nm. Based on the figure, the reduction of 4-nitrophenol using $Ag@Cu_2O$ and $Au@Cu_2O$ catalysts (Figure 5.11a and 5.11b) was not completed after 1 hour. On the other hand, the reduction was achieved using $AuAg@Cu_2O$ core-shell catalyst (Figure 5.11c). This result suggests that $AuAg$ core performs better than Au and Ag core. Furthermore, we also determined the catalytic property of $Au@Cu$ hollow core-shell structures (Figure 5.11d). Interestingly, the reduction rate of 4-nitrophenol was found to be faster than $Au@Cu_2O$ core-shell structure. This result suggests two implications. First, the metallic core is the active site of the reaction rather than the Cu_2O shell, since it was observed that the reaction is faster for hollow structure. This is due to better transport of the reactants from the solution into the metallic core. Second, the $NaBH_4$ used in the reaction was consumed *via* the reduction of Cu_2O shell. As a result, the activity of $M@Cu_2O$ core-shell would be slower than that of $M@Cu$ hollow core-shell structure. In order to support the first implication, we decided to further inhibit the transport of reactants between the core and the solution by using $M@Cu_2O@Zn(OH)_2$ core-shell structure. As expected with a passivized structure, there were no observed degradation of 4-nitrophenol when $M@Cu_2O@Zn(OH)_2$ was used as a catalyst (Figure 5.11e and 5.11f).

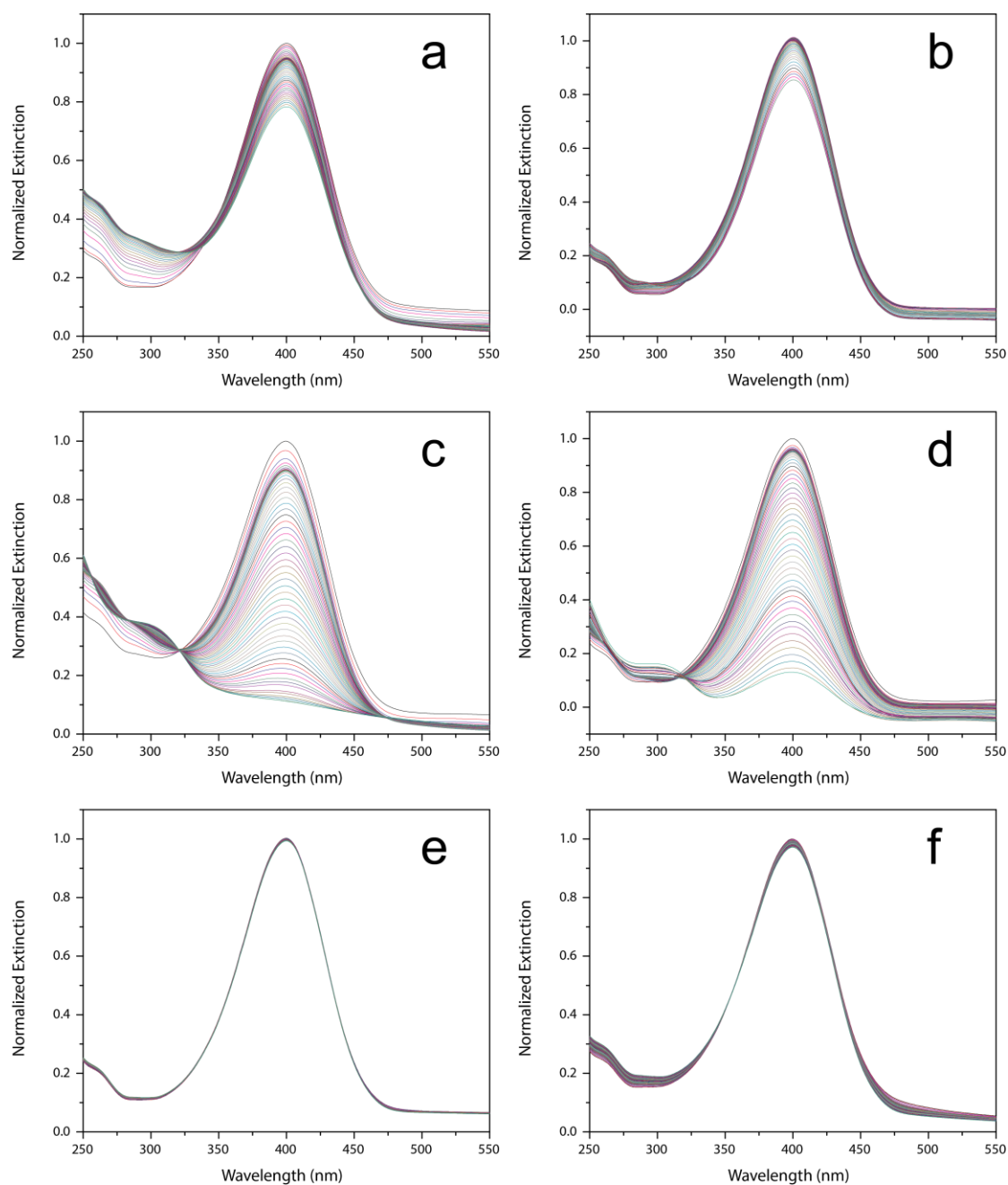


Figure 5.11 Catalytic reduction of 4-nitrophenol with various $M@Cu_2O$, $M@Cu$, and $M@Cu_2O@ZnO$ core-shell catalyst: (a) $Ag@Cu_2O$, (b) $Au@Cu_2O$, (c) $AuAg@Cu_2O$, (d) Hollow $Au@Cu_2O$, (e) $Ag@Cu_2O@ZnO$, and (f) $AuAg@Cu_2O@ZnO$. (Sampling interval is every 1 minute and total measurement duration is 1 hour).

The concentration profile of 4-nitrophenol during reduction using $M@Cu_2O$ and $M@Cu_2O@Zn(OH)_2$ were determined as shown in Figure 5.12. Based on the figure, there is an induction time observed during the reduction of 4-nitrophenol from 15 to

20 min. for $AuAg@Cu_2O$ and $Au@Cu$ core-shell structure; while the induction time for $Au@Cu_2O$ and $Ag@Cu_2O$ was found to be around 30 minutes. The induction time can be attributed to the diffusion of 4-nitrophenol and $NaBH_4$ into the metallic core.

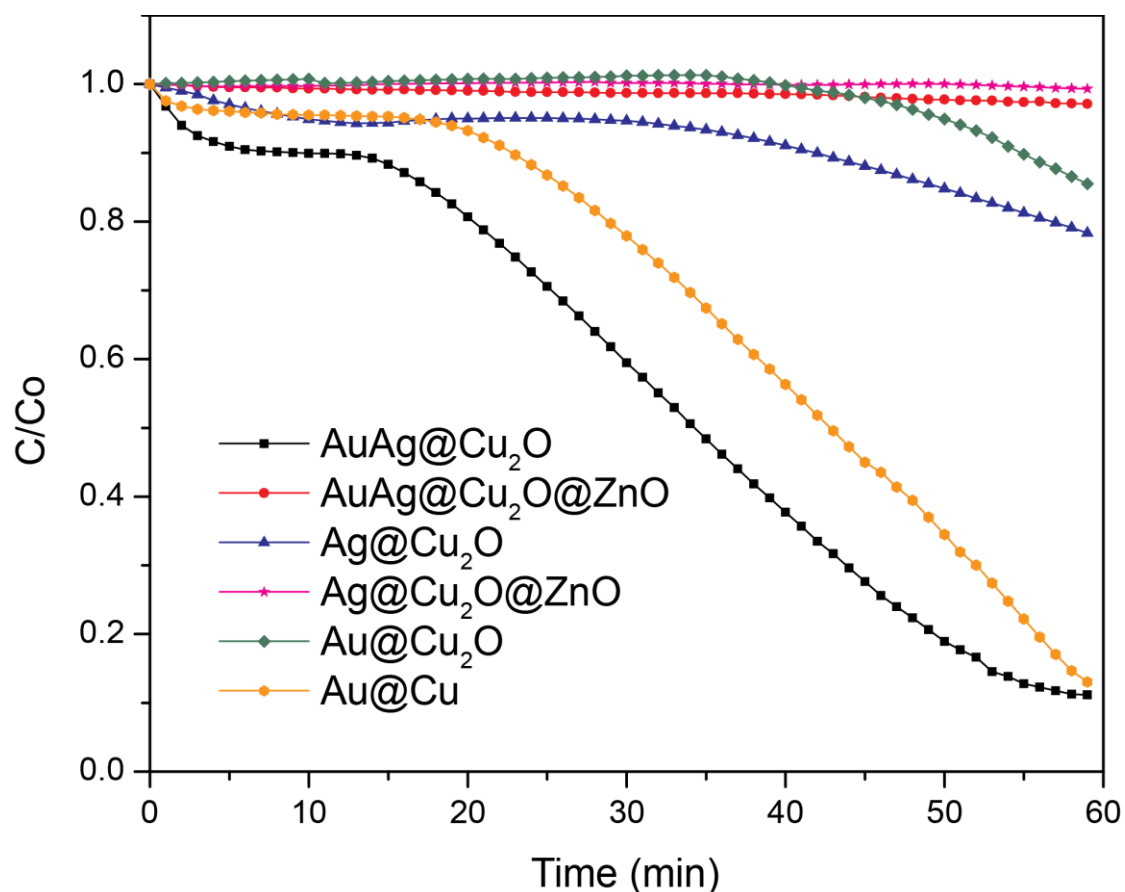


Figure 5.12 Concentration profile of 4-Nitrophenol during reduction with $NaBH_4$ at various types of catalyst.

5.3.4 Photocatalytic Degradation of Methyl Orange using $M@Cu_2O$ and $M@Cu_2O@Zn(OH)_2$ Core-Shell

Similar to Chapter 4, the photocatalytic properties of $M@Cu_2O@ZnO$ core-shells were determined and were compared with Cu_2O CSPAR, $Cu_2O@ZnO$ CSPAR and Cu_2O NPs on ZnO hollow sphere. Among these $M@Cu_2O@ZnO$ catalysts, only

$Au@Cu_2O@ZnO$ catalyst was found to possess a catalytic property towards Methyl orange degradation (Figure 5.13).

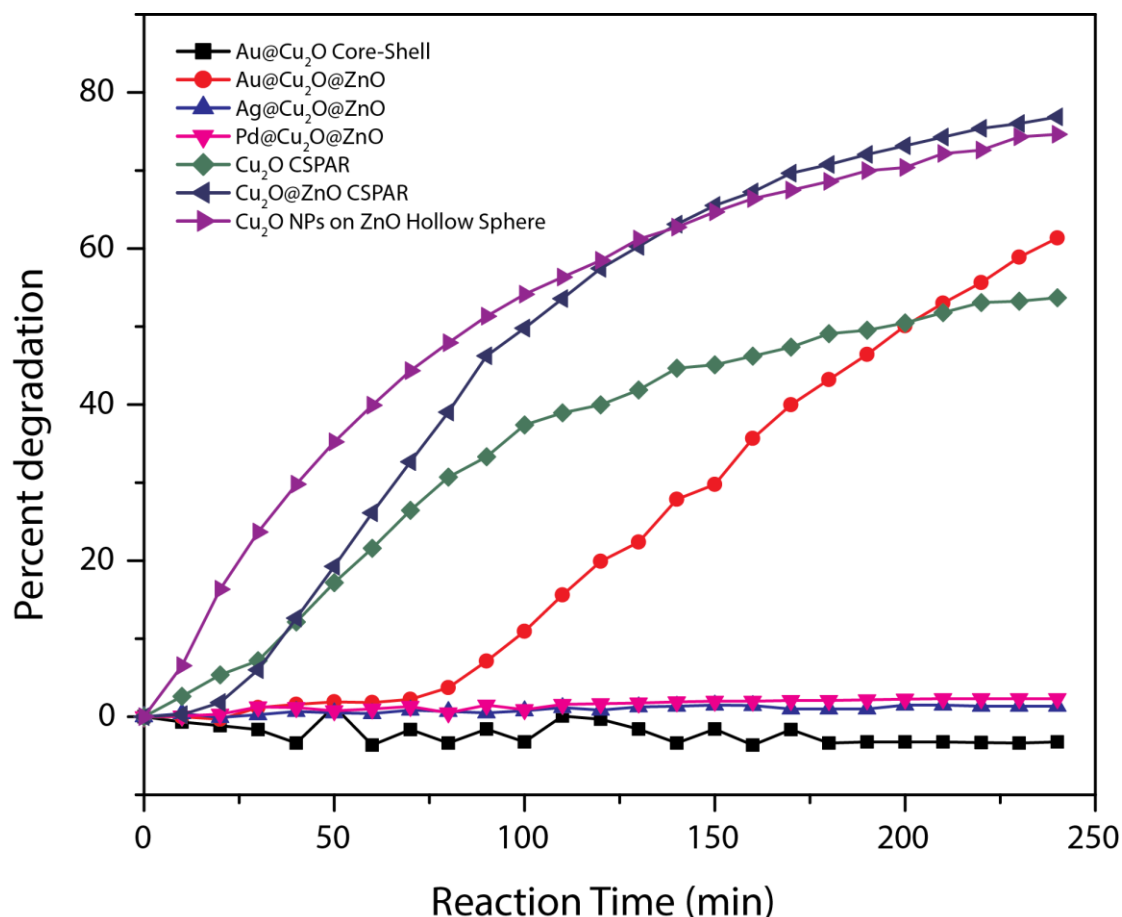


Figure 5.13 Concentration profile of Methyl Orange during photocatalytic degradation at various types of catalyst.

Compared with $Cu_2O@ZnO$ CSPAR and Cu_2O NP on ZnO hollow sphere, the photocatalytic activity of $Au@Cu_2O@ZnO$ is lower, and an induction duration was also found between 0 to 70 min of the reaction. The reduction in degradation activity may be due to diffusion limitation and effective charge separation of photogenerated holes and electrons. In fact, the presence of Au core modifies the heterojunctions that further separates photogenerated holes and electrons compared with the p-n junction of Cu_2O and ZnO (Figure 5.14a). The Schottky barrier between Au and Cu_2O was

reported to be 0.4 eV^{11} , which is low compared with other metal. As a result, photogenerated holes may diffuse into the gold due to thermal energy. The methyl orange molecule needs to diffuse inside the Au core to be degraded. As a result, the induction time between 0 to 70 min was observed before degradation. On the other hand, replacing the Au core with Ag core resulted in no photocatalytic activity (Fig. 5.13). This inhibition of activity can be attributed to a larger Schottky barrier between Ag and Cu_2O contacts¹²⁻¹⁴. The larger barrier inhibits further separation of photogenerated holes with electrons. In addition, the Ag core significantly increases the Fermi level of Cu_2O before forming a heterojunction with ZnO (Fig. 5.14b). As a result, a broken gap between Cu_2O and ZnO layers may be formed and no carrier transport can occur between the p-n junction. Furthermore, this broken gap may result to recombination of charge carriers. In addition to Ag cores, Pd cores were also found to possess no photocatalytic property towards methyl orange degradation (Fig. 5.13). Compared to $Au@Cu_2O@ZnO$ catalyst, Pd and Cu_2O essentially forms an ohmic contact due to a lower work function of Pd compared with the Fermi level of Cu_2O ¹². This contact enables the migration of photogenerated holes between Pd and Cu_2O without resistance (Fig. 5.14c). The $Pd@Cu_2O@ZnO$ core-shell structure possess an energy diagram that effectively separates the photogenerated holes and electrons; wherein the holes are located inside the Pd core and the electrons are located on the ZnO shell (Fig. 5.14c). This diagram suggests that methyl orange photodegradation may be caused by photogenerated holes rather than photogenerated electrons. Comparing both the energy diagrams for $Au@Cu_2O@ZnO$ and $Pd@Cu_2O@ZnO$ (Fig. 5.14a and c), the distribution of photogenerated holes on Cu_2O is larger for $Au@Cu_2O@ZnO$ and the distribution of holes on the metal is more on

$Pd@Cu_2O@ZnO$. As a result, methyl orange degradation using $Pd@Cu_2O@ZnO$ can occur, if the molecule can diffuse inside the Pd core. Although recent report suggests that Pd and Cu_2O can form a Schottky contact on the (100) facet of Cu_2O ,¹⁵ the current system consists of Cu_2O polycrystallites which possess both (111) and (100) facets. Thus, the Fermi-level of Cu_2O given in Figure 5.14 is an average.

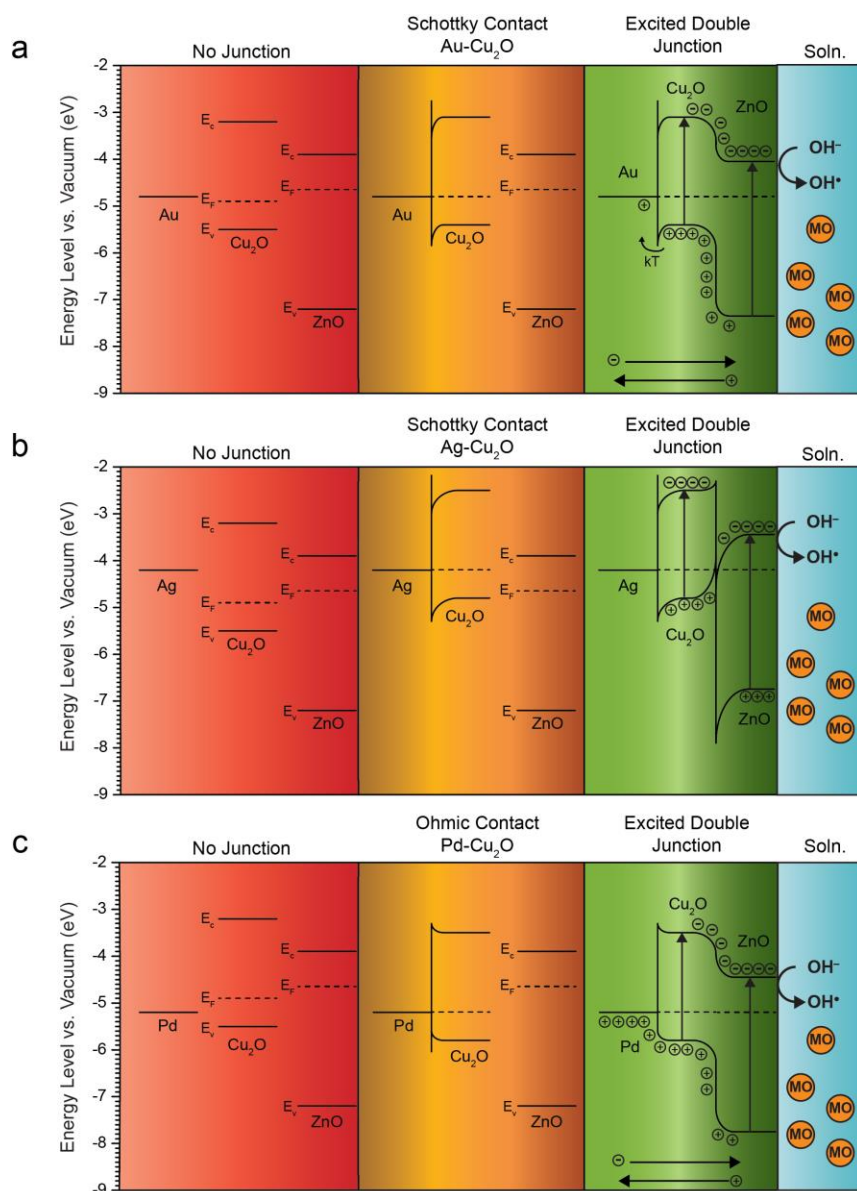


Figure 5.14 Energy level diagram of different $M@Cu_2O@ZnO$ core-shell structures: (a) $Au@Cu_2O@ZnO$, (b) $Ag@Cu_2O@ZnO$, and (c) $Pd@Cu_2O@ZnO$. (Appendix 3-2 displays the values of E_v , E_c , E_F , and E_g)

5.4 Conclusion

In summary, a seed-mediated approach was developed to prepare monodispersed M@Cu₂O and M@Cu₂O@Zn(OH)₂ core-shell structures. These core-shell structures can be used as a precursor for transformative synthesis such as chemical reduction and thermal treatment. These transformations result to either M@Cu, M@Cu₂O@ZnO or M@CuO@ZnO core-shell structure. The transformation mechanism is similar with Chapter 4, wherein a reduction-dissolution mechanism is used to explain the chemical reduction of M@Cu hollow core-shell structure. On the other hand, the transformation during thermal treatment can be explained by the Ostwald ripening phenomenon. In addition, M@Cu₂O serve as a catalyst for the reduction of 4-nitrophenol, where the metallic core functioned as the active site. On the other hand, Au@Cu₂O@ZnO core-shell structures can also serve as a photocatalysis towards methyl orange degradation. This study extends the seed-mediated and chemical transformation approach for Cu₂O core-shell based structure as introduced in Chapter 3 and Chapter 4.

Reference

- 1 Nozik, A. J. & Memming, R. Physical Chemistry of Semiconductor–Liquid Interfaces. *The Journal of Physical Chemistry* **100**, 13061-13078, doi:10.1021/jp953720e (1996).
- 2 Li, J. & Zeng, H. C. Nanoreactors - Size tuning, functionalization, and reactivation of Au in TiO₂ nanoreactors. *Angew Chem Int Edit* **44**, 4342-4345, doi:DOI 10.1002/anie.200500394 (2005).
- 3 Zhang, N., Liu, S. & Xu, Y.-J. Recent progress on metal core@semiconductor shell nanocomposites as a promising type of photocatalyst. *Nanoscale* **4**, 2227-2238, doi:10.1039/C2NR00009A (2012).
- 4 Li, M. *et al.* Synthesis of Au–CdS Core–Shell Hetero-Nanorods with Efficient Exciton–Plasmon Interactions. *Adv. Funct. Mater.* **21**, 1788-1794, doi:10.1002/adfm.201002233 (2011).

- 5 Zhang, N., Fu, X. & Xu, Y.-J. A facile and green approach to synthesize Pt@CeO₂ nanocomposite with tunable core-shell and yolk-shell structure and its application as a visible light photocatalyst. *J Mater Chem* **21**, 8152-8158, doi:10.1039/c1jm10100e (2011).
- 6 Zhang, L., Blom, D. A. & Wang, H. Au-Cu₂O Core-Shell Nanoparticles: A Hybrid Metal-Semiconductor Heteronanostructure with Geometrically Tunable Optical Properties. *Chem. Mater.* **23**, 4587-4598, doi:10.1021/cm202078t (2011).
- 7 Meir, N. *et al.* Studying the chemical, optical and catalytic properties of noble metal (Pt, Pd, Ag, Au)-Cu₂O core-shell nanostructures grown via a general approach. *Journal of Materials Chemistry A* **1**, 1763-1769, doi:10.1039/C2TA00721E (2013).
- 8 Yang, H. G. & Zeng, H. C. Preparation of hollow anatase TiO₂ nanospheres via Ostwald ripening. *Journal of Physical Chemistry B* **108**, 3492-3495, doi:10.1021/jp0377782 (2004).
- 9 Yec, C. C. & Zeng, H. C. Synthetic Architecture of Multiple Core-Shell and Yolk-Shell Structures of (Cu₂O@)_nCu₂O (n=1-4) with Centricity and Eccentricity. *Chem. Mater.* **24**, 1917-1929, doi:10.1021/cm300672r (2012).
- 10 Pang, M. L., Wang, Q. X. & Zeng, H. C. Self-Generated Etchant for Synthetic Sculpturing of Cu₂O-Au, Cu₂O@Au, Au/Cu₂O, and 3D-Au Nanostructures. *Chem-Eur J* **18**, 14605-14609, doi:DOI 10.1002/chem.201202765 (2012).
- 11 Olsen, L.C., Bohara, R.C. & Urie, M.W. Explanation for low efficiency Cu₂O Schottky-barrier solar cells. *Appl. Phys. Lett.* **34**, 47-49, doi: 10.1063/1.90593 (1979)
- 12 Siah, S.C., Lee, Y.S., Segal, Y. & Buonassisi, T. Low contact resistivity of metals on nitrogen-doped cuprous oxide (Cu₂O) thin-films. *J. Appl. Phys.* **112**, 084508, doi: 10.1063/1.4758305 (2012).
- 13 Wang, Z., Zhao, S., Zhu, S., Sun, Y. & Fang, M. Photocatalytic synthesis of M/Cu₂O (M = Ag, Au) heterogeneous nanocrystals and their photocatalytic properties. *Crystengcomm* **13**, 2262-2267, doi:10.1039/C0CE00681E (2011).
- 14 Li, J. *et al.* Ag@Cu₂O Core-Shell Nanoparticles as Visible-Light Plasmonic Photocatalysts. *ACS Catal* **3**, 47-51, doi:10.1021/cs300672f (2013).
- 15 Wang, L. *et.al.* Designing p-Type semiconductor-metal hybrid structures for improved photocatalysis. *Angew. Chem. Int. Ed.* **53**, 5107-5111, doi: 10.1002/anie.201310635(2014).

Chapter 6. Nanobubbles on a Microbubble: Synthesis and Self-Assembly of Hollow Manganese Silicate and Its Metal-Doped Derivatives

Abstract

We developed a surface-catalyzed dual templating strategy to synthesize and organize hollow spheres of manganese silicate as well as a wide variety of its metal-doped structural derivatives (where metal dopant = Fe, Co, Ni, Cu, Y, La, Ce, Nd, Eu, Gd, Er, and Yb). The size of hollow spheres obtained is in the range of only 7–9 nm. In addition, the resultant nanospheres can also be formed into an even greater hollow sphere, giving rise to an interesting “*bubbles within a bubble*” assemblage in submicron regime (*e.g.*, ~200 to 270 nm). The hierarchical hollow structures of this type were further tested for catalytic degradation (or decomposition) of organic dyes and used as solid precursors for transformative synthesis of other silicon-based functional hollow materials.

6.1 Introduction

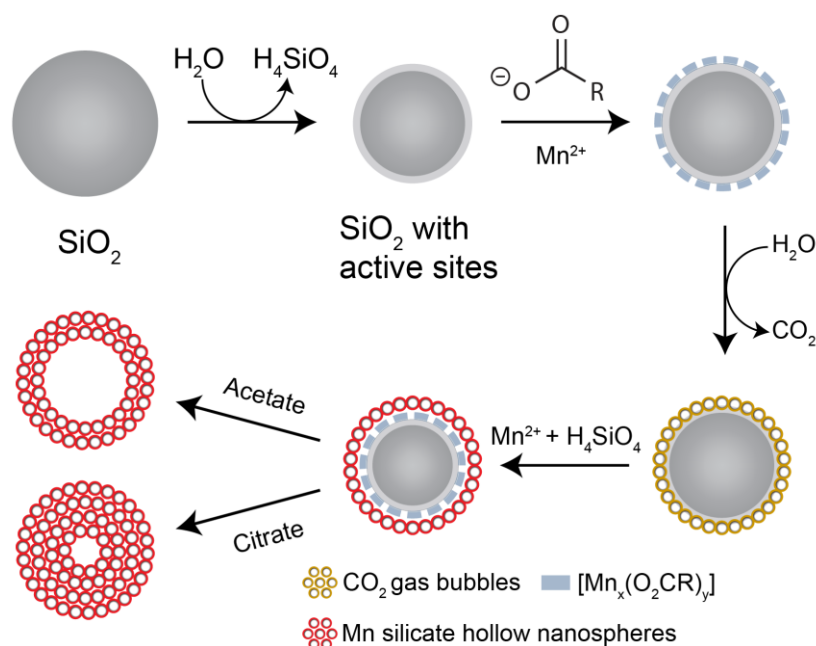
Manganese compounds have been commonly regarded as efficient catalysts towards oxidation reaction, and they are widely abundant in nature¹⁻³. For instance, the photosystem II protein complex, which is responsible for the photo-oxidation of water in green plants, is composed of a Mn tetramer complex $Mn_4O_4Ca^4$. Not only the manganese compounds have a wide range of composition, but also have a large

variety of morphology. Among these solids, colloidal manganese-based hollow structures stand out as a class of interesting materials, since they may offer improved physicochemical performance owing to a significant increase in their surface area to volume ratio.

Colloidal inorganic hollow structures are particles that possess an internal void and have sizes ranging from several angstroms up to several microns⁵⁻⁷. These hollow structures are usually prepared using template-based methodologies, among which is the use of gas-liquid interface template⁸. Nevertheless, this method requires forming gas bubbles on which growth units could deposit and thus generate shell morphology. For example, gas bubbles can be introduced to solution phase through *in situ* reactions that generate gaseous species. Under hydrothermal conditions, very often, organic acids or acid anions decompose into small molecules such as CH₄, CO₂ and H₂, and the gas products depend on an actual reaction pathway⁹⁻¹¹. For instance, decarboxylation of acetic acid would yield both CH₄ and CO₂ while the hydrolysis produces CO₂ and H₂ under such reaction conditions^[10]. Furthermore, the decomposition reactions could be hastened through heterogeneous catalysis by the solid wall or any solid phases (such as colloidal particles) available inside a reactor. Therefore, solid phases present in the system can lower the activation energy of reaction,⁹ and at the same time can determine reaction kinetics of decomposition^{9,10}.

Although gas bubble templates have been widely reported for the preparation of micrometer-scale or submicron hollow structures, the preparation of hollow structures in a nano-regime (*i.e.*, nanobubbles with a diameter < 10 nm) using this approach has not been realized^{8,12-15}. Furthermore, self-assembly of resultant nanobubbles into a

larger hollow structure appears to be a challenging research. Herein, we describe a hydrothermal synthesis of nanospheres of manganese silicate and its transition metal- and rare earth metal-doped derivatives as well as self-integration of product nanospheres into submicron hollow assemblages. In this synthesis, submicron SiO_2 beads serve both as a starting silicon source and as a solid catalyst for the adsorption and decomposition of carboxylate anions. While the *in situ* formed gases serve as a soft template for forming nanobubbles of manganese silicate, the starting silica solid beads function as a hard template for the assembly of these tiny bubbles into an even greater hollow configuration, or a larger “bubble”, of manganese silicate. As illustrated in Scheme 6.1 1, we will further demonstrate that the decomposition of adsorbed Mn-carboxylate complexes on the active surface of SiO_2 beads is the primary mechanism for the formation of final hierarchical hollow structure. This synthetic strategy can be described as a *surface-catalyzed dual templating process* since the formation of the nanometer-sized gas template is catalyzed and formed at the surface of the submicron solid template. In addition to manganese silicate nanobubbles, metal-doped derivatives of this structure can also be prepared by adding other metal salts in the reaction system. In order to test the applicability of these nanobubbles, we also studied their catalytic property towards the oxidative degradation (or decomposition) of organic dyes, and used these nanobubble assemblies as a solid precursor for lithium ion intercalation.



Scheme 6.1 Schematic illustration of surface-catalyzed dual templating process, where CO_2 gas bubbles serve as a soft template for deposition of Mn-silicate nanospheres (*i.e.*, nanobubbles) and SiO_2 precursor bead provides silicon source and works as a hard template for assemblage of resultant nanospheres.

6.2 Experimental Section

Chemicals and reagents. The following chemicals were used in this work: tetraethyl orthosilicate (TEOS, $\geq 99.0\%$, Aldrich), ammonia solution (25%, Merck), manganese (II) acetate tetrahydrate ($\text{Mn}(\text{CH}_3\text{COO})_2 \cdot 4\text{H}_2\text{O}$, $\geq 99\%$, Aldrich), manganese (II) sulfate monohydrate (99%, Alfa Aesar), sodium acetate anhydrous (99%, Alfa Aesar), maleic acid disodium salt anhydrous ($\geq 98.0\%$, Fluka), sodium tartrate dihydrate dibasic ($\geq 98.0\%$, Riedel-de Haen), sodium citrate tribasic dihydrate ($\geq 99.0\%$, Sigma-Aldrich), iron (II) sulfate heptahydrate ($\geq 99.0\%$, Sigma-Aldrich), cobalt (II) sulfate heptahydrate ($\geq 99\%$, Sigma-Aldrich), nickel (II) sulfate hexahydrate (99%, Sigma), copper (II) sulfate pentahydrate (99.5%, Nacalai Tesque), yttrium (III) nitrate hexahydrate (99.9%, Strem chemicals), lanthanum (III) nitrate hexahydrate ($\geq 96.0\%$,

Merck), cerium (III) nitrate hexahydrate (99%, Aldrich), neodymium (III) nitrate hexahydrate (99.9%, Strem chemicals), europium (III) nitrate hexahydrate (99.9%, Alfa Aesar), gadolinium (III) nitrate hexahydrate (99.9%, Strem chemicals), erbium (III) nitrate hydrate (99.9%, Strem chemicals), ytterbium (III) nitrate hydrate (99.9%, Alfa Aesar), methylene blue (C.I. 62015, Merck), rhodamine 6G (95%, Sigma), methyl orange (C.I. 13025, Merck), hydrogen peroxide solution (30%, Merck) and deionized water.

Synthesis of SiO₂ precursor beads. SiO₂ beads were synthesized according to a previous report with minor modifications^[16]. Briefly, TEOS (2.5 mL) was mixed with ethanol (46.0 mL) under magnetic stirring (1000 rpm). Ammonia solution (5 mL) was added into the solution and was stirred for 4 h. Afterwards, the solution was centrifuged at 3000 g for 10 min and the resulting precipitate (silica beads) was washed with ethanol (30 mL), and dried in an electric oven at 60 °C for 30 min.

Synthesis of manganese silicate nanobubbles. In a typical synthesis, 0.80 mmol of Mn(CH₃COO)₂•4H₂O was dissolved in 10 mL of deionized water in a Teflon liner while the above prepared SiO₂ beads (50 mg) were dispersed in another 10 mL of deionized water with ultrasonication. Subsequently, the SiO₂ suspension was poured into the Mn(CH₃COO)₂ in the Teflon liner and was stirred for 5 min. The Teflon liner was then transferred to a stainless steel autoclave and was heated at 180 °C for 12 h inside an electric oven. The autoclave was cooled at room temperature for 3 h. The product solution was centrifuged at 4000 g for 2 min and the resulting precipitate was washed with deionized water (10 mL), followed by ethanol (10 mL), and the precipitate was dried at 80 °C for 6 h.

Synthesis of doped manganese silica nanobubbles. The synthetic procedure for metal-doped nanobubbles of manganese silica was similar to that used in nanobubbles of manganese silicate with a slight modification. Briefly, 0.04 mmol of transition metal salts such as FeSO_4 , CoSO_4 , NiSO_4 , CuSO_4 or rare earth metal salts such as $\text{Y}(\text{NO}_3)_3$, $\text{La}(\text{NO}_3)_3$, $\text{Ce}(\text{NO}_3)_3$, $\text{Nd}(\text{NO}_3)_3$, $\text{Eu}(\text{NO}_3)_3$, $\text{Gd}(\text{NO}_3)_3$, $\text{Er}(\text{NO}_3)_3$, $\text{Yb}(\text{NO}_3)_3$ and 0.80 mmol of $\text{Mn}(\text{CH}_3\text{COO})_2 \bullet 4\text{H}_2\text{O}$ were dissolved in 10 mL of H_2O in a Teflon liner to obtain a Mn to dopant ratio of 20:1. During this period, SiO_2 beads (50 mg) were dispersed in another 10 mL of deionized water with ultrasonication. Afterwards, the SiO_2 suspension was poured into the $\text{Mn}(\text{CH}_3\text{COO})_2$ and dopant solution in the Teflon liner and was stirred for 5 min. The Teflon liner was then transferred to a stainless steel auto-clave and was heated at 180 °C for 12 h inside an electric oven. The autoclave was cooled at room temperature for 3 h. The product solution was centrifuged at 4000 g for 2 min and the resultant precipitate was washed with deionized water (10 mL), followed by ethanol (10 mL), and the precipitate was dried at 80 °C for 6 h.

Evaluation of catalytic activity. The degradation of organic dye molecules via advanced oxidation process was investigated with the nanobubbles of manganese silicate. This catalyst (20 mg) was dispersed in 100 mL of various dye solutions: methylene blue (100 mg/L), rhodamine 6G (150 mg/L), and methyl orange (100 mg/L). On the other hand, 50 mg of the same nanobubble catalyst was also used for the degradation of a higher concentration of methylene blue (500 mg/L). The prepared solution was immersed in a water bath at 60 °C for 1 h under magnetic stirring. Afterwards, hydrogen peroxide (10 mL, 30%) was added into the solution and was

stirred for 1 h. During this period, liquid samples (5 mL) were withdrawn from the solution and were centrifuged at 4000 g for 1 min. The resulting supernatant was diluted 10-fold before transferring into a quartz cuvette (path-length, 10 mm), and its absorption spectra were acquired using UV-Vis spectroscopy (UV-2450, Shimadzu). Absorption peaks at 665, 526, and 463 nm were used respectively to determine the concentrations of methylene blue, rhodamine 6G, and methyl orange in the supernatant.

Materials characterization. Morphology and structure of the samples were investigated with transmission electron microscopy (TEM, JEM-2010, 200 kV) and high-resolution TEM (HRTEM, JEM-2100F, 200 kV). Chemical bonding information was acquired using Fourier transformed infrared spectroscopy (FTIR, FTS-2500ARX, Bio-Rad). The composition and elemental distribution were determined using energy dispersive X-ray spectroscopy (EDX, Oxford Instruments). Crystallographic information was established by powder X-ray diffraction (XRD, D8 Advanced, Bruker, Cu K α radiation at 1.5406 Å). Nitrogen adsorption and desorption isotherms were measured with a gas-sorption analyzer (NOVA-3000, Quantachrome Instruments). The specific surface area of the sample and its pore size distribution were calculated using Brunauer-Emmett-Teller (BET) method and Barrett-Joyner-Halenda (BJH) desorption curve analysis, respectively.

6.3 Results and Discussion

6.1.1 Manganese Silicate Nanobubbles

Shown in Figure 6.1a, spherical SiO₂ beads with a mean diameter of *ca* 270 nm were first synthesized using a modified Stöber method^{16,17}. This solid precursor was mixed with an aqueous solution of manganese acetate and heat-treated under hydrothermal conditions. The process led to the formation of submicron hollow spheres in about the same dimensional range, as shown in Figure 6.1b. Detailed in Figures 6.1c–1d, intriguingly, the hollow spheres were composed of even smaller hollow spheres with diameters only between 7 and 9 nm. We describe this product morphology as *spherically assembled nanobubbles* of manganese silicate, that is, *bubbles within a bubble*.

We believe that *in situ* generation of gas-bubble template and related gas-liquid interface are responsible for the formation of this hierarchical hollow structure. As summarized in Scheme 6.1, first, a small portion of the SiO₂ phase is hydrolyzed to form H₄SiO₄ and at the same time surface active sites are generated for the adsorption of Mn-carboxylate species (equation 1)⁹. Second, the active sites and associated metal ions (*e.g.*, Mn²⁺) decrease the activation energy for decomposition of carboxylate (Scheme 6.1). Third, carboxylate groups decompose into CO₂ and other gaseous products under hydrothermal condition (equations 2 to 4)¹⁰. Fourth, the tiny gas-bubbles form an interface with solution phase that serves as a soft template for the deposition of manganese silicate through ion-exchange of Mn²⁺ with H₄SiO₄ (equation 5)¹⁸. And finally, these reactions (equations 2 to 5) would continue until SiO₂ phase is entirely consumed or dissolved, thus forming submicron hollow assemblages comprising nanobubbles of manganese silicate (Scheme 6.1).

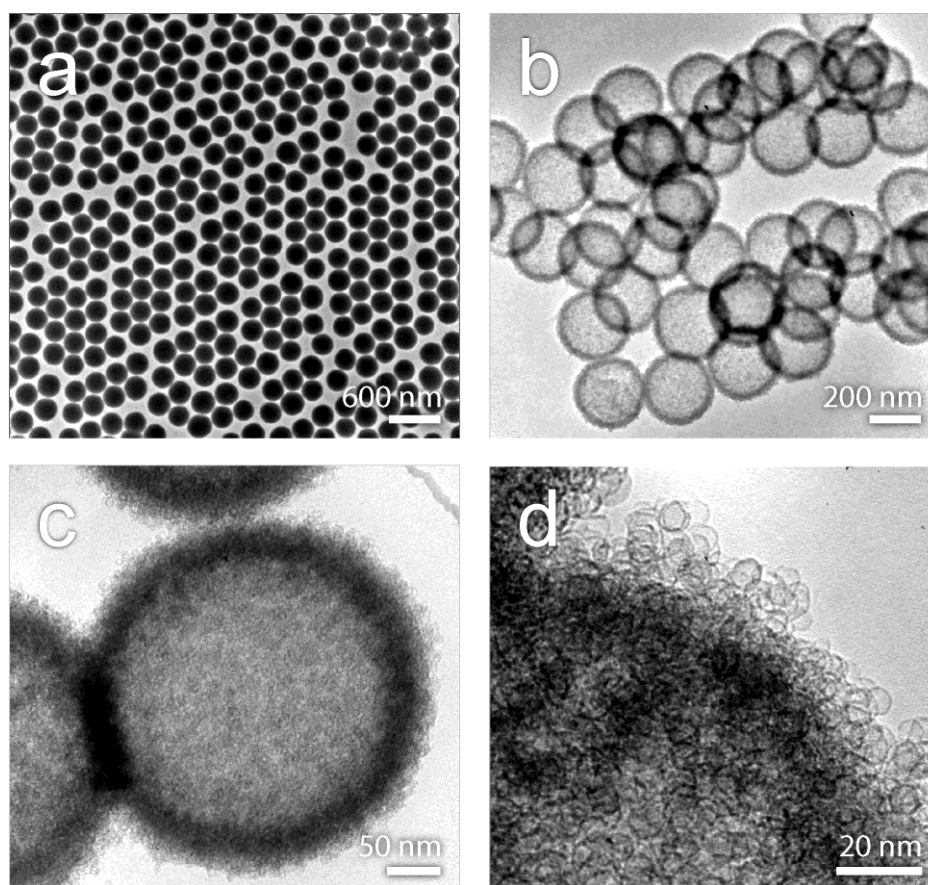
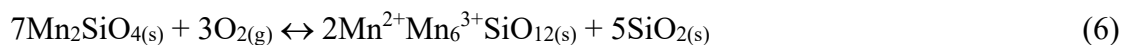
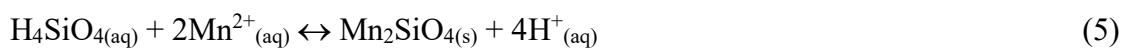
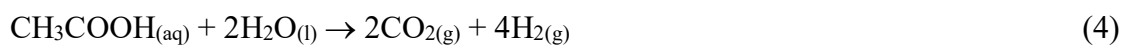
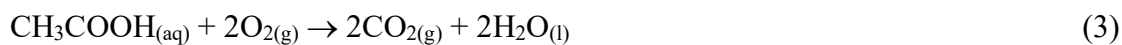


Figure 6.1 Representative TEM images: (a) SiO₂ precursor beads; and (b-d) product samples (i.e., spherically assembled nanobubbles of manganese silicate) synthesized according to Scheme 6.1 1 at different magnifications.

In addition, Mn₂SiO₄ can undergo metamorphism to form braunite 1Q under hydrothermal conditions (equation 6).^[18]



Elemental composition for the bubble samples was affirmed with energy dispersive X-ray spectroscopy (Appendix 4-1A), and both manganese and silicon were homogeneously distributed. In addition, the atomic ratio between manganese and silica is 1:2.6. In Figure 6.2a, X-ray diffraction (XRD) technique indicates the presence of braunite-1Q ($\text{Mn}^{2+}\text{Mn}_6^{3+}\text{SiO}_{12}$ or $\text{Mn}^{2+}\text{Mn}_6^{3+}[\text{O}_8|\text{SiO}_4]$, JCPDS no. 89-5661) and other manganese silicate phases (Mn_2SiO_4 , JCPDS no. 74-0716, and $\text{Mn}_5\text{Si}_3\text{O}_{12}$, JCPDS no. 37-0221) with a trace amount of hausmannite (Mn_3O_4 , JCPDS no. 80-0382).

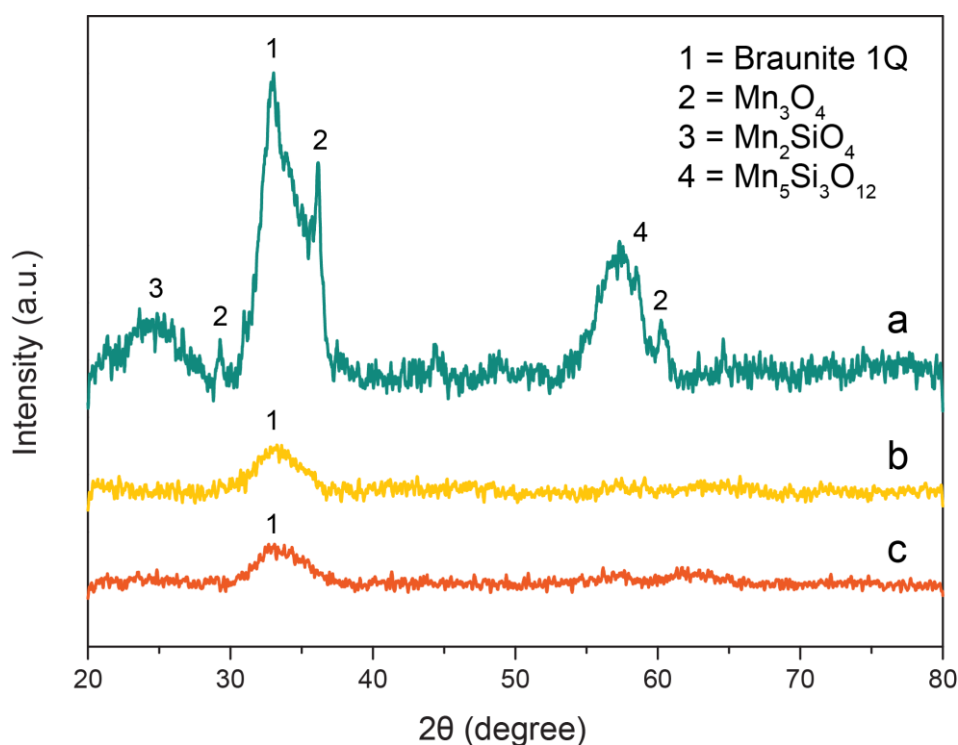


Figure 6.10 X-ray diffraction patterns of nanobubbles of manganese silicate synthesized with different kinds of carboxylate anions: (a) acetate, (b) maleate, and (c) citrate.

The thermal stability of manganese silicate nanobubbles under aerobic conditions was determined. Surprisingly, the nanobubble morphology was retained even after heated at a temperature as high as 800°C for 12 h (Appendix 4-1B). In fact, heating

can be employed as a means to deplete an unwanted phase. For instance, hausmannite phase can be eliminated completely at 700°C, leaving only pure braunite 1Q (Appendix 4-1B) for the nanobubbles. Specific surface area of the as-synthesized nanobubbles was determined to be 316 m²/g using Brunauer-Emmett-Teller (BET) method on N₂ adsorption isotherm (Appendix 4-1C). Even after heated at a high temperature of 800°C for a long period of 12 h, the specific surface area of the sample could still have a value of 52 m²/g (Table 6.1). This decrease can be attributed to changes in pore structure of nanobubbles, resulting in the overall reduction of pore volume (Appendix 4-1C). In addition to this reason, the distance between nanobubbles decreased after heating, which results to better packing.

Table 6.1. Summary of BET Analysis and BJH Desorption Analysis for Manganese Silicate Samples

Physical property	As-synthesized	Thermally treated
Surface area	316.1 m ² /g	52.1 m ² /g
Pore volume	0.151 mL/g	0.068 mL/g
Pore size	3.2 nm	3.0 nm
Pore surface area	88.4 m ² /g	27.6 m ² /g

From Table 6.1, the pore volume was reduced from 0.151 to 0.068 mL/g, and the pore diameter distribution of the heated samples were observed to widen from 30 to 160 Å.

On the other hand, these nanobubbles collapsed under prolonged exposure of electron beam (Appendix 4-1D). This change can be described as cavities solidifying into another phase when illuminated by a focused electron beam during TEM measurements above the magnification of 150,000× (Appendix 4-1D). In addition, we found that these recrystallized areas possessed an interplanar spacing of 0.21 nm that corresponds to the {220} crystal planes of hausmannite Mn₃O₄ (Appendix 4-1D).

6.3.2 Doped Manganese Silicate Nanobubbles

In addition to the manganese silicate nanobubbles, metal doped-derivatives of this structure were also prepared by mixing other metal salts with manganese acetate during the synthesis. Figures 6.3 and 6.4 displays some TEM images of the first-row transition metal doped and rare earth element doped-manganese silicates with a nominal experimental ratio of manganese to dopant at 20:1, respectively. The morphology of doped-nanobubbles is similar to that in Figure 6.1c,d, without noticeable changes.

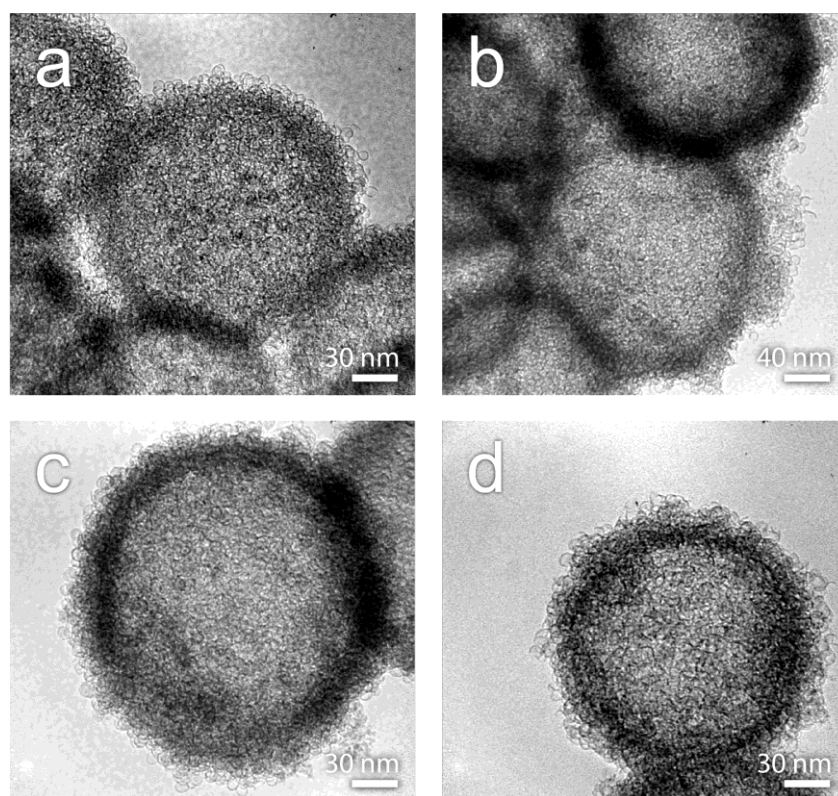


Figure 6.3 Representative TEM images of spherically assembled nanobubbles of manganese silicate doped with the first-row transition metal elements: (a) Fe, (b) Co, (c) Ni, and (d) Cu. The experimental ratio between manganese and dopant was set at 20:1.

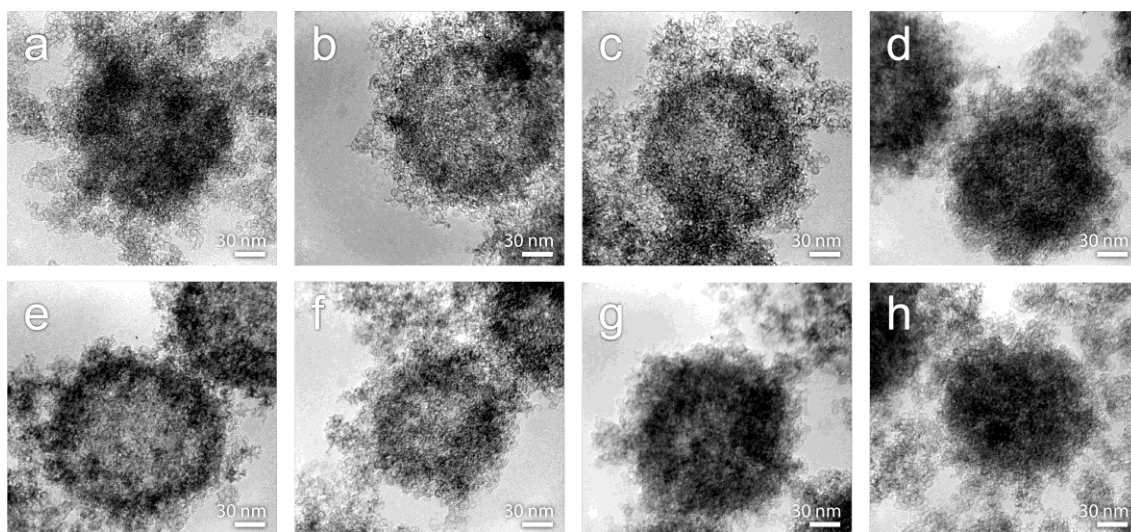


Figure 6.4 Representative TEM images of spherically assembled nanobubbles of manganese silicate doped with rare earth elements: (a) Y, (b) La, (c) Ce, (d) Nd, (e) Eu, (f) Gd, (g) Er, and (h) Yb. The nominal experimental ratio between manganese and dopant is 20:1.

However, plate-like structures were observed when the experimental ratio of manganese to dopant was decreased to 10:1, as shown in Figure 6.5. This observation indicates a maximum amount of metal dopant that the final doped nanobubbles can accommodate. When exceeding this threshold limit, heterogeneous growth of a secondary phase would become operative, which will be further discussed in later subsections.

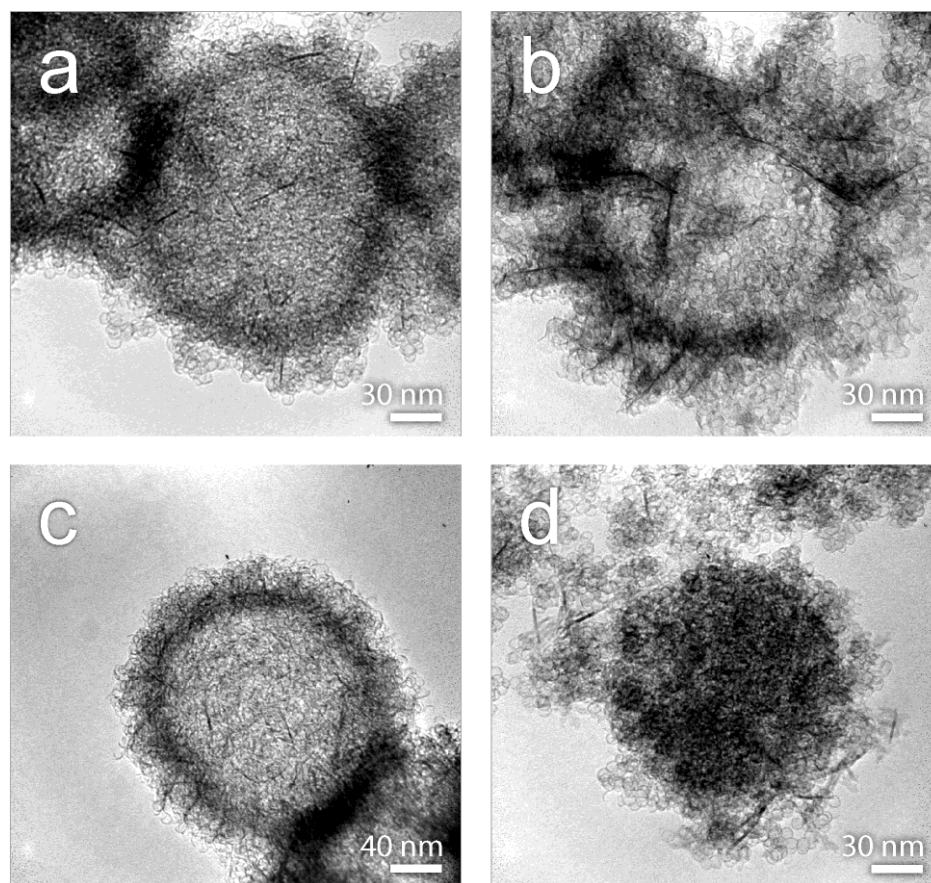


Figure 6.5 Representative TEM images of manganese silicate doped with other elements: (a) Fe, (b) Co, (c) Ni, and (d) La. The experimental ratio between manganese and dopant is 10:1.

In addition to the TEM characterization, EDX elemental composition analysis and structural mapping of these doped-derivatives confirmed the presences of doped elements of Fe, Co, Ni, Cu, Y, La, Ce, Nd, Eu, Gd, Er, and Yb as reported in Appendix 4-1A. With the exception of La, this investigation revealed that the actual manganese to dopant ratio was greater than the nominal experimental value (Appendix 4-1A). This ratio suggests that the formation of metal-doped manganese silicate nanobubbles might involve ionic exchange or substitution between Mn and the metal dopant during the synthesis. In Figures 6.6 and 6.7, X-ray diffraction patterns for both transition

metal and rare earth doped nanobubbles are very similar to that of the manganese silicate nanobubbles (Figure 6.2a) except for the case of Ce, which forms CeO_2 phase.

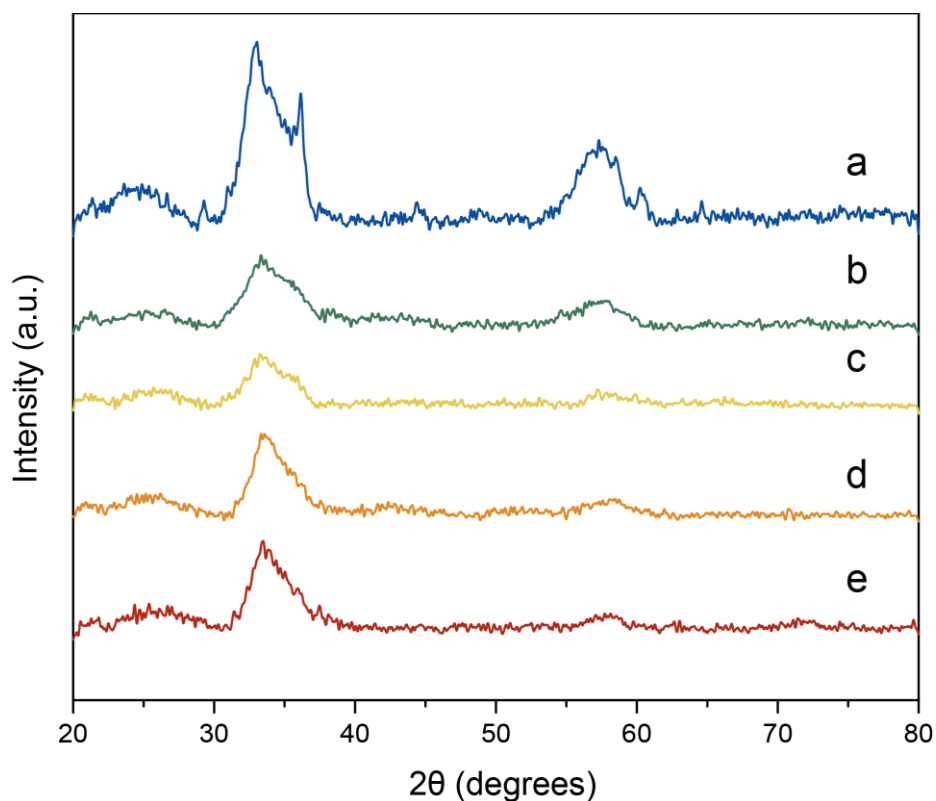


Figure 6.6 X-ray diffraction patterns of transition metal doped manganese silicate: (a) undoped, (b) Fe, (c) Co, (d) Ni and (e) Cu. The experimental manganese to dopant ratio is 20:1.

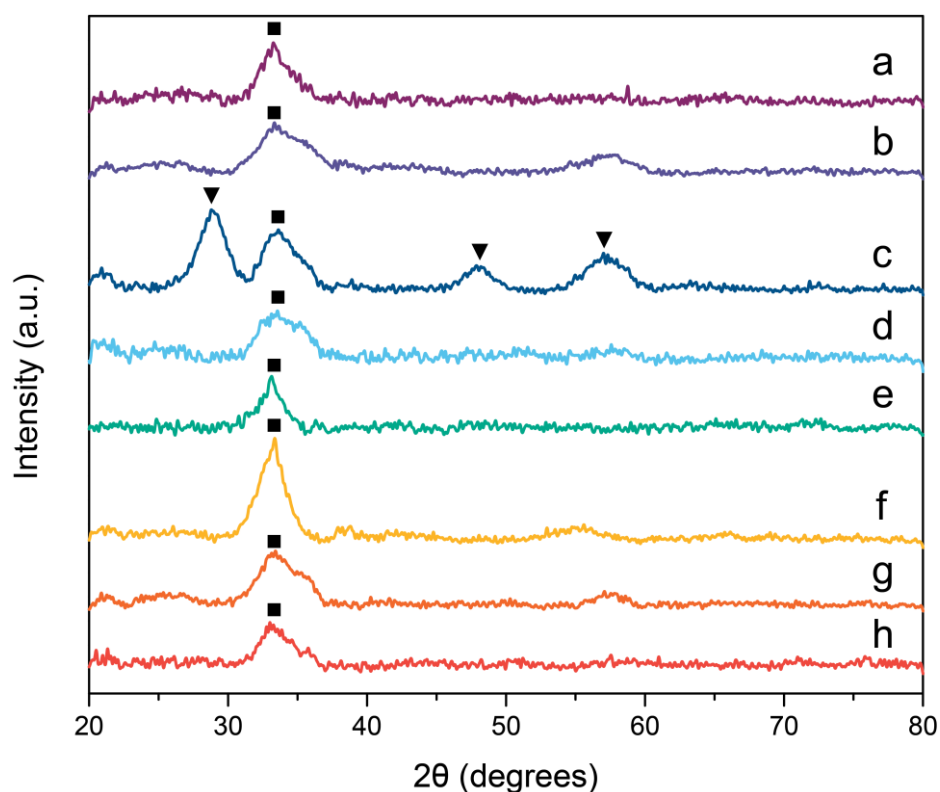


Figure 6.7 X-ray diffraction patterns of rare earth doped manganese silicate: (a) Y, (b) La, (c) Ce, (d) Nd, (e) Eu, (f) Gd, (g) Er, and (h) Yb. (■ = Braunitz 1Q, and ▼ = CeO₂) The experimental manganese to dopant ratio is 20:1.

In addition to the above finding on the similarity, three observations were made in the XRD results. First, the hausmannite Mn₃O₄ peak was observed to be lower than that in the manganese silicate nanobubbles (Figure 6.2a). Second, with the exception of Ce, no peaks were observed for oxides and silicates variants of the doped metals. Moreover, third, diffraction peak for braunitz 1Q was observed to shift at higher 2-theta angles for doped manganese silicates. These results may suggest that doping cations do not disrupt the original manganese silicate structure since no additional diffraction peaks for other compounds were observed for most cases. As demonstrated in Figures 6.3 and 6.4, a large variety of dopants, both divalent and trivalent metal ions, can be included into the nanobubbles of manganese silicate without altering their

structural configuration. Thus, the synthetic approach also allows sophisticated compositional tailoring for product nanobubbles when there is a need (Appendix 4-1A).

6.3.3 Synthetic Mechanism of Manganese Silicate Nanobubbles

The formation mechanism of manganese silicate nanobubbles was investigated through several designed experiments. These tests include determining the pH value of synthesis system before and after reaction, the presence of RCO_2^- vibration peaks in manganese silicate nanobubbles, the effect of different carboxylate anions, and different metal acetates on the final manganese silicate morphology, the effect of manganese and other metal ions on the SiO_2 spheres without carboxylate anions, and finally, the effect of various synthetic parameters such as temperature, reaction time, pH, and amount of precursor used in synthesis. Based on these experiments, we validated that *in-situ* CO_2 evolution occurred during the synthesis. Several experimental findings evidenced the formation of evolving gas in the following.

The solution pH decreased from 8 to 5 after the hydrothermal process, indicating that CO_2 and H_2CO_3 were formed (equations 1 to 5). In Figure 8, IR vibrational spectrum of nanobubbles of manganese silicate did not display RCO_2^- vibrational modes while those peaks were observed at 1551 and 1400 cm^{-1} for samples processed at room temperature (Appendix 4-2A)¹⁹. This result may indicate that acetate anions decompose under hydrothermal conditions. On the other hand, for the starting SiO_2 beads, vibration peaks at 3626 , 3438 , 3171 , 1637 , 1215 , 1095 , 794 , and 461 cm^{-1} can be attributed to the presence of water-species and silica^{20,21}.

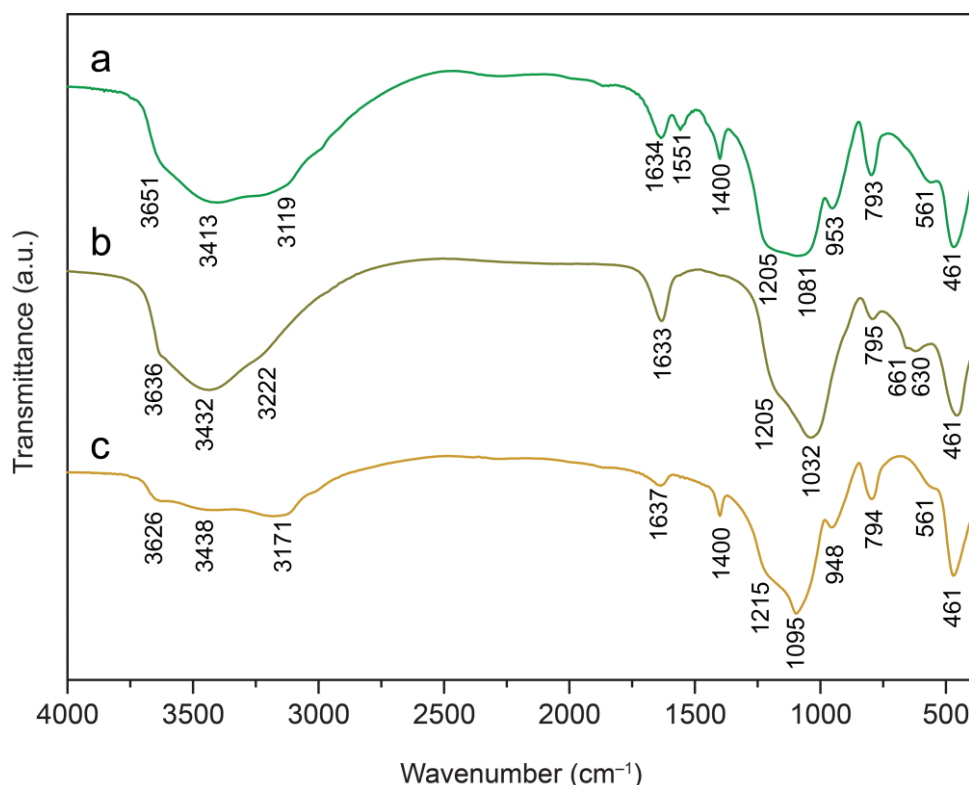


Figure 6.8 Comparison of FTIR spectra of different samples: (a) sample processed at room temperature for 12 h (Appendix 4-2A), (b) nanobubbles of manganese silicate synthesized at 180°C for 12 h (Appendix 4-2A), and (c) SiO₂ precursor beads (Figure 6.1a).

In addition to acetate, nanobubbles of manganese silicate can also be produced when other carboxylate anions were used, confirming the indispensability of these anions in synthesis, as shown in Figure 6.9 (and Appendix 4-2B).

In Figure 6.2b and 6.2c, XRD patterns for the samples synthesized with manganese maleate and citrate revealed that only pure braunite 1Q phase was formed in these two samples compared with that using acetate anions (Figure 6.2a; hausmannite Mn₃O₄ was included in this sample). The observed changes can be attributed to different chelating abilities of ligands with manganese ions. The stability of coordination bonds for multidentate maleate and citrate on manganese ions is greater than that for

monodentate acetate (Appendix 4-2C)^{22,23}. In this regard, due to its lower stability, a small portion

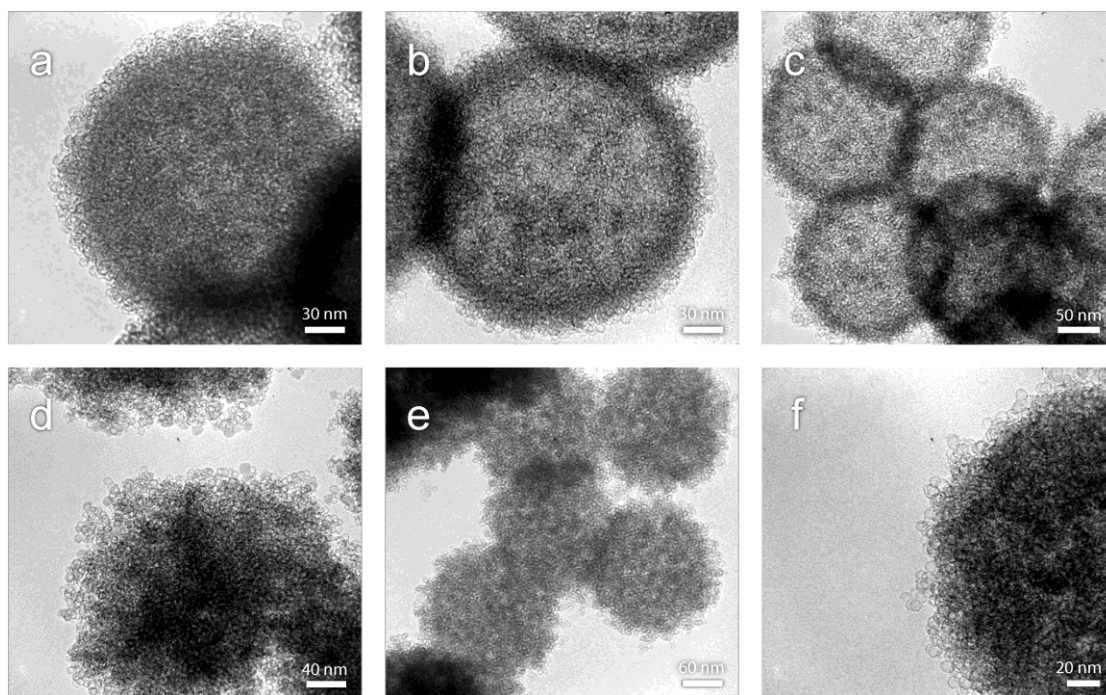


Figure 6.9 Spherically assembled nanobubbles of manganese silicate prepared with different carboxylate ions. All reaction solutions were heated under hydrothermal conditions at 180°C for 12 h with 50 mg of SiO₂ precursor beads, 0.80 mmol of MnSO₄, and 1.6 mmol of sodium acetate (a), 1.6 mmol of disodium maleate (b), 1.60 mmol of sodium tartrate (c), 1.6 mmol of sodium citrate (d), and 0.30 mmol of sodium citrate (e-f).

of manganese acetate was converted straightly to the Mn₃O₄ spinel even before reacting with H₄SiO₄ (and possibly other silicate oligomers which were produced from condensation of H₄SiO₄; equations 5 and 6). In comparison, the chance of the latter two manganese carboxylates to react with H₄SiO₄ would be higher because of their slower decomposition rates. In addition to the phase control, the type of carboxylate groups used in the synthesis also determines the interior space of the final aggregation of nanobubbles of manganese silicate. Illustrated in Scheme 6.1, the resultant shell thickness of spherical assemblages of nanobubbles is thinner if one uses acetate, maleate or tartrate anions (Figure 6.9a–c). On the other hand, the central space

can be wiped off when citrate anions are used in the synthesis. This significant difference in bubble assemblage can be attributed to tridentate capacity of citrate. For example, the multiple chelating abilities of citrate ligand not only forms manganese-citrate complexes, but also brings these complexes onto the surface of silica beads. This extra binding of citrate anion may provide capping effect on silica that prevents the silica core from rapid dissolution (Scheme 6.1). Thus, more nanobubbles of manganese silicate are formed inwardly, and less central interior is left for the assemblages using the Mn-citrate precursor (Figure 6.9d–f). Identical to those in Figure 6.1, in all these cases, nanobubbles of manganese silicate can also be obtained at a 100% morphological yield. An analysis for the size variation between initial silica and products also supports the above postulation (Appendix 4-2B).

During the preparation of doped manganese silicate, when the experimental ratio of manganese-to-dopant reached 10:1, other product morphologies were observed (Figure 6.5) in addition to the nanobubbles. In fact, when this ratio was continuously decreased, the product morphology could be entirely different. Using Stöber silica beads and other transition metal salts, our further syntheses yielded hollow spheres for other transition-metal or rare earth metal silicates under similar reaction conditions. Instead of the nanobubbles, however, the shells of the resultant hollow spheres were composed of nanometer-sized thin platelets for the syntheses with transition metal elements Fe, Co, and Ni while polycrystalline hollow spheres were found for the cases with rare earth elements La and Ce, as reported in Figure 6.10. Not unexpectedly, these results are consistent with previous reports on the hollow metal-silicate structures (Appendix 4-2D)²⁴⁻²⁶. In addition to this experiment, we have studied the effect of excluding carboxylate anion in synthesis by using metal sulfate precursors.

As shown in Figure 6.11, both CoSO_4 and NiSO_4 yielded flexible platelets while MnSO_4 formed nanoparticles

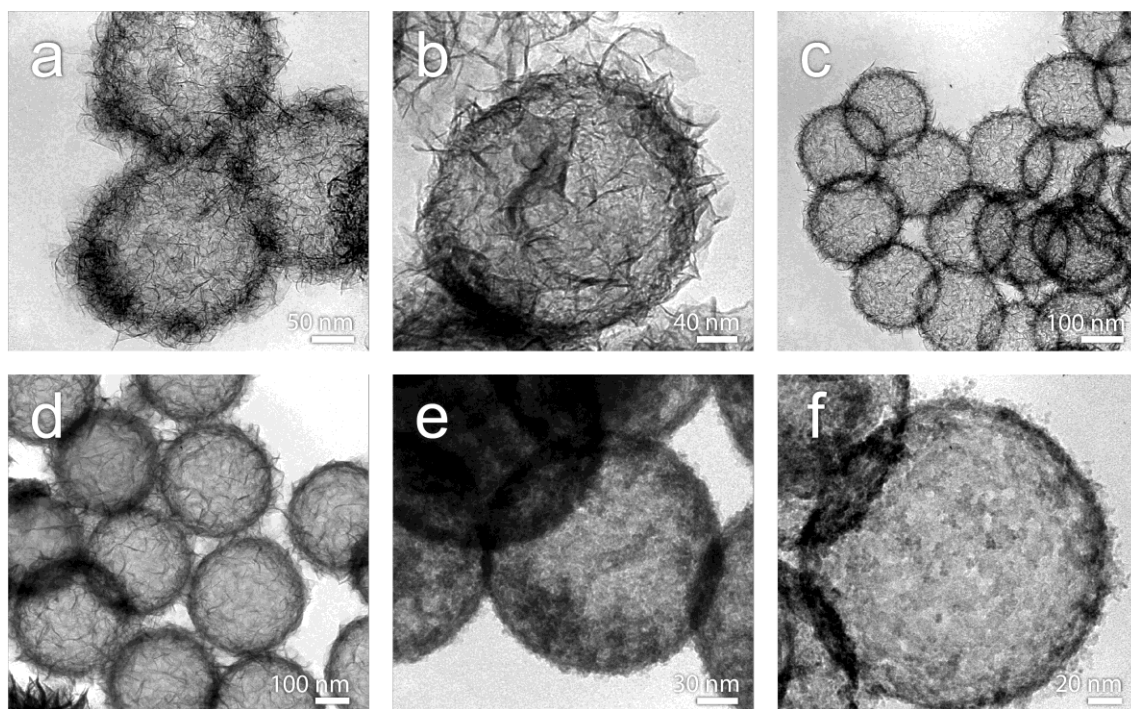


Figure 6.10 Hollow spheres of metal silicates synthesized using 50 mg of SiO_2 spheres, 5 mmol of NaCH_3COO , and 20 mL of H_2O under hydrothermal conditions (180°C) with: (a) 0.80 mmol of FeSO_4 , (b) 0.10 mmol of CoSO_4 , (c) 0.20 mmol of NiSO_4 , (d) 0.125 mmol of $\text{Mn}(\text{CH}_3\text{COO})_2$ and 0.125 mmol of $\text{Ni}(\text{CH}_3\text{COO})_2$ (without using NaCH_3COO in this case), (e) 0.80 mmol of $\text{La}(\text{NO}_3)_3$, and (f) 0.2 mmol of $\text{Ce}(\text{CH}_3\text{COO})_3$.

on the surface of SiO_2 and FeSO_4 produced nanocrystals. Based on these results, we believe that only Mn^{2+} has a catalytic activity towards the decomposition of carboxylate anion, because the same structures were obtained for Co and Ni silicates with or without carboxylate anions (see Figures 6.9 and 6.10). In this regard, the formation of plate-like structures for both Co and Ni silicates can only be ascribed to the template effect of SiO_2 spheres. The unique catalytic activity of Mn^{2+} may be attributed to two factors, namely, strength of carboxylate-to-metal coordination bond and possible formation of manganese oxide during the reaction process. As described

by Irving and Williams, the stability of high-spin complexes of the first-row transition metals follow this series:

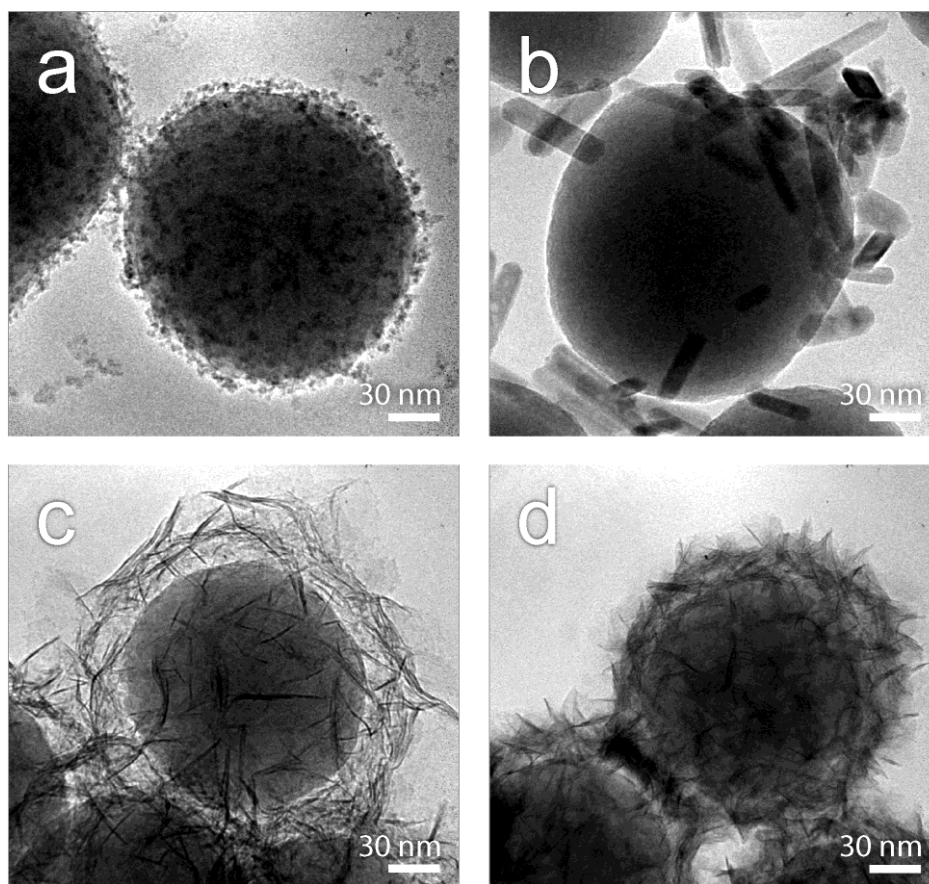


Figure 6.11 Hydrothermal treatment of SiO_2 with different metal sulfate salts: (a) MnSO_4 , (b) FeSO_4 , (c) CoSO_4 and (d) NiSO_4 . Experimental conditions: 0.8 mmol of metal sulfate mixed with 50 mg of SiO_2 beads in 20 mL of H_2O , then heated at 180°C for 12 h.

$\text{Mn}^{2+} < \text{Fe}^{2+} < \text{Co}^{2+} < \text{Ni}^{2+} < \text{Cu}^{2+} > \text{Zn}^{2+}$ ²⁷. Since divalent manganese is the least stable in this series, the decomposition of Mn-acetate or with other carboxylate groups to nanostructured gas (CO_2) bubbles is relatively easy. On the other hand, Fe, Co, and Ni complexes share similar stability constants (Appendix 4-2C) that result in the formation of similar hollow structures (Figure 6.10a to 6.10c) in the presence of carboxylate anion. This explanation is supported by the presence of carboxylate RCO_2^- vibration modes ($1547\text{--}1558\text{ cm}^{-1}$ and $1410\text{--}1428\text{ cm}^{-1}$; Appendix 4-2D) ¹⁹ on

the hollow spheres of Fe, Co, and Ni silicates because of slower decomposition reactions.

In addition, literature data on the thermal decomposition of acetate salts of Mn, Co, Ni, and Cu follow a similar trend, which also extends on malonate salts²⁸⁻³³. On the other hand, adsorbed carboxylate groups were also found in La and Ce silicates (Figure 6.10e,f). For this reason, easy decomposition of Mn-carboxylate implicates the readiness of the aggregative gas template and thus the deposition of the nanobubbles of manganese silicate. Although the proposed synthetic mechanism is supported by our experiments, it should be pointed out that direct observation on *in situ* formation of the manganese silicate nanobubbles is difficult to make at this stage of research because of the required hydrothermal conditions.

As mentioned earlier, the catalytic activity of Mn^{2+} towards carboxylate decomposition may also be attributed to the formation of manganese oxides under the hydrothermal conditions. Manganese oxides of different valence have been reported to function as an effective catalyst towards oxidation reaction. Therefore, the formation of CO_2 gas bubbles from carboxylate oxidation is possible³⁴⁻³⁷. In our present study, the formation of manganese oxides was also confirmed by hydrothermal treatment of $\text{Mn}(\text{CH}_3\text{COO})_2$ salt in the absence of SiO_2 spheres (Appendix 4-2E). These polydispersed crystallites were determined to be a mixture of MnO , Mn_3O_4 , $\text{MnO}(\text{OH})$, $\text{Mn}_{2.03}\text{O}_4$, and MnO_2 and other manganese oxide phases through XRD (Appendix 4-2E). This experiment confirms that manganese oxides can be formed under hydrothermal conditions and therefore the resultant manganese oxides can also catalyze the oxidation of carboxylate anions.

Apart from the reaction temperature (Appendix 4-2A), other synthetic parameters such as reaction temperature, pressure, time, pH value and precursor type and amount have also been investigated and optimized (Appendix 4-2F to Appendix 4-2J). In general, high reaction temperature and prolonged reaction time favor the formation of nanobubbles, and hydrothermal condition is essential since it may prevent the *in situ* formed gas-bubbles from escaping to the gas phase. We also found that acidic starting solution (pH < 4.8) is not in favor of nanobubbles on the surface of silica owing to the difficulty of forming carboxylate anions and therefore the resultant Mn-carboxylate complexes. Furthermore, nanobubbles were also observed for the reaction of MnSO_4 and Na_2CO_3 ; while hollow micro spheres were only observed for phosphate at alkaline conditions (Appendix 4-2J). These results support the observation that gas-forming species are required to generate nanobubbles. All the observations are consistent with the synthetic path proposed in Scheme 6.1.

Although CO_2 gas bubbles formed at the surface SiO_2 template are both thermodynamically and kinetically dynamic, other chemical constituents (*e.g.*, Mn^{2+} , RCO_2^- and *etc.*) are also present in solution. These solution species would accumulate and solidify on the gas/liquid interface of the CO_2 gas bubble thus lowering its surface tension and preventing its detachment from the SiO_2 substrate.^[38,39] In addition to this explanation, we also observed that the surface of partially hydrolyzed SiO_2 spheres is rather rough, exhibiting surface grooves with various sizes. Thus, the rough SiO_2 substrate may also help to entrap CO_2 gas bubbles formed during carboxylate decomposition.

6.3.4 Catalytic Applications of Manganese Silicate Nanobubbles

Due to the excellent catalytic activity of manganese based solid compounds and the unique morphology of these hollow structures, we chose to study their adsorption and catalytic properties towards the degradation of cationic organic dyes, *e.g.*, rhodamine-6G and methylene blue, *via* advanced oxidation process (AOP)^{40,41}. In this study, reported in Figure 6.12 (also Appendix 4-3A), the nanobubbles of manganese silicate and the dye solution were allowed to establish adsorption equilibrium for a period of 60 min. After establishing equilibrium, 20 and 30% of the initial rhodamine 6G and methylene blue molecules were adsorbed on the nanobubbles of manganese silicate, respectively. Upon the addition of oxidant H₂O₂, the concentration of methylene blue (100 mg/L) decreased to *ca* 18% of its initial value after 5 min and the reaction finished just in a total of 15 min (Figure 6.12). Similarly, the concentration of rhodamine 6G decreased to 18% of its initial value after 10 min and the reaction completed within 30 min (Figure 6.12). Our further experiments showed that the manganese silicate nanobubbles can catalyze the degradation of methylene blue at an even higher concentration (500 mg/L, Figure 6.12). In contrast to methylene blue and rhodamine 6G, which are cationic dyes, both adsorption and catalytic activity of these manganese silicate nanobubbles towards degradation and/or decomposition of anionic dyes were poor. As an example of this type of organic dyes, in Figure 6.11, we also showed the adsorption-degradation process of methyl orange (an anionic organic dye).

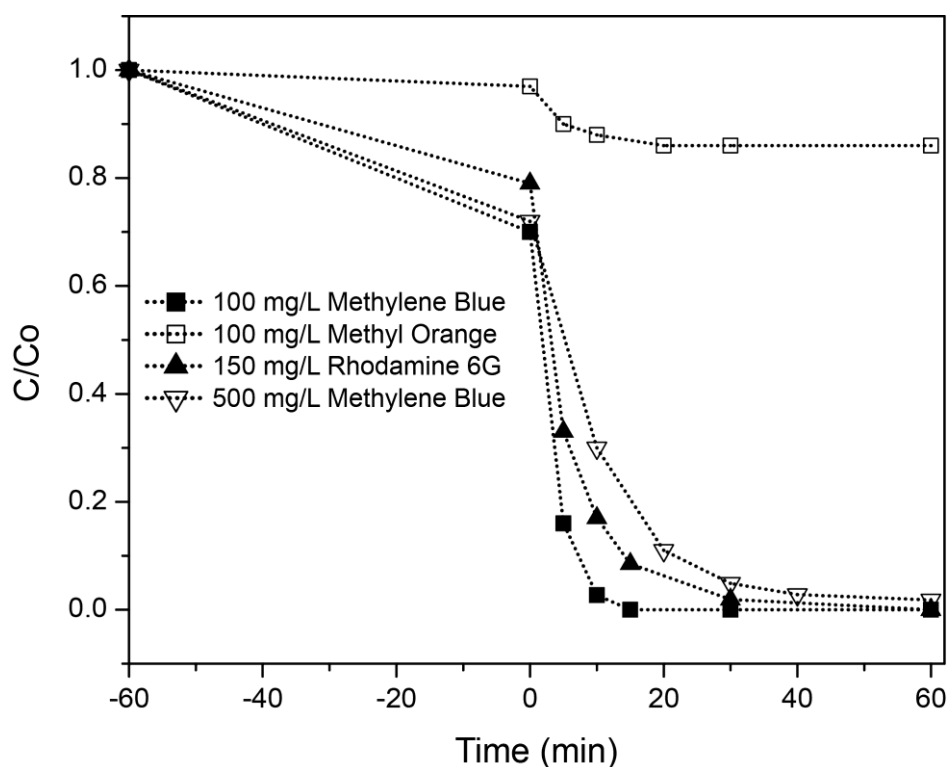


Figure 6.12 Relative concentration (C/C_0) profiles of methylene blue, rhodamine 6G, and methyl orange during adsorption (–60 to 0 min) and catalytic decomposition (0 to 60 min) processes at 60°C. 20 mg of nanobubbles of manganese silicate and 100 mL of a dye solution were used in each experiment. C is process concentration, and C_0 is starting concentration; the oxidant H_2O_2 was added at 0 min.

These results revealed that the surface charge of the manganese silicate nanobubbles is negative as evidenced by the presence of Si–OH species (Figure 6.8). In this regard, the nanobubbles of manganese silicate can also be used to perform selective treatment of organic dyes since they can preferably adsorb and catalyze the degradation of cationic organic dyes.

In order to exploit other applications, we also investigated the exchangeability of metal ions for the prepared hollow structures. When the self-assembled nanobubbles of manganese silicate were used as a template for lithium intercalation, polycrystalline hollow spheres of Li_2SiO_3 and $LiMn_2O_4$ were observed (Appendix 4-3B). In view of

their tailorable composition and unique morphology, such hollow structures may find their applications as cathode materials for secondary Li-ion batteries⁴²⁻⁴⁴. Therefore, the nanobubbles of manganese silicate (Figures 6.1 and 6.9) and their metal-doped derivatives (Figures 6.3 and 6.4), including other spherical hollow structures of transition-metal silicates synthesized in this work (Figure 6.10), can be used as solid precursors for the preparation of other functional materials.

In addition to this application, Gd-doped manganese silicate nanobubbles are magnetically responsive since its aqueous suspension can be separated by exposing it in a magnetic field (Appendix 4-3C). This result is consistent with our previous work; wherein Gd-based colloidal coordination polymer spheres exhibited magnetic property.^[45]

6.4 Conclusion

In summary, hierarchical hollow assemblages (~200 to 270 nm) comprised of smaller nanobubbles (< 10 nm) of manganese silicate and their metal-doped derivatives can be prepared under hydrothermal conditions using a surface-catalyzed dual templating approach. In this process, adsorption and decomposition of Mn-carboxylates are important in gas bubble generation since these processes dictate the product morphology. In addition, Mn²⁺ also serve as a catalyst towards the decomposition of carboxylate anions while a strong metal to silica interaction was observed for other transition metal, which can be described as a templating effect. The nanobubbles of manganese silicate obtained can work as an effective heterogeneous catalyst and serve as a versatile solid precursor for transformative synthesis of other functional hollow materials.

Reference

- (1) Shen, Y. F.; Zerger, R. P.; Deguzman, R. N.; Suib, S. L.; Mccurdy, L.; Potter, D. I.; Oyoung, C. L. Manganese Oxide Octahedral Molecular Sieves: Preparation, Characterization, and Applications. *Science* **1993**, *260*, 511–515.
- (2) Tusar, N. N.; Jank, S.; Glaser, R. Manganese-Containing Porous Silicates: Synthesis, Structural Properties and Catalytic Applications. *ChemCatChem* **2011**, *3*, 254–269.
- (3) Hage, R.; Iburg, J. E.; Kerschner, J.; Koek, J. H.; Lempers, E. L. M.; Martens, R. J.; Racherla, U. S.; Russell, S. W.; Swarthoff, T.; Vavliet, M. R. P.; *et al.* Efficient Manganese Catalysts for Low-Temperature Bleaching. *Nature* **1994**, *369*, 637 – 639.
- (4) Yano, J.; Kern, J.; Sauer, K.; Latimer, M. J.; Pushkar, Y.; Biesiadka, J.; Loll, B.; Saenger, W.; Messinger, J.; Zouni, A.; *et al.* Where Water is Oxidized to Dioxygen: Structure of the Photosynthetic Mn₄Ca Cluster. *Science* **2006**, *314*, 821–825.
- (5) Du, H.; Jiao, L.; Wang, Q.; Yang, J.; Guo, L.; Si, Y.; Wang, Y.; Yuan, H. Facile Carbonaceous Microsphere Templated Synthesis of Co₃O₄ Hollow Spheres and Their Electrochemical Performance in Supercapacitors. *Nano Res.* **2012**, *6*, 87–98.
- (6) Sun, Z.; Liao, T.; Liu, K.; Jiang, L.; Kim, J. H.; Dou, S. X. Robust Superhydrophobicity of Hierarchical ZnO Hollow Microspheres Fabricated by Two-Step Self-Assembly. *Nano Res.* **2013**, *6*, 726–735.
- (7) Wang, Z.; Zhou, L.; David Lou, X. W. Metal Oxide Hollow Nanostructures for Lithium-Ion Batteries. *Adv. Mater.* **2012**, *24*, 1903–1911.
- (8) Peng, Q.; Dong, Y.; Li, Y. ZnSe Semiconductor Hollow Microspheres. *Angew. Chem. Int. Ed.* **2003**, *42*, 3027–3030.
- (9) Palmer, D.A.; Drummond, S.E. Thermal Decarboxylation of Acetate. Part I. The Kinetics and Mechanism of Reaction in Aqueous Solution. *Geochim. Cosmochim. Acta* **1986**, *50*, 813–823.
- (10) McCollom, T. M.; Seewald, J. S. Experimental Study of the Hydrothermal Reactivity of Organic Acids and Acid Anions: II. Acetic Acid, Acetate, and Valeric Acid. *Geochim. Cosmochim. Acta* **2003**, *67*, 3645–3664.
- (11) Onwudili, J. A.; Williams, P. T. Hydrothermal Reactions of Sodium Formate and Sodium Acetate as Model Intermediate Products of the Sodium Hydroxide-

- Promoted Hydrothermal Gasification of Biomass. *Green Chem.* **2010**, *12*, 2214–2224.
- (12) Gu, F.; Li, C. Z.; Wang, S. F.; Lü, M. K. Solution-Phase Synthesis of Spherical Zinc Sulfide Nanostructures. *Langmuir* **2006**, *22*, 1329–1332.
- (13) Wu, C. Z.; Xie, Y.; Lei, L. Y.; Hu, S. Q.; OuYang, C. Z. Synthesis of New-Phased VOOH Hollow “Dandelions” and Their Application in Lithium-Ion Batteries. *Adv. Mater.* **2006**, *18*, 1727–1732.
- (14) Wu, Z. C.; Yu, K.; Zhang, S. D.; Xie, Y. Hematite Hollow Spheres with a Mesoporous Shell: Controlled Synthesis and Applications in Gas Sensor and Lithium Ion Batteries. *J. Phys. Chem. C* **2008**, *112*, 11307–11313.
- (15) Wan, J.; Stone, H. A. Coated Gas Bubbles for the Continuous Synthesis of Hollow Inorganic Particles. *Langmuir* **2011**, *28*, 37–41.
- (16) Yao, K. X.; Zeng, H. C. Simultaneous Chemical Modification and Structural Transformation of Stöber Silica Spheres for Integration of Nanocatalysts. *Chem. Mater.* **2012**, *24*, 140–148.
- (17) Stöber, W.; Fink, A.; Bohn, E. Controlled Growth of Monodisperse Silica Spheres in the Micron Size Range. *J. Colloid Interface Sci.* **1968**, *26*, 62–69.
- (18) Deer, W. A.; Howie, R. A.; Zussman, J. *Rock-Forming Minerals, Orthosilicates*; 2nd Edition Vol. 1A; The Geological Society, 1982; pp 348
- (19) Ito, K.; Bernstein, H. J. The Vibrational Spectra of the Formate, Acetate, and Oxalate Ions. *Can. J. Chem.* **1956**, *34*, 170–178
- (20) Galeener, F. L.; Lucovsky, G. Longitudinal Optical Vibrations in Glasses: GeO₂ and SiO₂. *Phys. Rev. Lett.* **1976**, *37*, 1474–1478.
- (21) Wakabayashi, H.; Tomozawa, M. Diffusion of Water into Silica Glass at Low Temperature. *J. Am. Ceram. Soc.* **1989**, *72*, 1850–1855.
- (22) Schwarzenbach, G. Der Chelateffekt. *Helv. Chim. Acta* **1952**, *35*, 2344–2359.
- (23) Hancock, R. D.; Martell, A. E. The Chelate, Cryptate and Macrocyclic Effects. *Comments Inorg. Chem.* **1988**, *6*, 237–284.
- (24) Wang, J.; Xu, C. H.; Yao, M.; Chen, J.; Xu, G. J. A Facile Route to Prepare Hierarchical Magnetic Cobalt–Silica Hollow Nanospheres with Tunable Shell Thickness. *J. Nanopart. Res.* **2009**, *12*, 1161–1166.

- (25) Fang, Q.; Xuan, S.; Jiang, W.; Gong, X. Yolk-like Micro/Nanoparticles with Superparamagnetic Iron Oxide Cores and Hierarchical Nickel Silicate Shells. *Adv. Funct. Mater.* **2011**, *21*, 1902–1909.
- (26) Wang, Y.; Tang, C.; Deng, Q.; Liang, C.; Ng, D. H. L.; Kwong, F.; Wang, H.; Cai, W.; Zhang, L.; Wang, G. A Versatile Method for Controlled Synthesis of Porous Hollow Spheres. *Langmuir* **2010**, *26*, 14830–14834.
- (27) Irving, H.; Williams, R. J. P. The Stability of Transition-Metal Complexes. *J. Chem. Soc.* **1953**, 3192–3210.
- (28) Mohamed, M. A.; Halawy, S. A. Kinetic and Mechanistic Study of the Non-isothermal Decomposition of Manganese(II) Acetate Tetrahydrate. *Thermochim. Acta* **1994**, *242*, 173–186.
- (29) Mohamed, M. A.; Halawy, S. A.; Ebrahim, M. M. The Non-isothermal Decomposition of Cobalt Acetate Tetrahydrate. *J. Therm. Anal.* **1994**, *41*, 387–404.
- (30) Mohamed, M. A.; Halawy, S. A.; Ebrahim, M. M. Non-Isothermal Tetrahydrate Decomposition of Nickel Acetate Tetrahydrate. *J. Anal. Appl. Pyrolysis* **1993**, *27*, 109–118.
- (31) Mohamed, M. A. Non-isothermal Dehydration and Decomposition of Manganese(II) Malonate Dihydrate. *J. Anal. Appl. Pyrolysis* **1994**, *30*, 59–72.
- (32) Mohamed, M. A.; Galwey, A. K.; Halawy, S. A. Kinetic and Thermodynamic Study of the Non-isothermal Decompositions of Cobalt Malonate Dihydrate and of Cobalt Hydrogen Malonate Dihydrate. *Thermochim. Acta* **2000**, *346*, 91–103.
- (33) Mohamed, M. A.; Galwey, A. K.; Halawy, S. A. Kinetic and Thermodynamic Studies of the Non-isothermal Decompositions of Nickel Malonate Dihydrate and Nickel Hydrogen Malonate Dihydrate. *Thermochim. Acta* **1998**, *323*, 27–36.
- (34) Gandhe, A. R.; Rebello, J. S.; Figueiredo, J. L.; Fernandes, J. B. Manganese Oxide OMS-2 as an Effective Catalyst for Total Oxidation of Ethyl Acetate. *Appl. Catal., B* **2007**, *72*, 129–135.
- (35) Dharmarathna, S.; King'ondo, C. K.; Pedrick, W.; Pahalagedara, L.; Suib, S. L. Direct Sonochemical Synthesis of Manganese Octahedral Molecular Sieve (OMS-2) Nanomaterials Using Cosolvent Systems, Their Characterization, and Catalytic Applications. *Chem. Mater.* **2012**, *24*, 705–712.

- (36) Son, Y. C.; Makwana, V. D.; Howell, A. R.; Suib, S. L. Efficient, Catalytic, Aerobic Oxidation of Alcohols with Octahedral Molecular Sieves. *Angew. Chemie Int. Ed.* **2001**, *40*, 4280–4283.
- (37) Jiao, F.; Frei, H. Nanostructured Manganese Oxide Clusters Supported on Mesoporous Silica as Efficient Oxygen-evolving Catalysts. *Chem. Commun.* **2010**, *46*, 2920–2922.
- (38) Ducker, W. A. Contact Angle and Stability of Interfacial Nanobubbles. *Langmuir* **2009**, *25*, 8907–8910.
- (39) Seddon, J. R. T.; Lohse, D.; Ducker, W. A.; Craig, V. S. J. A Deliberation on Nanobubbles at Surfaces and in Bulk. *Chemphyschem* **2012**, *13*, 2179–2187.
- (40) Tušar, N. N.; Maučec, D.; Rangus, M.; Arčon, I.; Mazaj, M.; Cotman, M.; Pintar, A.; Kaučič, V. Manganese Functionalized Silicate Nanoparticles as a Fenton-Type Catalyst for Water Purification by Advanced Oxidation Processes (AOP). *Adv. Funct. Mater.* **2012**, *22*, 820–826.
- (41) Park, J.; Jang, I.; Kwon, B.; Jang, S.; Oh, S. Formation of Manganese Oxide Shells on Silica Spheres with Various Crystal Structures Using Surfactants for the Degradation of Methylene Blue Dye. *Mater. Res. Bull.* **2013**, *48*, 469–475.
- (42) Lou, X. W.; Archer, L. A.; Yang, Z. C. Hollow Micro-/Nanostructures: Synthesis and Applications. *Adv. Mater.* **2008**, *20*, 3987–4019.
- (43) Rangappa, D.; Murukanahally, K. D.; Tomai, T.; Unemoto, A.; Honma, I. Ultrathin Nanosheets of Li_2MSiO_4 (M = Fe, Mn) as High-Capacity Li-Ion Battery Electrode. *Nano Lett.* **2012**, *12*, 1146–1151.
- (44) He, G.; Popov, G.; Nazar, L. F. Hydrothermal Synthesis and Electrochemical Properties of $\text{Li}_2\text{CoSiO}_4/\text{C}$ Nanospheres. *Chem. Mater.* **2013**, *25*, 1024–1031.
- (45) Li, C. C.; Zeng, H. C. Coordination Chemistry and Antisolvent Strategy to Rare-Earth Solid Solution Colloidal Spheres. *J. Am. Chem. Soc.* **2012**, *134*, 19084–19091.

Chapter 7. Conclusions and Recommendations

This dissertation examined template-based synthetic approach for hollow and core-shell hollow structures and their electrochemical, catalytic, and photocatalytic properties. The major findings in this work are stated in the following paragraphs.

7.1 Conclusions

Seed mediated synthesis coupled with sequential Ostwald ripening is a simple and effective synthetic approach for hollow Cu_2O multi-shelled core-shell structures, since this approach has successfully synthesized 20 Cu_2O homogeneous hollow core-shell structures with different centricity and eccentricity at room temperature. Moreover, this approach allows the control of the overall morphology, size and shell thickness of the product by simply varying the number of seed amount and reaction time. This approach offers an improvement in the size and morphology monodispersity since the probability of homogeneous nucleation occurring is low. Therefore size and structural monodispersity depends on the seed material. In addition to their preparation, the correlation between the number of Cu_2O shells and its optical and electrochemical property was investigated. It was observed that multi-shelled Cu_2O core-shell exhibits Mie scattering that results in a red-shift in its extinction peak. This finding has shown that the optical absorbance of a material can be tuned by increasing the number of material layer and by generating an interior cavity within these layers. In addition to its optical property, multi-shelled Cu_2O core-shell with thinner shell structure shows improved electrochemical sensitivity towards glucose molecule while non-hollow multi-shelled Cu_2O core-shell has lower glucose

sensitivity compared with hollow structures. This improvement is due to an increase in surface area of the material and an increase in the diffusion rate of glucose.

The reactivity and structural transformation of Cu_2O homogeneous core-shell structure with different reactivity gradient and its $\text{Zn}(\text{OH})_2$ passivated structure were examined under different types of reaction. These reactions include chemical reduction, electrochemical reduction, anion exchange and thermal treatment under different atmosphere. These transformations result in several interesting hollow/hollow core-shell structure such as Cu, Cu/ZnO, multilayered $\text{Cu}_2\text{O}/\text{ZnO}$, multilayered CuO hollow spheres, and Cu/ Cu_2O nanoparticle on ZnO hollow spheres (Cu NP-ZnO). For non-passivated structures, it was found that the structural transformation starts to occur at the polycrystalline shell before the single crystal core, which results in a hollow structure. Similarly, the structural transformation of $\text{Zn}(\text{OH})_2$ passivated structure is similar to non-passivated structures at lower reactant concentration. However, the sequence of transformation is different when the reactant concentration was increased. In this case, a single crystal core immediately reacted before the polycrystalline shell, which results in an asymmetric core-shell structure. These findings provide an understanding on how a homogeneous core-shell material transform, which may be useful in designing engineered hollow materials.

In addition to investigating the reactivity of the homogeneous core-shell material, the photocatalytic activity towards methyl orange degradation of Cu_2O core-shell, $\text{Cu}_2\text{O}/\text{ZnO}$ core-shell, and Cu NP-ZnO. It was found that Cu NP-ZnO performed better than the other materials. This is due to the ease of access of photogenerated holes, which produce hydroxyl radical ion, in Cu NP-ZnO. This result demonstrates a strong correlation of structural feature and functional property.

In the same way as Cu₂O multi-shelled structure, seed-mediated coupled with Ostwald ripening is also applicable for hollow metal core and oxide shelled structure. These structures include M@Cu₂O, M@Cu₂O@Zn(OH)₂ and M@Cu₂O@ZnO (M = Au, Ag, AuAg, and Pd) core-/yolk-shell. The amount of metal core within the multi-shelled structure is determined by the aggregative condition of metal seeds during the synthesis and these can be controlled by the amount of surfactant, ions, and metal seeds. In addition to their preparation, the reactivity and structural transformation of M@Cu₂O and M@Cu₂O@Zn(OH)₂ during chemical reduction and thermal treatment were also determined. Compared with Cu₂O CSPAR and Zn(OH)₂ encapsulated Cu₂O CSPAR, these structures exhibited different structural and chemical transformation which are influenced by the presence of metal core and excess surfactants. A catalytic effect was observed during the chemical reduction of M@Cu₂O core-shell, which can be observed as a twenty fold decreased in the prerequisite amount of NaBH₄ compared with Cu₂O CSPAR. On the other hand, the as-synthesized M@Cu₂O@Zn(OH)₂ are stable during chemical reduction due to the presence of excess PVP. M@Cu₂O structures also demonstrated catalytic activity towards 4-nitrophenol reduction. On the other hand, M@Cu₂O@ZnO core-shell structures were used to study the mechanism of methyl orange degradation. We found that photogenerated holes are primarily responsible for dye degradation based on comparison of the energy band structure of different M@Cu₂O@ZnO core-shell catalyst. The rate of methyl orange degradation occurred faster for catalysts with easily accessible photogenerated holes rather than electrons.

Hierarchical hollow assemblages (200 nm) composed of manganese silicate nanosphere (< 7 nm) and its transition metal and rare earth doped derivatives were

prepared for the first time using a surface catalyzed dual templating approach. The formation mechanism of this unique structure was investigated, and it was deduced that nano-sized CO₂ gas formed in-situ served as a soft-template for the nanosphere while SiO₂ served as the micro-template. In addition to its formation, other transition metals and rare earth metals can be doped into the bubbled structure to provide added functionality. Several applications of this material were investigated such as its catalytic activity towards advanced oxidation process and its transformative synthesis towards lithium intercalation. This unique structure exhibited excellent adsorption capacity and the catalytic degradation property towards cationic dye. Being the first of its kind, this material may serve as a starting point for another future work such as its applications in energy storage and catalysis.

7.2 Recommendations for Future Work

1. It should be noted that the yield of Cu₂O multishelled structures is less than 5 mg. To address this problem, future studies should develop a method to increase the yield of this material. It is also interesting to apply the seed-mediated and sequential Ostwald ripening approach to one-dimensional material like nanowires since these materials have larger surface area compared to its spherical form.
2. In Chapter 4, the preparation of Cu hollow sphere and Cu nanoparticles embedded on Zn(OH)₂ hollow sphere were described. Compared with conventional catalysts, these structures may possess an improvement in catalytic activity towards hydrogenation of syngas to CH₃OH and electrochemical reduction of aqueous carbonates and dissolved CO₂ to CH₄. This possible improvement in activity may be due to the large surface area that hollow structures possess.

3. Although the photocatalytic activities of Au@Cu₂O@ZnO and Pd@Cu₂O@ZnO towards methyl orange degradation are less compared with Cu₂O@ZnO and Cu NPs embedded on ZnO hollow sphere, the M@Cu₂O@ZnO configuration may be useful for reduction reactions. This suggestion can be rationalized by considering the M@Cu₂O@ZnO band structure configuration. For these configurations, both Au and Pd core allow better charge separation of the holes and electrons, wherein the electrons are isolated on the solution interface. This feature can be useful for studying photocatalytic reduction reactions.






































4. The assembly of manganese silicate hollow spheres into its submicron derivatives is a new type of microstructure. Therefore, more fundamental studies about the formation mechanism and practical implications of the assembled structure should be conducted. It should be noted that during the lithium intercalation process LiMn₂O₄ were generated. It would be interesting, if during the delithiation process, λ-MnO₂ phase could be generated since this structure is similar to the cubane Mn₄O₄, which is an important structure for the oxygen evolution reaction from water.

5. Due to its unique architecture and large surface area, the applicability of the assembled manganese silicate hollow spheres as a molecule or particle carrier could be further investigated. In particular, metal and oxide active sites can be embedded within the nanobubbles, which may result in an increase in active site density per particle. In addition, the nanobubbles can act as a cage for the metal and oxide catalyst that results in inhibition of further growth and coalescence. In the field of molecular storage, these nanobubbles may have slower molecular release compared with micro scaled hollow structure. As a result, this structure maybe find its application in delayed drug delivery release.


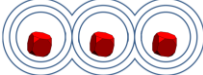


Appendix 1

Appendix 1-1A Structural Details of Major $(\text{Cu}_2\text{O}@)_n\text{Cu}_2\text{O}$ Products

Table A-1. Excess ascorbate and nitrate anions present in the reaction solution.

Type	Structure Description	Core/Yolk	Structure	Corresponding Figure on Chapter 3
A	Core, truncated cube	None		3.4a
B	Core-Shell			3.4b, 3.4a-d, 3.11a-c
C	Yolk-Shell			3.4c, 3.11d, 3.13a
D	Core-Shell			3.4d, 3.7a, 3.12a, 3.12b
E	Core-Shell			3.4f, 3.7c, 3.12c, 3.12d, 3.13b-d
F	Yolk-Shell			3.4e, 3.7b, Fig A-4-2a
G	Yolk-Shell			3.4g, 3.7d
H	Core-Shell			3.3a, 3.8a, 3.8b
I	Core-Shell			3.3c
J	Core-Shell			3.3e, 3.4h, 3.8c, 3.8d
K	Core-Shell			3.3g
L	Yolk-Shell			3.3b
M	Yolk-Shell			3.3d
N	Yolk-Shell			3.3f
O	Yolk-Shell			3.3h
P	Core-Shell			3.9c, 3.9d
Q	Core-Shell			3.4i, 3.9a, 3.9b
R	Bean pod			3.14a
S	Bean pod			3.14b

Appendix 1

Type	Structure Description	Core/Yolk	Structure	Corresponding Figure on Chapter 3
T	Bean pod			3.14c
U	Bean pod			3.14d

Appendix 1-1B Illustrative Experimental Details

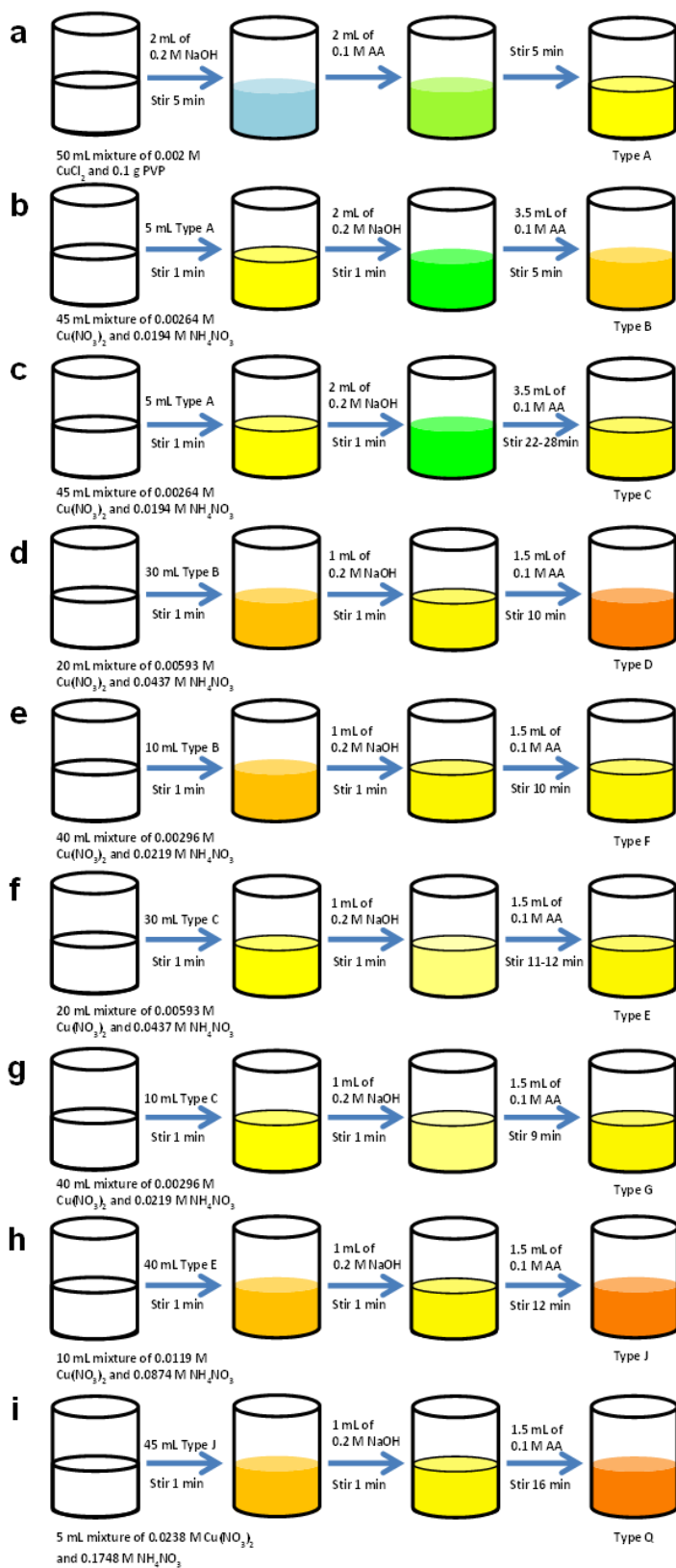
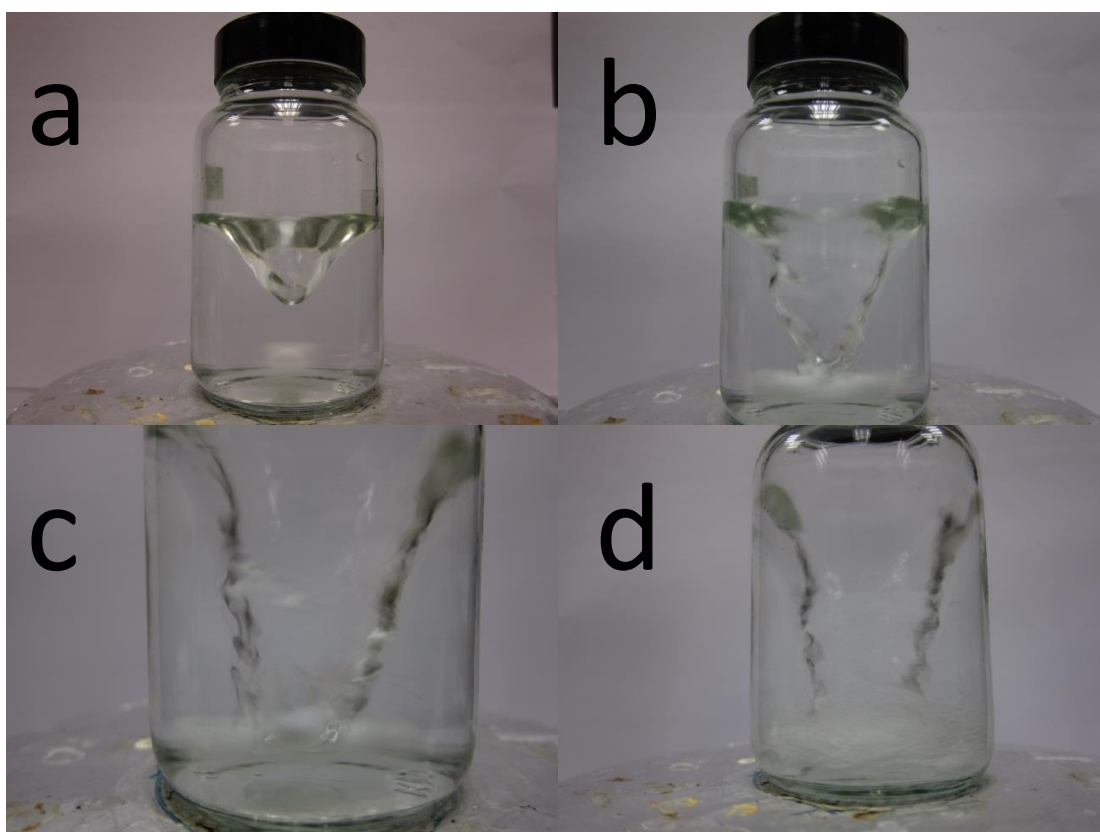


Table A-2. Excess ascorbate and nitrate anions present in the reaction solution.

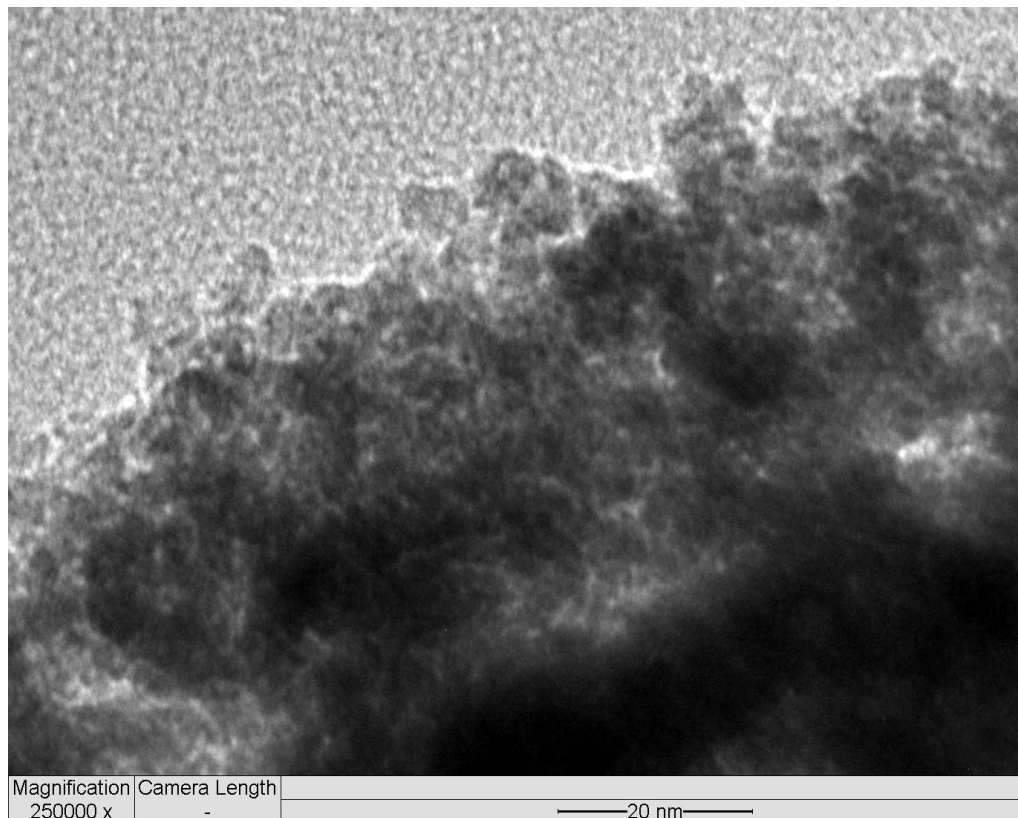
Structure and previous seed amount (mL)	Excess AA amount before reaction (mmol)	Excess AA concentration before reaction (M)	Total excess AA amount after reaction (mmol)	Total excess AA concentration after reaction (M)	Cumulative NO ₃ ⁻ amount (mmol)
Type A	-	-	0.10	1.8 × 10 ⁻³	0.87
Type B or C (5 mL)	0.0090	1.8 × 10 ⁻⁴	0.24	4.3 × 10 ⁻³	0.96
Double-Shell (10 mL)	0.0433	8.66 × 10 ⁻⁴	0.075	1.4 × 10 ⁻³	1.05
Triple-Shelled Bean Pod (25 mL)	0.0356	7.12 × 10 ⁻⁴	0.067	1.3 × 10 ⁻³	1.37
Double-Shell (30 mL)	0.130	2.6 × 10 ⁻³	0.16	3.0 × 10 ⁻³	1.39
Triple-Shell (40 mL)	0.123	2.5 × 10 ⁻³	0.15	2.8 × 10 ⁻³	1.93

Table A-2 summarizes the amount of ascorbate anions (from AA; see Experimental Section) and nitrate anions present in the reaction solution during the transfer of seed particles in the growth solution and after the addition of precursors. It can be observed that structures synthesized using a low seed amount lacks excess anions (ascorbate and NO₃⁻) to electrostatically stabilize the particle compared with a higher seed amount. As stated in the main text, when a low amount of seed was used to synthesize (Cu₂O@)_nCu₂O ($n = 2$ or 3), peanut- or bean-pod-like structures were observed and it was attributed to the interconnection of (Cu₂O@)_{n-1}Cu₂O seeds before the subsequent deposition of Cu(OH)₂ aggregates. At this condition (also refer to Experimental Section in the main text), the amounts of anions (excess ascorbate and NO₃⁻) that stabilize the particles were lower before and after the reaction, compared with the synthesis of freestanding (Cu₂O@)_nCu₂O spheres. Therefore, particles would easily interconnect at a lower seed amount (i.e., at a lower concentration of anions) generating peanut- or bean-pod-like (Cu₂O@)_nCu₂O.



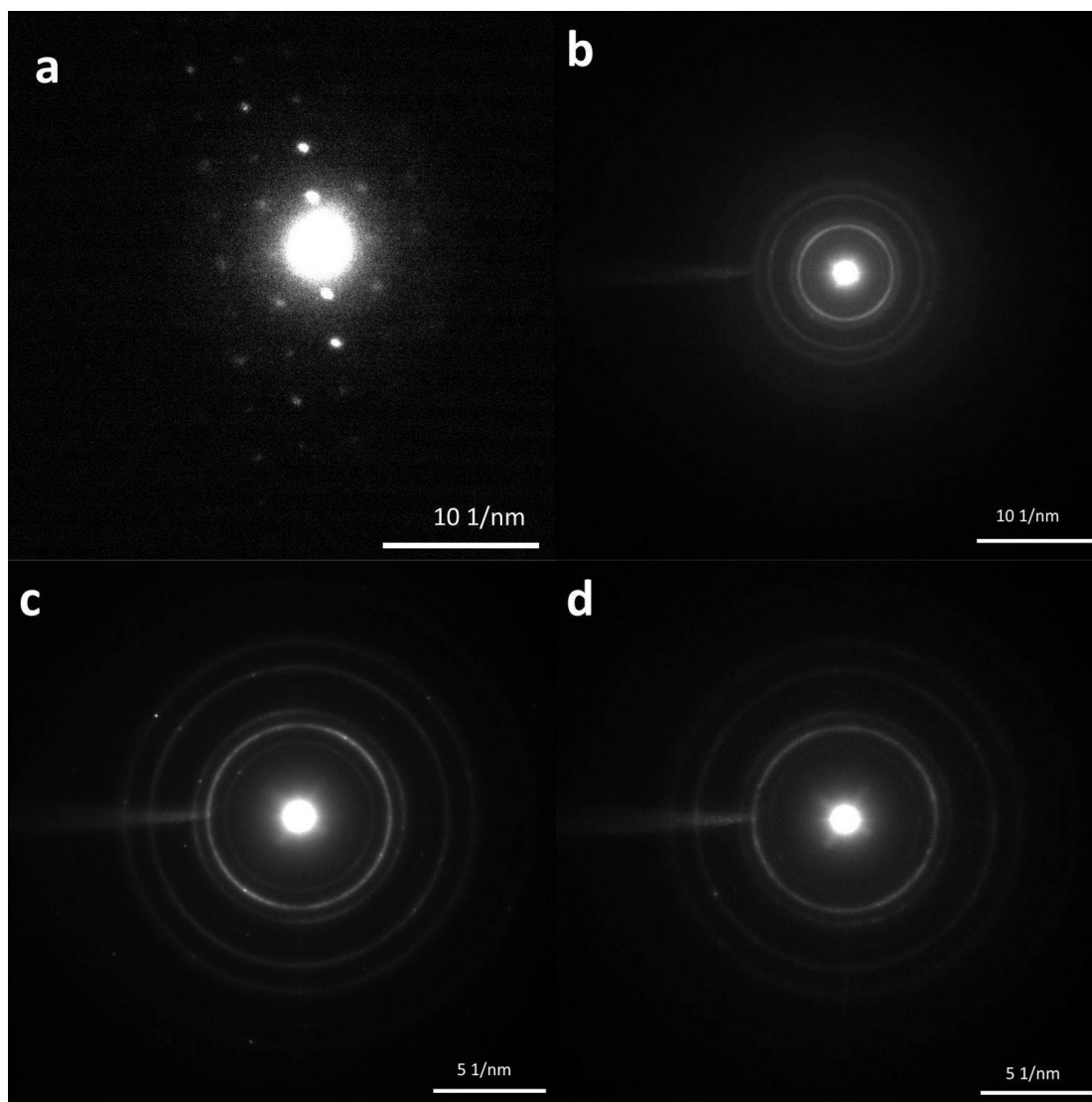
Experimental setup at different stirring rate: (a) 600 rpm, (b) 880 rpm, (c) 1100 rpm, and (d) 1500 rpm.

Appendix 1-2A High Resolution TEM Characterization



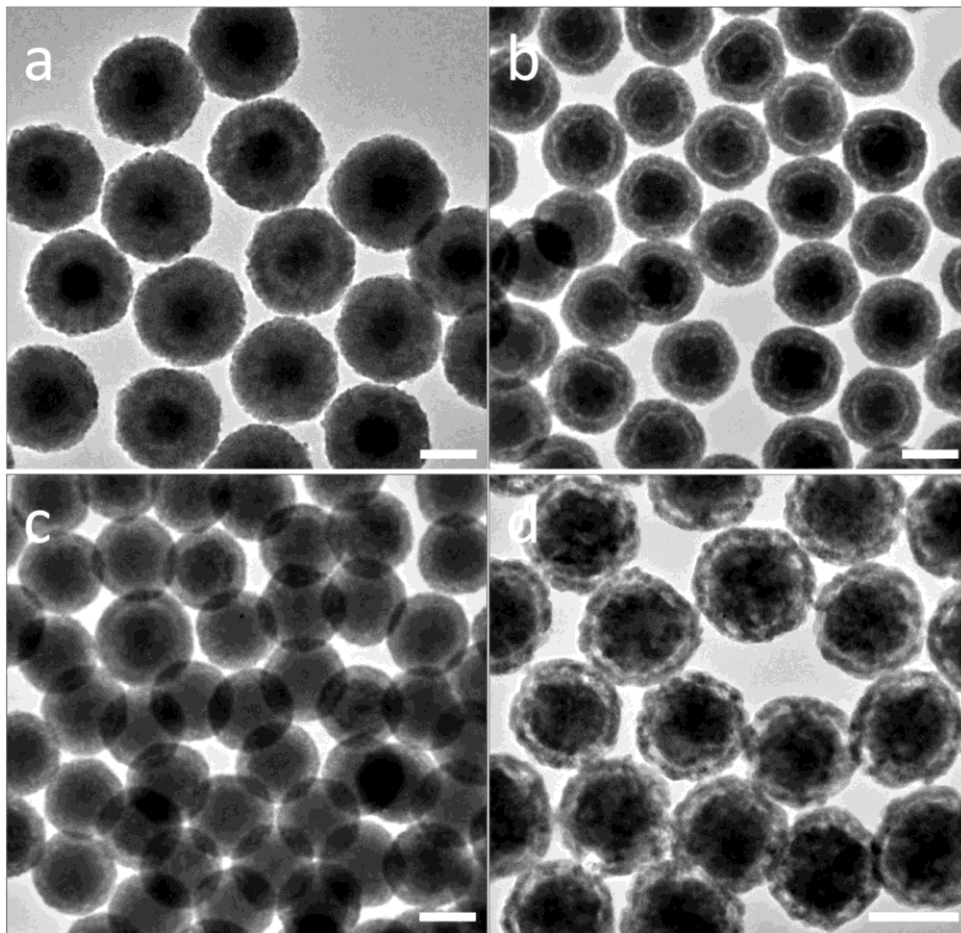
High-resolution TEM (HRTEM) image of the Cu_2O shell structure, which indicates that the shell comprises of numerous small Cu_2O nanocrystallites.

Appendix 1-2B Selected Area Electron Diffraction (SAED) Characterization

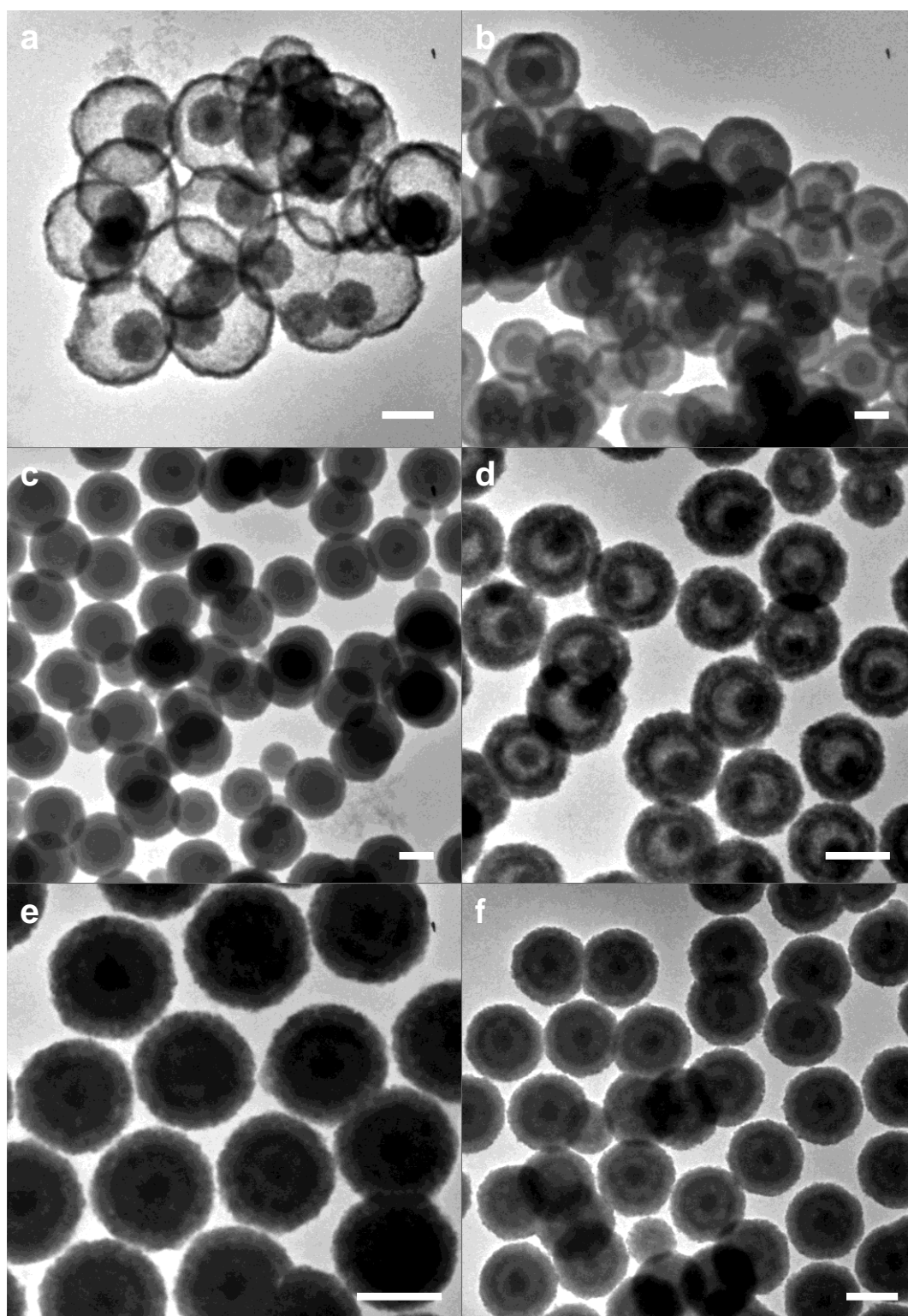


Selected area electron diffraction (SAED) study of different Cu_2O structures: (a) truncated cube (seed), (b) core-shell $\text{Cu}_2\text{O}@\text{Cu}_2\text{O}$, (c) yolk-shell $\text{Cu}_2\text{O}@\text{Cu}_2\text{O}$, and (d) double-shelled structure $(\text{Cu}_2\text{O}@\text{Cu}_2\text{O})_2$. This investigation shows that the pristine Cu_2O nanocubes (seeds) are single-crystalline (see diffraction spots) while the shells formed on the seeds are polycrystalline (see diffraction rings).

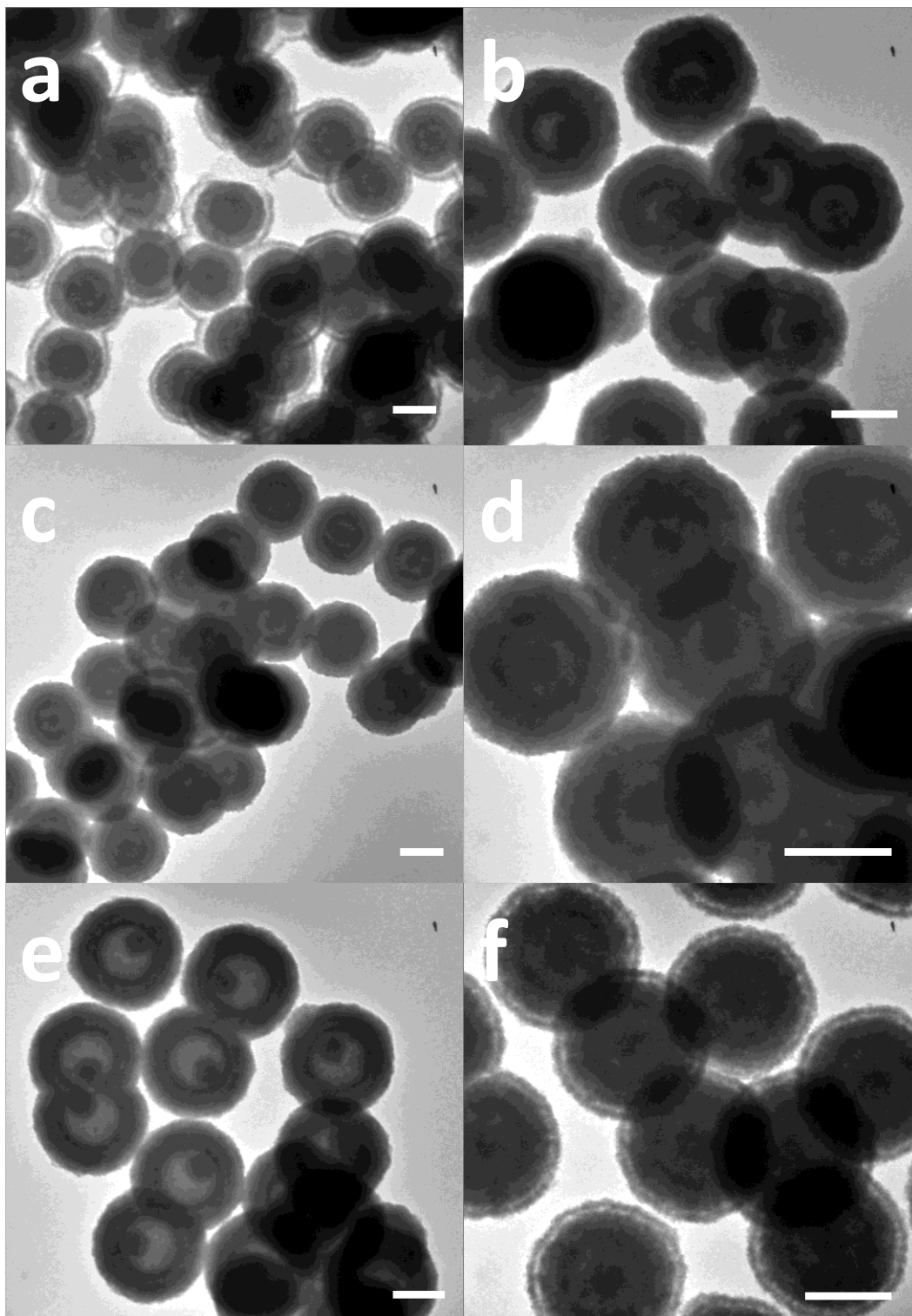
Appendix 1-3A Effect of Seed Amount on $(\text{Cu}_2\text{O})_n@ \text{Cu}_2\text{O}$ Growth



Effect of amount of seed used in the growth of the 1st shell: (a) 10 mL of type A, 200 nm; (b) 30 mL of type A, 150 nm; (c) 40 mL of type A, 140 nm; and (d) 50 mL of type A, 125 nm. Reaction time: 10 minutes. Scale bar: 100 nm.



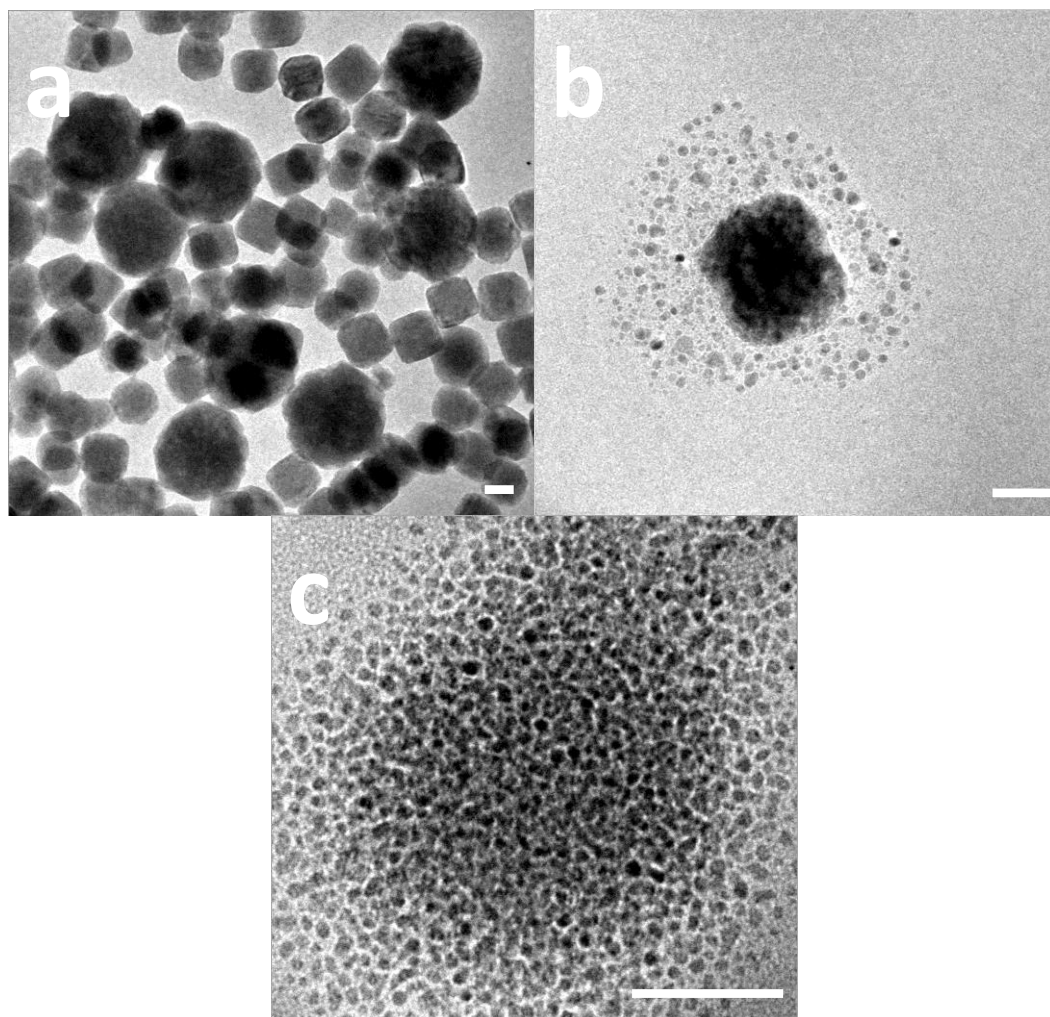
Effect of amount of seed used in the growth of the 2nd shell: (a) 5 mL of core-shell, 15 min of reaction; (b) 7 mL of core-shell, 15 min of reaction; (c) 10 mL of core-shell, 8 min of reaction; (d) 20 mL of yolk-shell, 8 min of reaction; (e) 25 mL of core-shell, 8 min of reaction; and (f) 30 mL of core-shell, 8 min of reaction. Scale bar: 200 nm.



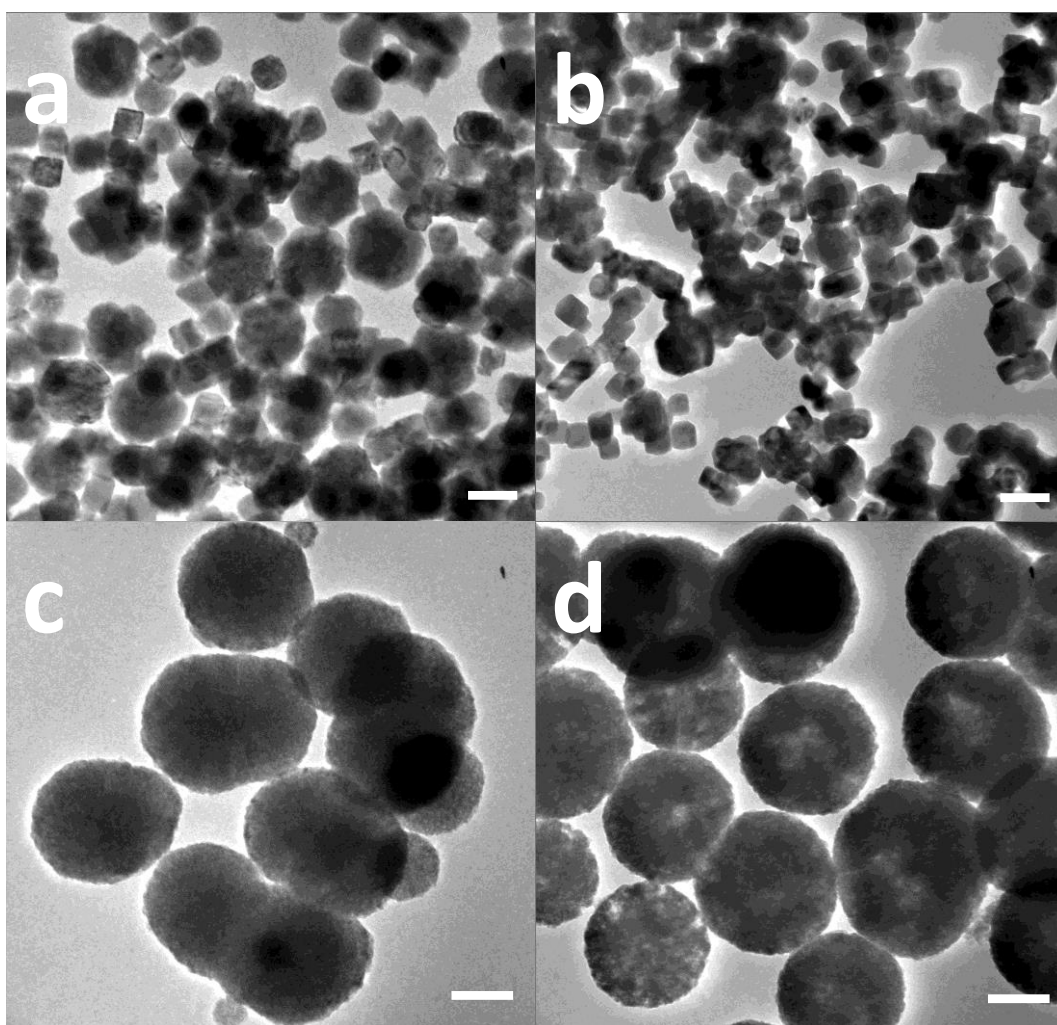
Effect of amount of seed used in the growth of the 3rd shell: (a) 10 mL of single-shelled core-shell structure used in the second shell growth and 25 mL of double-shelled structure used in the third shell growth (8 min for the second shell growth + 8 min for the third shell growth), (b) 20 mL of single-shelled yolk-shell structure used in the second shell growth and 25 mL of double-shelled structure used in the third shell growth, (c) 25 mL of single-shelled core-shell

structure used in the second shell growth and 25 mL of double-shelled structure used in the third shell growth, (d) 25 mL of single-shelled core-shell structure used in the second shell growth and 40 mL of double-shelled structure used in the third shell growth, (e) 25 mL of single-shelled yolk-shell structure used in the second shell growth and 44 mL of double-shelled structure used in the third shell growth, and (f) 30 mL of single-shelled core-shell structure used in the second shell growth and 40 mL of double-shelled structure used in the third shell growth. Scale bar: 200 nm.

Appendix 1-3B Effect of NH_4NO_3 , and Other Ions on $(\text{Cu}_2\text{O})_n@ \text{Cu}_2\text{O}$ Growth

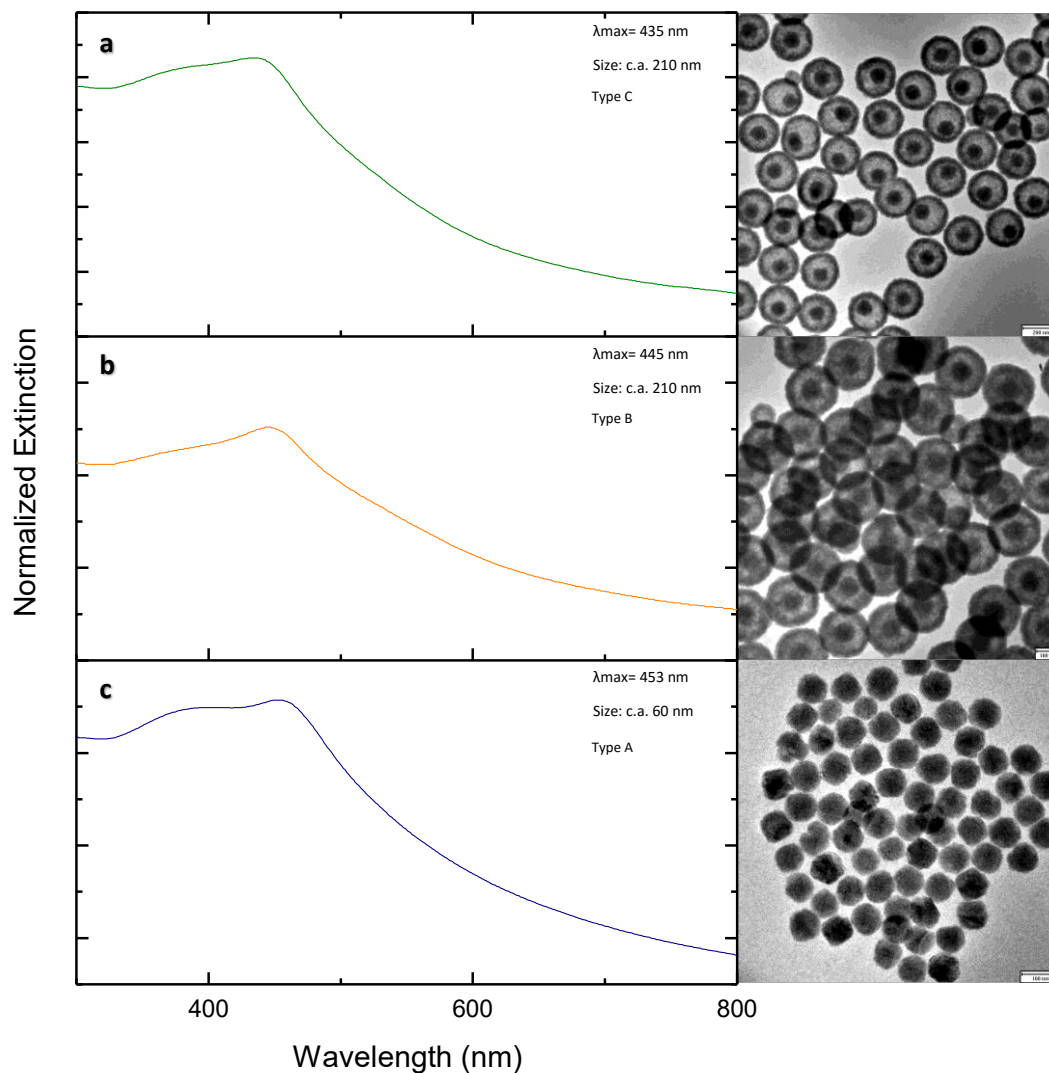


Effect of NH_4NO_3 salt on the shell growth: (a) in the absence of NH_4NO_3 , (b) 9 mmol of NH_4NO_3 used in synthesis, and (c) 11 mmol of NH_4NO_3 used in synthesis. Scale bar: 40 nm.

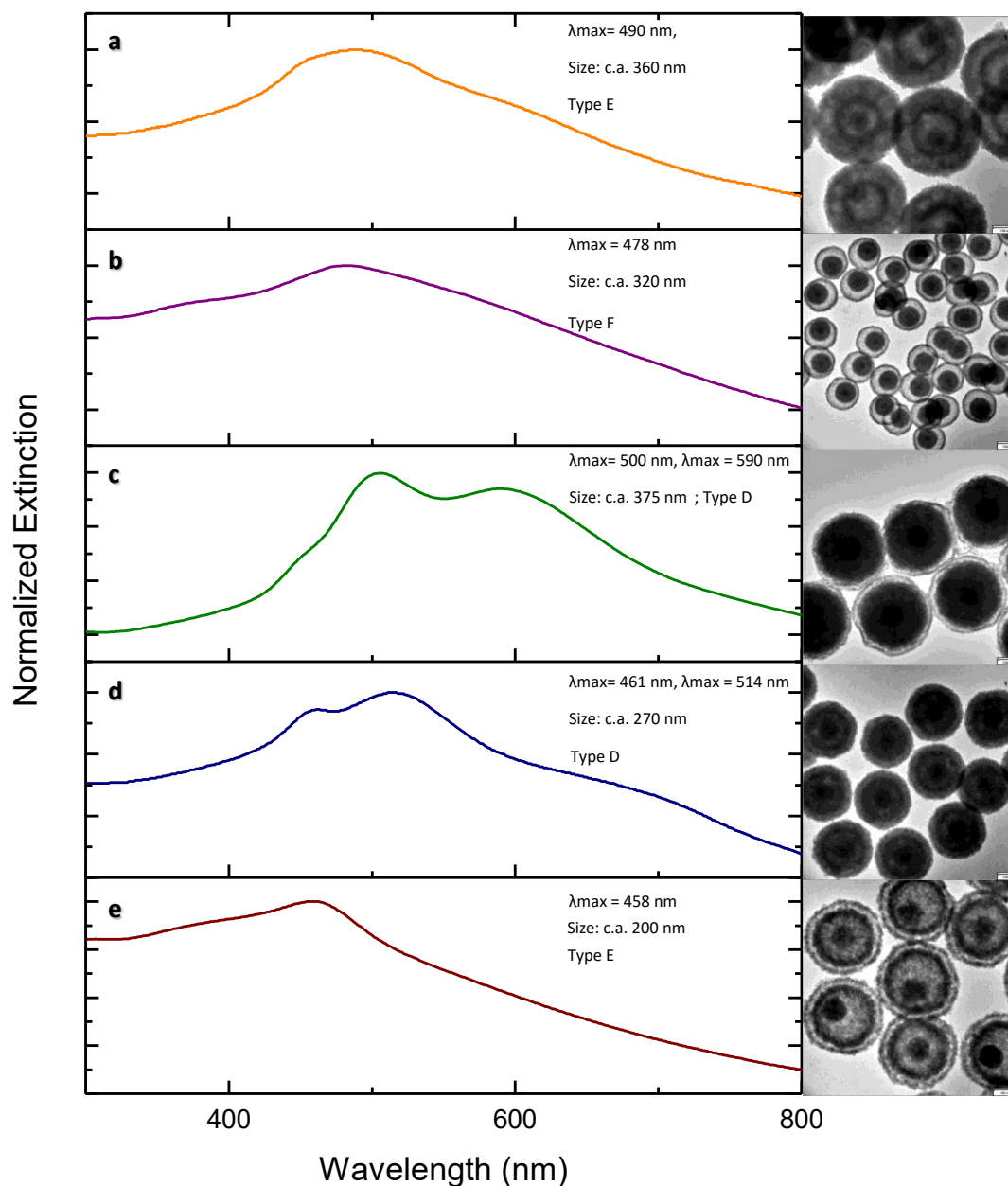


Effects of different cations and anions on the growth of the 1st-shell: (a) 0.8744 mmol of KNO_3 used in synthesis, (b) 1.7499 mmol of KNO_3 used in synthesis, (c) 0.8744 mmol of NH_4Cl used in synthesis, and (d) 1.7512 mmol of NH_4Cl used in synthesis. Scale bar: 100 nm.

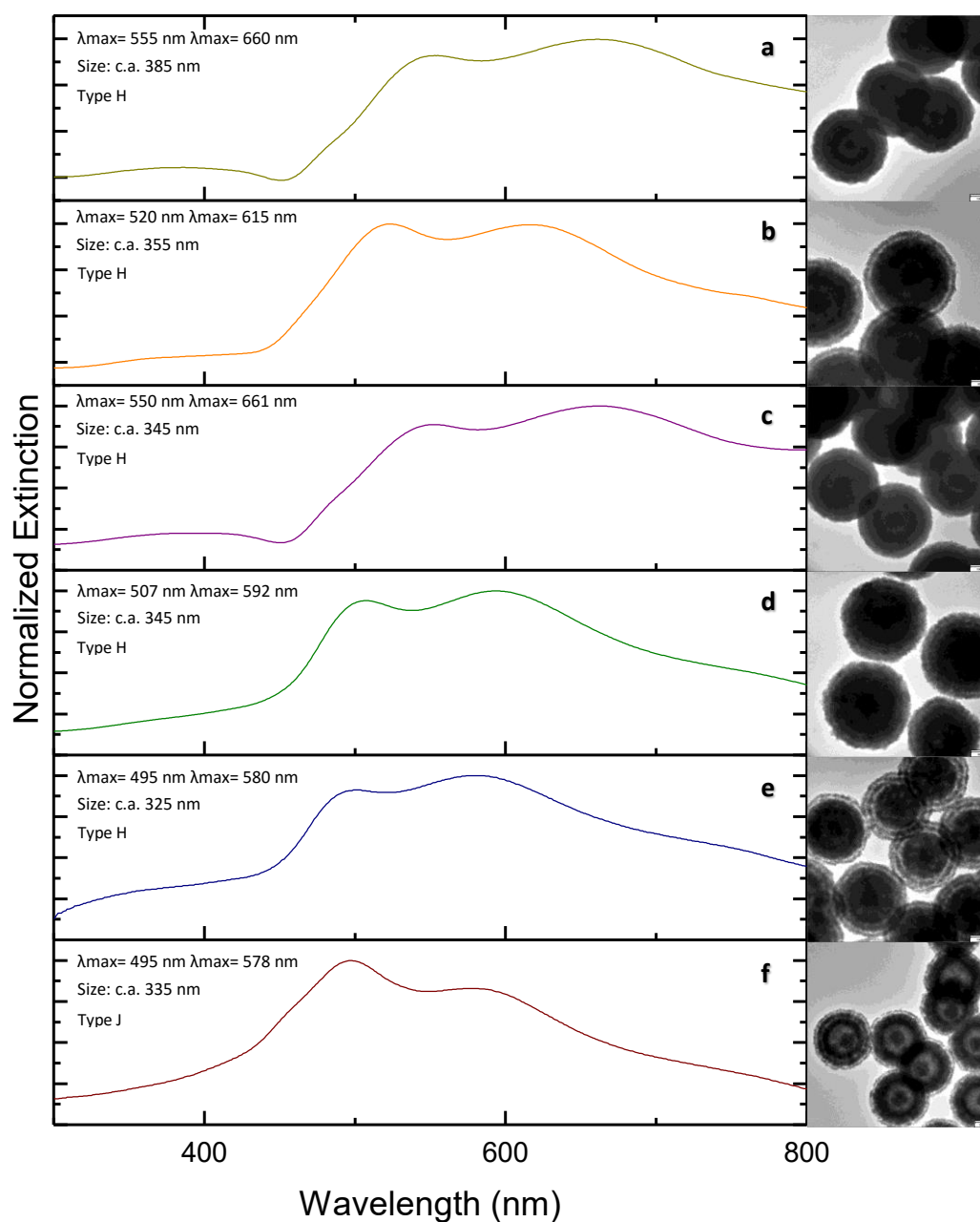
Appendix 1-4A Correlation of Structure and Optical Property



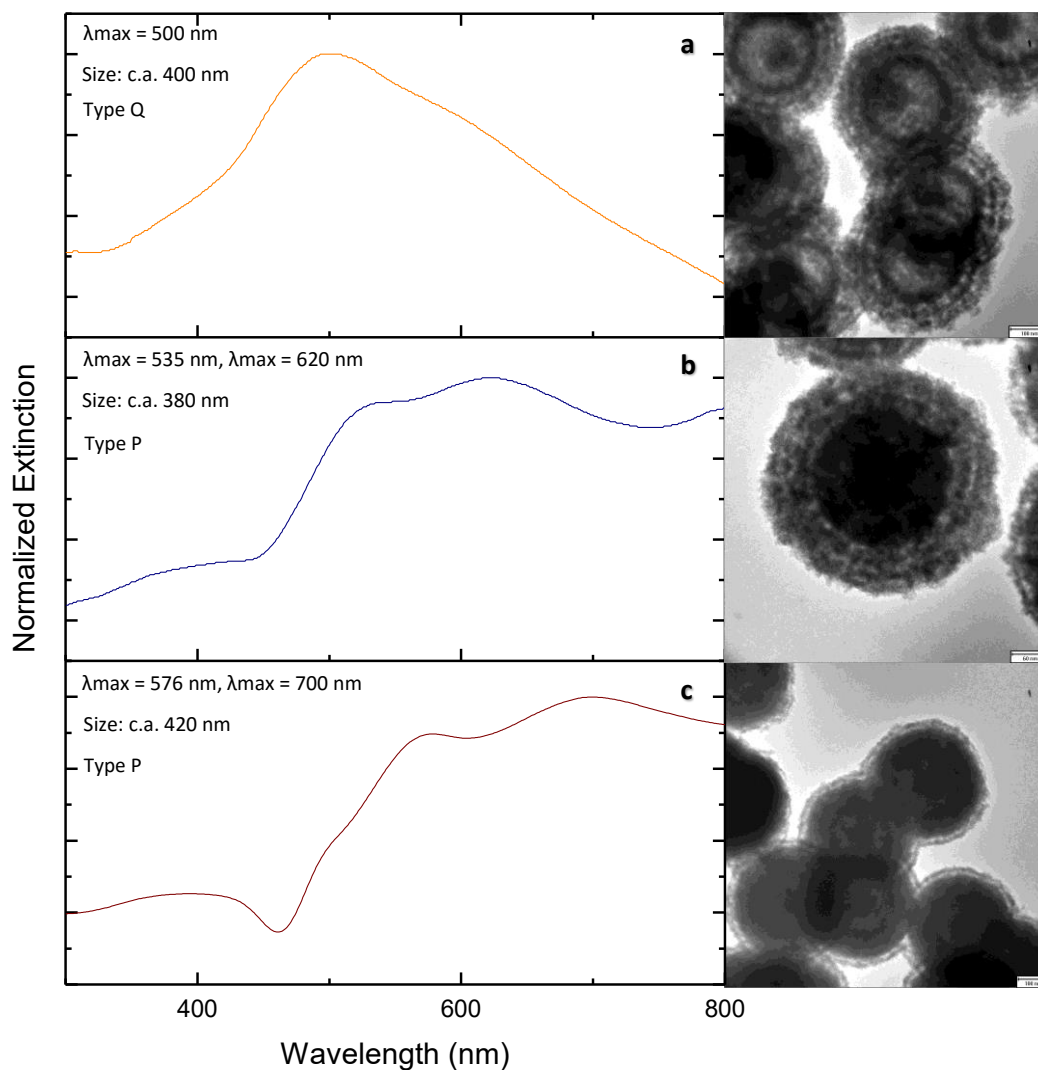
Extinction spectra of pristine Cu_2O seed (bottom image), single-shelled core-shell structure (middle image), and single-shelled yolk-shell structure (top image) and their corresponding TEM images. Inset labels: wavelength of maximum peak, average size of the structure and type of structure (Figure 1 of main text). Both type B (b) and type C (a) structures exhibit a blue shift in their extinction peak compared with type A (c) due to the effect of polycrystalline shell (crystallite size at 5-6 nm) absorption.



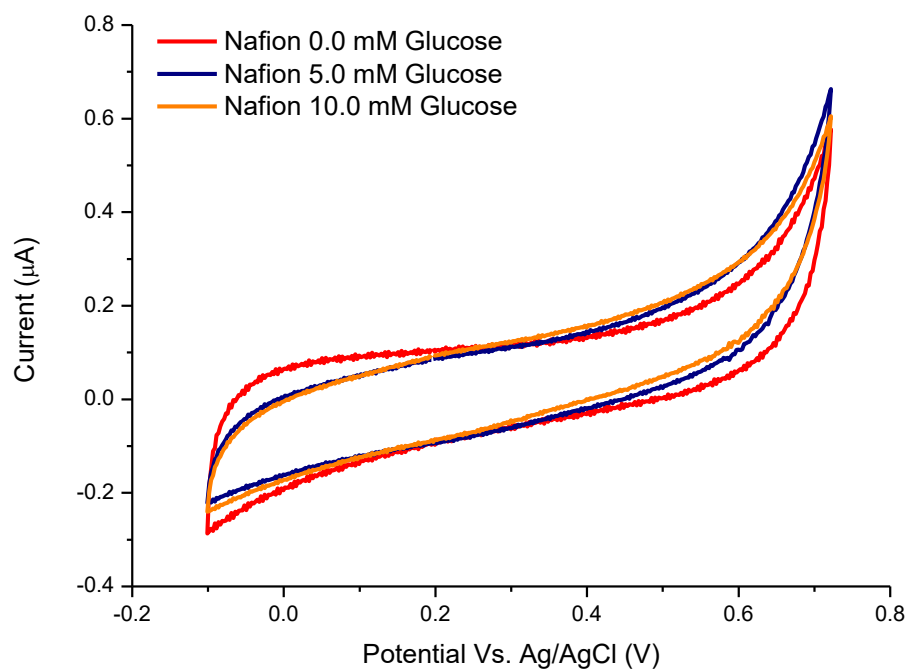
Extinction spectra of different double-shelled core-shell structures and their corresponding TEM images. Inset labels: wavelengths of maximum peaks, average size of the structure, and type of structure (Figure 1 of main text). All double-shelled structures exhibit a red-shift in their extinction peak compared with type A structure due to the contribution of scattering. Interestingly, eccentric structures type E (a and e) and type F (b) give essentially only one extinction peak compared with concentric structures type D (c and d).



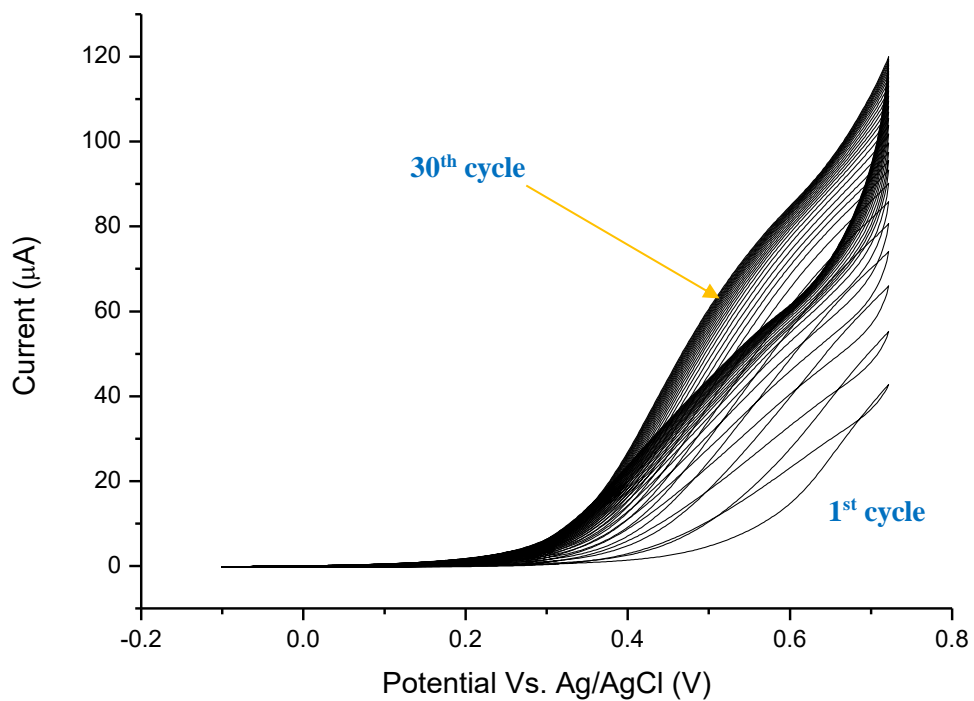
Extinction spectra of triple-shelled core-shell structures and their corresponding TEM images. Inset labels: wavelengths of maximum peaks, average size of the structure, and type of structure (Figure 1 of main text). All triple-shelled structures exhibit two extinction peaks, which are further red-shifted compared with the double-shelled structures. The multiple peak features are due to the appearance of higher-order modes at Mie scattering resonances because of phase-retardation effects when the sphere size is comparable to the wavelength of incident light. In comparison, it can be seen that structures with smaller and thinner shells exhibit extinction peaks at lower wavelengths (blue-shifted). For example, type H (a) and type H (e) show the highest and the lowest wavelengths, respectively, in their extinction peaks.



Extinction spectra of different quadruple-shelled structures and their corresponding TEM images. Inset labels: wavelengths of maximum peaks, average size of the structure, and type of structure. All quadruple-shelled structures exhibited a red-shift in their extinction peak compared with single, double, and triple-shelled structures. Eccentric structure type Q (a) exhibits only a single extinction peak compared with a concentric structure type P (b and c). In comparison, it can be seen that structures with more thin-shells (b) shows a blue-shift on their extinction peaks.

Appendix 1-4B Additional Electrochemical Measurements

Cyclic voltammogram of Nafion-modified GCE with different glucose concentrations: 0.0 mM (red), 5.0 mM (blue), and 10.0 mM (orange) glucose. Scan rate: 50 mVs^{-1} .



Cyclic voltammograms of thick-shelled type P structure with 5.0 mM glucose in nitrogen saturated 0.10 M NaOH at different cycles. Scan rate: 50 mVs^{-1} .

Appendix 2

Appendix 2-1 Additional Methodology

For upscale synthesis and reaction, the synthetic solutions were prepared in 250 mL beakers and were stirred using a 45 mm × 8 mm (length × diameter) magnetic stirring bar at a nominal speed setting of 850 rpm (stirrer model: Corning PC-420D).

Upscale synthesis of Cu₂O CSPAR. After the synthesis of Cu₂O core, 15.0 mL of the as-synthesized Cu₂O core suspension was transferred to a solution mixture of Cu(NO₃)₂·3H₂O (0.36 mmol) and NH₄NO₃ (2.6 mmol) in 135 mL of deionized water. The solution was stirred magnetically for 1 min, followed by the dropwise addition (0.086 mL/s) of 6.00 mL of 0.20 M NaOH; the solution was stirred for another 1 min. Finally, 10.5 mL of 0.10 M ascorbic acid was added drop wise (0.027 mL/s) and the solution was further stirred for 5 min.

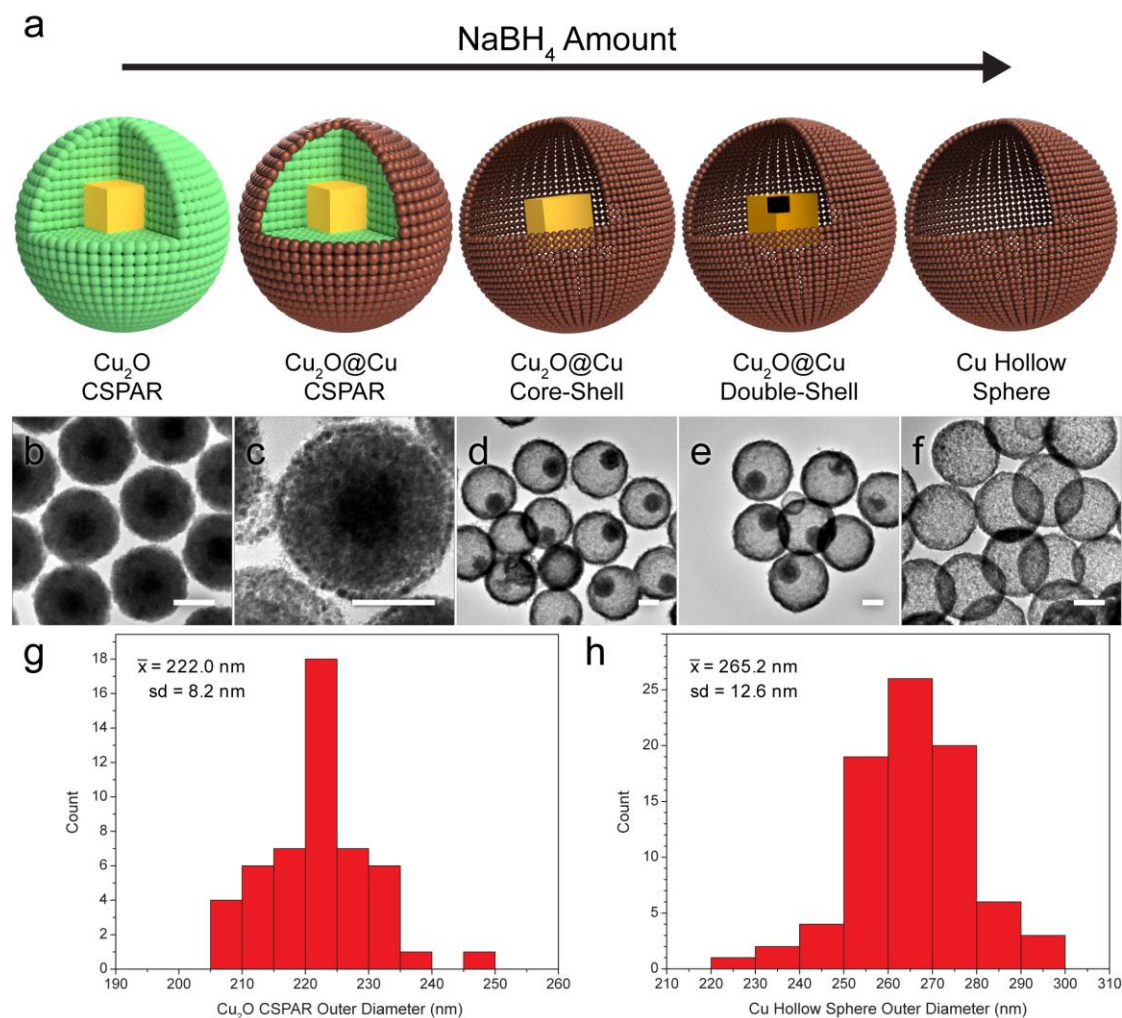
Upscale synthesis of Zn(OH)₂ passivated CSPAR. After the up-scaled synthesis of Cu₂O CSPAR, 90.0 mL of the as-synthesized Cu₂O CSPAR were transferred to a solution mixture of Zn(CH₃COO)₂ (0.30 mmol) in 60.0 mL of deionized water. The solution was stirred magnetically for 1 min, followed by the dropwise addition (0.086 mL/s) of 6.00 mL of 1.0 M NaOH; the solution was further stirred for 25 min.

Upscale synthesis of Cu nanoparticle embedded Cu₂O@Zn(OH)₂ hollow spheres. After the synthesis of Zn(OH)₂ passivated Cu₂O CSPAR, the suspension was centrifuged and washed with 50.0 mL deionized water. The obtained solid was dispersed in 150. mL H₂O and was transferred to a reaction vessel. The suspension was stirred for 1 min at 900 rpm, followed by the addition of 3.00 mL of 150. mg/mL NaBH₄ solution in 50. mM NaOH. The suspension was stirred for another 30 min. The transparent orange solution was centrifuged at 3800 g for 5 min, then the product was washed with deionized water followed by ethanol. It should be noted that if the solid residue is black after centrifugation, copper nanoparticle/branch aggregation occurred, whereas non-aggregated particles forms an orange film.

Voltammetric measurement of Cu₂O CSPAR and Cu hollow spheres. Before modification, glassy carbon electrode (GCE, 3 mm diameter) was prepared by a slight

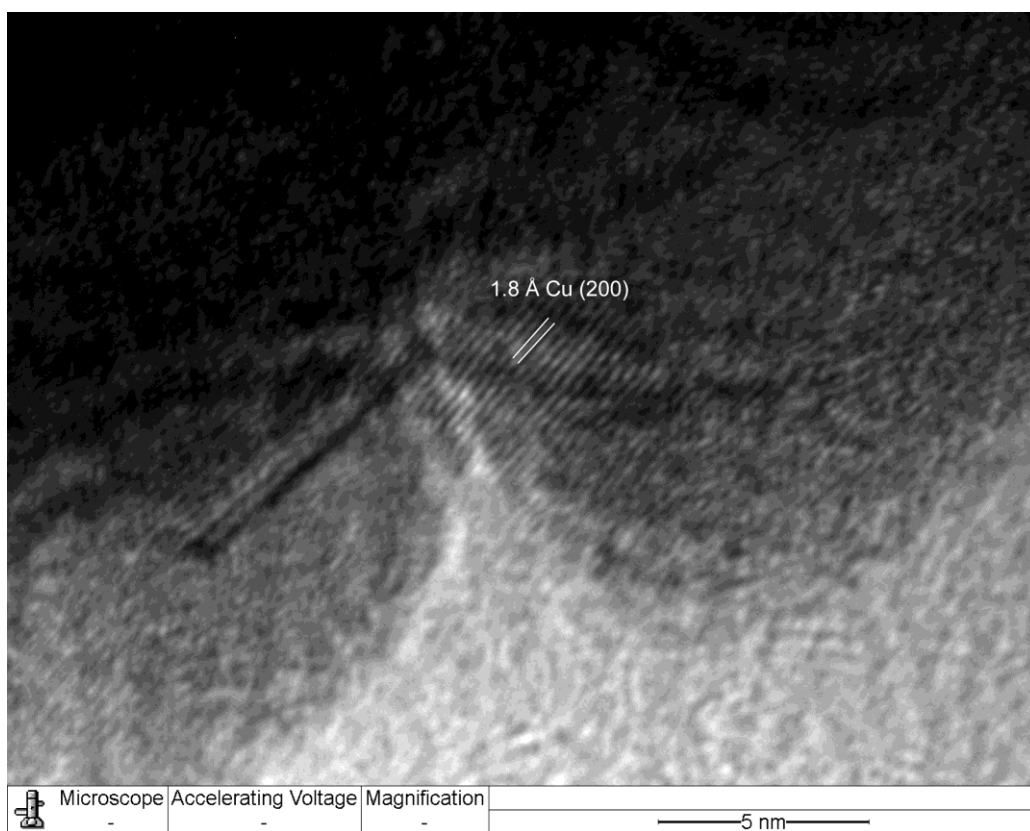
modification of a reported methodology.¹ Briefly, the GCE was polished using successive slurries of 1.0, 0.30, and 0.050 micron alumina slurries on chamois leather followed by ultrasonication in deionized water for 10 min between slurries. Afterwards, a potential of +1.80 V vs. Ag/AgCl was applied onto the electrode for 1 min in 0.10 M NaOH in a three-electrode cell using Ag/AgCl/KCl (3.0 M) and Pt gauze acting as the reference and counter electrode, respectively. A suspension of catalyst was prepared by mixing 1.0 mg of Cu₂O CSPAR or Cu hollow sphere with 0.99 mL of deionized water, 0.25 mL of isopropyl alcohol, and 5.00 μL of 5% w/w Nafion solution. The resulting mixture was sonicated for 30 min and 6.10 μL of the mixture was casted onto the surface of GCE. The electrode was dried overnight at 40 mBar atmosphere to prevent the oxidation of copper. Voltammetric measurements of the modified electrode were performed under room temperature in a CO₂ saturated 0.50 M KHCO₃ (pH = 7.6) with a scan rate of 10.0 mV/s. The potential was converted to the RHE reference scale using: $E \text{ (vs RHE)} = E \text{ (vs Ag/AgCl)} + 0.210 \text{ V} + (0.0592 \text{ V} * \text{pH})$.

Appendix 2-2A Schematic illustration of the evolution of Cu hollow sphere during the reduction-complexation reaction of Cu₂O CSPAR

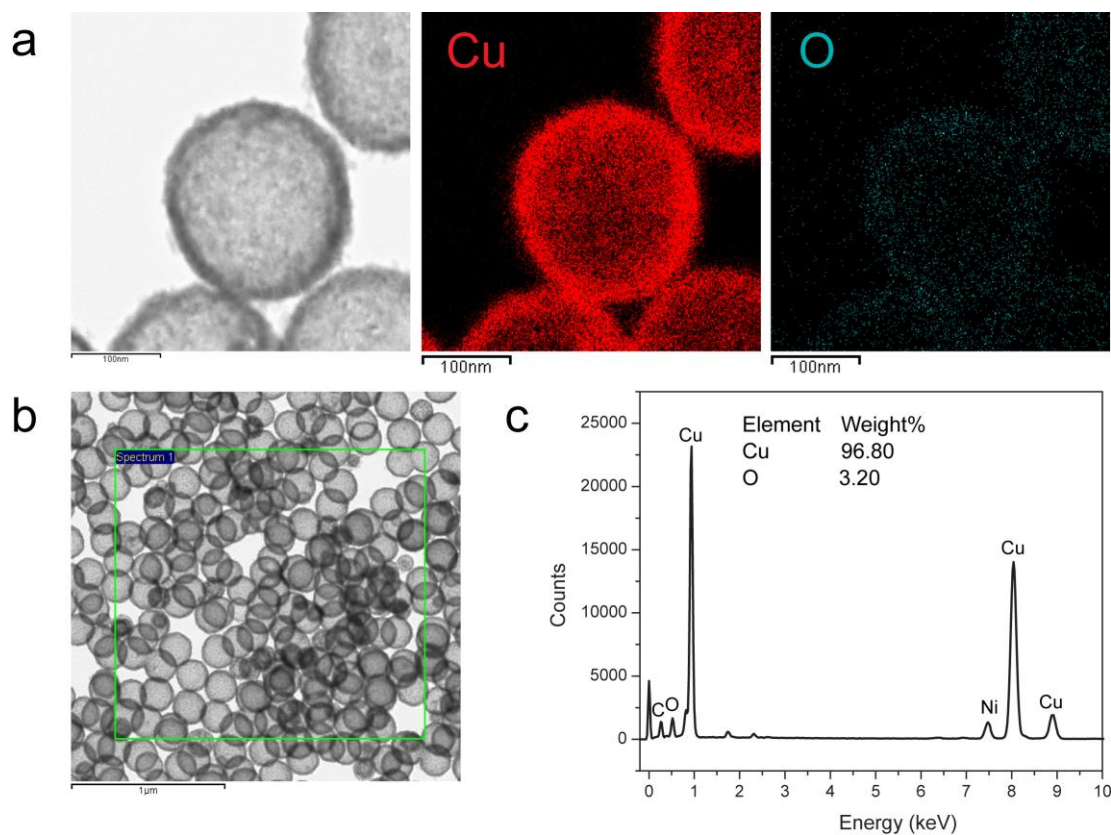


(a) Effect of increasing amount on NaBH₄ on the formation of Cu hollow sphere. Corresponding TEM image at various amount of NaBH₄: (b) 0, (c) 0.25, (d) 0.35, (e) 0.40, and (f) 0.50 mL of 20 mg/mL NaBH₄ solution. Size distribution of (g) Cu₂O CSPAR and (h) Cu hollow sphere. All scale bars are 100 nm.

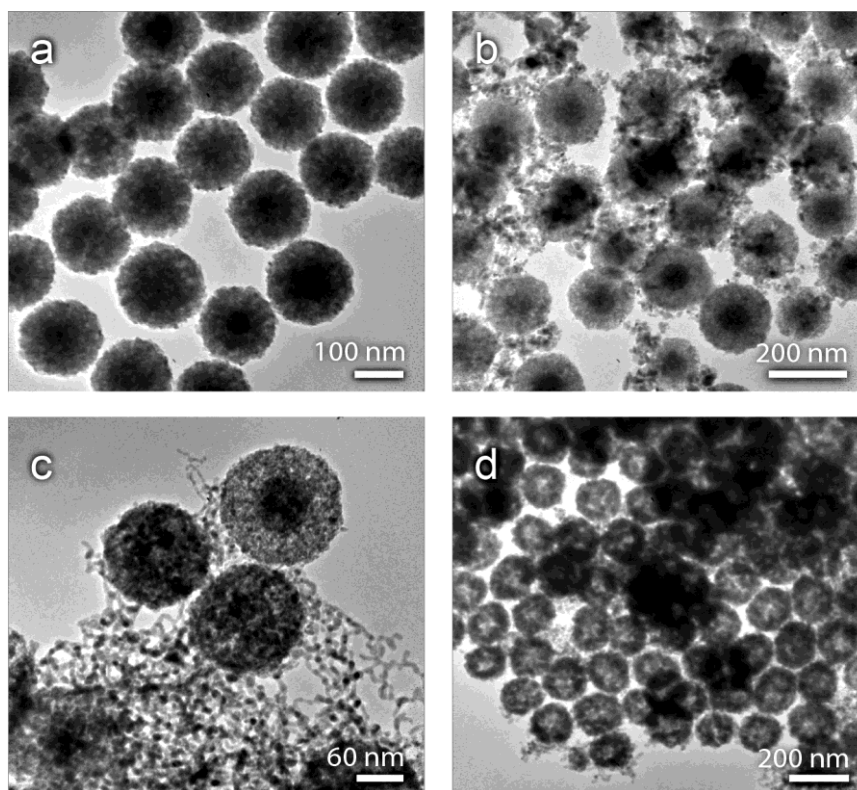
Appendix 2-2B High resolution TEM image of Cu hollow sphere



The presence of Cu (200) lattice plane confirms the reduction of Cu₂O CSPAR.

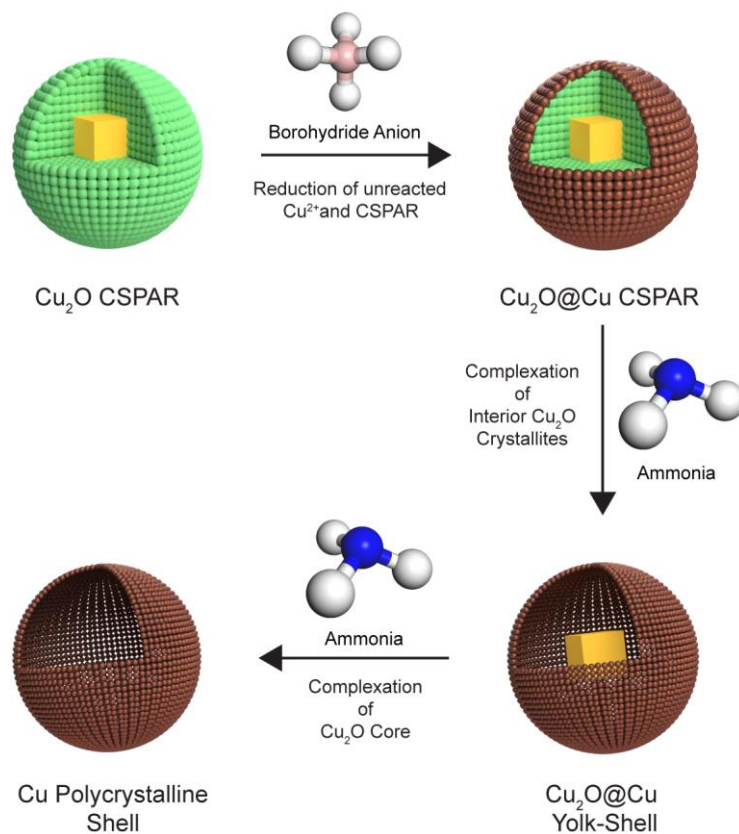
Appendix 2-2C Energy dispersive X-ray analysis of Cu hollow sphere

(a) Elemental maps of the Cu_2O CSPAR reduction-complexation product. (b) Scanning transmission electron micrograph of Cu hollow sphere for quantitative analysis, and (c) corresponding EDX spectrum and quantitative analysis of (b).

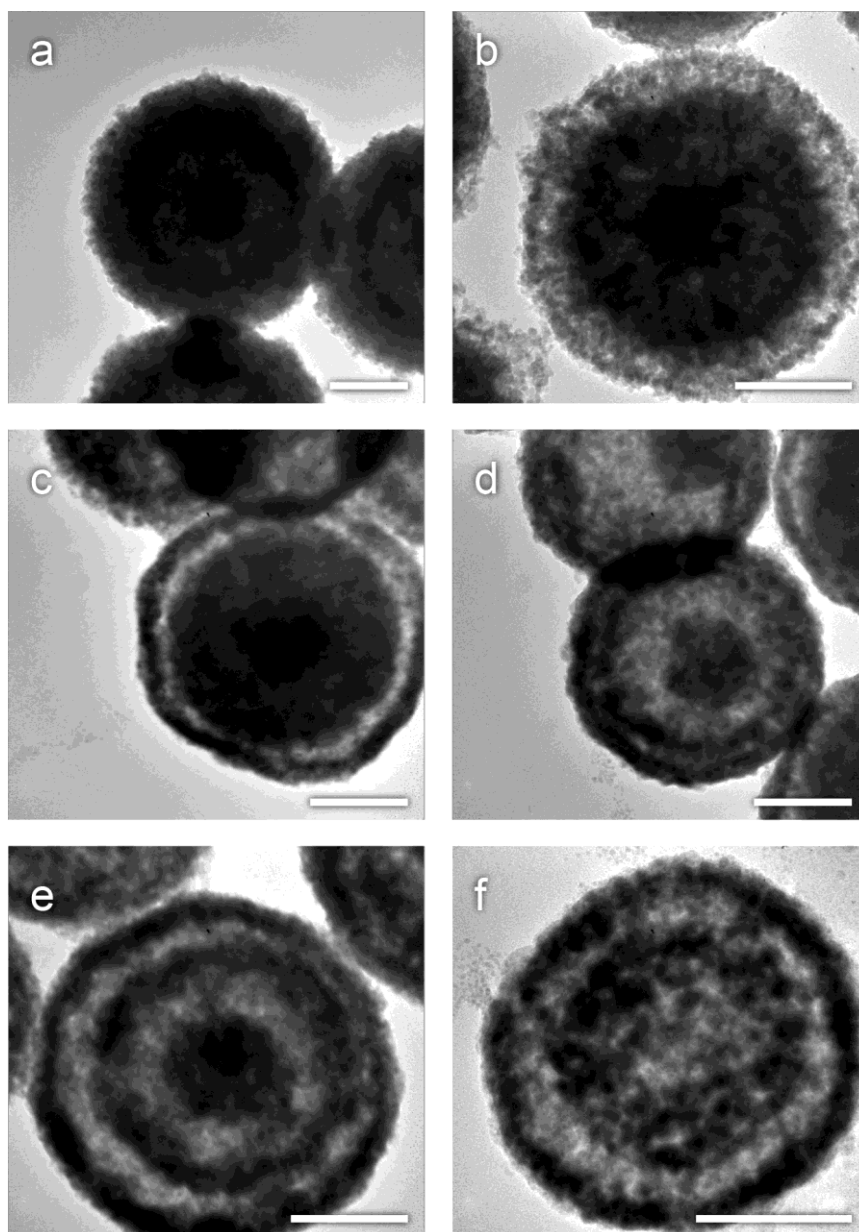
Appendix 2-2D Mechanism verification for the reduction-complexation of Cu₂O CSPAR

TEM image of the reaction product of redispersed Cu₂O CSPAR in 50.0 mL of H₂O with 0.40 mL of 10. mg/mL NaBH₄ with the following ions: (a) NaOH, pH = 12, (b) no additive, pH = 6.6, (c) 0.010 mmol Cu(NO₃)₂, and (d) 0.010 mmol of Cu(NO₃)₂ + 0.10 mmol of NH₄NO₃. These results indicate the necessity of Cu²⁺ and NH₄⁺ to form hollow spheres during this reaction.

Appendix 2-2E Schematic illustration of proposed transformation mechanism of Cu_2O CSPAR during reduction-complexation reaction

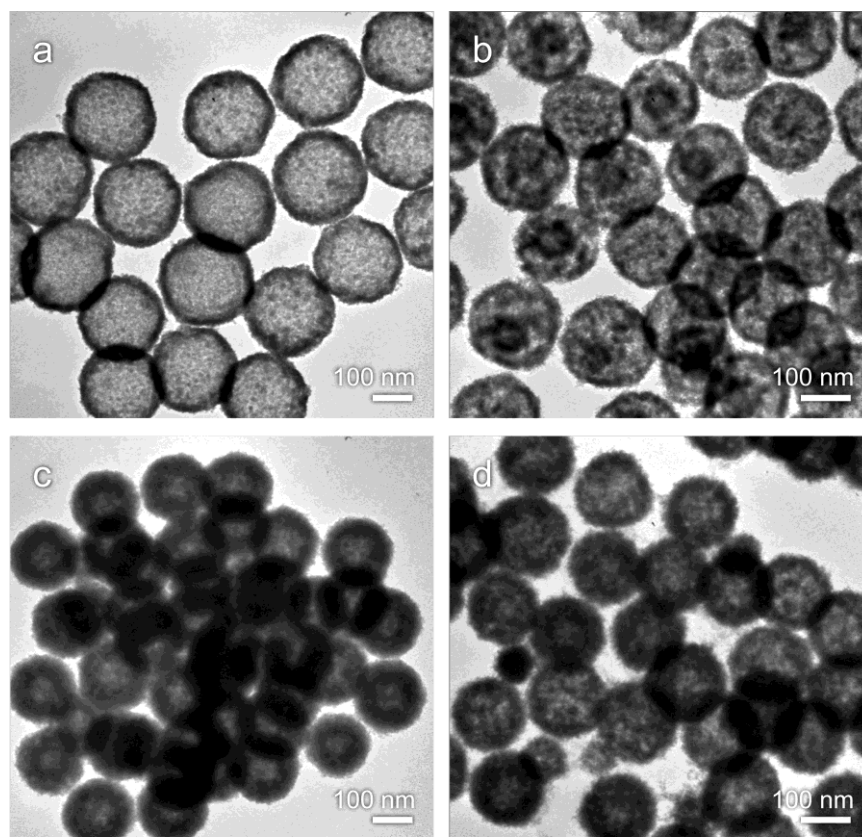


During the addition of NaBH_4 , $\text{Cu}@Cu_2\text{O}$ CSPAR are formed through the reduction of excess Cu^{2+} and surface particles. Due to the reducing conditions, ammonia would only dissolve the interior Cu_2O crystallites, since the dissolution of Cu requires the formation of oxide film.² The process would continue until the internal Cu_2O single crystal core is completely dissolved.

Appendix 2-2F Extension of the reduction-complexation mechanism for the transformation of double-shell Cu_2O CSPAR.

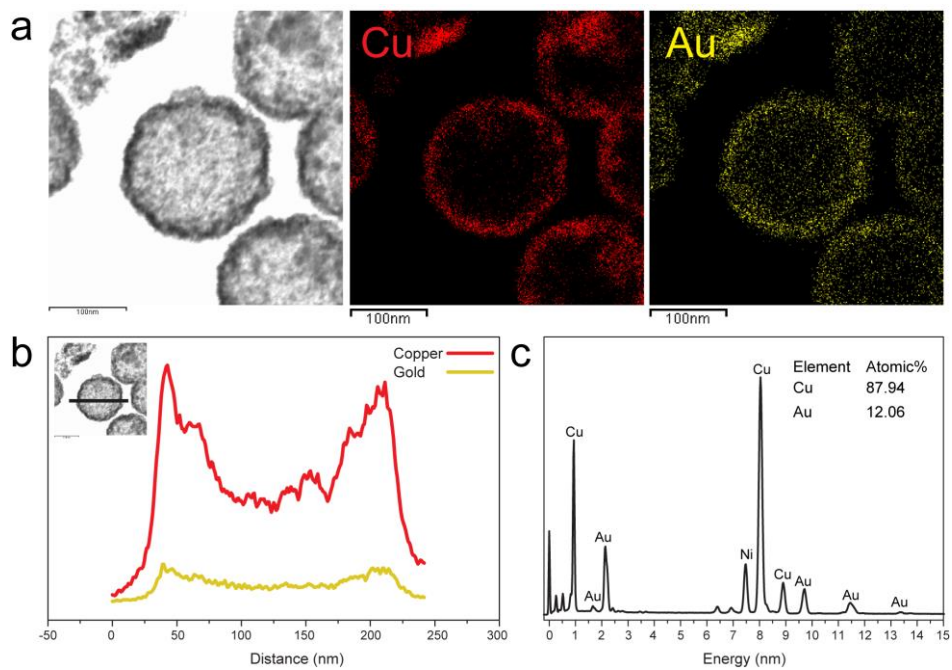
Reaction of Cu_2O double-shelled CSPAR at various amount of NaBH_4 : (a) 0, (b) 0.10, (c) 0.20, (d) 0.30, (e) 0.40, and (f) 0.50 mL of 20 mg/mL NaBH_4 solution. This extension permits the manipulation of size and architecture of Cu hollow spheres. (All scale bars are 100 nm.)

Appendix 2-3A Galvanic exchange-reduction product of Cu_2O CSPAR with various cations



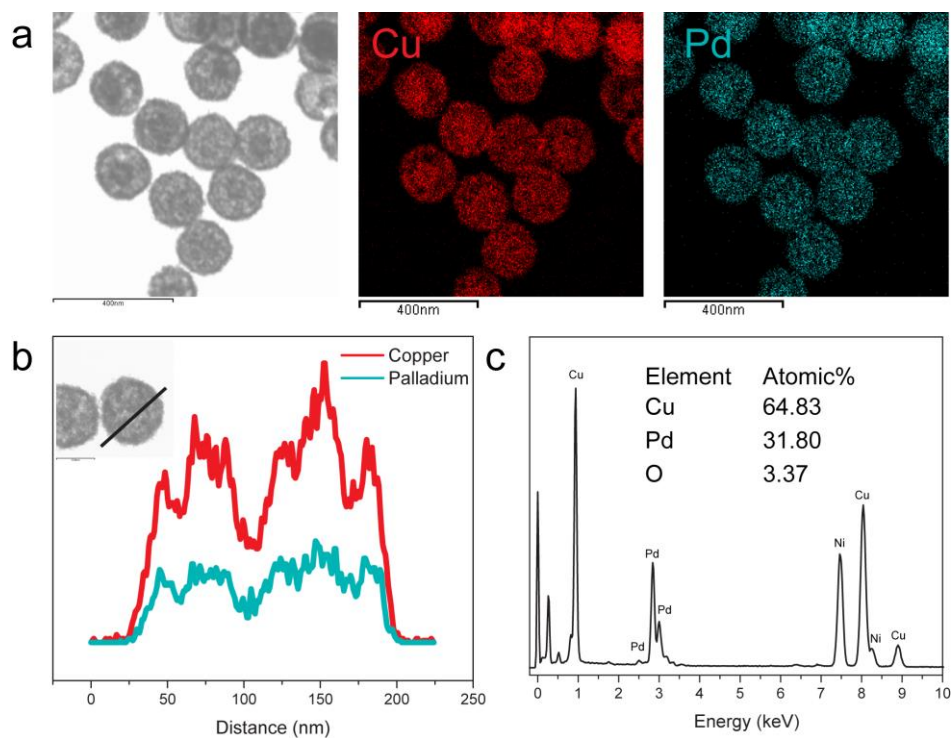
TEM image of the reaction product of Cu_2O CSPAR with 20. mM metal ion solution: (a) 1.00 mL Au, (b) 2.00 mL Pd, (c) 1.00 mL Pt, and (d) 0.50 mL Au and 0.50 mL Pt solution.

Appendix 2-3B Energy dispersive X-ray analysis of galvanic exchange product of Au³⁺ and Cu₂O CSPAR



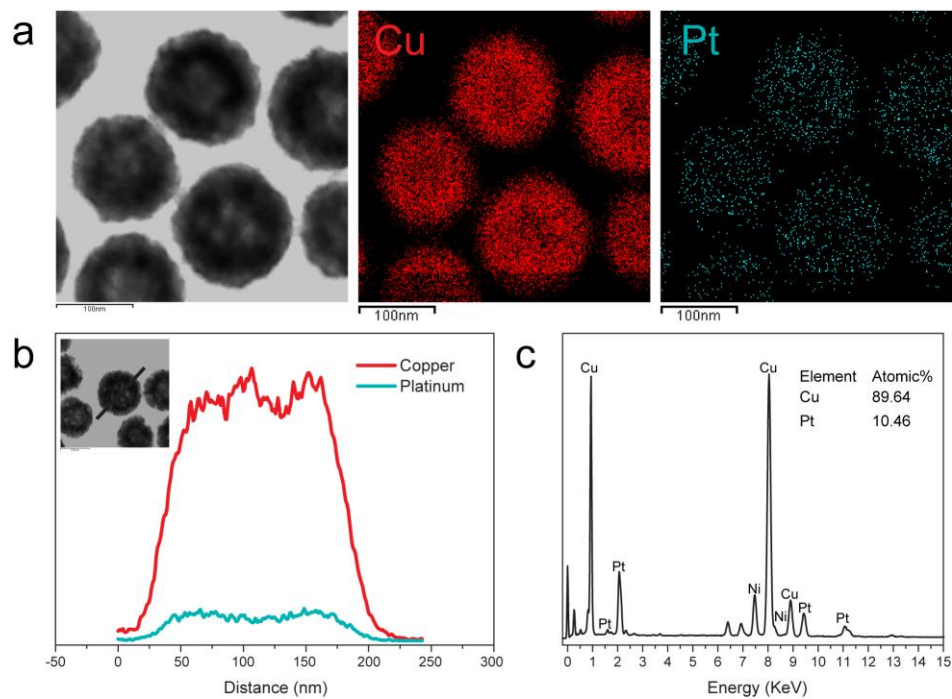
(a) Elemental maps of Cu, and Au, (b) line scan analysis, and (c) EDX spectrum.

Appendix 2-3C Energy dispersive X-ray analysis of galvanic exchange product of Pd²⁺ and Cu₂O CSPAR

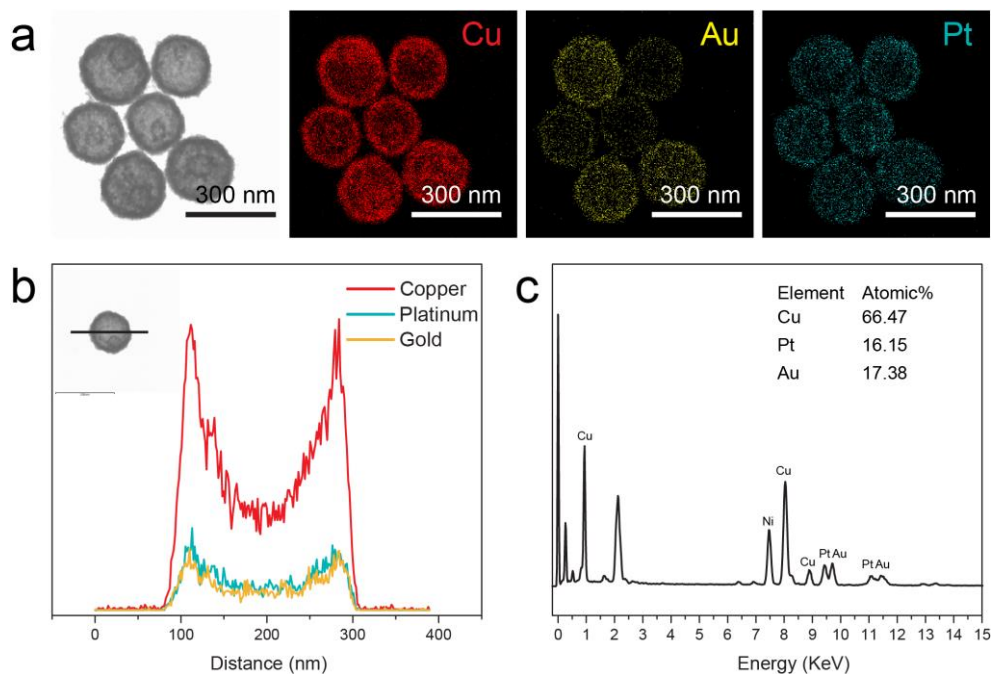


(a) elemental maps of Cu, and Pd, (b) line scan analysis, and (c) EDX spectrum.

Appendix 2-3D Energy dispersive X-ray analysis of galvanic exchange product of Pt⁴⁺ and Cu₂O CSPAR

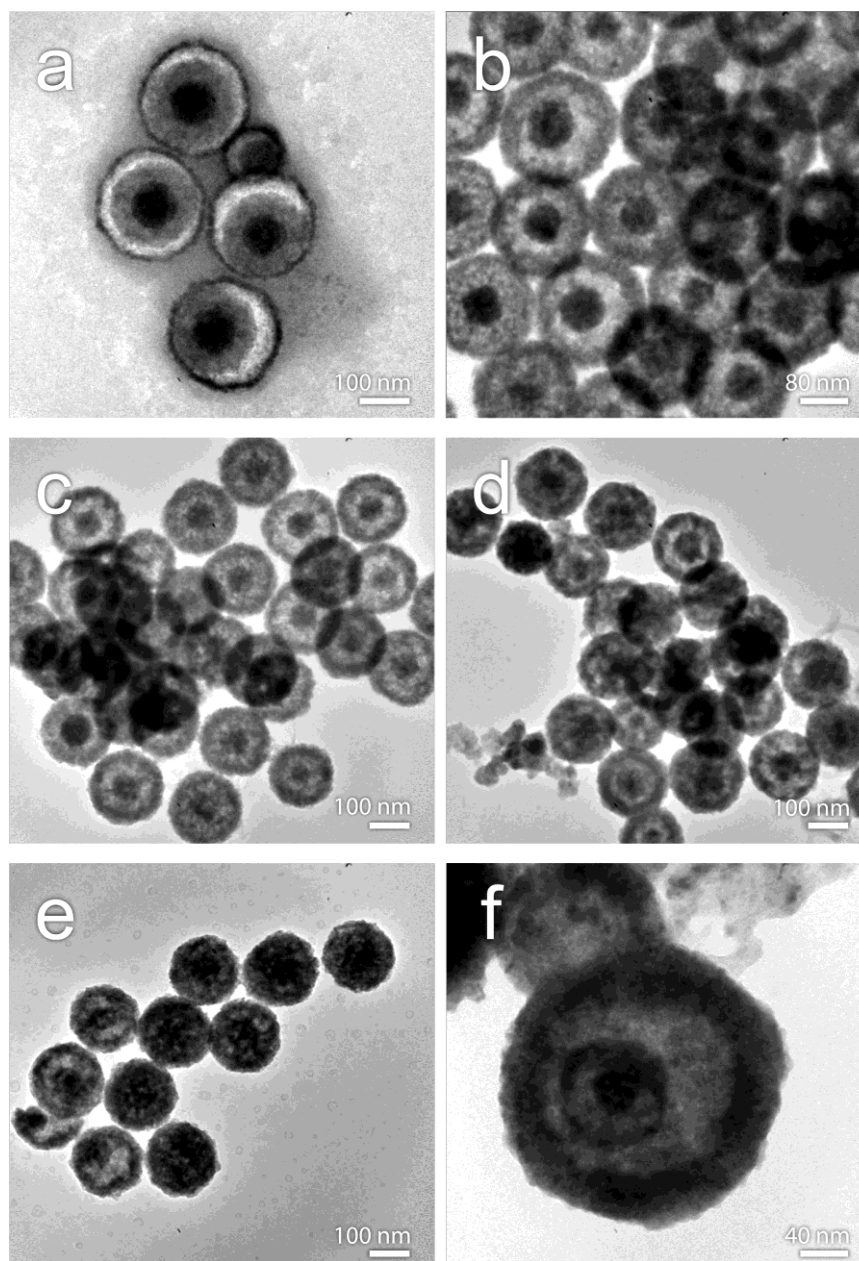


(a) elemental maps of Cu and Pt, (b) line scan analysis, and (c) EDX spectrum.

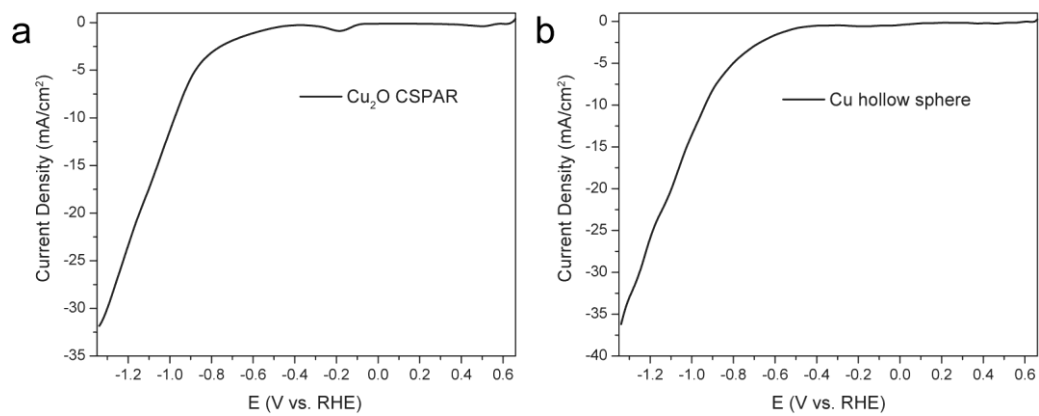
Appendix 2-3E Energy dispersive X-ray analysis of galvanic exchange product of Au³⁺, Pt⁴⁺, and Cu₂O CSPAR

(a) elemental maps of Cu,Au, and Pt, (b) line scan analysis, and (c) EDX spectrum.

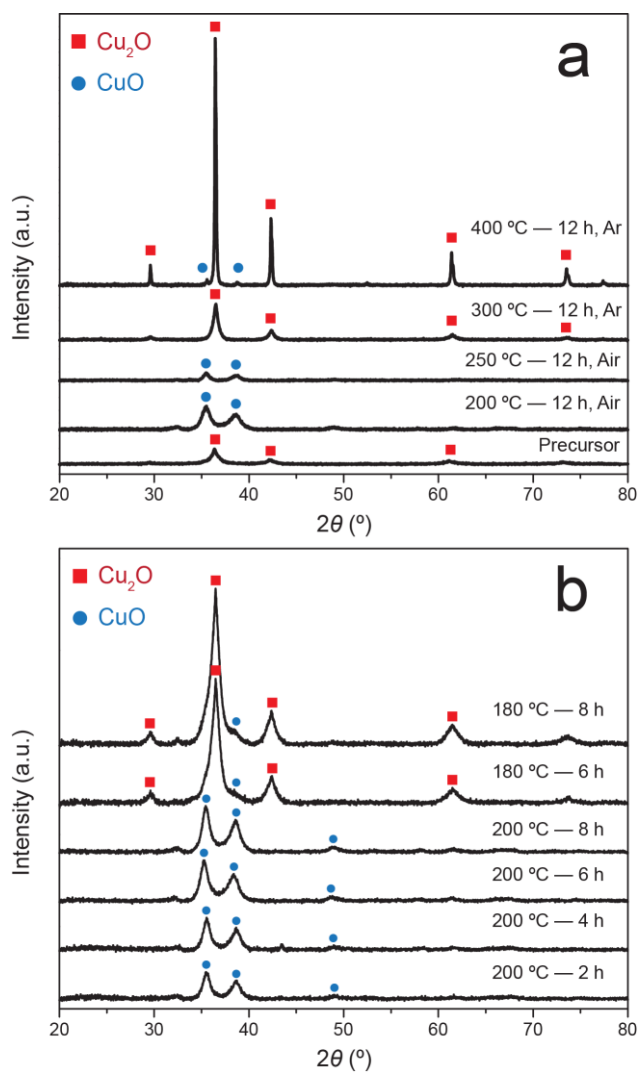
Appendix 2-4A Electrochemical reduction of Cu_2O CSPAR at different amount of applied potential



(a) -0.60, (b) -0.70, (c) -0.80, (d) -0.90, (e) -1.0, and (f) -1.2 V vs. Ag/AgCl/KCl (3.0 M).

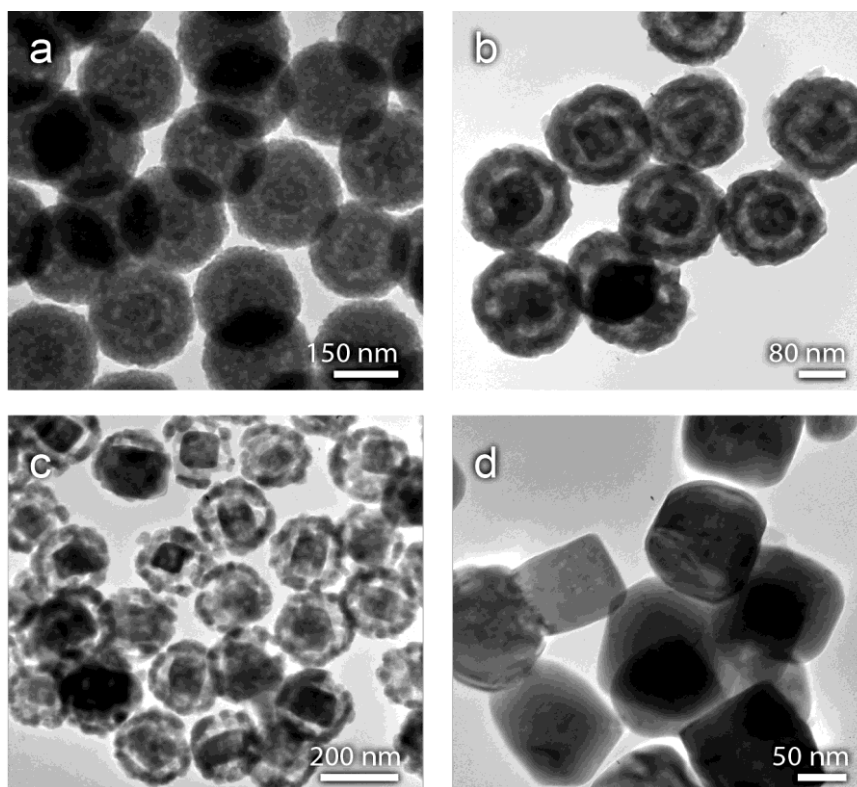
Appendix 2-4B Linear sweep voltammograms of Cu₂O CSPAR and Cu hollow sphere.

Appendix 2-5A XRD patterns of Cu₂O CSPAR and double-layered Cu₂O CSPAR after thermal treatment at various temperatures and atmospheres



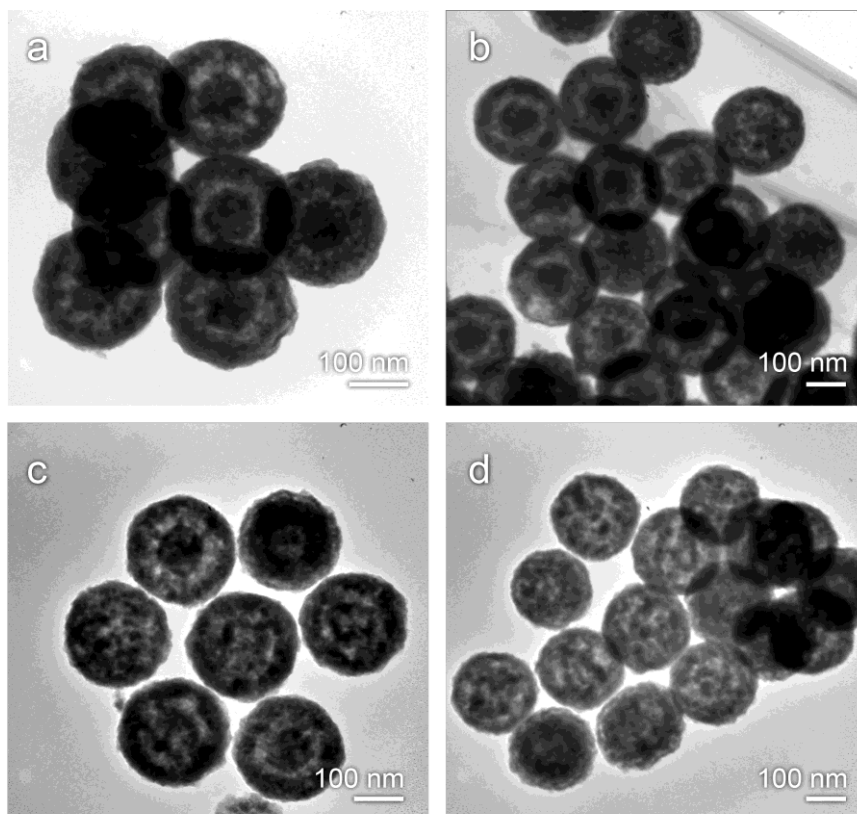
(a) thermal treatment product of Cu₂O CSPAR, and (b) thermal treatment product of double-layered Cu₂O CSPAR under aerobic conditions.

Appendix 2-5B Thermal treatment of Cu₂O CSPAR under Argon flow for 12 hours at various temperatures



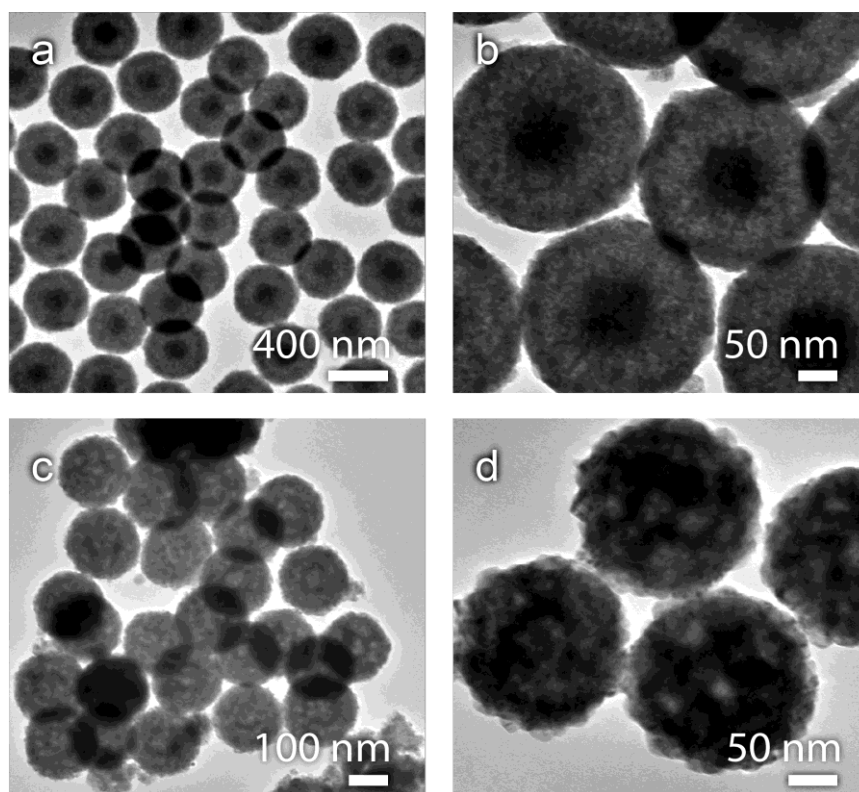
(a) 200, (b) 300, (c) 350, and (d) 400 °C

Appendix 2-5C Thermal treatment of Cu_2O CSPAR 200 °C at ambient atmosphere



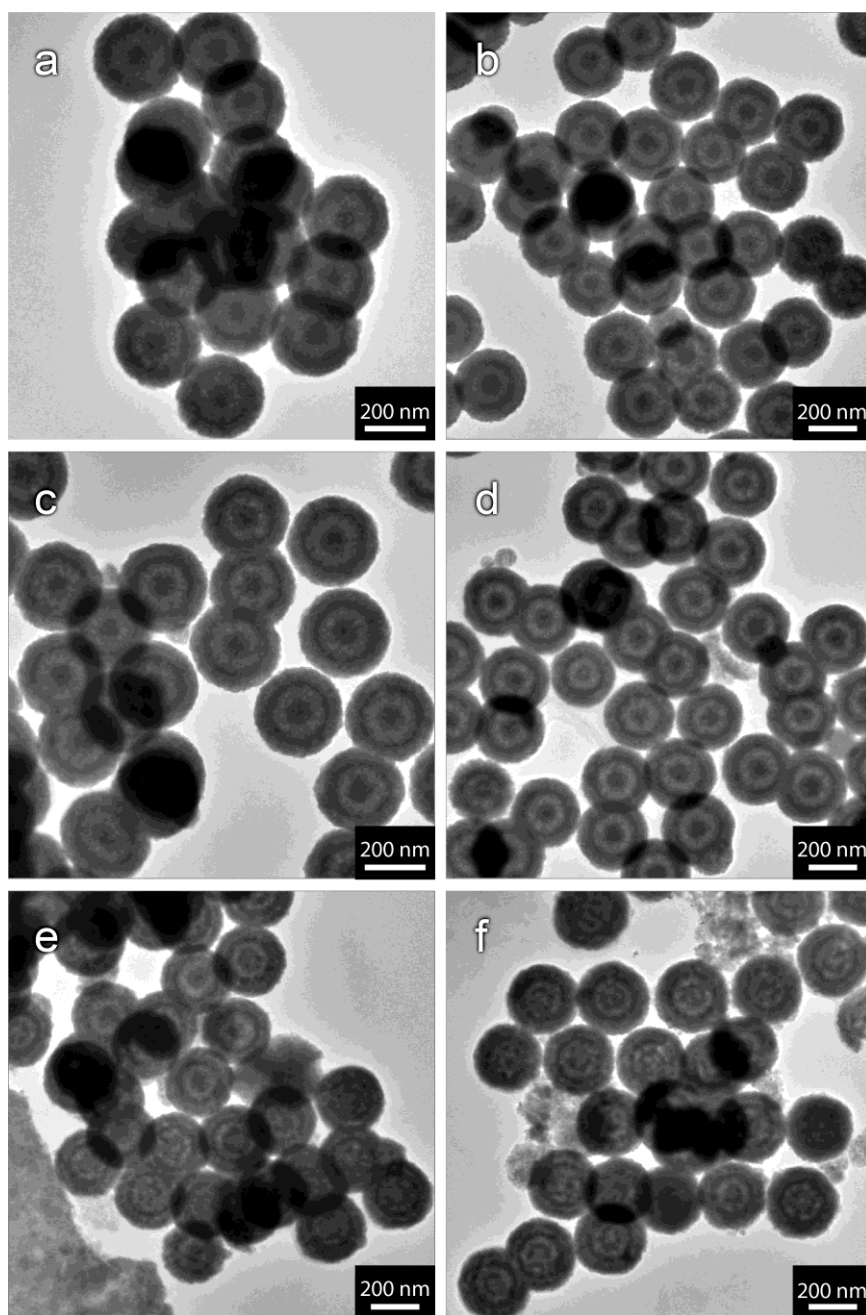
(a) 4, (b) 6, (c) 8, (d) 12 h.

Appendix 2-5D Thermal treatment of Cu_2O CSPAR at various temperatures for 1 hour under ambient atmosphere



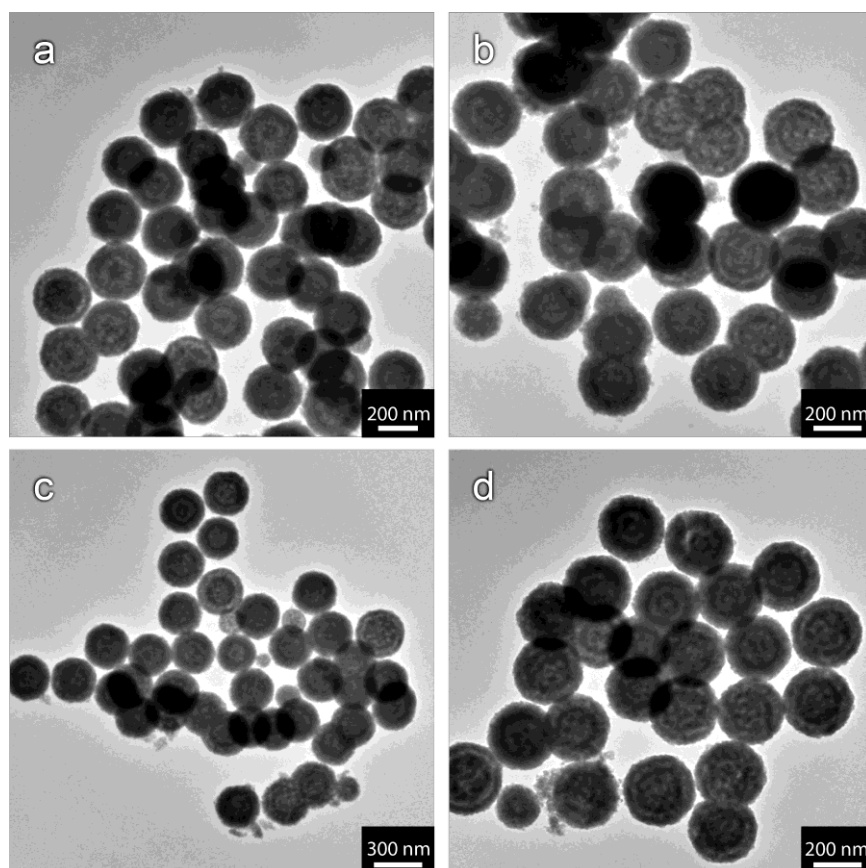
(a) precursor, (b) 200 °C, (c) 300 °C, and (d) 400 °C

Appendix 2-5E Heat Treatment of Cu₂O Double Core-Shell Structure on Cu Plate at 180 °C



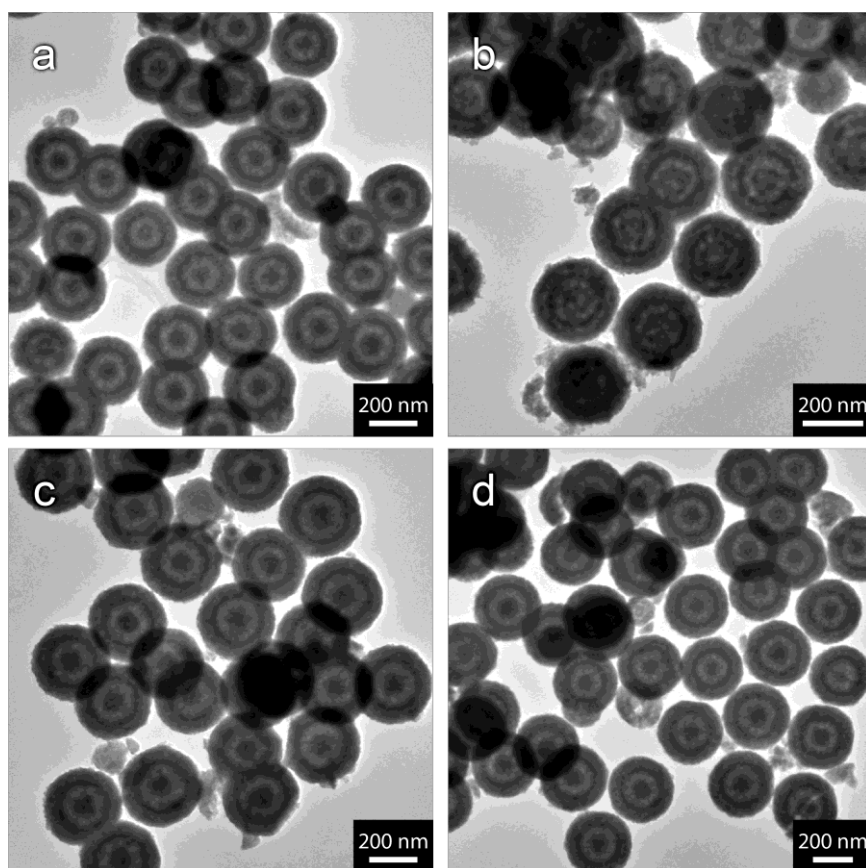
(a) 1 h, (b) 2 h, (c) 4 h, (d) 6 h, (e) 8 h, and (f) 12 h

Appendix 2-5F Heat Treatment of Cu_2O Double Core-Shell Structure on Cu Plate at 200 °C



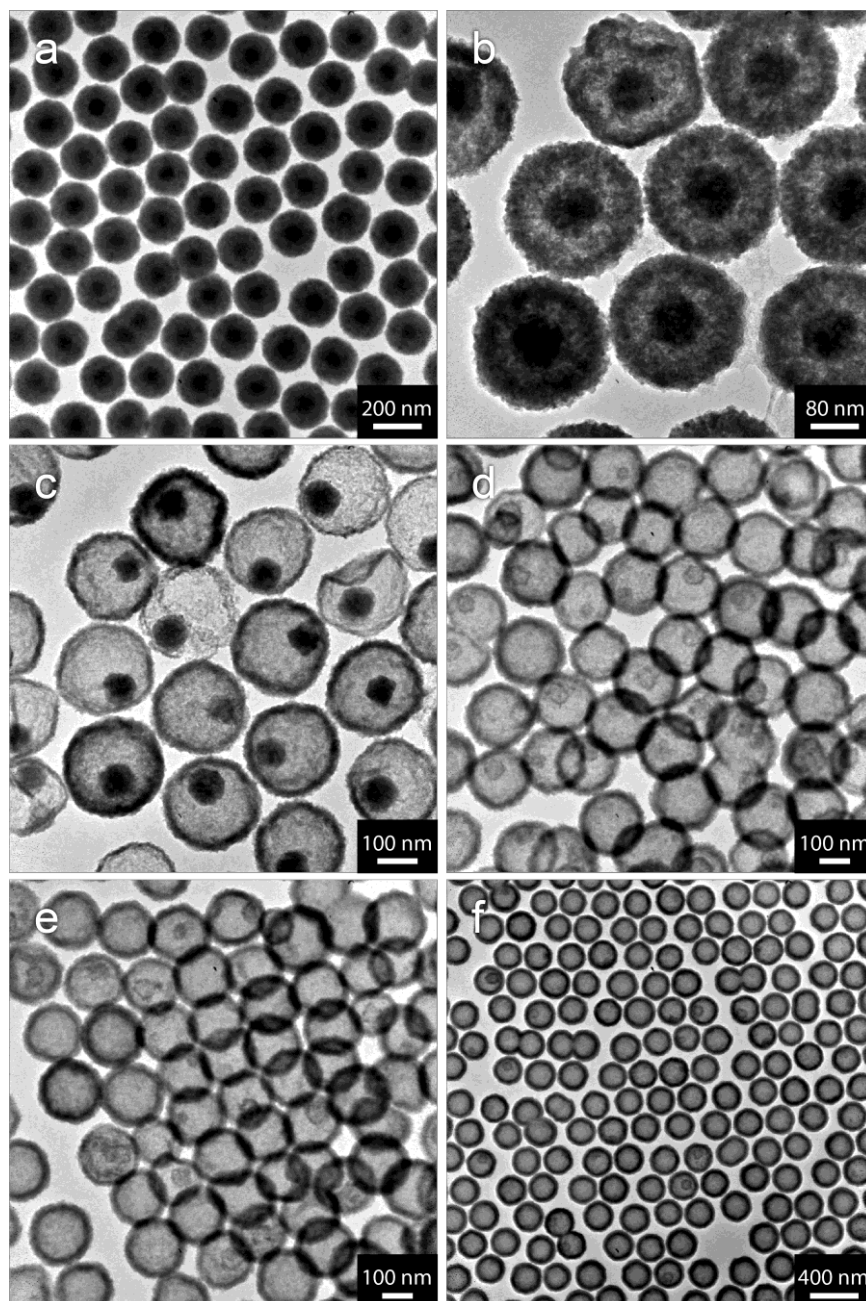
(a) 1 h, (b) 2 h, (c) 4 h, and (d) 8 h

Appendix 2-5G Effect of Cu_2O Double Shell amount on Thermal Treatment Heated at $180\text{ }^\circ\text{C}$



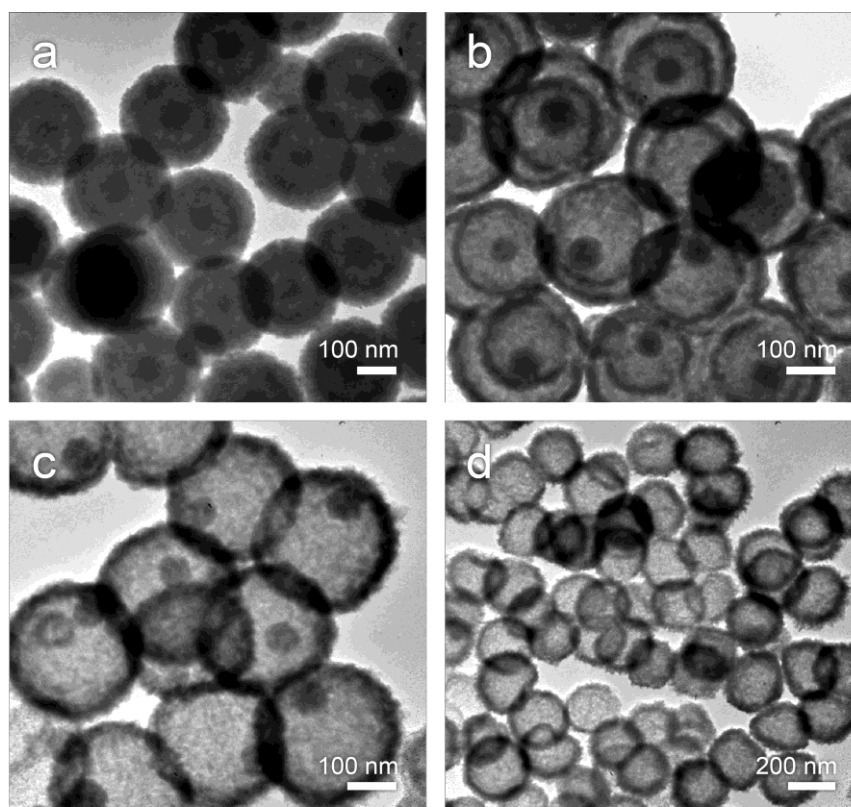
(a) 0.2 mg/cm^2 , 6 h, (b) 0.2 mg/cm^2 , 8 h, (c) 0.4 mg/cm^2 , 6 h, and (d) 0.4 mg/cm^2 , 8 h.

Appendix 2-6A Anion exchange reaction of Cu_2O with $(\text{NH}_4)_2\text{S}$ at various $\text{Cu}_2\text{O}:(\text{NH}_4)_2\text{S}$ ratio reacted for 10 min



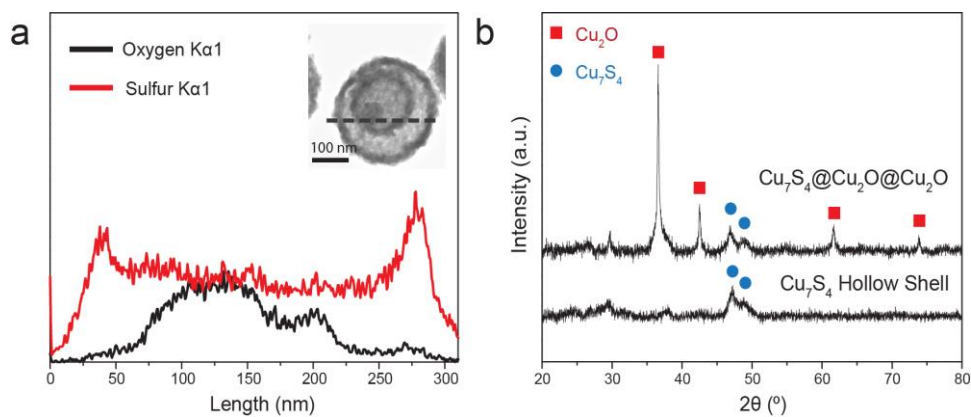
(a) precursor, (b) 1:0.4, (c) 1:0.8, (d) 1:1.6, (e) 1:32, and (f) 1:60.

Appendix 2-6B Extension of anion exchange reaction on double-shelled Cu_2O CSPAR at various $\text{Cu}_2\text{O}:(\text{NH}_4)_2\text{S}$ ratio



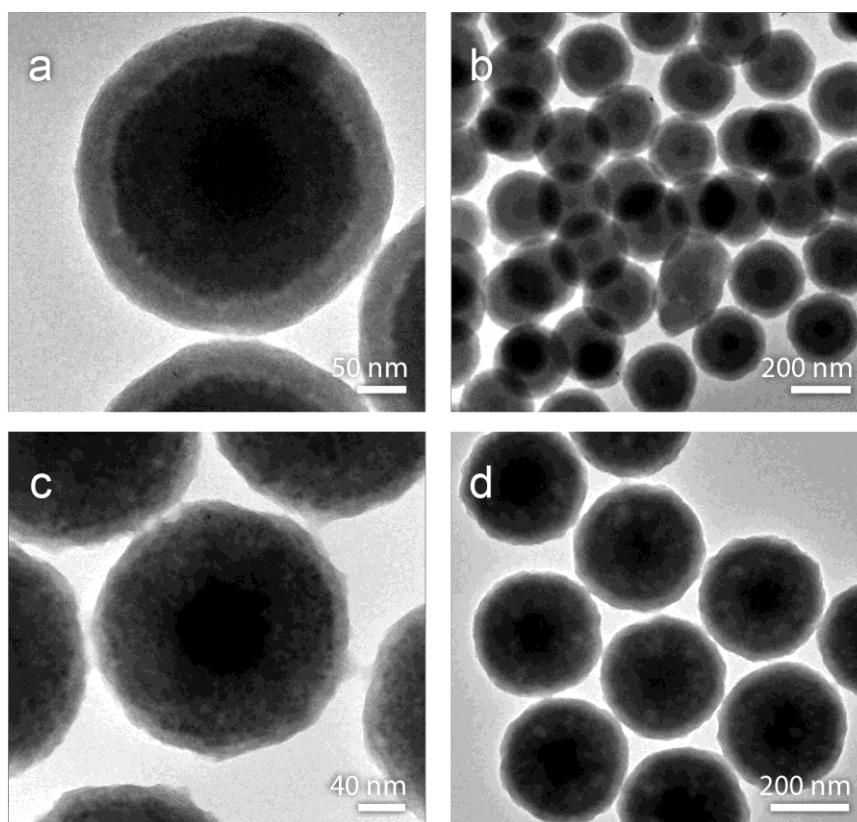
(a) precursor (b) 1:0.5, (c) 1:0.6, and (d) 1:1

Appendix 2-6C Additional characterization of anion exchange product of double-shelled Cu_2O CSPAR



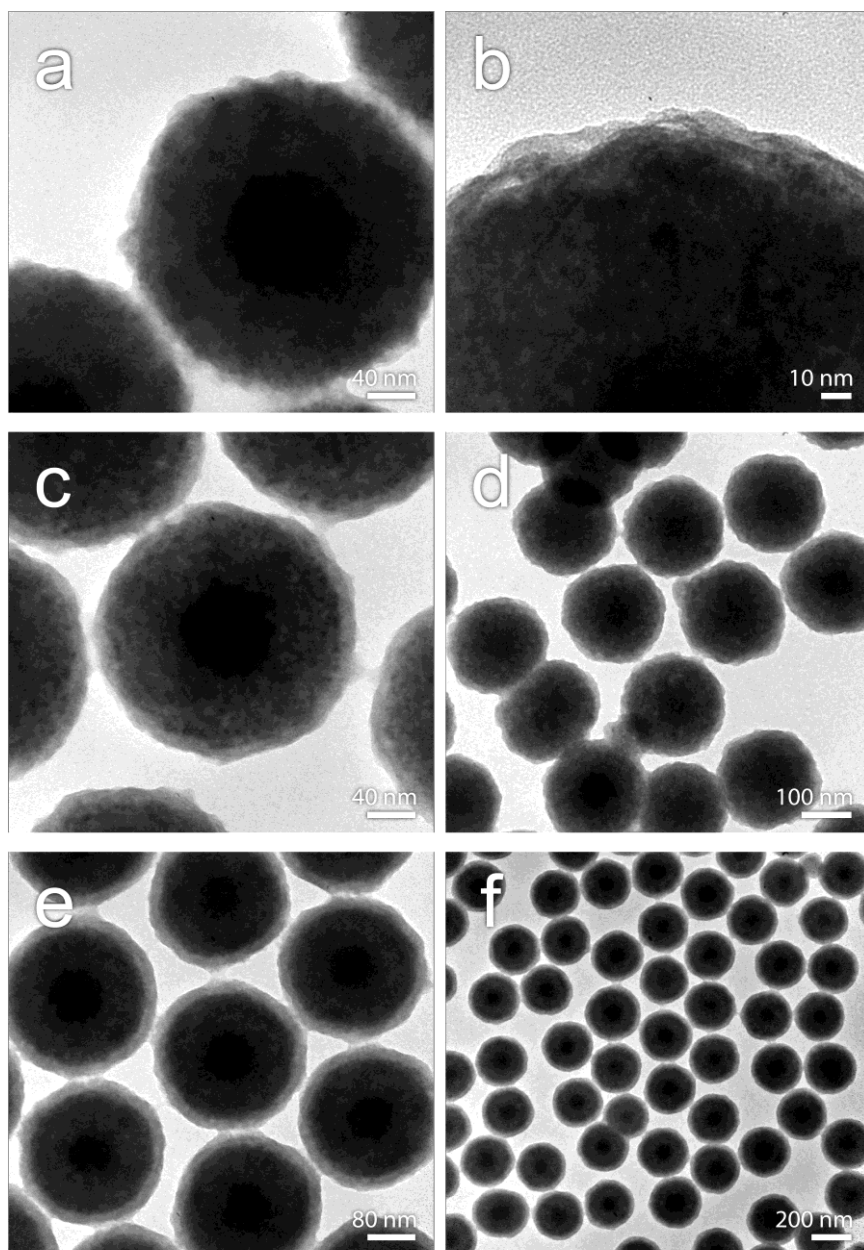
(a) EDX-line scan of partially reacted double-shelled Cu_2O CSPAR, and (b) X-ray diffraction characterization of partially and completely reacted double-shelled Cu_2O CSPAR.

Appendix 2-7A Effect of NaOH amount on the passivation of Cu_2O CSPAR



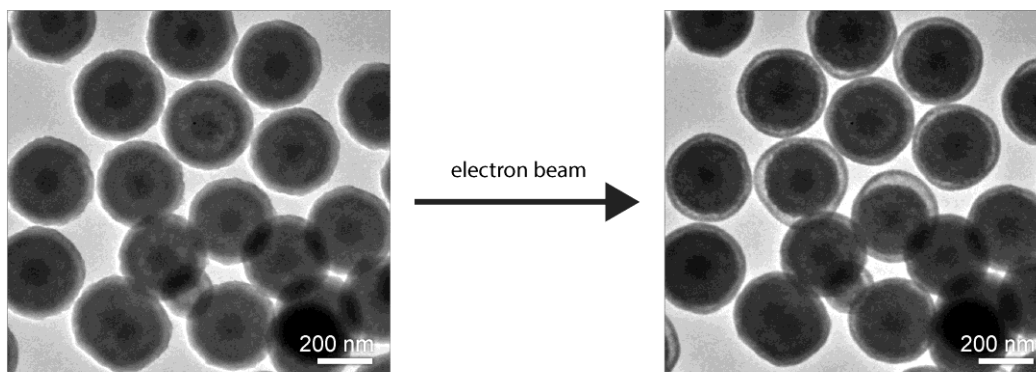
(a-b) 1.50 mL of 1.0 M NaOH and (c-d) 2.00 mL of 1.0 M NaOH (Reaction duration: 25 min).

Appendix 2-7B Effect of reaction duration on Zn(OH)₂ passivation of Cu₂O CSPAR using 2.0 mL of 1.0 M NaOH

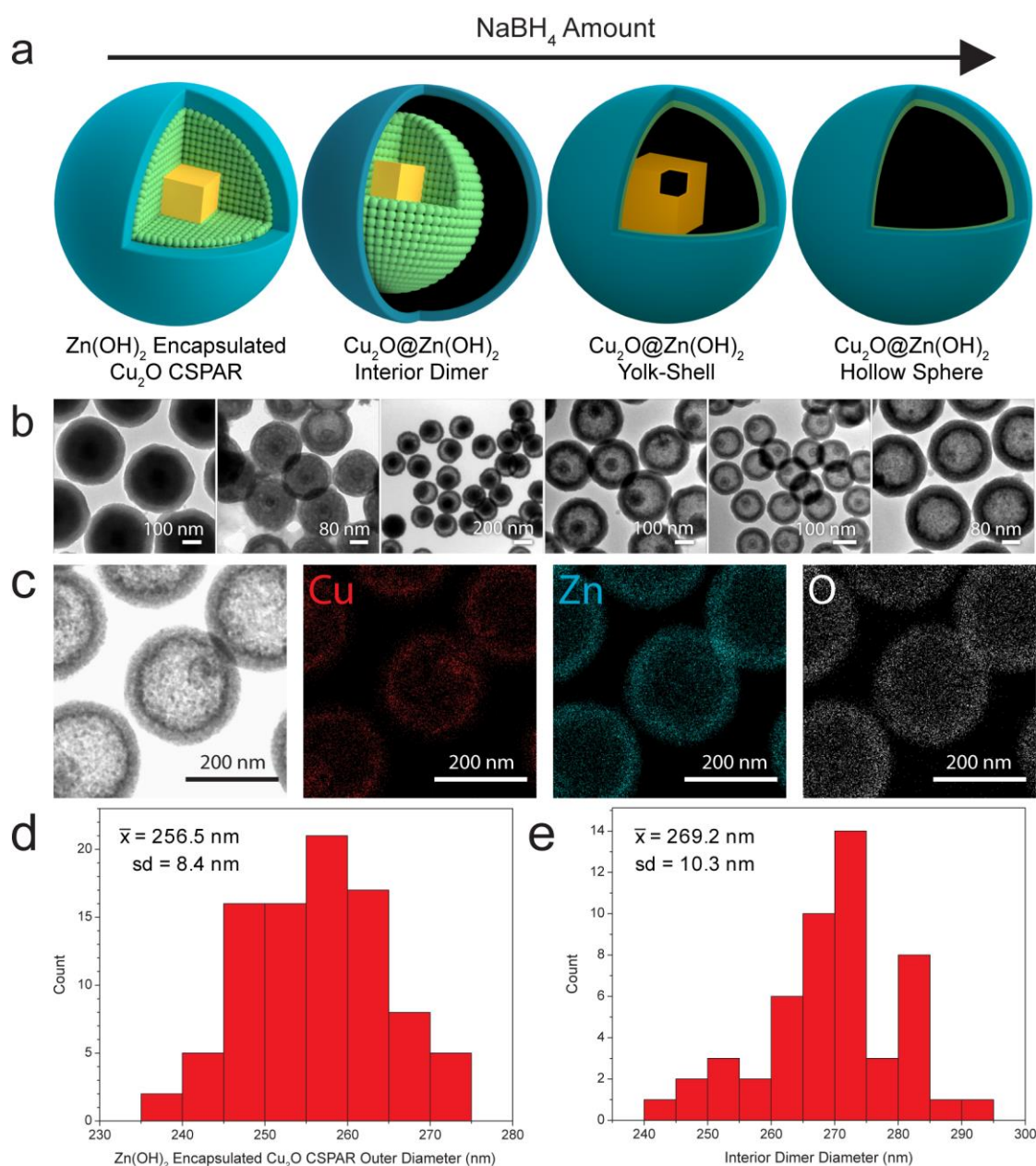


(a-b) 15, (c-d) 25, and (e-f) 50 min.

Appendix 2-7C Effect of prolonged electron beam exposure on Zn(OH)_2 passivated CSPAR

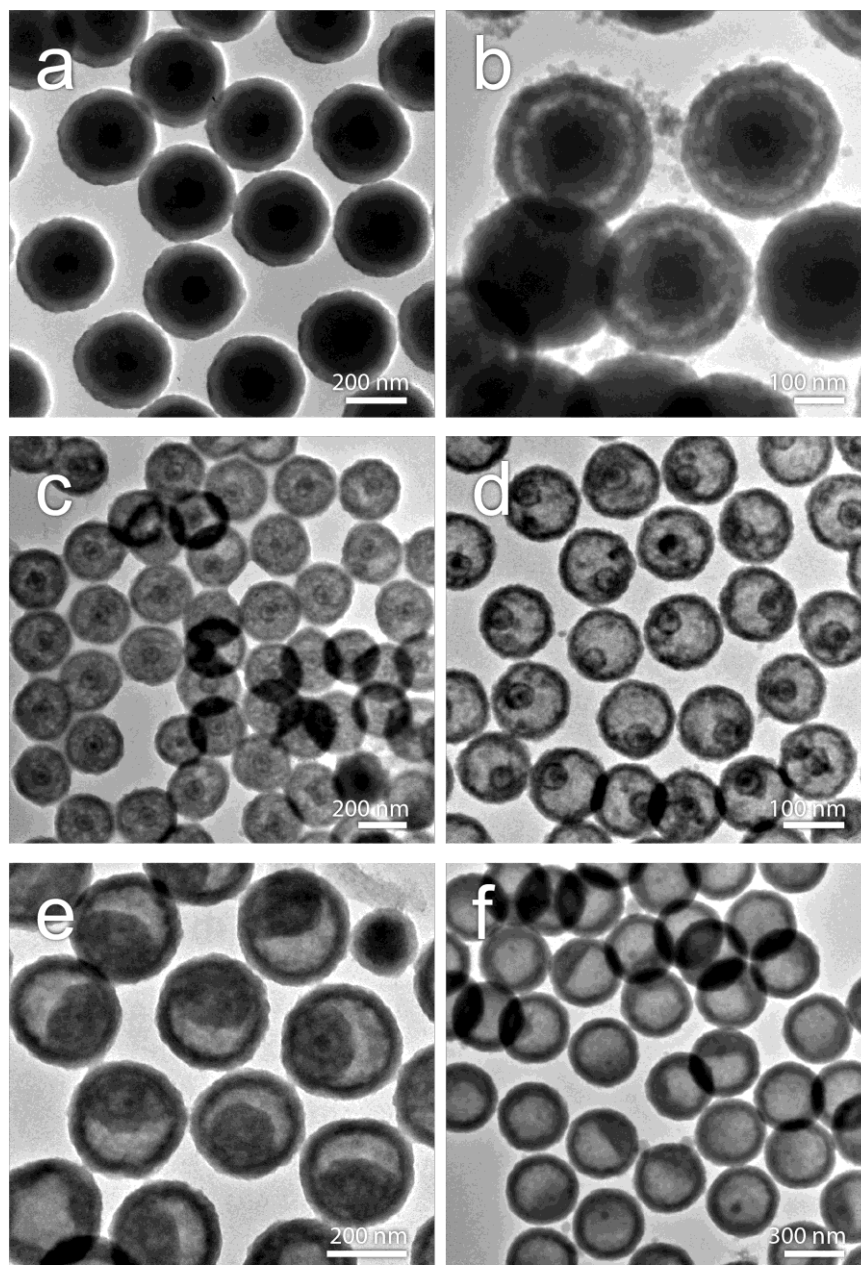


Appendix 2-8A Transformation of as-synthesized $\text{Zn}(\text{OH})_2$ encapsulated Cu_2O CSPAR during reduction-complexation reaction



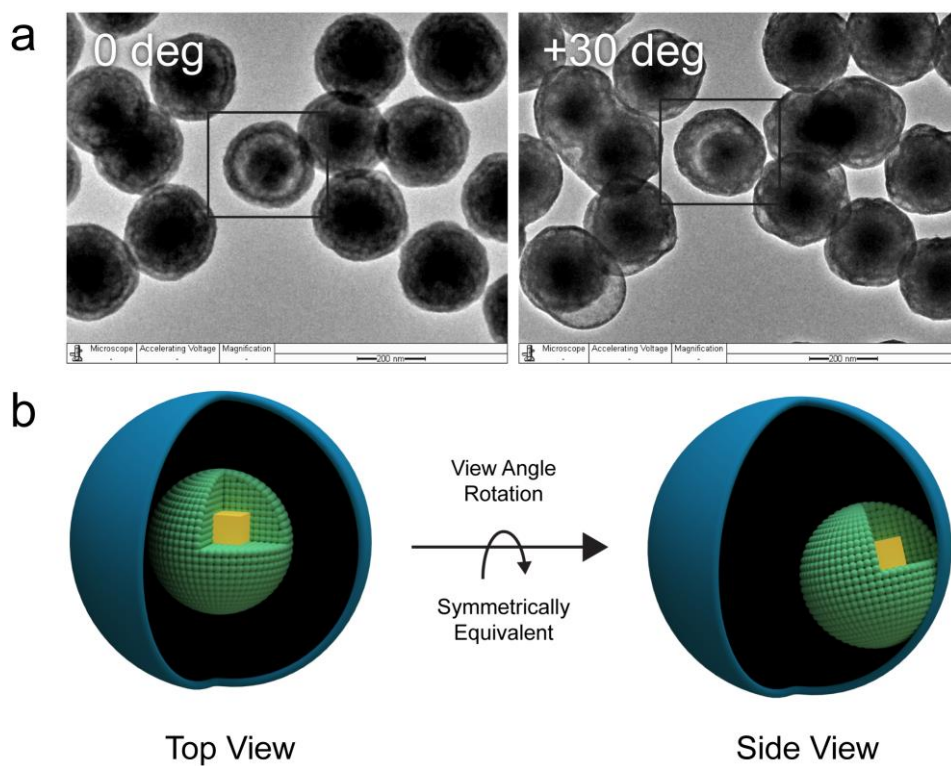
(a) Schematic illustration of structural changes of $\text{Zn}(\text{OH})_2$ encapsulated Cu_2O CSPAR as a function of NaBH_4 amount. (b) Corresponding TEM image of the reduction-complexation product using 1.00 mL of 0, 180, 200, 210, 220, and 240 mg/mL NaBH_4 solution, respectively. (c) STEM image and EDX elemental maps of the reduction-complexation product, and particle size distribution of (d) $\text{Zn}(\text{OH})_2$ passivated CSPAR and (e) $\text{Cu}_2\text{O}@Zn(\text{OH})_2$ interior dimer.

Appendix 2-8B TEM images of the reduction-complexation product of as-synthesized Zn(OH)₂ passivated CSPAR at different reaction durations and NaBH₄ amount



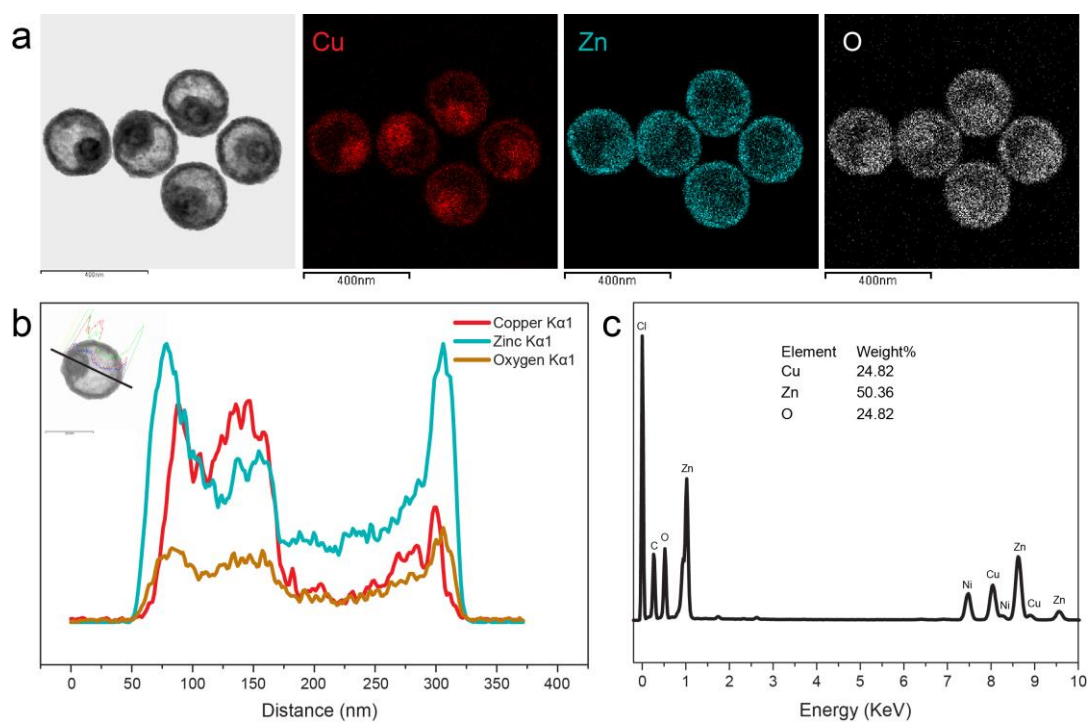
(a) 15 min, 150 mg, (b) 90 min, 150 mg, (c) 15 min, 180 mg, (d) 30 min, 180 mg, (e) 15 min, 200 mg, and (f) 90 min, 200 mg.

Appendix 2-8C Symmetrical feature of $\text{Cu}_2\text{O}@Zn(\text{OH})_2$ interior dimer



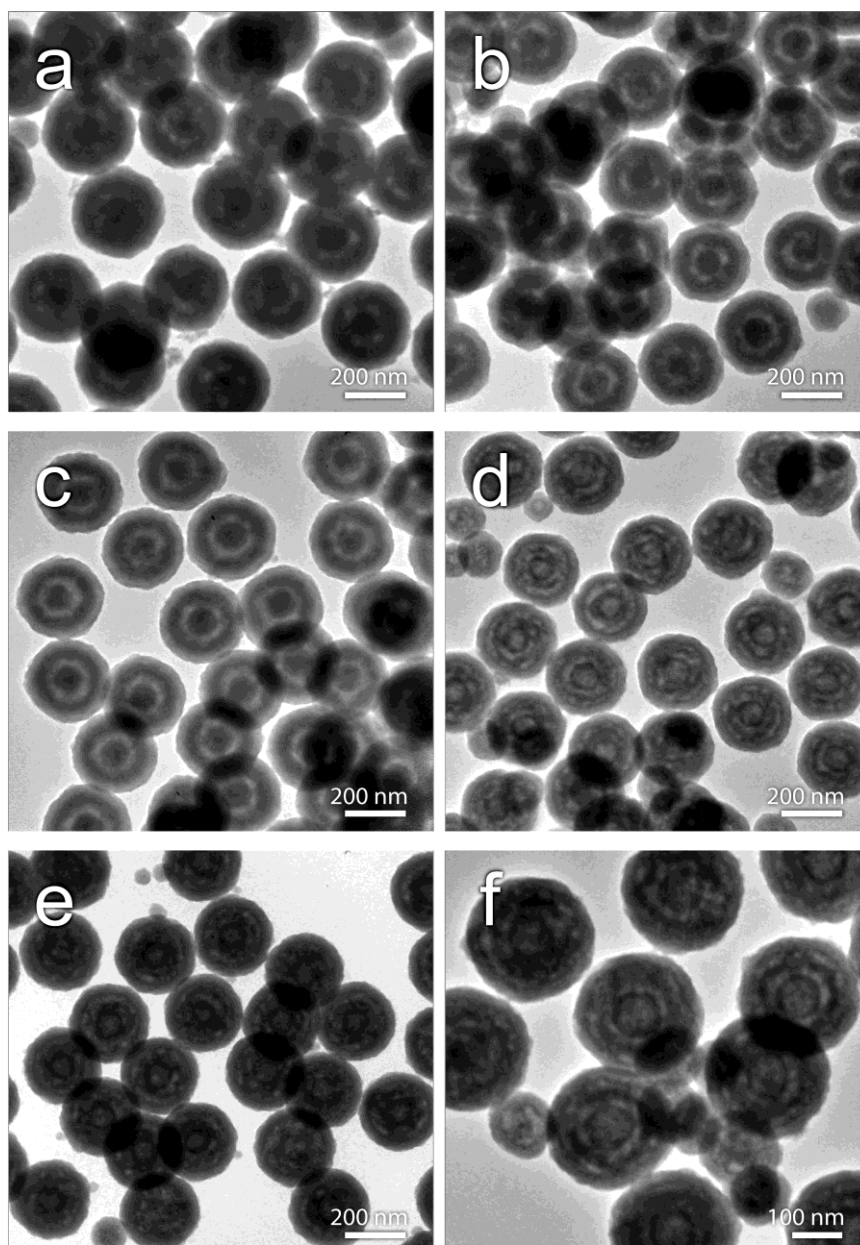
(a) TEM images of $\text{Cu}_2\text{O}@Zn(\text{OH})_2$ interior dimer at different x-axis angle. (b) Schematic diagram of the symmetrical equivalence of $\text{Cu}_2\text{O}@Zn(\text{OH})_2$ interior dimers.

Appendix 2-8D Energy dispersive X-ray analysis of thermal treated $\text{Cu}_2\text{O}@Zn(\text{OH})_2$



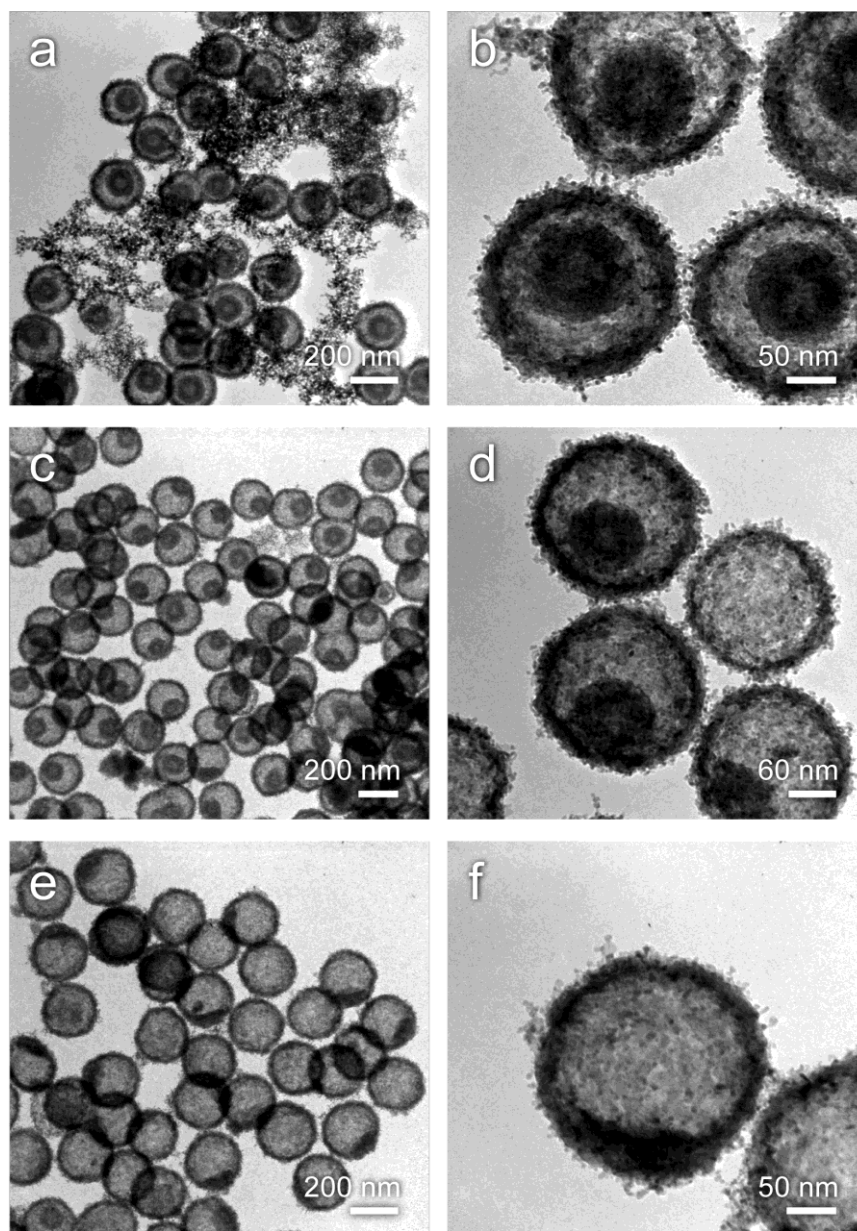
(a) Elemental maps of Cu, Zn, and O, (b) line scan analysis, and (c) EDX spectrum.

Appendix 2-8E Reduction-complexation product of as-synthesized Zn(OH)₂ passivated CSPAR using a 260 nm Cu₂O CSPAR precursor at various amount of NaBH₄



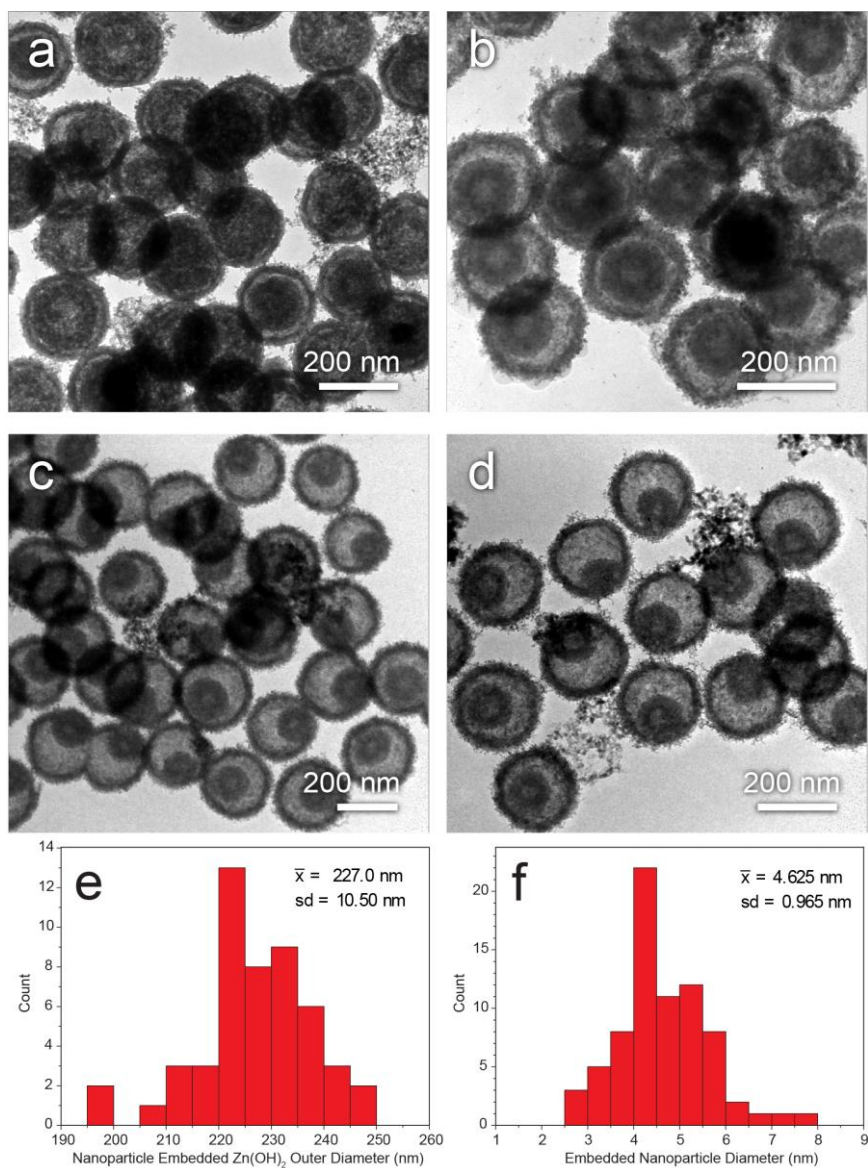
(a) 60, (b) 100, (c) 150, (d) 160, (e) 180, and (f) 200 mg. (Reaction duration: 15 min).

Appendix 2-8F TEM images of the reduction-complexation product of Zn(OH)₂ passivated CSPAR under low ionic concentration at different reaction durations



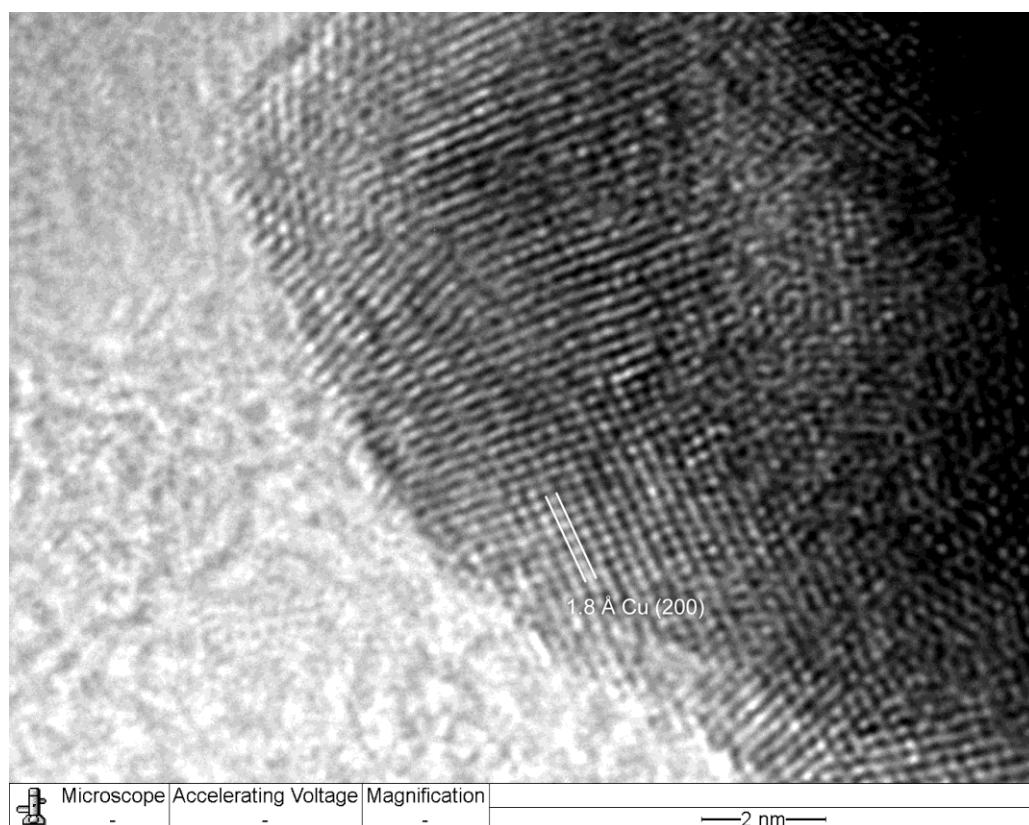
(a-b) 5, (c-d) 30, and (e-f) 60 min. (NaBH₄ amount: 150 mg)

Appendix 2-8G TEM images of the reduction-complexation product of Zn(OH)_2 passivated CSPAR under low ionic concentration at different NaBH_4 amount

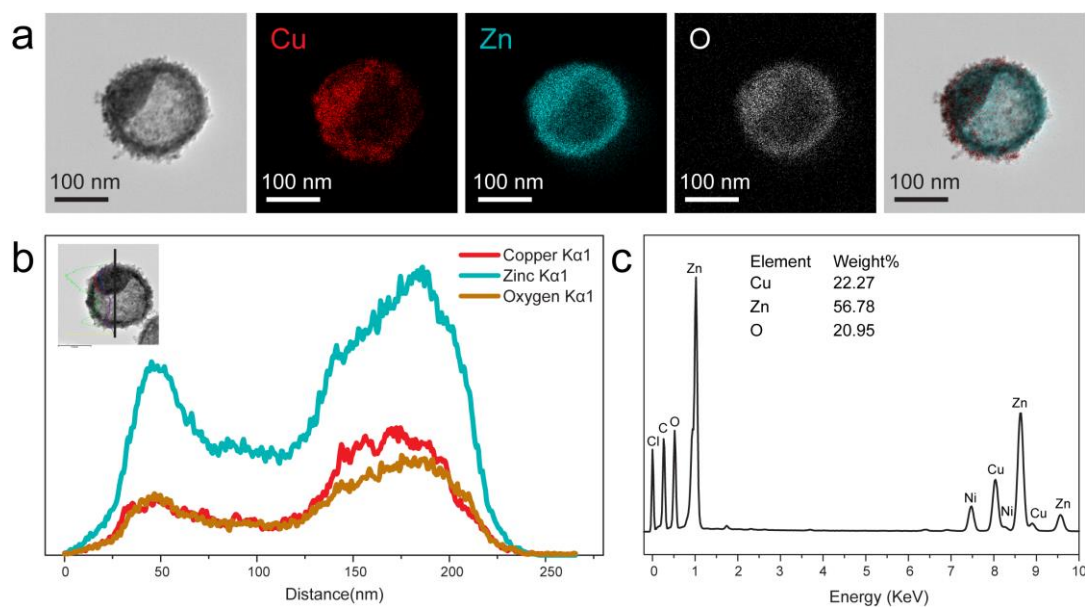


(a) 100, (b) 150, (c) 200, and (d) 300 mg. Size distribution of (e) outer diameter of reduction product, and (f) embedded nanoparticles. (Reaction duration: 5 min.)

Appendix 2-8H High resolution TEM image of Cu nanoparticle embedded Zn(OH)₂ hollow sphere

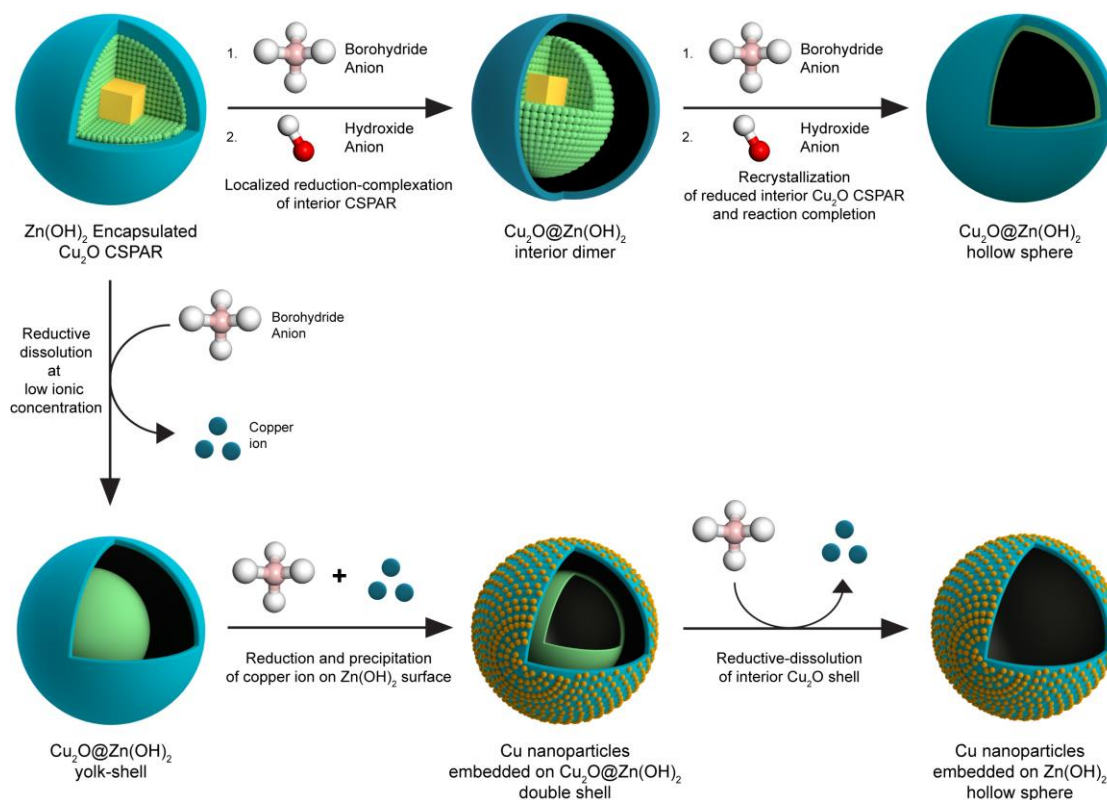


Appendix 2-8I Energy dispersive X-ray analysis of Cu nanoparticles embedded on Zn(OH)₂ hollow sphere



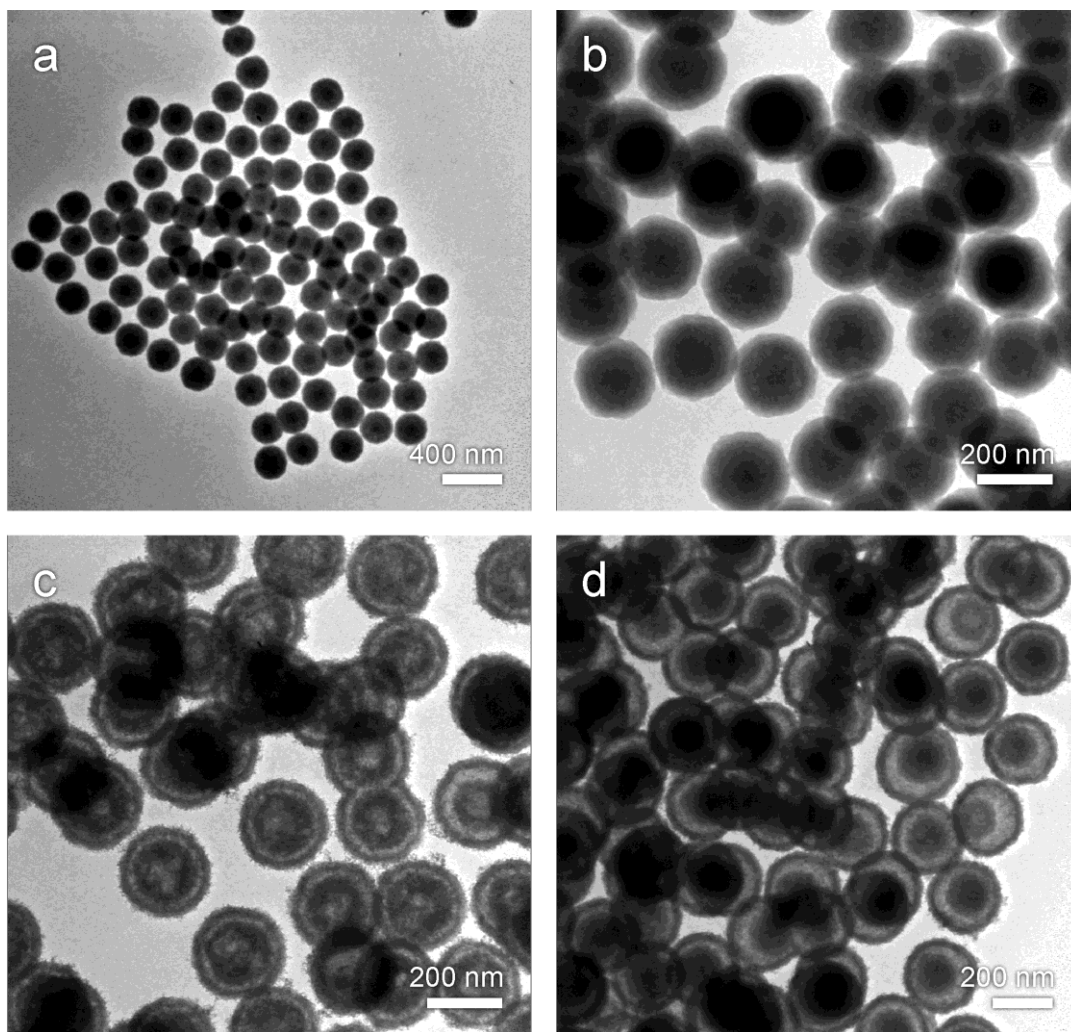
(a) elemental maps of Cu, Zn, and O, (b) line scan analysis, and (c) EDX spectrum.

Appendix 2-8J Schematic illustration of proposed transformation mechanism of $\text{Zn}(\text{OH})_2$ passivated Cu_2O CSPAR during reduction-complexation reactions



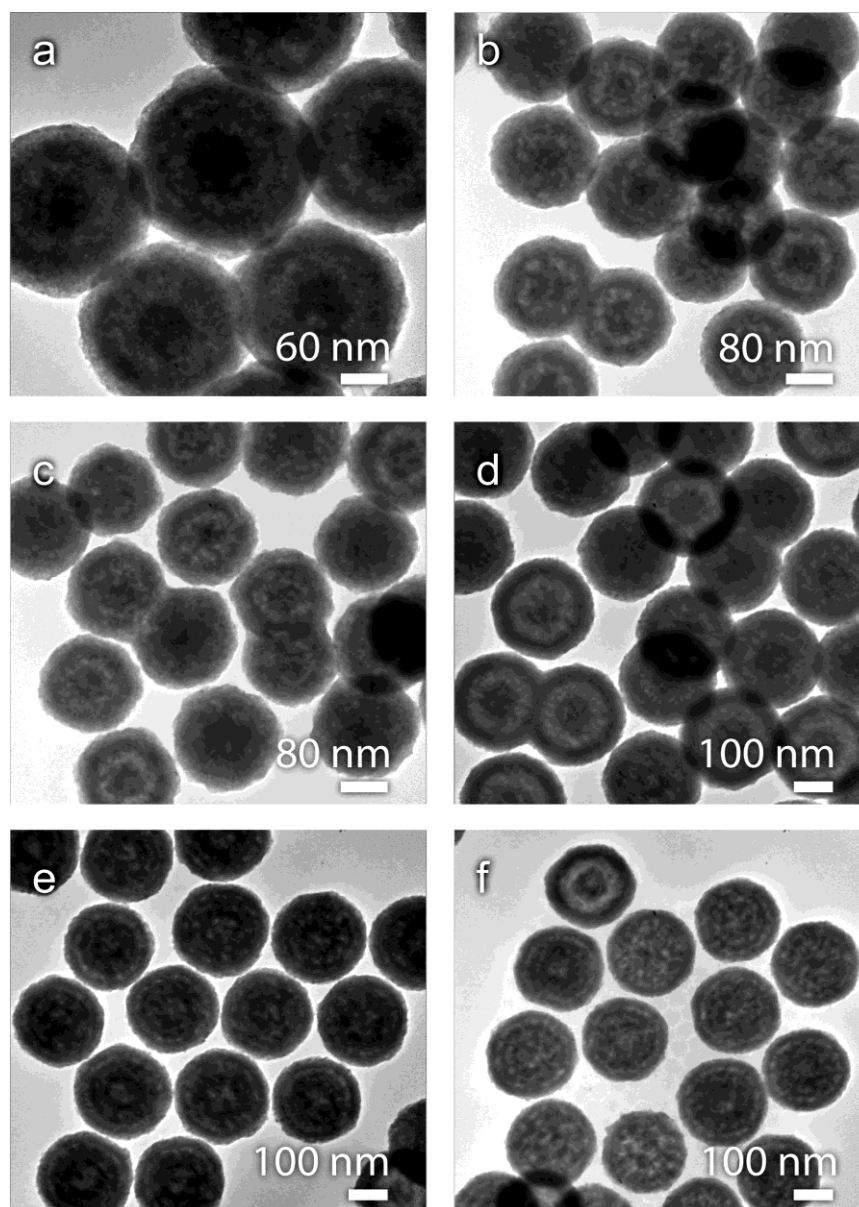
During the reduction of as-synthesized $\text{Zn}(\text{OH})_2$ passivated Cu_2O CSPAR, BH_4^- diffuses into the particle interior and reacts with Cu_2O at the $\text{Cu}_2\text{O}/\text{Zn}(\text{OH})_2$ interface. However, this process occurs locally due to uneven $\text{Zn}(\text{OH})_2$ shell thickness. In addition, OH^- would also dissolve interior Cu_2O to form an interior dimer and the dissolve $\text{Cu}(\text{OH})_4^{2-}$ would be reduced and precipitate at the interior $\text{Zn}(\text{OH})_2$ region. Whereas, this reduction-complexation process results in different product at low ionic concentration. At this condition, the same reductive dissolution occurs but dissolve copper ion can be reduced and precipitate at the exterior surface of $\text{Zn}(\text{OH})_2$ due to lower alkalinity. Extending the duration of this process results in complete dissolution of interior Cu_2O thus forming a Cu nanoparticle embedded on $\text{Zn}(\text{OH})_2$ hollow sphere.

Appendix 2-8K Up scaled synthesis and reactions of Cu_2O CSPAR, $\text{Zn}(\text{OH})_2$ passivated CSPAR, and Cu nanoparticle embedded $\text{Zn}(\text{OH})_2@ \text{Cu}_2\text{O}$

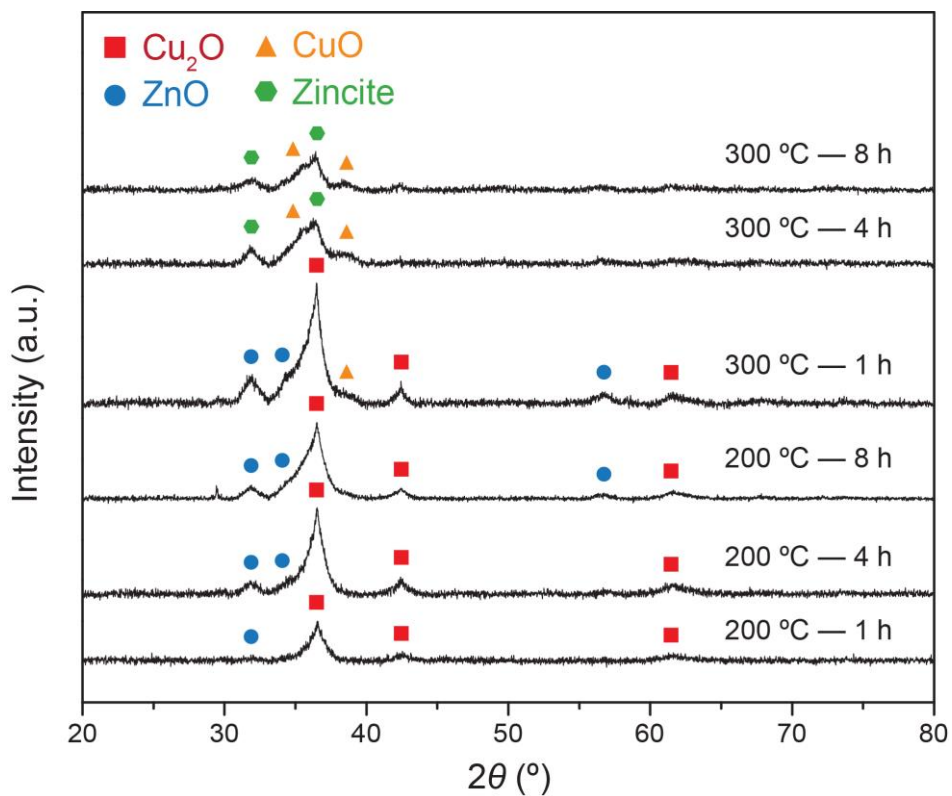


(a) Cu_2O CSPAR, (b) $\text{Zn}(\text{OH})_2$ passivated CSPAR, and (c and d). Cu nanoparticle embedded $\text{Zn}(\text{OH})_2@ \text{Cu}_2\text{O}$.

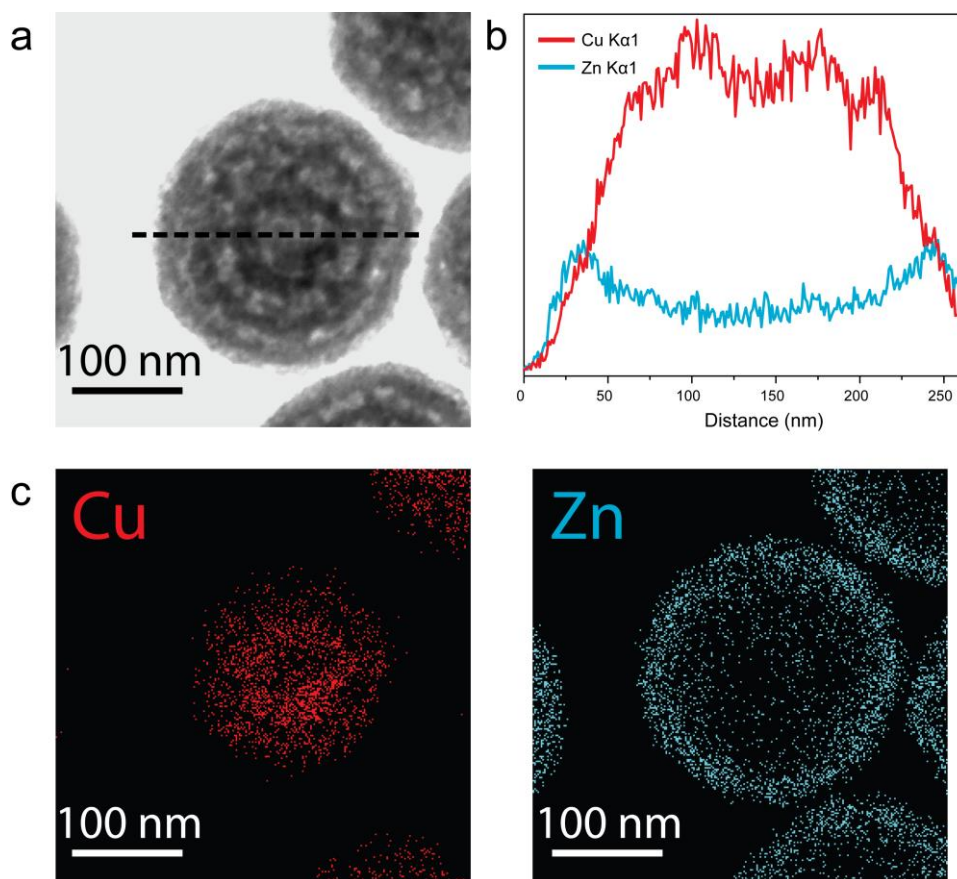
Appendix 2-9A TEM image of the calcined product of $\text{Zn}(\text{OH})_2$ passivated CSPAR at different temperature and durations



(a) 200 °C, 1 h, (b) 200 °C, 4 h, (c) 200 °C, 8 h, (d) 300 °C 1 h, (e) 300 °C, 4 h, and (f) 300 °C, 8 h.

Appendix 2-9B XRD patterns of Zn(OH)₂ passivated Cu₂O CSPAR during aerobic thermal decomposition at various temperatures

Appendix 2-9C Energy dispersive X-ray analysis of the decomposition product of Zn(OH)₂-passivated CSPAR at 300 °C



(a) STEM image of the product, (b) line scan analysis, and (c) Cu and Zn elemental map of the product.

Appendix 2-10 Summary of valence band energy level, conduction band energy level, work functions, band gaps used to construct Fig. 4.4a and 4.4b. The references of the values are given in the final column.

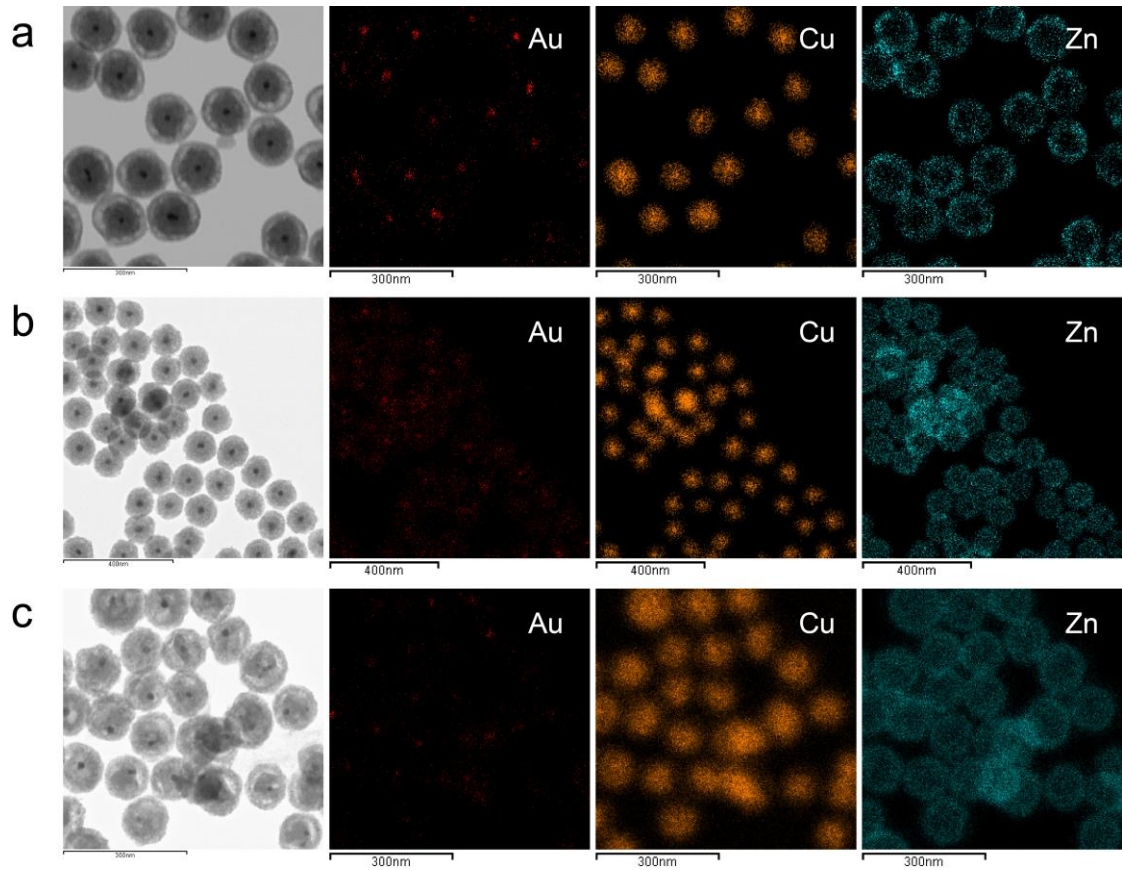
Material	E_v (eV)	E_c (eV)	Work Function (eV)	Band Gap (eV)	Reference
Cu ₂ O	-5.5	-3.2	4.9	2.3	3
ZnO	-7.2	-3.9	4.2	3.3	4,5

Reference

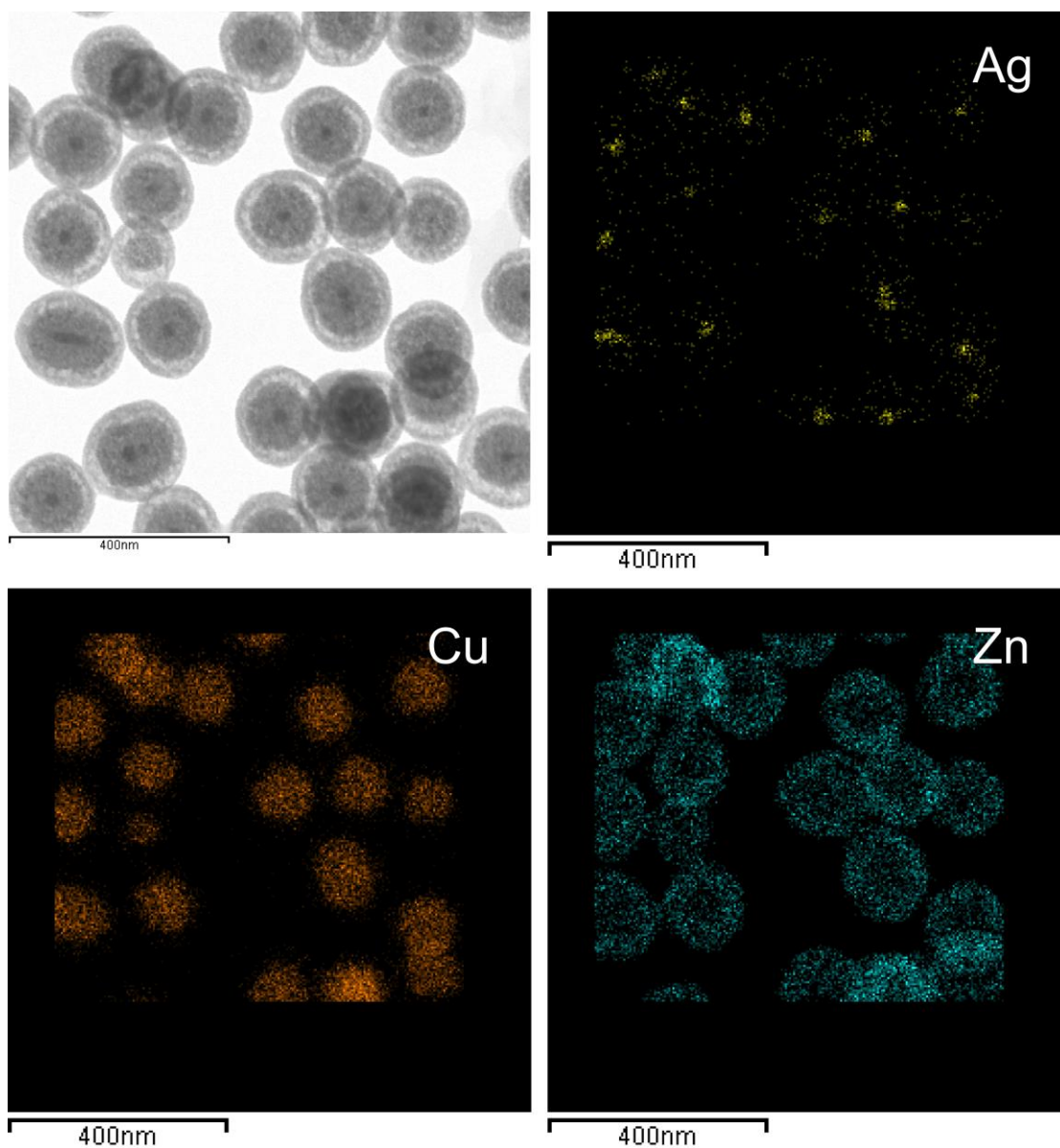
- 1 Kiema, G. K., Aktay, M. & McDermott, M. T. Preparation of reproducible glassy carbon electrodes by removal of polishing impurities. *J Electroanal Chem* **540**, 7-15, doi:10.1016/S0022-0728(02)01264-0 (2003).
- 2 Halpern, J. Kinetics of the Dissolution of Copper in Aqueous Ammonia. *J Electrochem Soc* **100**, 421-428, doi:10.1149/1.2780873 (1953).
- 3 Greiner, M.T., Helander, M.G., Tang, W.M., Wang, Z.B., Qiu, J. & Lu, Z.H. Universal energy-level alignment of molecules on metal oxides. *Nat. Mater.* **11**, 76-81, doi:10.1038/nmat3159 (2012)
- 4 Mora-Sero, I., Bertoluzzi, L., Gonzalez-Pedro, V., Gimenez, S., Fabregat-Santiago, F., Kemp, K.W., Sargent, E.H. & Bisquert, J. Selective contacts drive charge extraction in quantum dot solids via asymmetry in carrier transfer kinetics. *Nat. Commun.* **4**, doi:10.1038/ncomms3272 (2013)
- 5 Gutmann, S., Conrad, M., Wolak, M. A., Beerbom, M. M. & Schlaf, R. Work function measurements on nano-crystalline zinc oxide surfaces. *J. Appl. Phys.* **111**, 123710, doi/10.1063/1.4729527 (2012).

Appendix 3

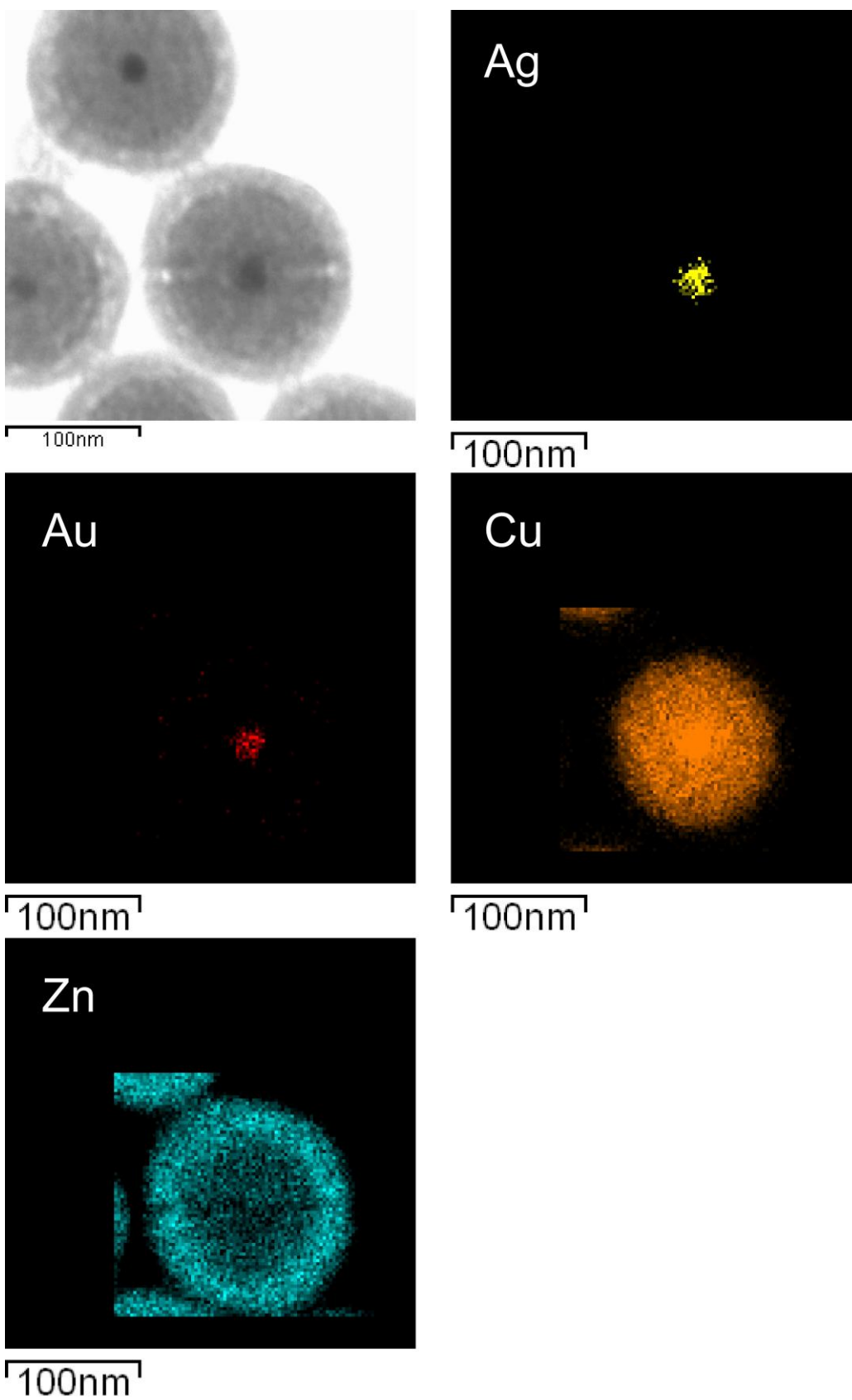
Appendix 3-1A EDX Elemental Mapping of M@Cu₂O@Zn(OH)₂ (M = Au, Ag, Au/Ag, and Pd) Core-Shell Structures



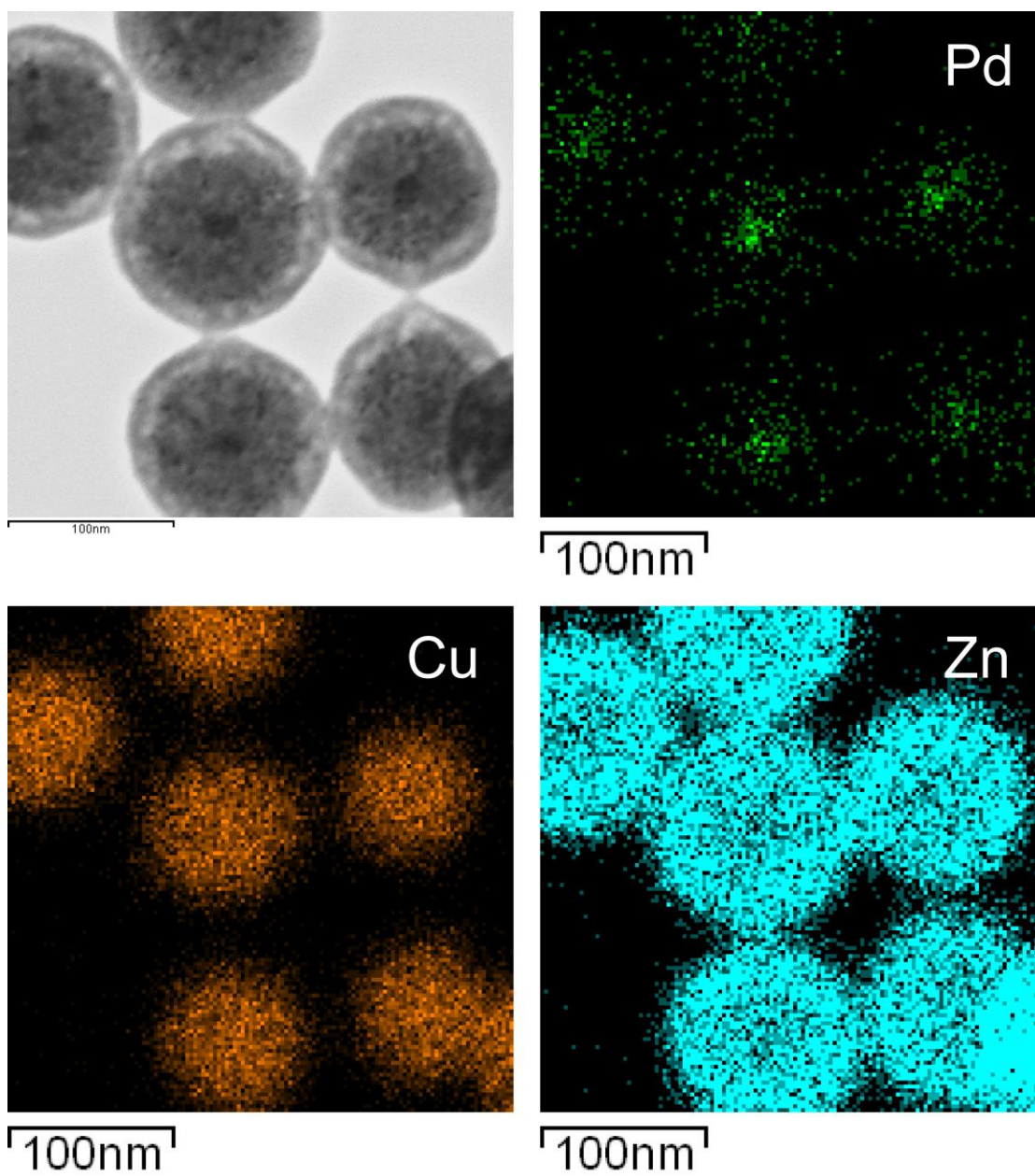
Elemental mapping for Au@Cu₂O@Zn(OH)₂: (a) as-synthesized Au@Cu₂O@Zn(OH)₂, (b) heat-treated at 200 °C for 12 h, and (c) heat-treated at 300 °C for 12 h.



Elemental mapping for Ag@Cu₂O@Zn(OH)₂

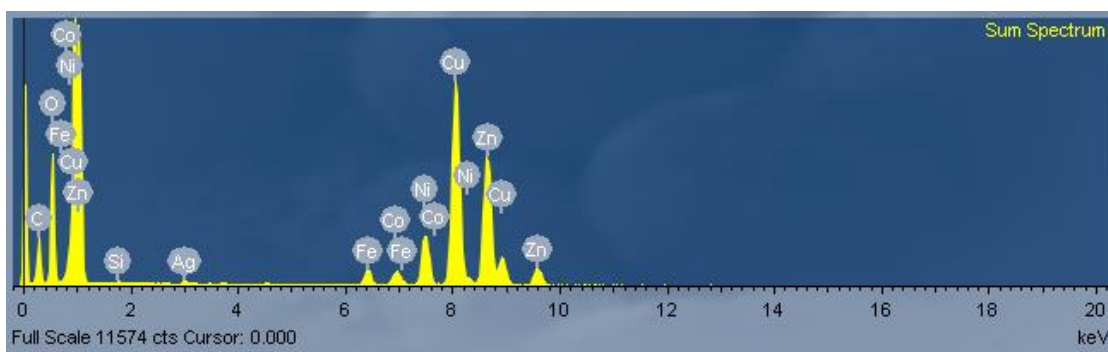


Elemental mapping for AuAg@Cu₂O@Zn(OH)₂

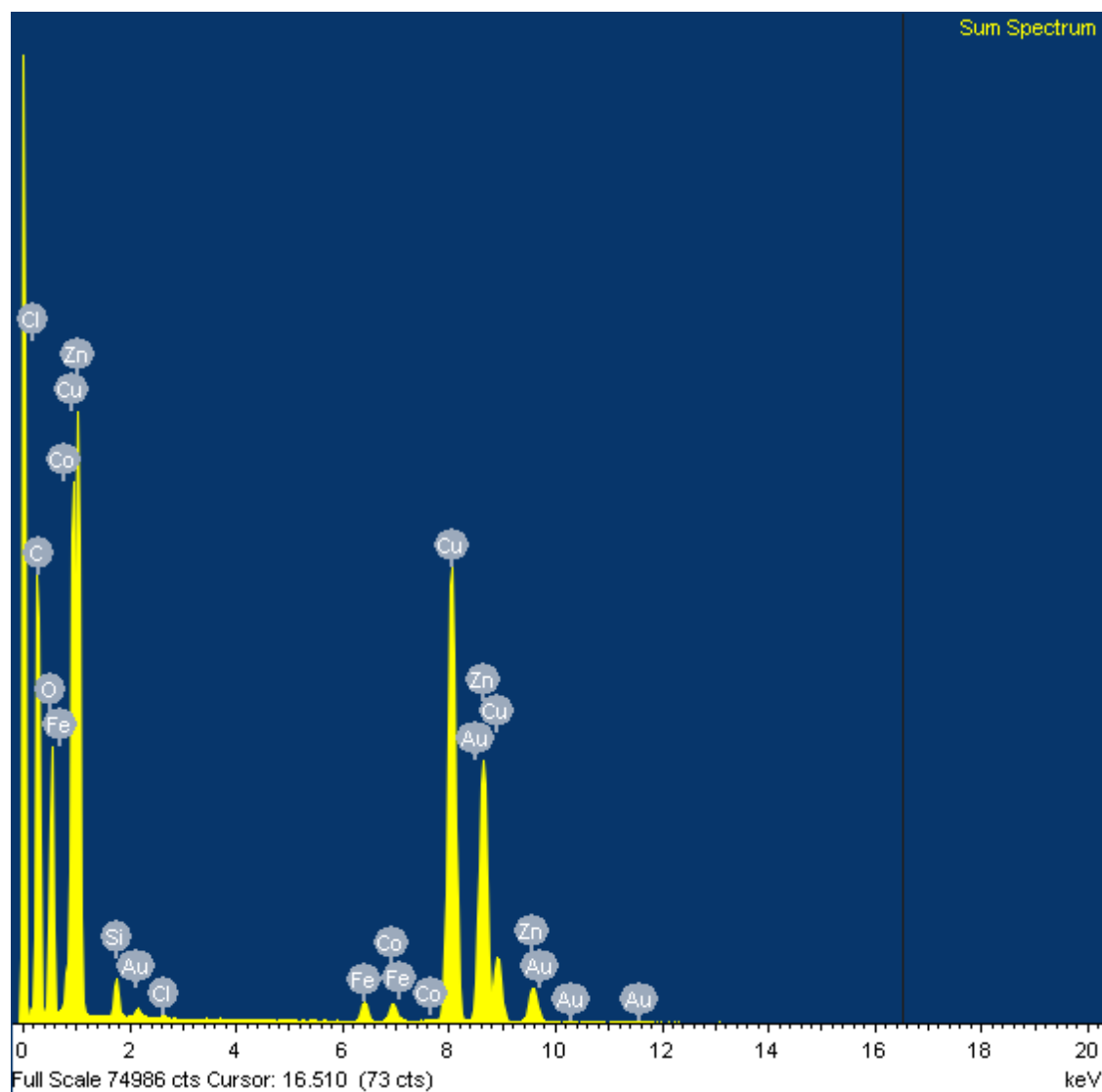


Elemental mapping for $\text{Pd@Cu}_2\text{O@Zn(OH)}_2$

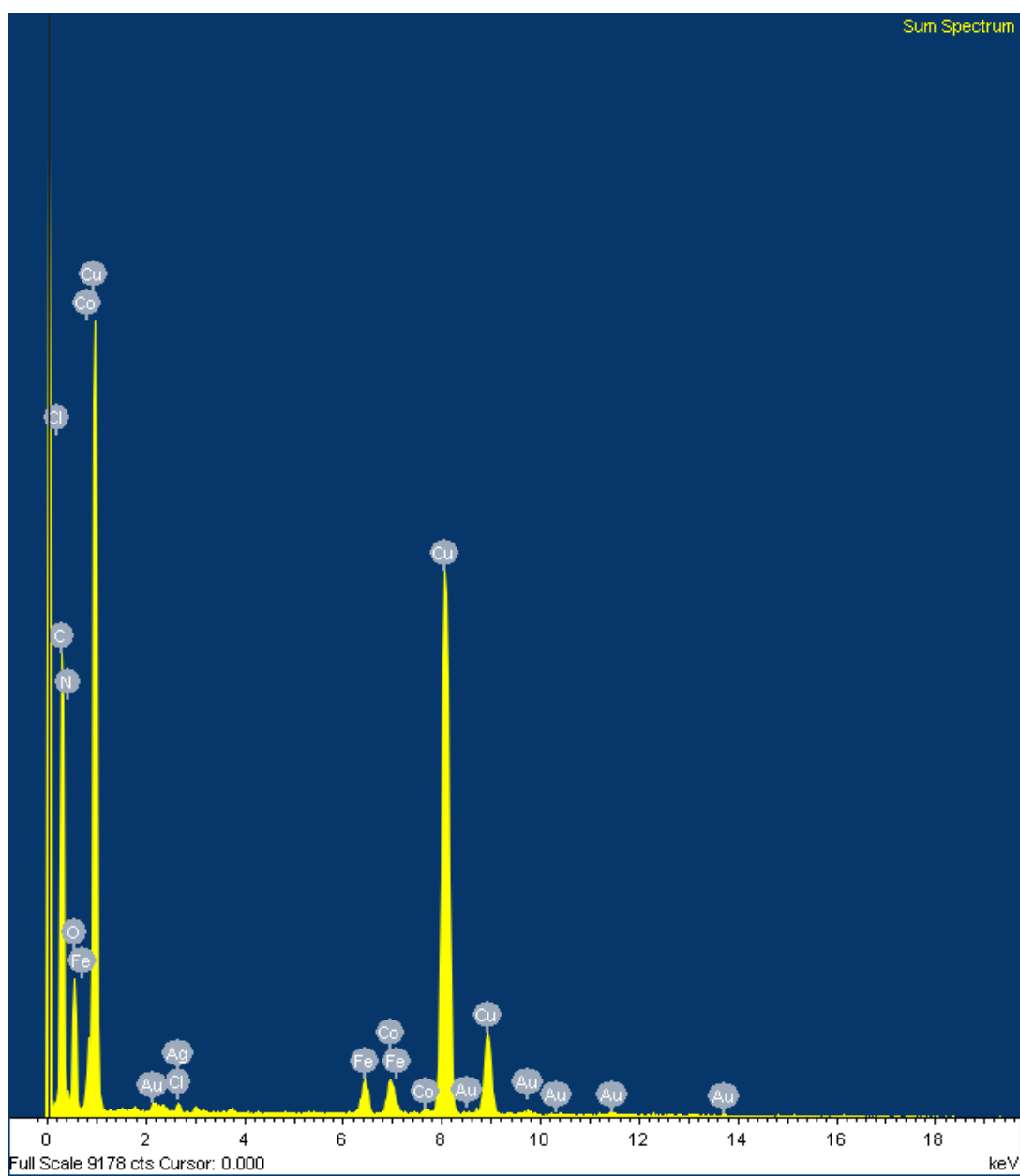
Appendix 3-1B Corresponding EDX Spectrum for M@Cu₂O@Zn(OH)₂



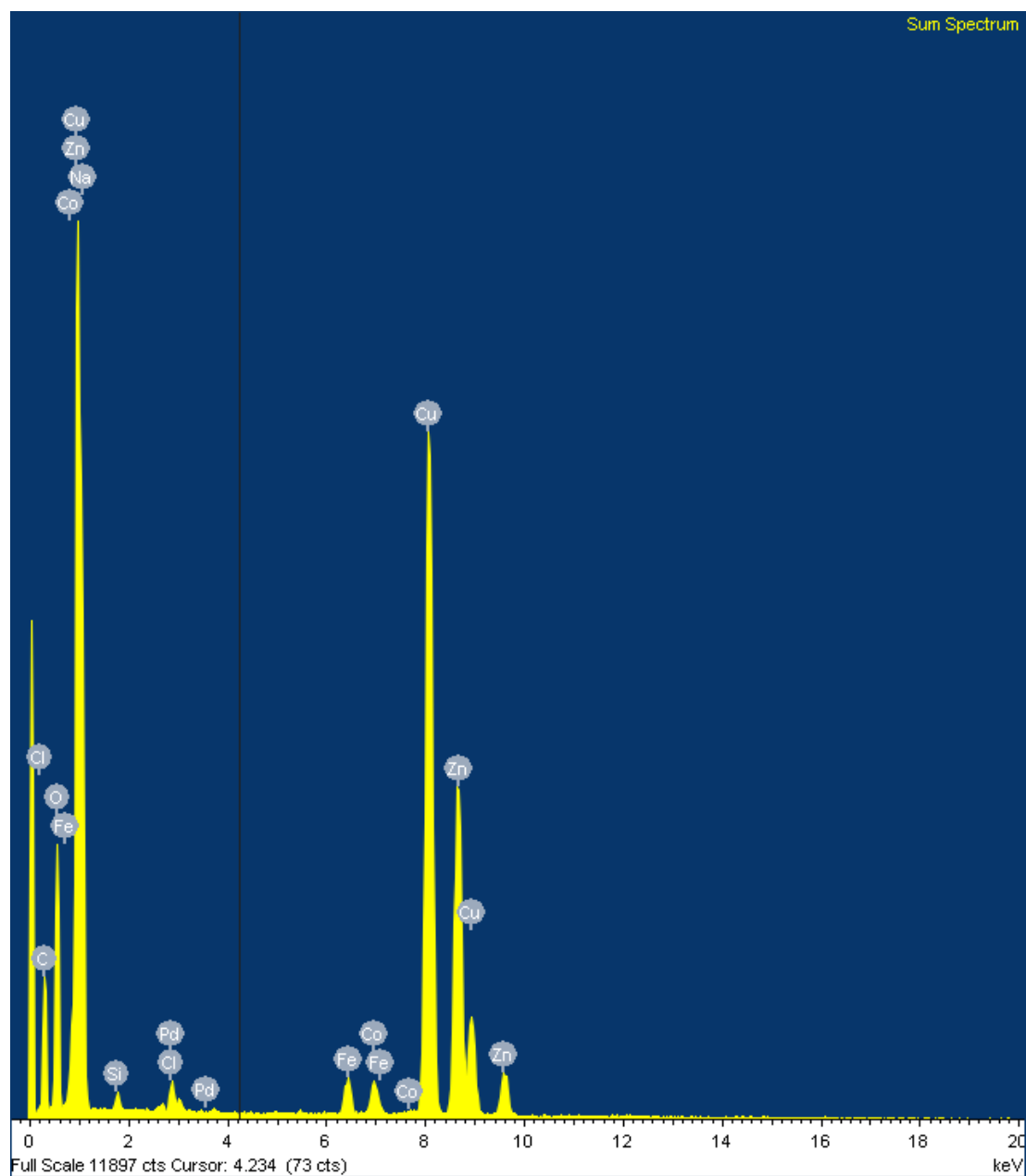
EDX spectrum for Ag@Cu₂O@Zn(OH)₂ core-shell structure



EDX spectrum for Au@Cu₂O@Zn(OH)₂ core-shell structure



EDX spectrum for AuAg@Cu₂O@Zn(OH)₂ core-shell structure



EDX spectrum for Pd@Cu₂O@Zn(OH)₂ core-shell structure

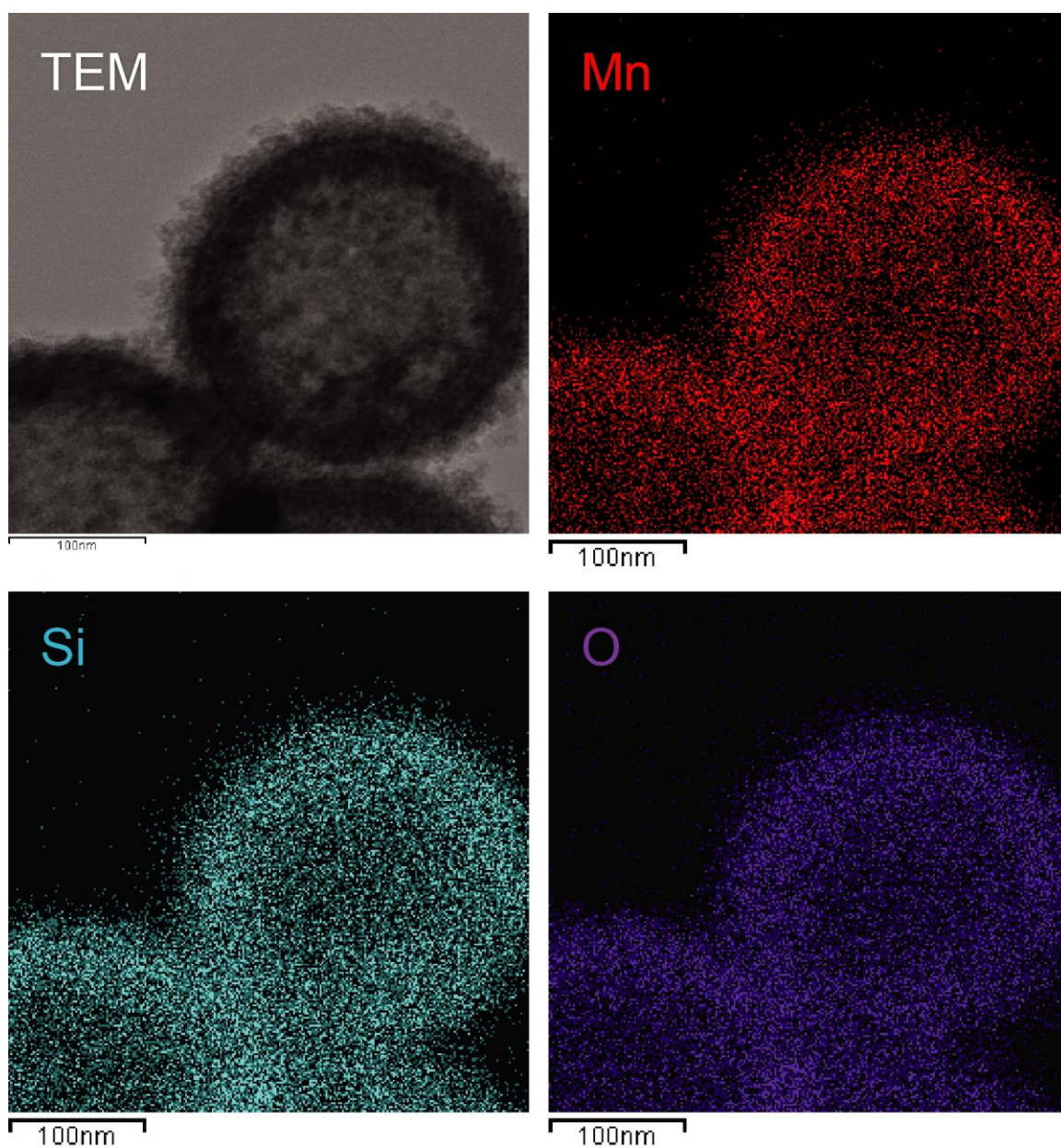
Appendix 3-2 Table of Valence, Conduction bands, Work Function, Band Gap used in Chapter 5

Material	E_v (eV)	E_c (eV)	Work Function (eV)	Band Gap (eV)	Reference
Cu ₂ O	-5.5	-3.2	4.9	2.3	1
ZnO	-7.2	-3.9	4.7	3.3	2-4
Au	N.A.	N.A.	4.8	N.A.	5
Ag	N.A.	N.A.	4.2	N.A.	4
Pd	N.A.	N.A.	5.2	N.A.	6

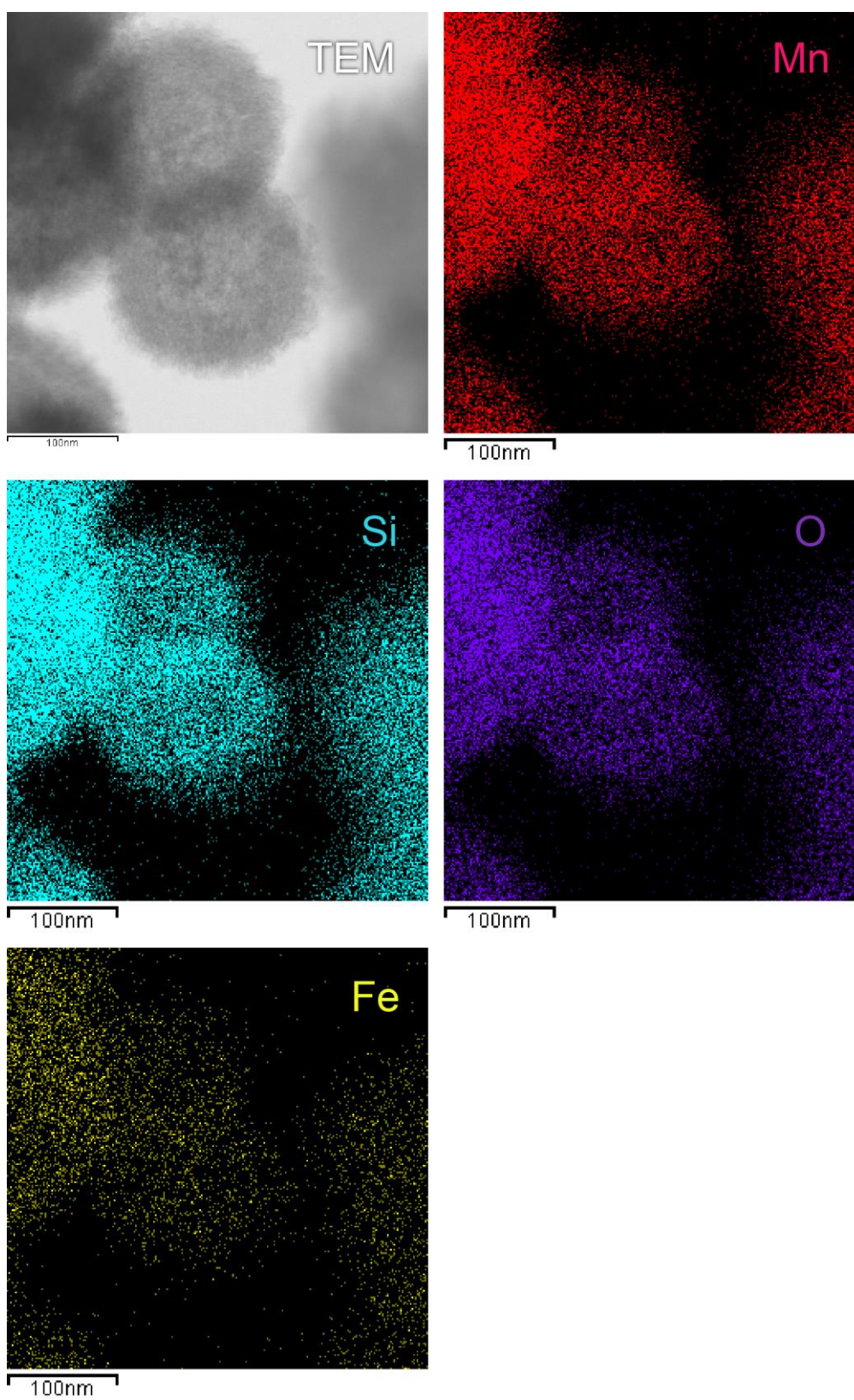
- 1 Greiner, M.T., Helander, M.G., Tang, W.M., Wang, Z.B., Qiu, J. & Lu, Z.H. Universal energy-level alignment of molecules on metal oxides. *Nat. Mater.* **11**, 76-81, doi:10.1038/nmat3159 (2012)
- 2 Mora-Sero, I., Bertoluzzi, L., Gonzalez-Pedro, V., Gimenez, S., Fabregat-Santiago, F., Kemp, K.W., Sargent, E.H. & Bisquert, J. Selective contacts drive charge extraction in quantum dot solids via asymmetry in carrier transfer kinetics. *Nat. Commun.* **4**, doi:10.1038/ncomms3272 (2013)
- 3 Gutmann, S., Conrad, M., Wolak, M. A., Beerbom, M. M. & Schlaf, R. Work function measurements on nano-crystalline zinc oxide surfaces. *J. Appl. Phys.* **111**, 123710, doi/10.1063/1.4729527 (2012).
- 4 Yan, F., Wang, Y., Zhang, J., Lin, Z., Zheng, J. & Huang, F. Schottky or Ohmic Metal–Semiconductor Contact: Influence on Photocatalytic Efficiency of Ag/ZnO and Pt/ZnO Model Systems. *Chemsuschem.* **7**, 101-104, doi: 10.1002/cssc.201300818 (2014)
5. Olsen, L.C., Bohara, R.C. & Urie, M.W. Explanation for low efficiency Cu₂O Schottky-barrier solar cells. *Appl. Phys. Lett.* **34**, 47-49, doi: 10.1063/1.90593 (1979)
6. Electron Work Function of the Elements in *CRC Handbook of Chemistry and Physics 95th Ed.* 12-124 (2014)

Appendix 4

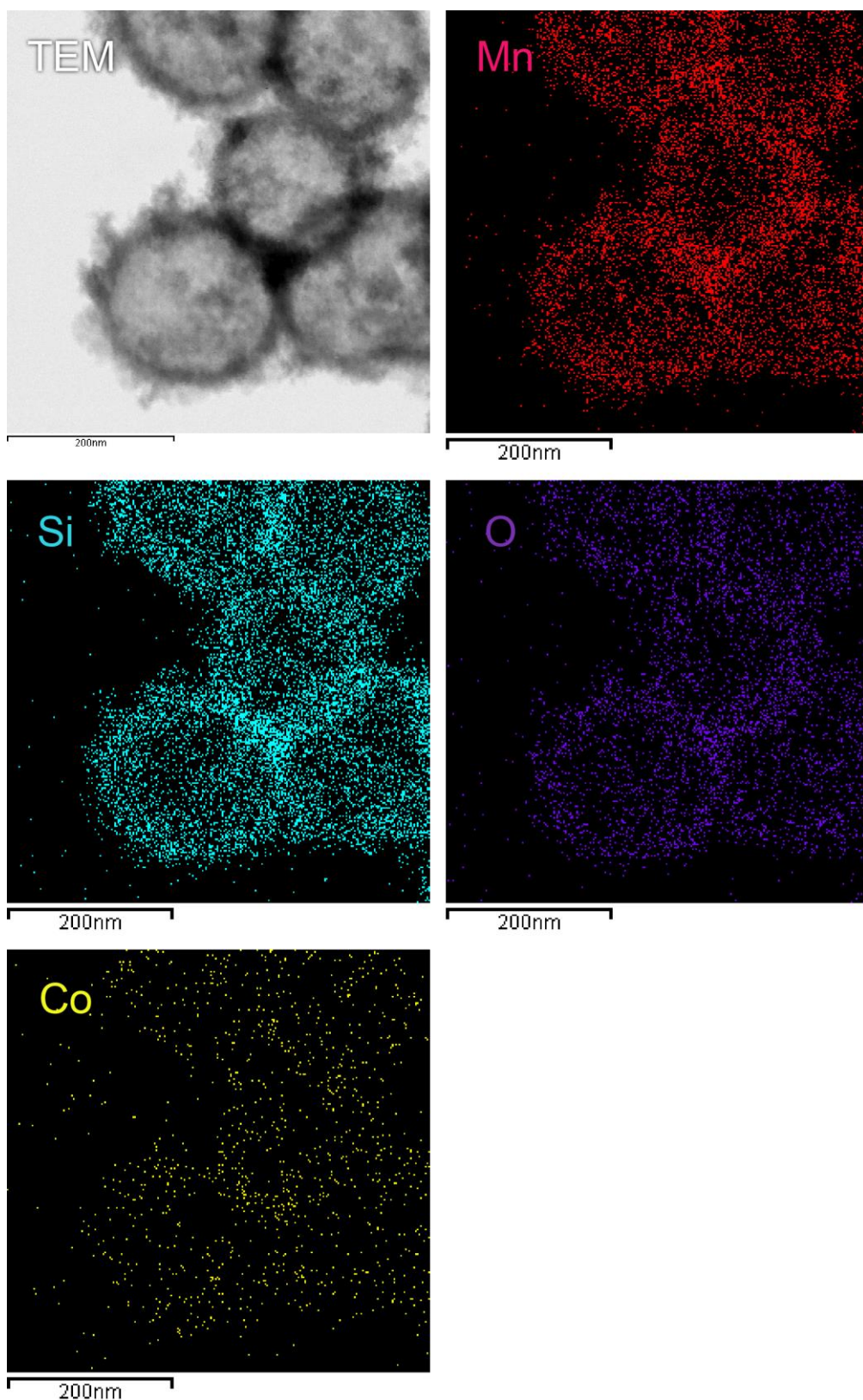
Appendix 4-1A EDX Analysis on Manganese Silicate and Its Doped Derivatives



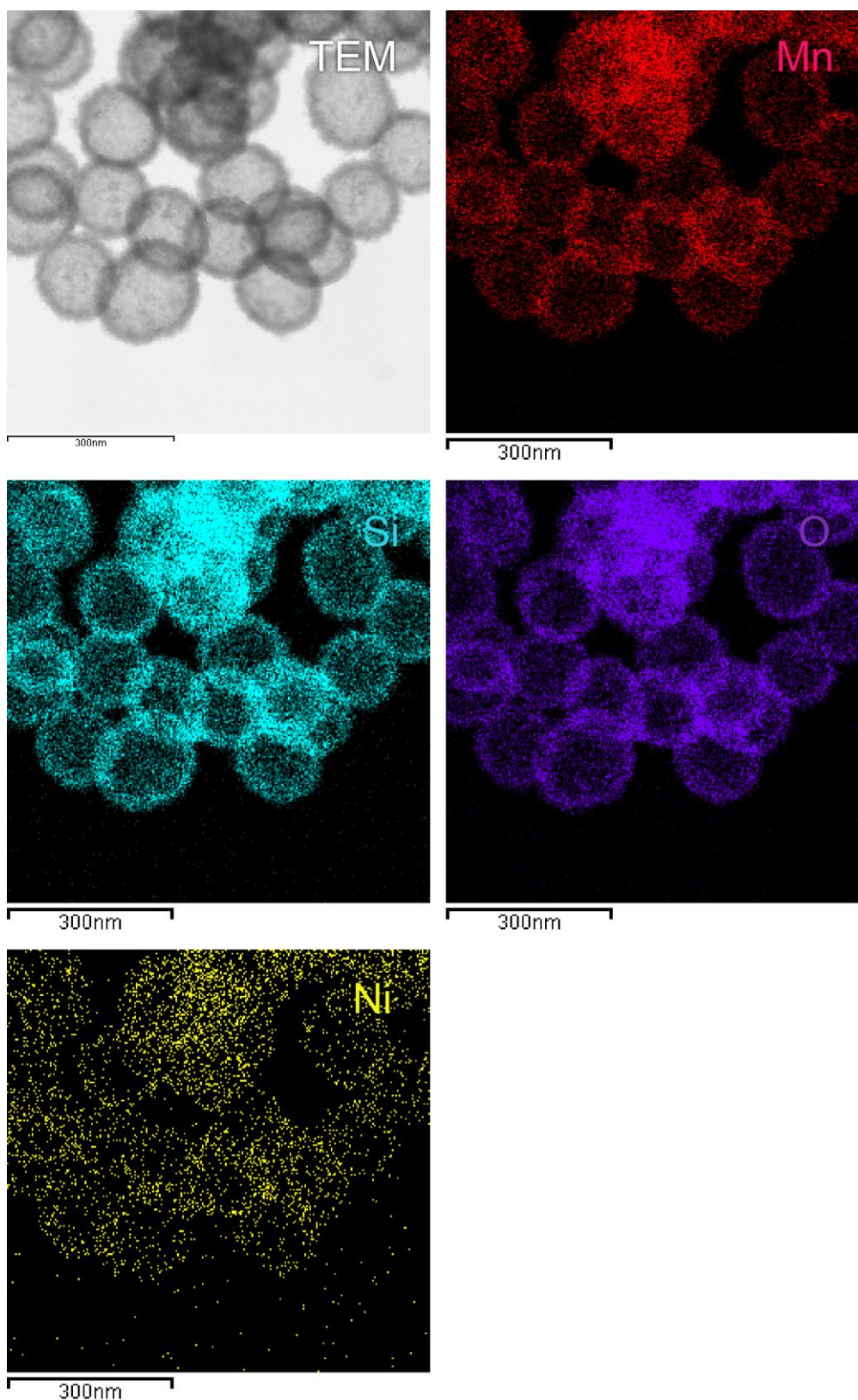
Elemental maps of spherically assembled nanobubbles of manganese silicate.



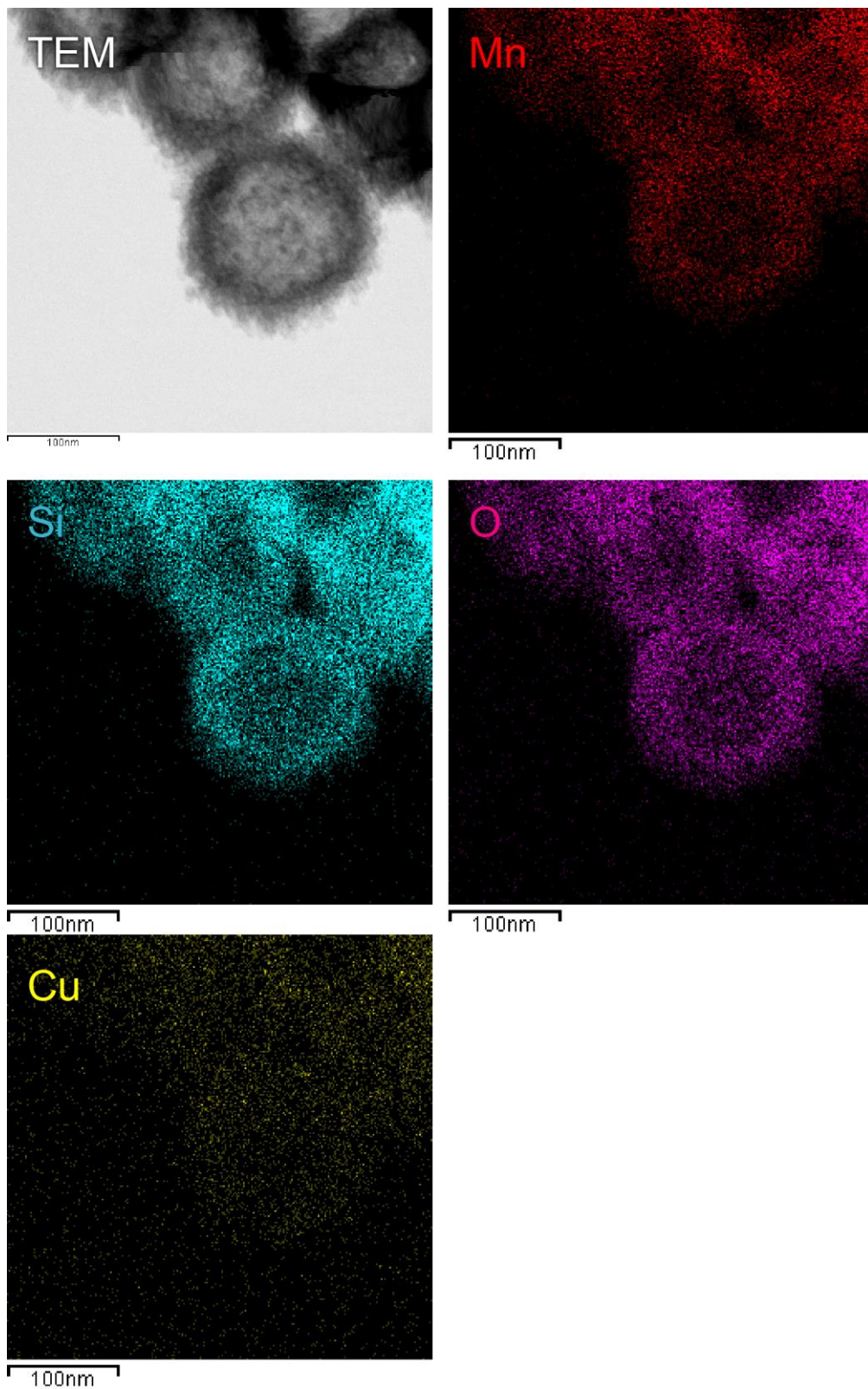
Elemental maps of spherically assembled nanobubbles of Fe doped manganese silicate (experimental Mn:Fe = 20:1).



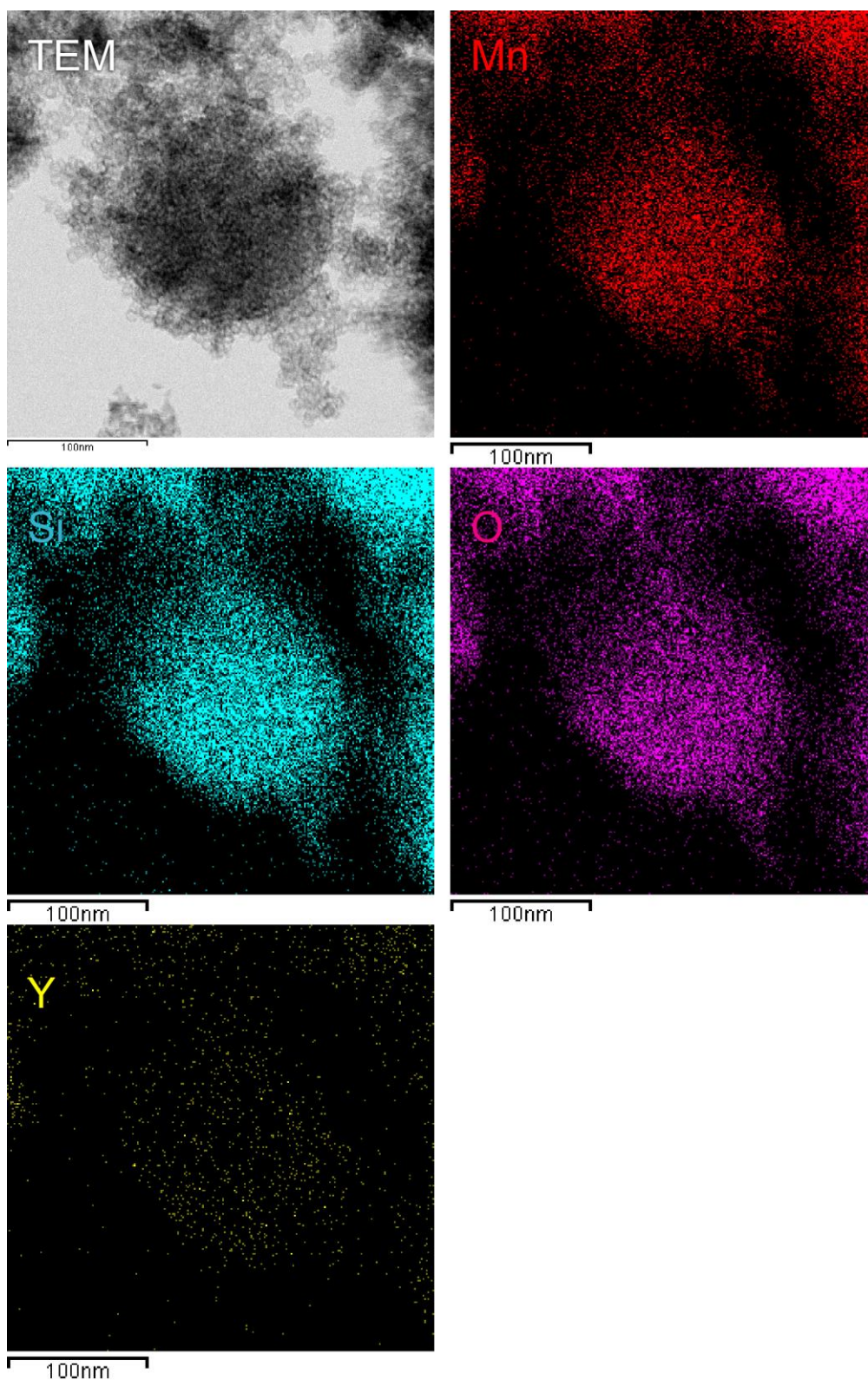
Elemental maps of spherically assembled nanobubbles of Co doped manganese silicate (experimental Mn:Co = 20:1).



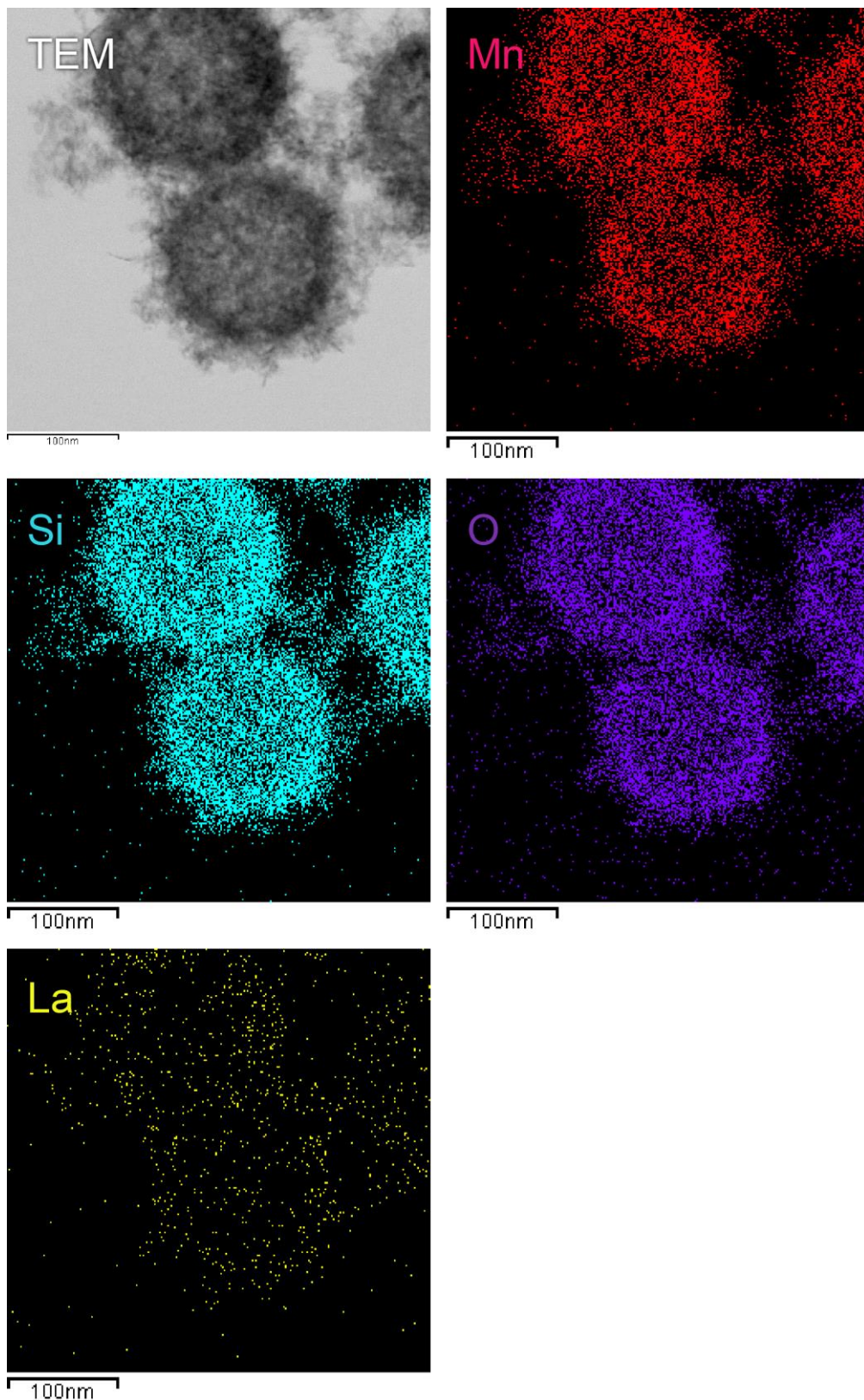
Elemental maps of spherically assembled nanobubbles of Ni doped manganese silicate (experimental Mn:Ni = 20:1).



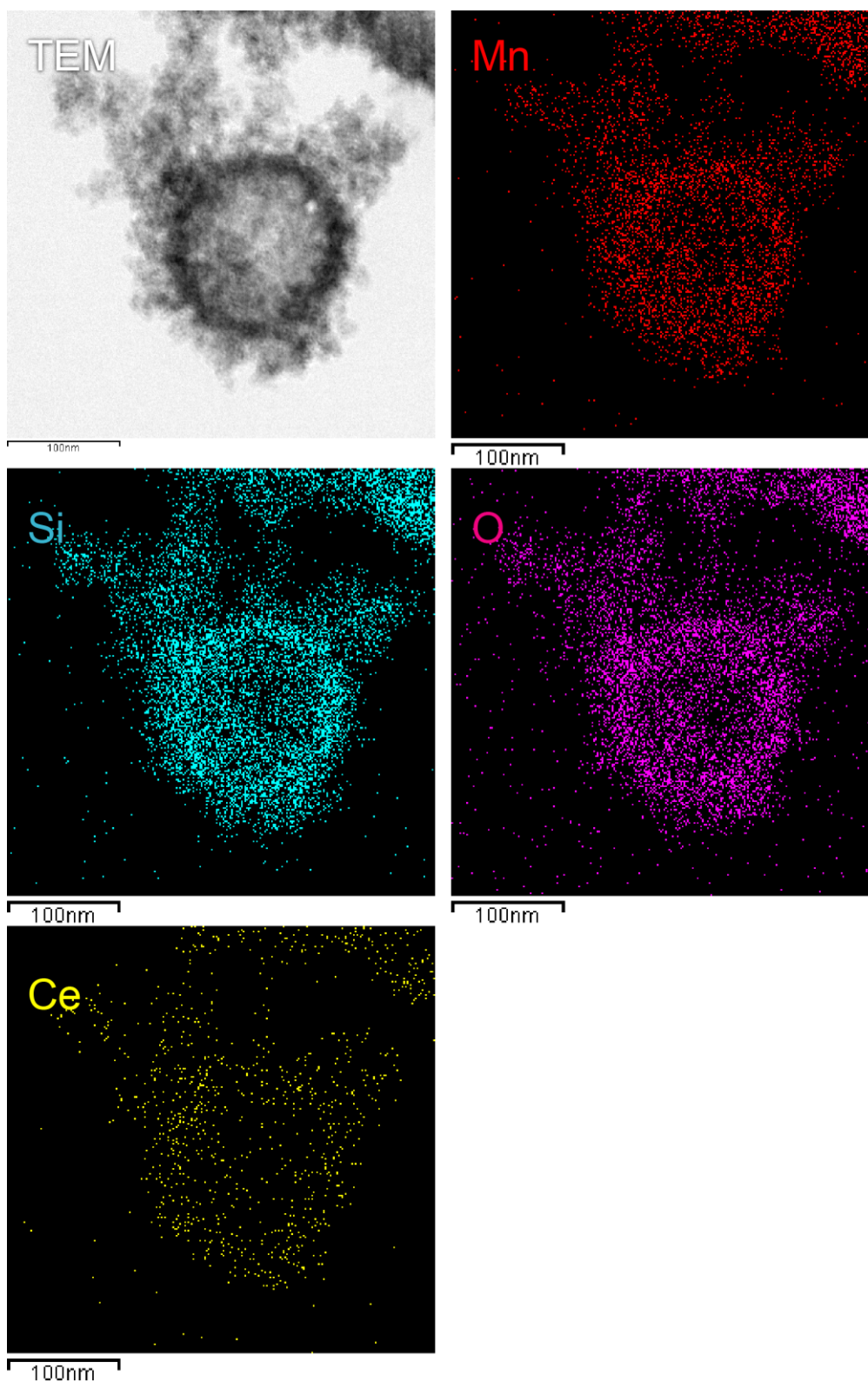
Elemental maps of spherically assembled nanobubbles of Cu doped manganese silicate (experimental Mn:Cu = 20:1).



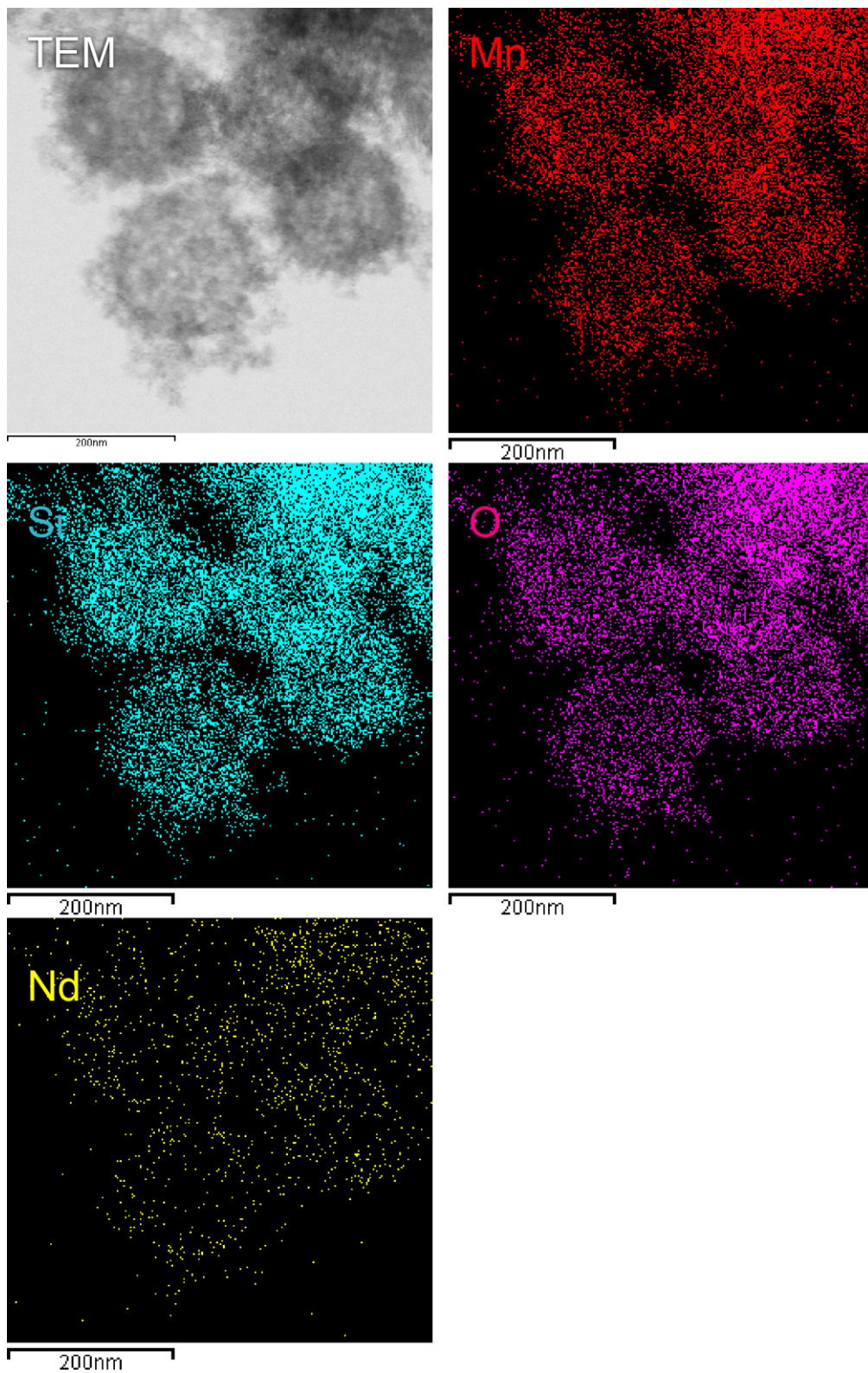
Elemental maps of spherically assembled nanobubbles of Y doped manganese silicate (experimental Mn:Y = 20:1).



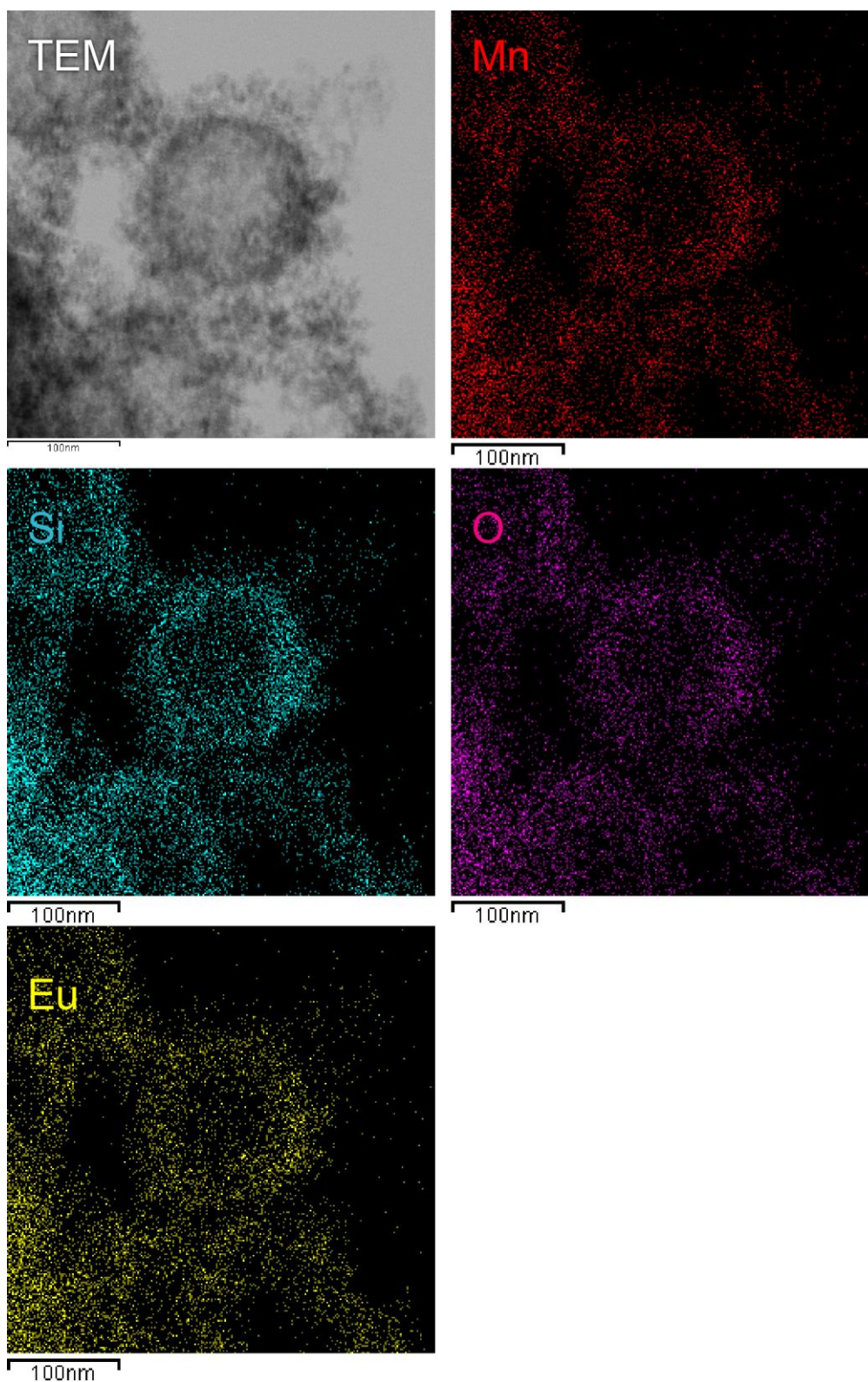
Elemental maps of spherically assembled nanobubbles of La doped manganese silicate (experimental Mn:La = 20:1).



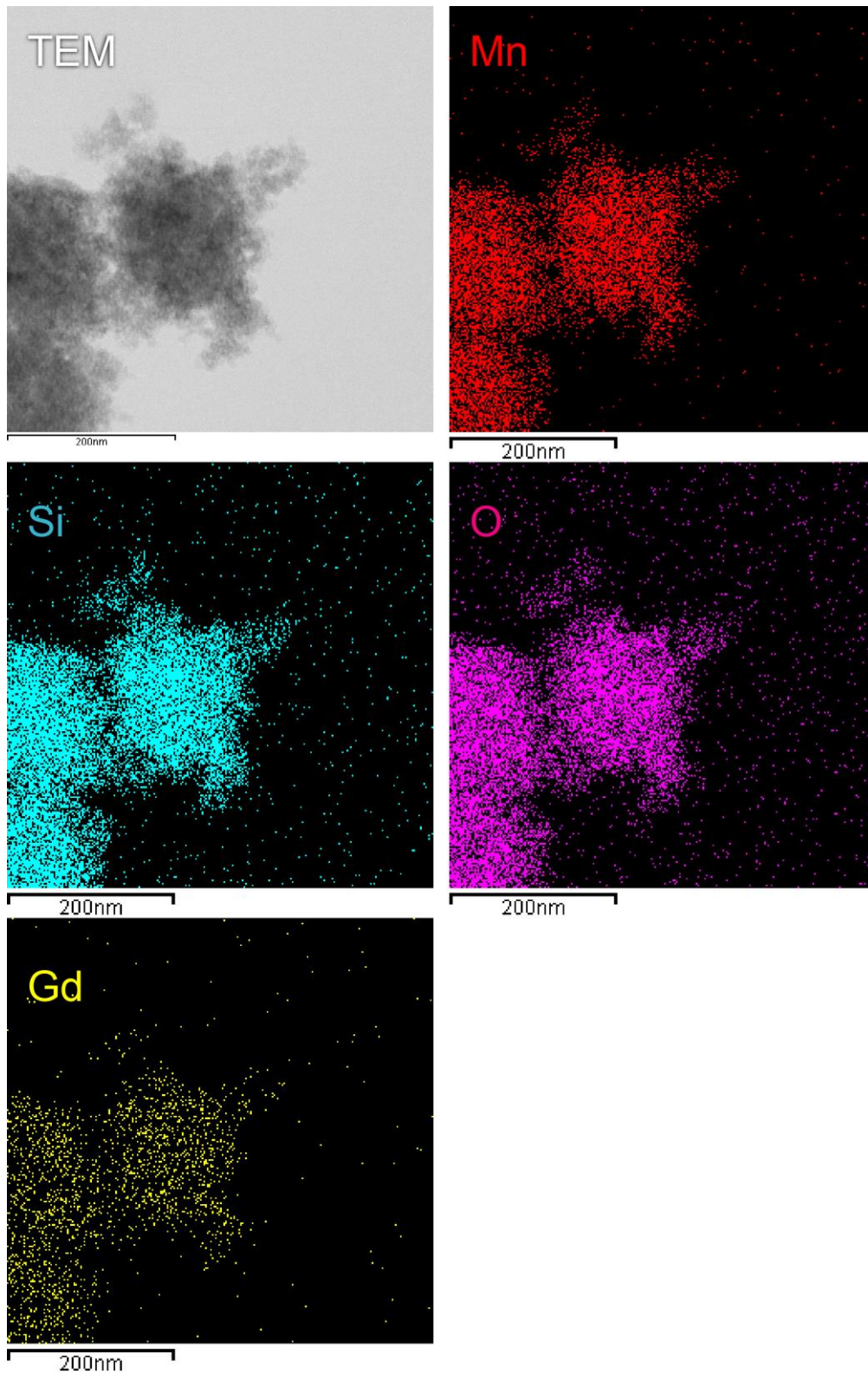
Elemental maps of spherically assembled nanobubbles of Ce doped manganese silicate (experimental Mn:Ce = 20:1).



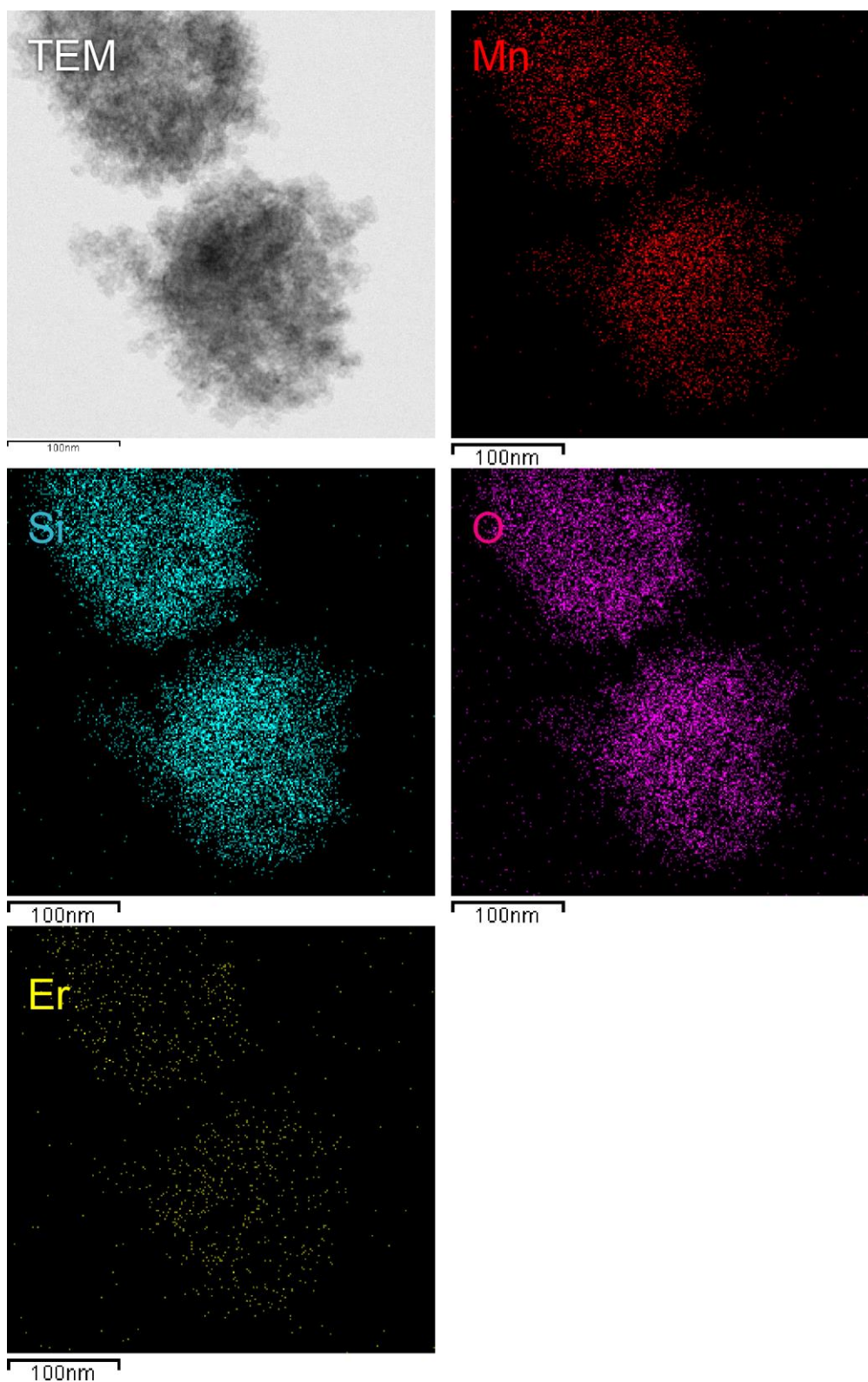
Elemental maps of spherically assembled nanobubbles of Nd doped manganese silicate (experimental Mn:Nd = 20:1).



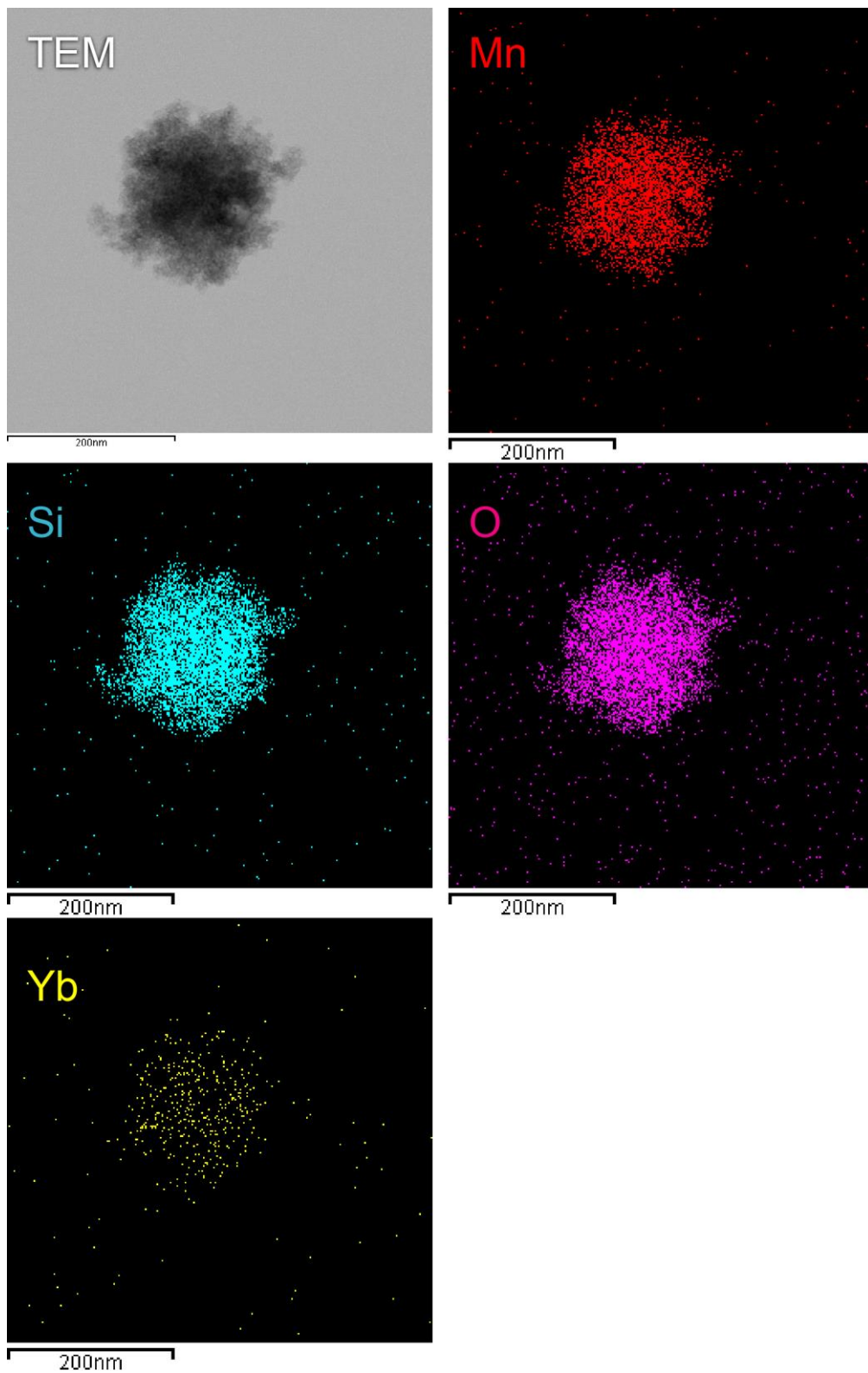
Elemental maps of spherically assembled nanobubbles of Eu doped manganese silicate (experimental Mn:Eu = 20:1).



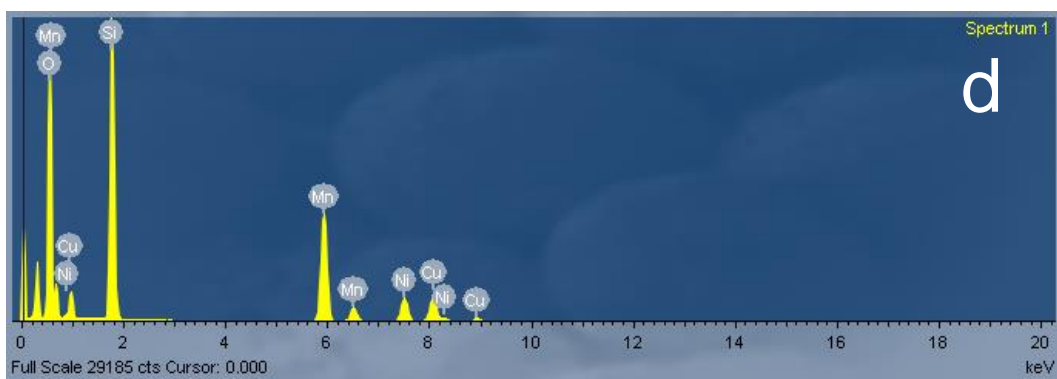
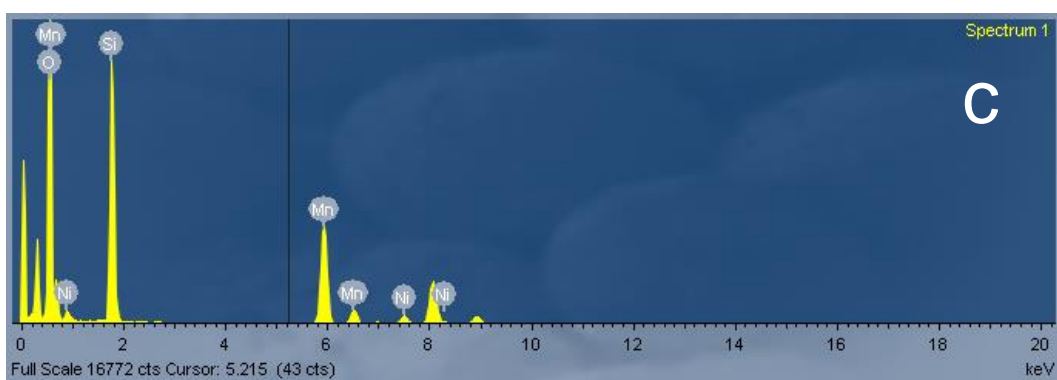
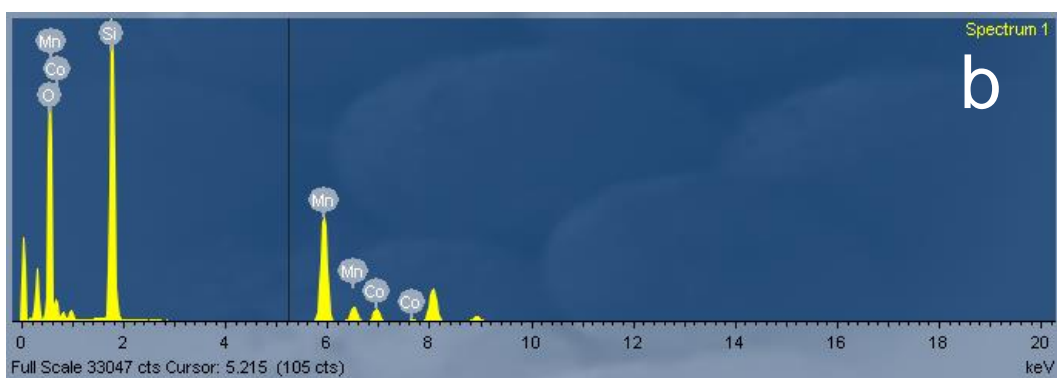
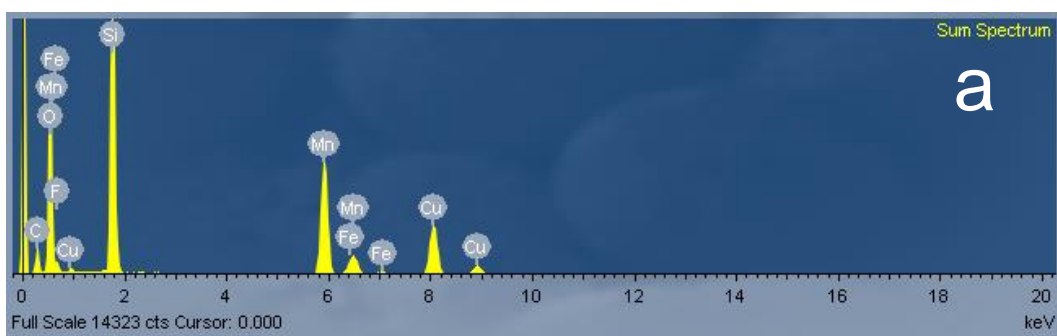
Elemental maps of spherically assembled nanobubbles of Gd doped manganese silicate (experimental Mn:Gd = 20:1).



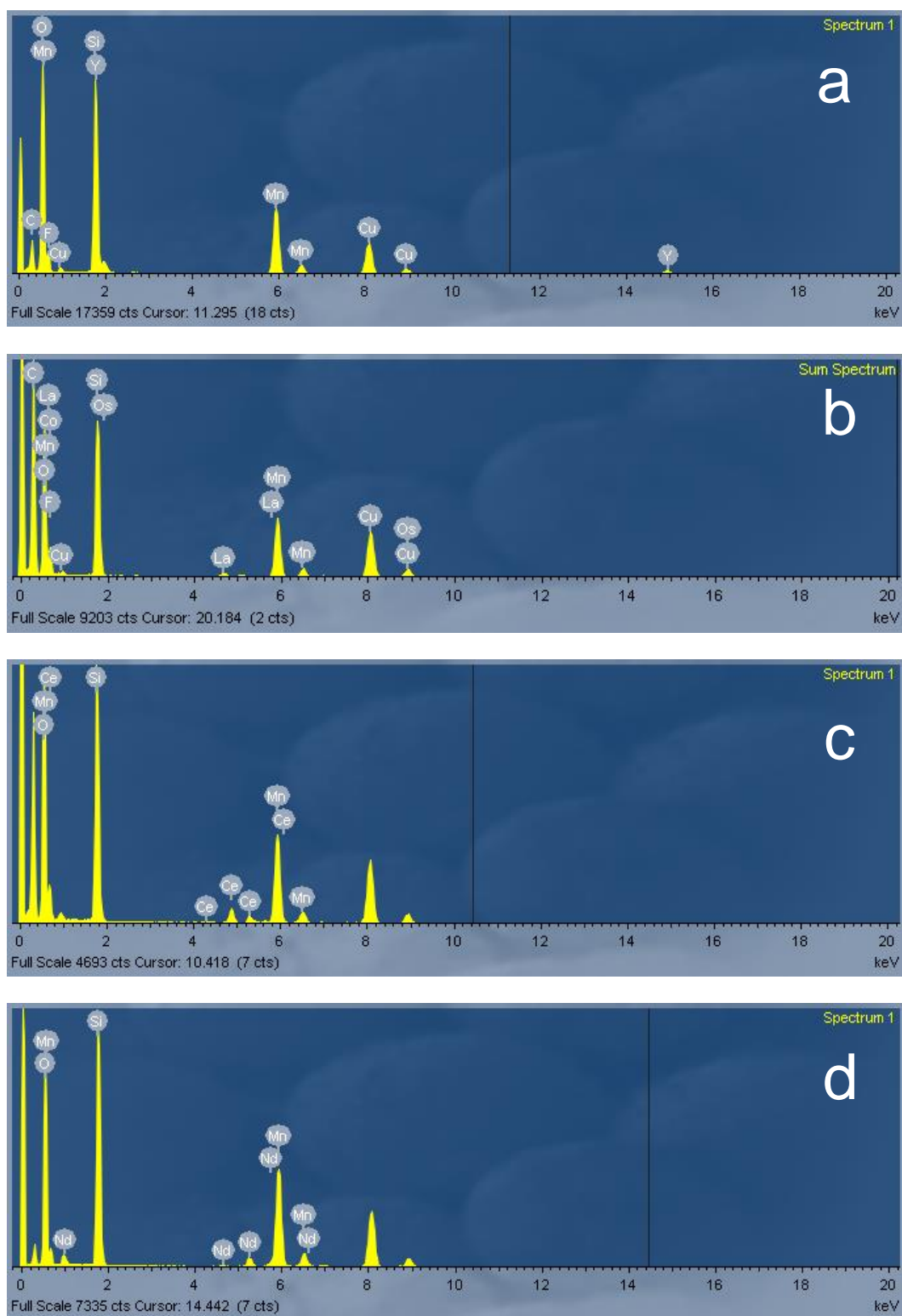
Elemental maps of spherically assembled nanobubbles of Er doped manganese silicate (experimental Mn:Er = 20:1).



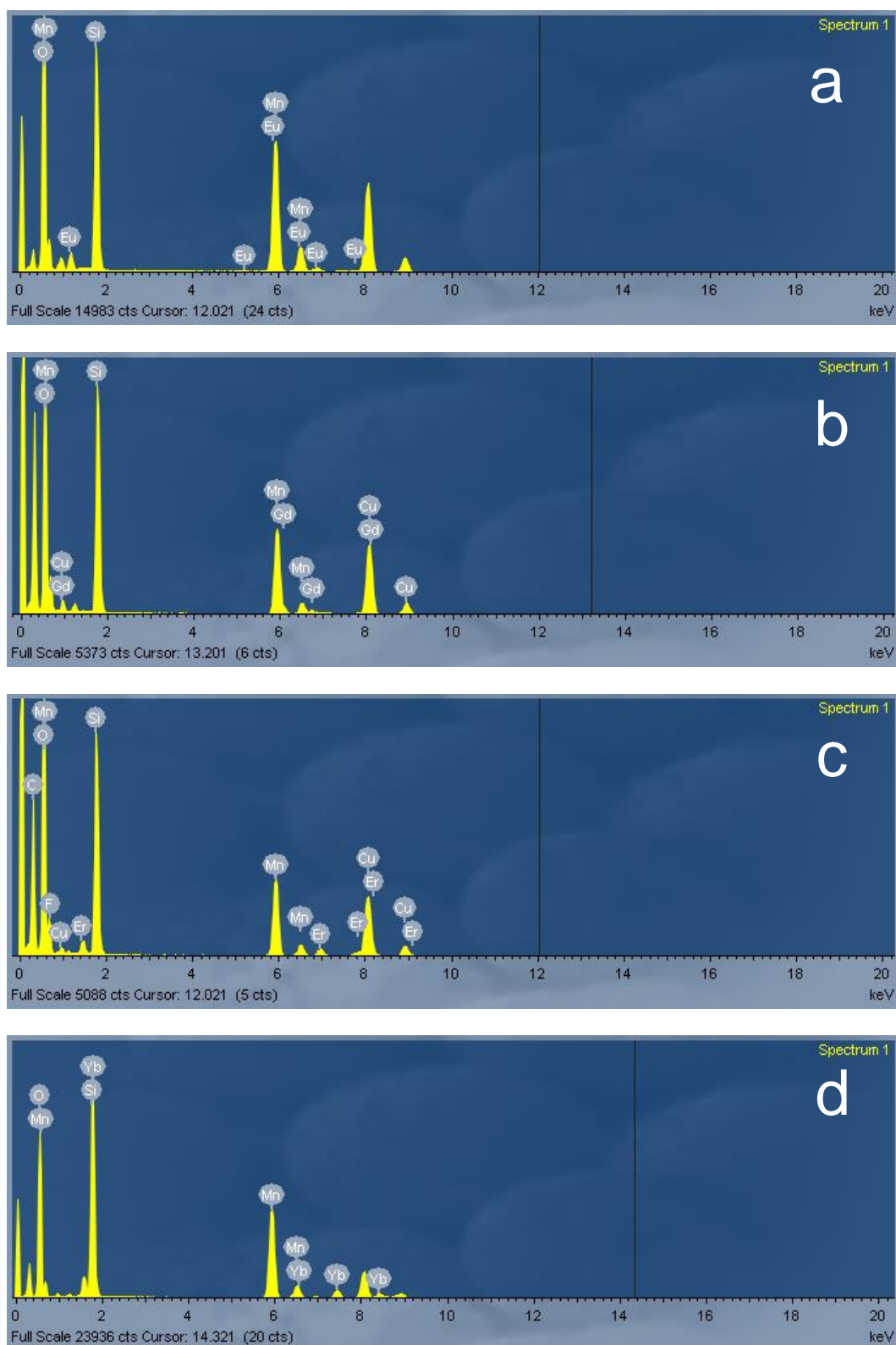
Elemental maps of spherically assembled nanobubbles of Yb doped manganese silicate (experimental Mn:Yb = 20:1).



Energy dispersive X-ray spectra of transition metal-doped manganese silicate with an experimental Mn:dopant ratio at 20:1 (dopant ions: (a) Fe^{2+} , (b) Co^{2+} , (c) Ni^{2+} , and (d) Cu^{2+}). Note: All samples were scanned on a Cu grid except for Cu^{2+} which was scanned on a Ni grid.



Energy dispersive X-ray spectra of rare earth metal-doped manganese silicate with an experimental Mn:dopant ratio at 20:1 (dopant ions: (a) Y^{3+} , (b) La^{3+} , (c) Ce^{3+} , and (d) Nd^{3+}).



Energy dispersive X-ray spectra of rare earth metal-doped manganese silicate with an experimental Mn:dopant ratio at 20:1 (dopant ions: (a) Eu^{3+} , (b) Gd^{3+} , (c) Er^{3+} , and (d) Yb^{3+}).

Table A-3. Comparison of the Actual Atomic Ratio between Manganese and Dopant Material

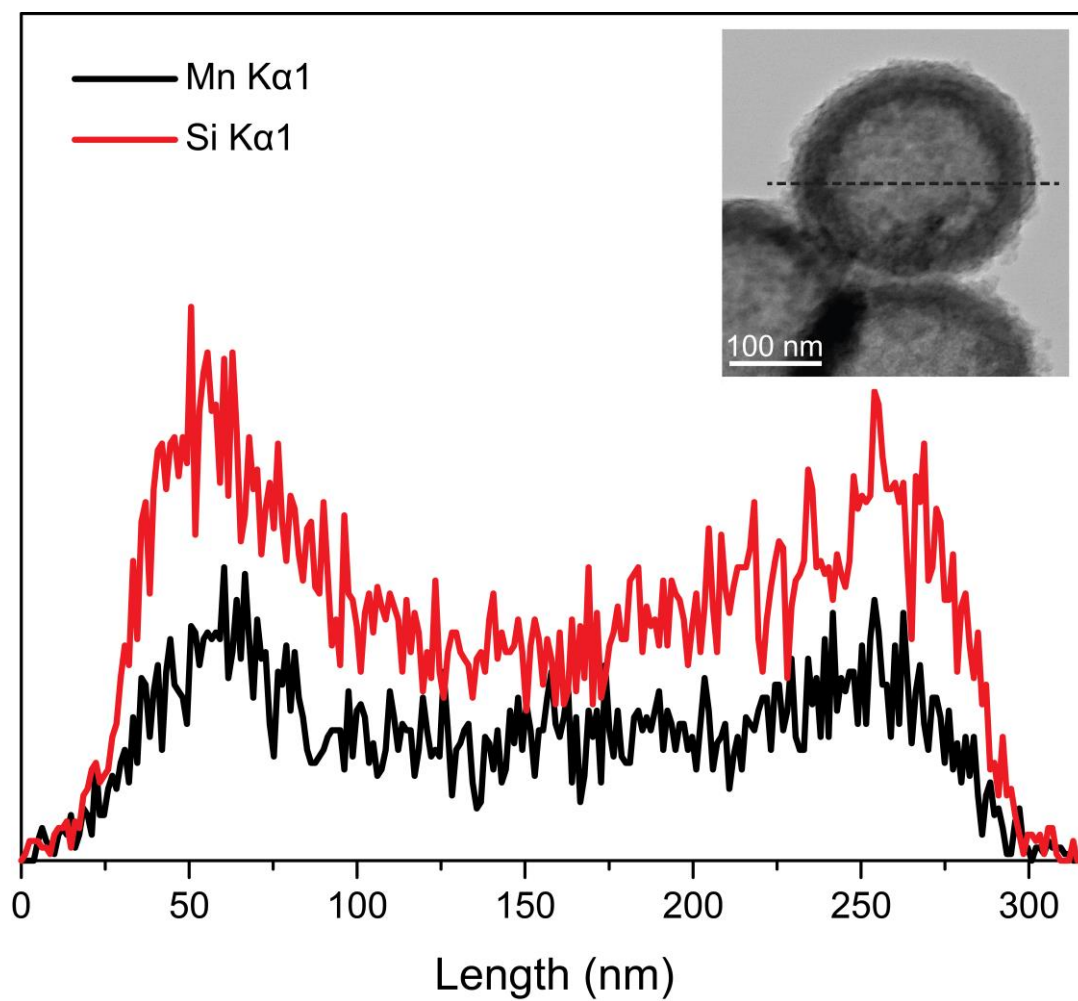
Metal ion	Experimental Mn:dopant atomic ratio	Observed Mn:dopant atomic ratio
Fe-doped	20:1	11.37 : 1
Co-doped	20:1	7.93 : 1
Ni-doped	20:1	12.16 : 1
Cu-doped	20:1	4.04 : 1
Y-doped	20:1	6.82 : 1
La-doped	20:1	19.35 : 1
Ce-doped	20:1	6.12 : 1
Nd-doped	20:1	9.63 : 1
Eu-doped	20:1	7.06 : 1
Gd-doped	20:1	12.1 : 1
Er-doped	20:1	10.06 : 1
Yb-doped	20:1	9.04 : 1

Table A-4. List of Emission Energy during Analysis of Doped Manganese Silicate Structure

Element Doped	Theoretical Emission Energy (KeV)	Obtained Emission Energy (KeV)
Fe	6.404(K α_1), 7.058(K $\beta_{1,3}$)	7.0
Co	6.930(K α_1), 7.649(K $\beta_{1,3}$)	6.94, 7.66
Ni	7.478(K α_1), 8.265(K $\beta_{1,3}$)	7.48, 8.30
Cu	8.048(K α_1), 8.905(K $\beta_{1,3}$)	8.10, 8.90
Y	14.958(K α_1)	14.98
La	4.651(L α_1)	4.65
Ce	4.840(L α_1), 5.262(L β_1)	4.85, 5.25
Nd	5.230(L α_1)	5.20
Eu	5.846(L α_1), 6.843(L $\beta_{2,15}$)	6.85
Gd	6.057(L α_1), 6.713(L β_1)	6.73
Er	6.949(L α_1)	6.98
Yb	7.416(L α_1), 8.402(L β_1)	7.42, 8.40

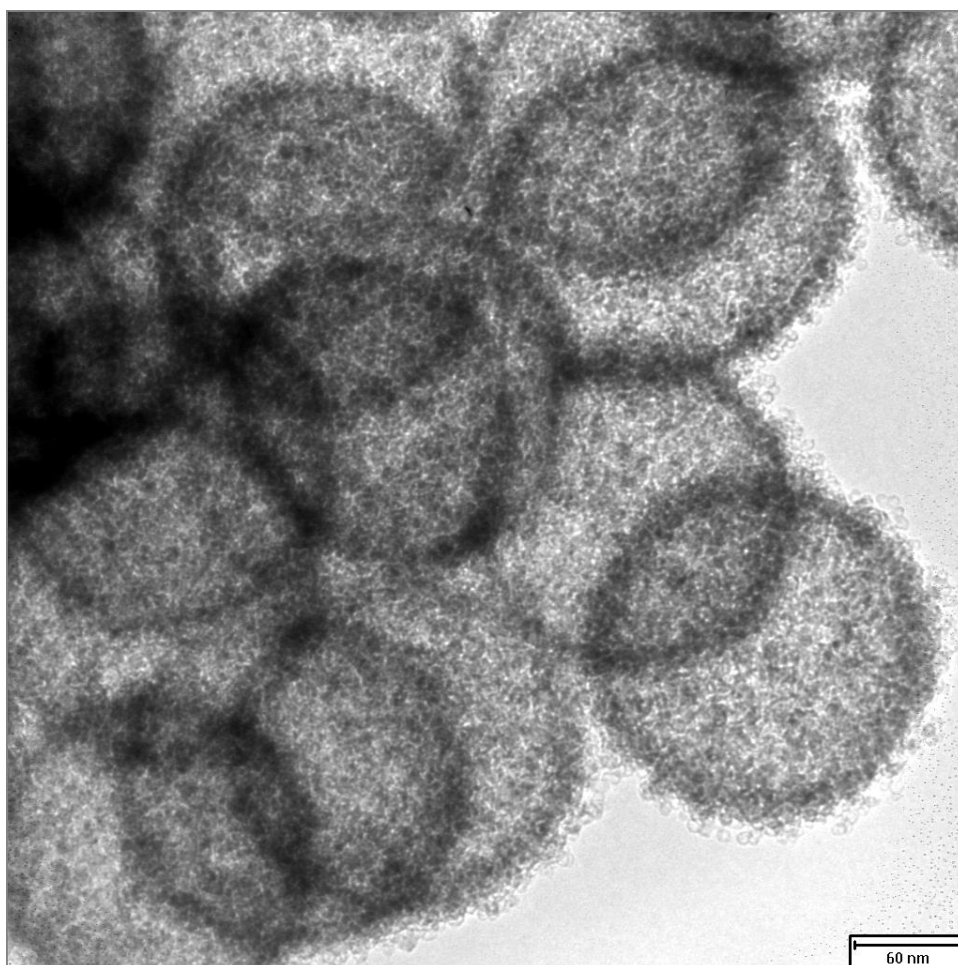
Theoretical Emission Energy were obtained from:

Kortright, J.B.;Thompson, A.C. X-Ray Emission Energies. In *X-Ray Data Booklet 3rd Edition* [Online]; Thompson, A.C., Ed.; Lawrence Berkeley National Laboratory: California, 2009; Chapter 1, pp 8-27. <http://xdb.lbl.gov/xdb-new.pdf> (accessed May 20, 2014)

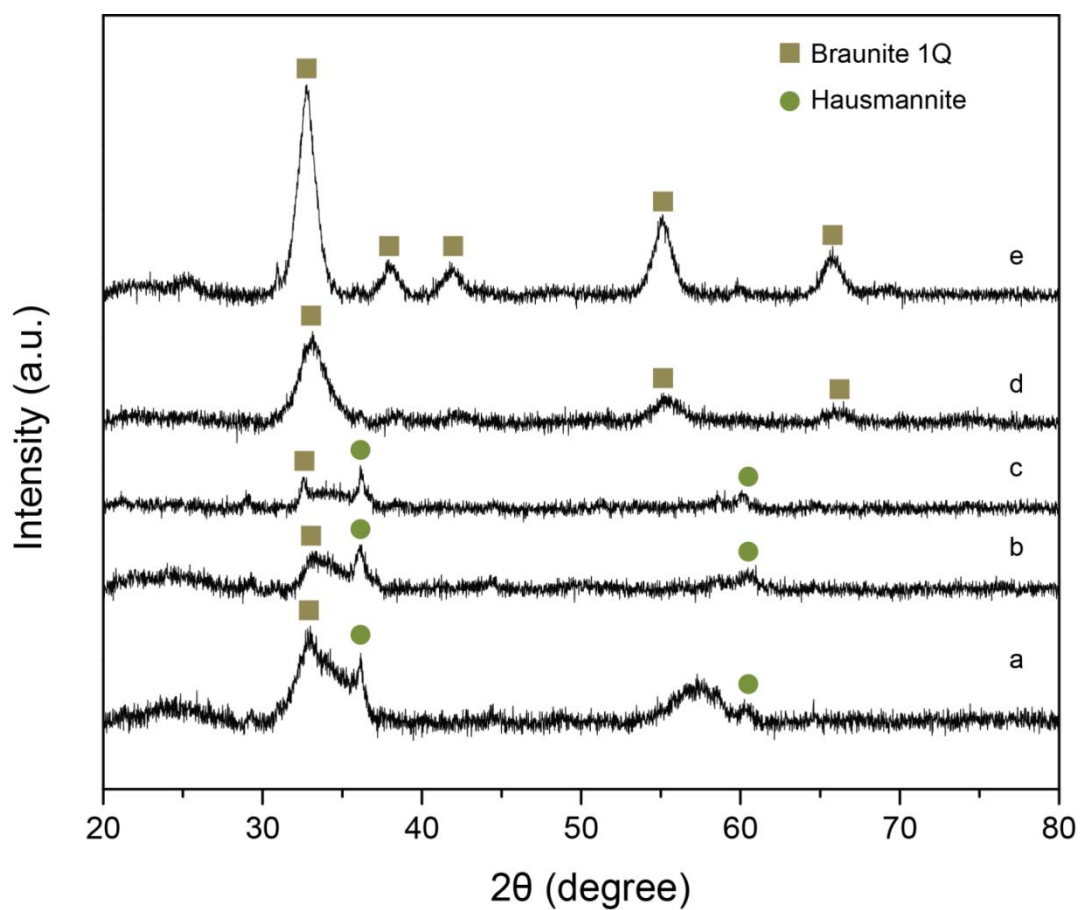


EDX line scan of manganese silicate structure. Inset: TEM image of manganese silicate.

Appendix 4-1B Thermal Stability of Hollow Nanospheres

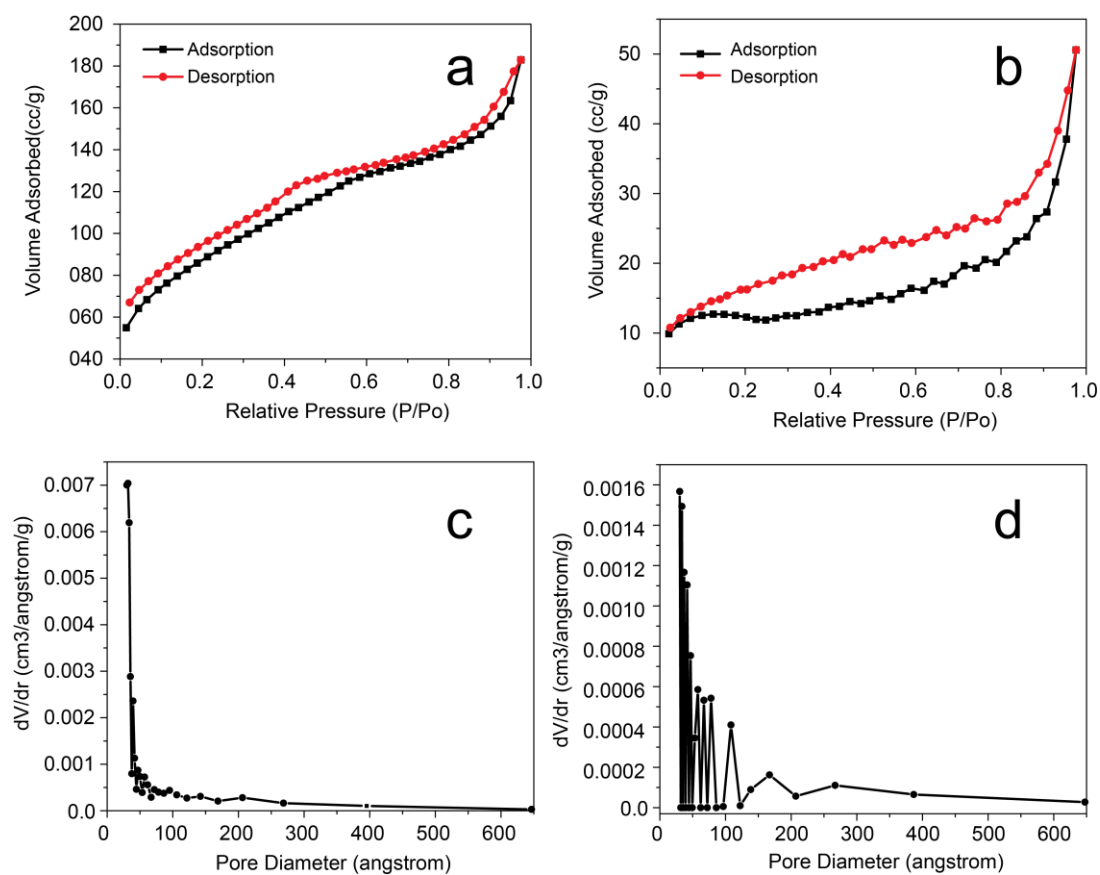


The as-synthesized (and dried) manganese silicate nanobubbles after heated at 800 °C for 12 hours using an electric furnace under laboratory air.



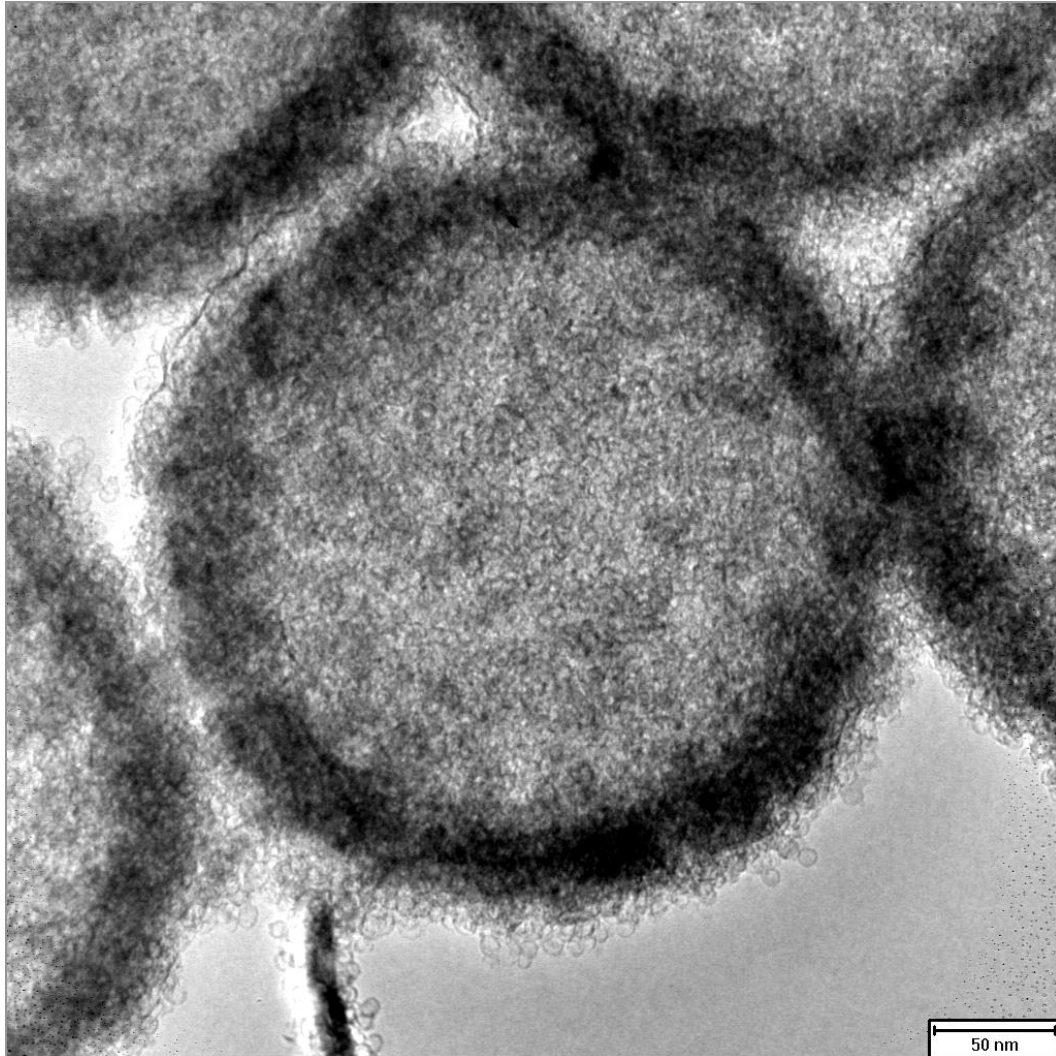
XRD patterns of the as-synthesized (and dried) manganese silicate nanobubbles after heated at different temperatures: (a) room temperature, (b) 400 °C, (c) 600 °C, (d) 700 °C, and (e) 800 °C for 12 hours using an electric furnace under laboratory air. Representative sample morphologies can be seen in 18.

Appendix 4-1C N₂ Adsorption and Desorption Characterization

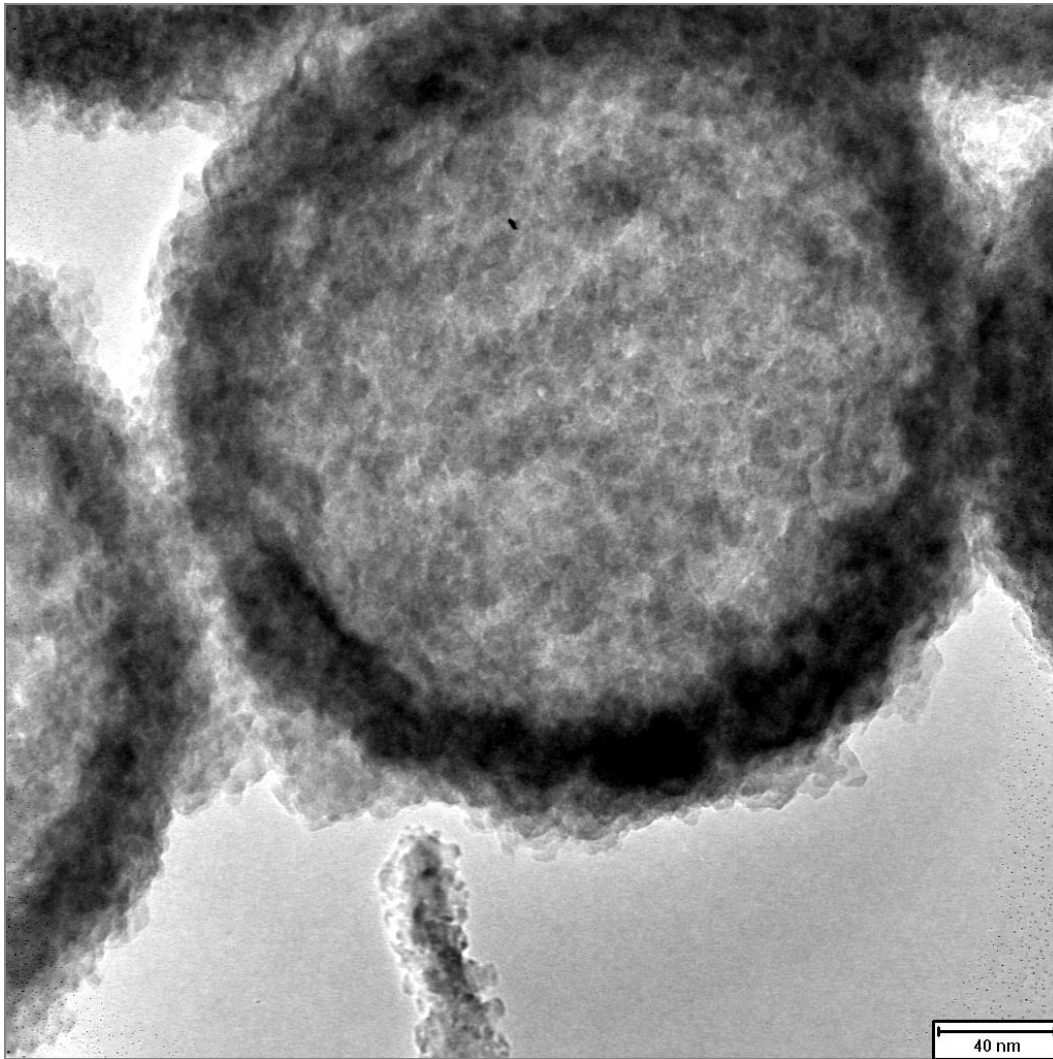


N₂ adsorption and desorption isotherm at 77 K for (a) spherically assembled nanobubbles of manganese silicate, and (b) spherically assembled nanobubbles of manganese silicate after heated at 800 °C for 12 hours, and corresponding BJH desorption pore size distribution of (c) spherically assembled nanobubbles of manganese silicate, and (d) spherically assembled nanobubbles of manganese silicate after heated at 800 °C for 12 hours.

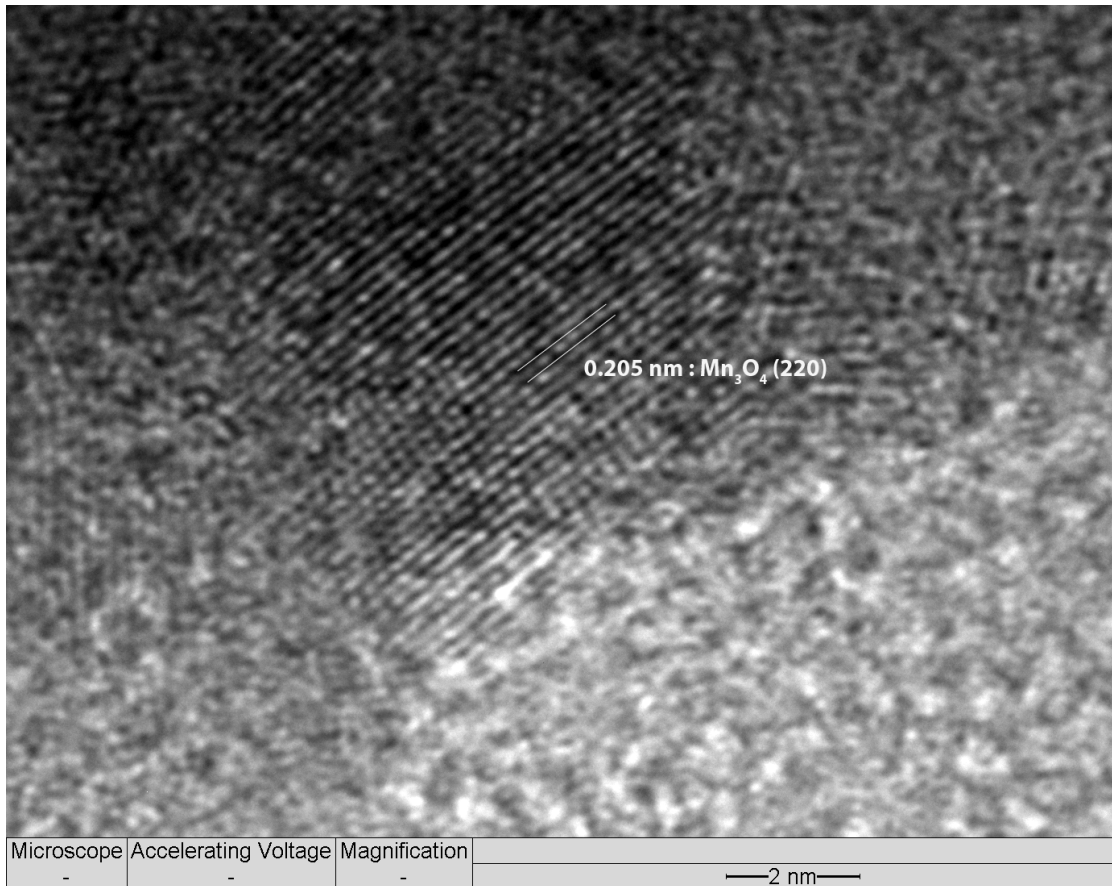
Appendix 4-1D Transformation under Focused Electron Beam Exposure



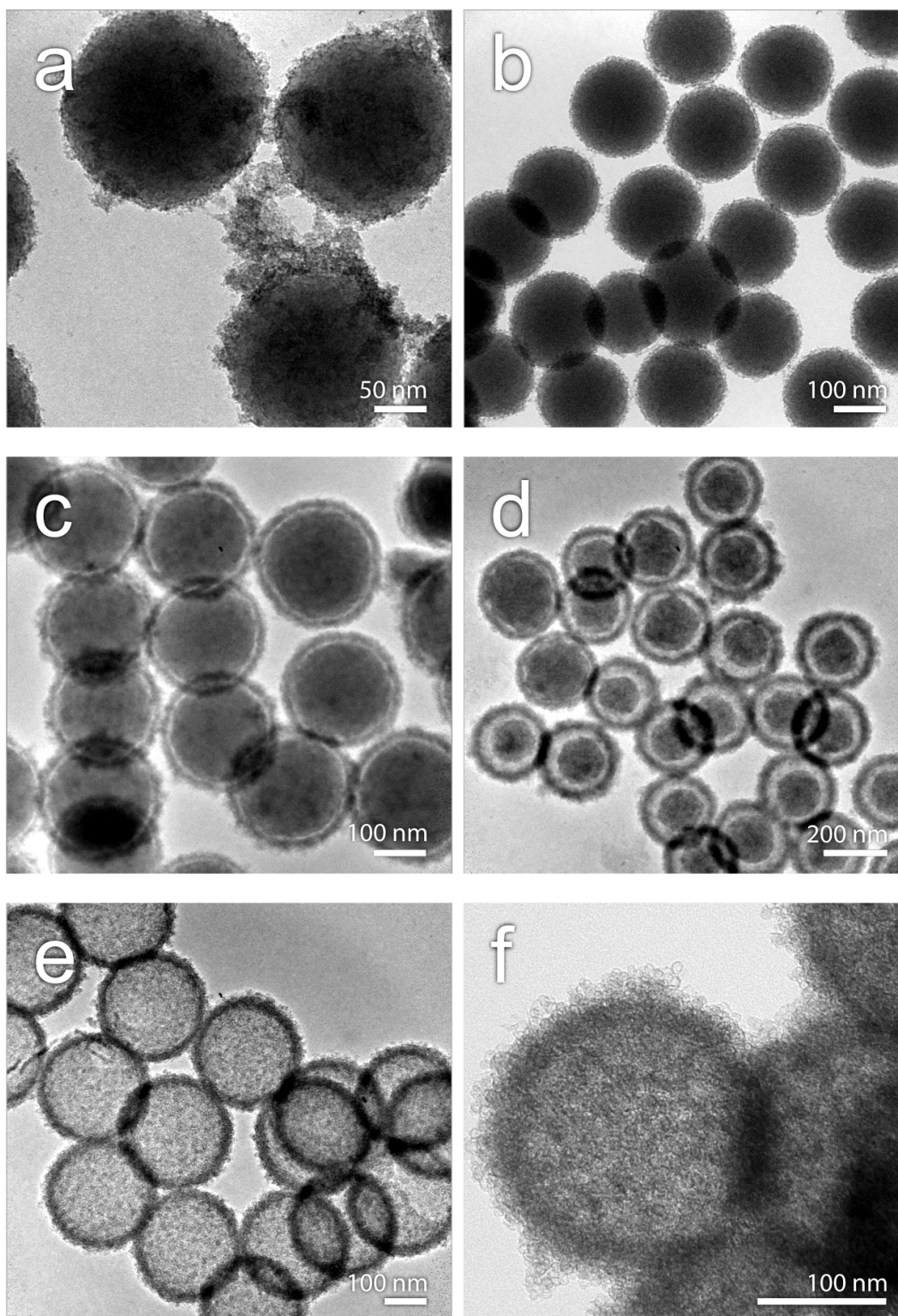
Nanobubbles before exposing in focused (TEM) electron beam with an accelerating voltage = 200 kV.



Nanobubbles after exposing in focused electron beam (accelerating voltage = 200 kV).



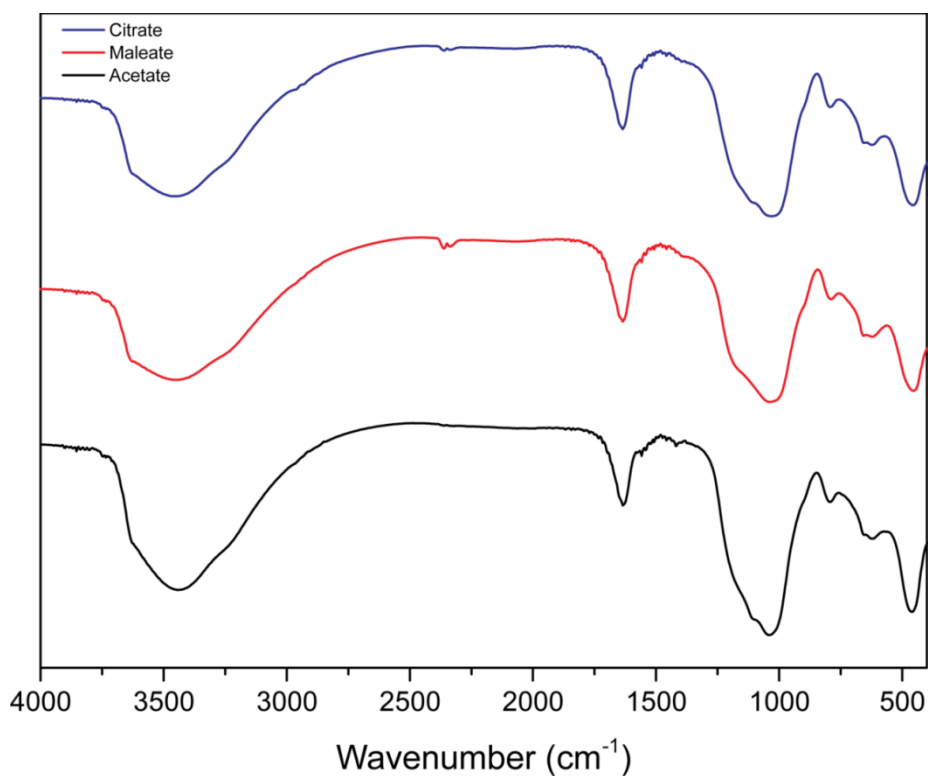
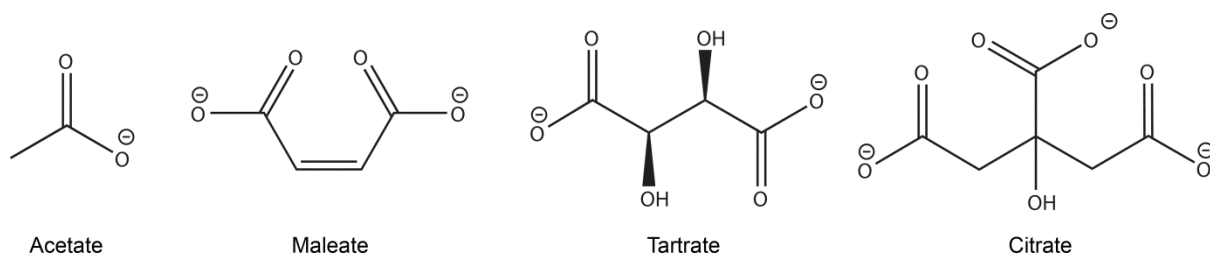
High resolution TEM of nanobubbles collapsed after focused electron beam exposure. The collapsed structure corresponds to Mn_3O_4 based on its lattice fringe.

Appendix 4-2A Effect of Reaction Temperature

Samples prepared at different reaction temperatures: (a) room temperature, (b) 100 °C, (c) 120 °C, (d) 150 °C, (e) 180 °C, and (f) 200 °C for 12 hours.

Appendix 4-2B Effect of Different Carboxylate Anions

Molecular structures of other carboxylate anions used in this work:



Comparison of FTIR spectra among the manganese silicate nanobubbles prepared with different carboxylate anions. All structures were synthesized using 50 mg of SiO₂ precursor beads, 0.8 mmol of MnSO₄, and 1.6 mmol of sodium carboxylate salts (i.e., with acetate, maleate, and citrate anions, respectively) in 20 mL of H₂O. The reactions were carried out at 180 °C for 12 hours.

Table A-5. Summary of Particle Size and Shell Thickness of Manganese Silicate Samples

Particle	Mean Diameter (nm)	% RSD	Shell Thickness (nm)	% RSD	Corresponding figure (Chapter 7)
SiO ₂ beads	263	4.44	N/A	N/A	Figure 7.1a
Mn-silicate (main text)	281	4.11	33	8.88	Figure 7.1b
Mn-silicate (Acetate)	228	5.13	22	14.32	Figure 7.9a
Mn-silicate (Maleate)	232	5.65	26	16.27	Figure 7.9b
Mn-silicate (Tartrate)	192	4.90	25	11.56	Figure 7.9c
Mn-silicate (Citrate)	187	7.34	N/A	N/A	Figure 7.9e

Appendix 4-2C Stability Constants of Metal Carboxylates

Table A-6. Stability Constants (K) of Metal Carboxylates

Metal ion	Acetate ion		Citrate ion
	Log K <i>T</i> = 25°C, <i>I</i> = 1.0	Log K <i>T</i> = 25°C, <i>I</i> = 0	Log K <i>T</i> = 25°C, <i>I</i> = 0.1
Mn ²⁺	0.69	1.40	4.15
Fe ²⁺	Not available	1.40	4.4
Co ²⁺	0.81	1.46	5.00
Ni ²⁺	0.83	1.43	5.40
Cu ²⁺	1.71	2.22	5.90
Zn ²⁺	0.63	1.57	4.98
La ³⁺	1.59	2.55	7.63
Ce ³⁺	1.71	Not available	7.39

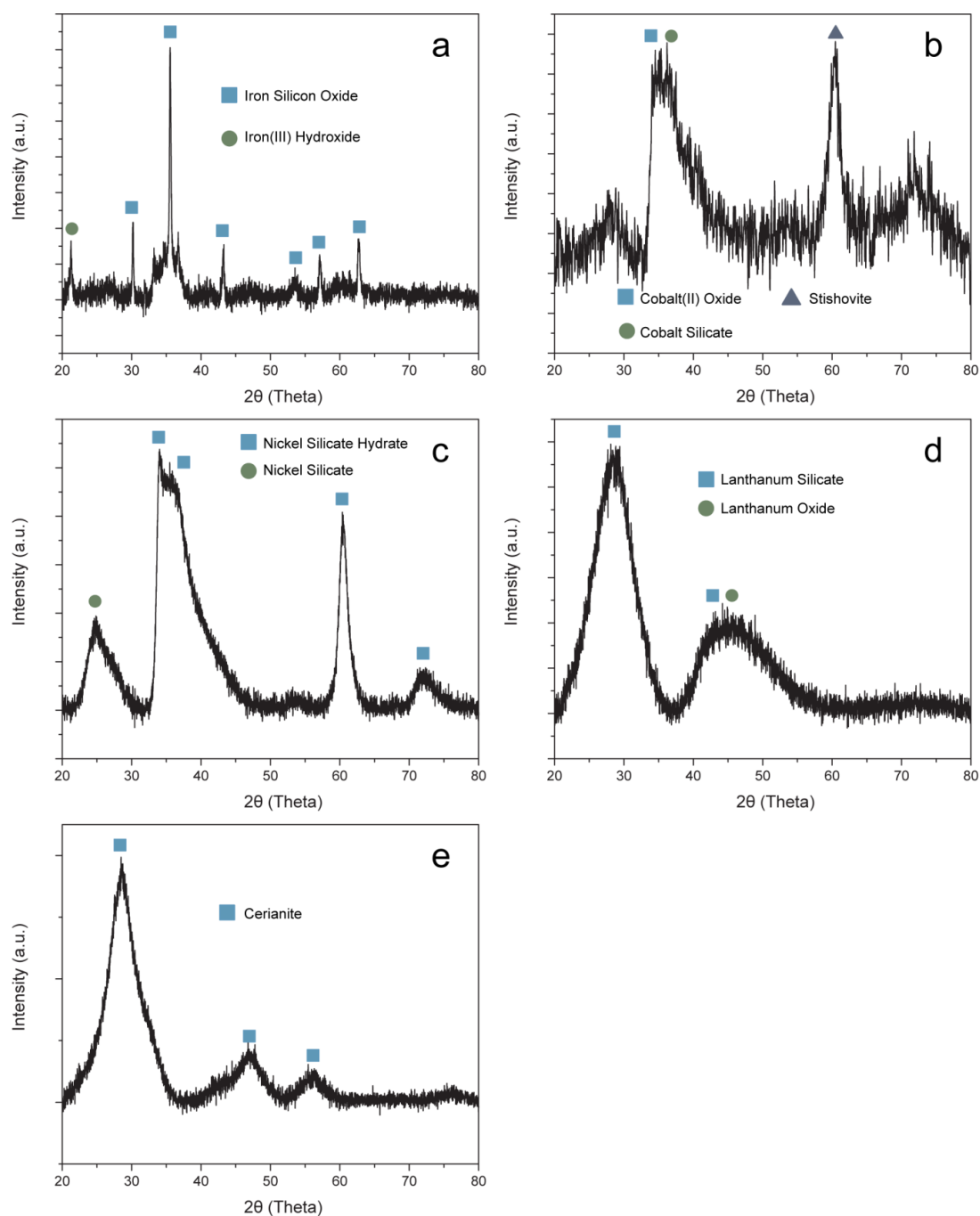
Data were obtained from: Martell, A.E. and Smith, R.M. *Critical Stability Constants* Vol. 3 (Plenum Press, 1977)

In the above table, *T* is the solution temperature and *I* is the additional ionic strength in molarity.

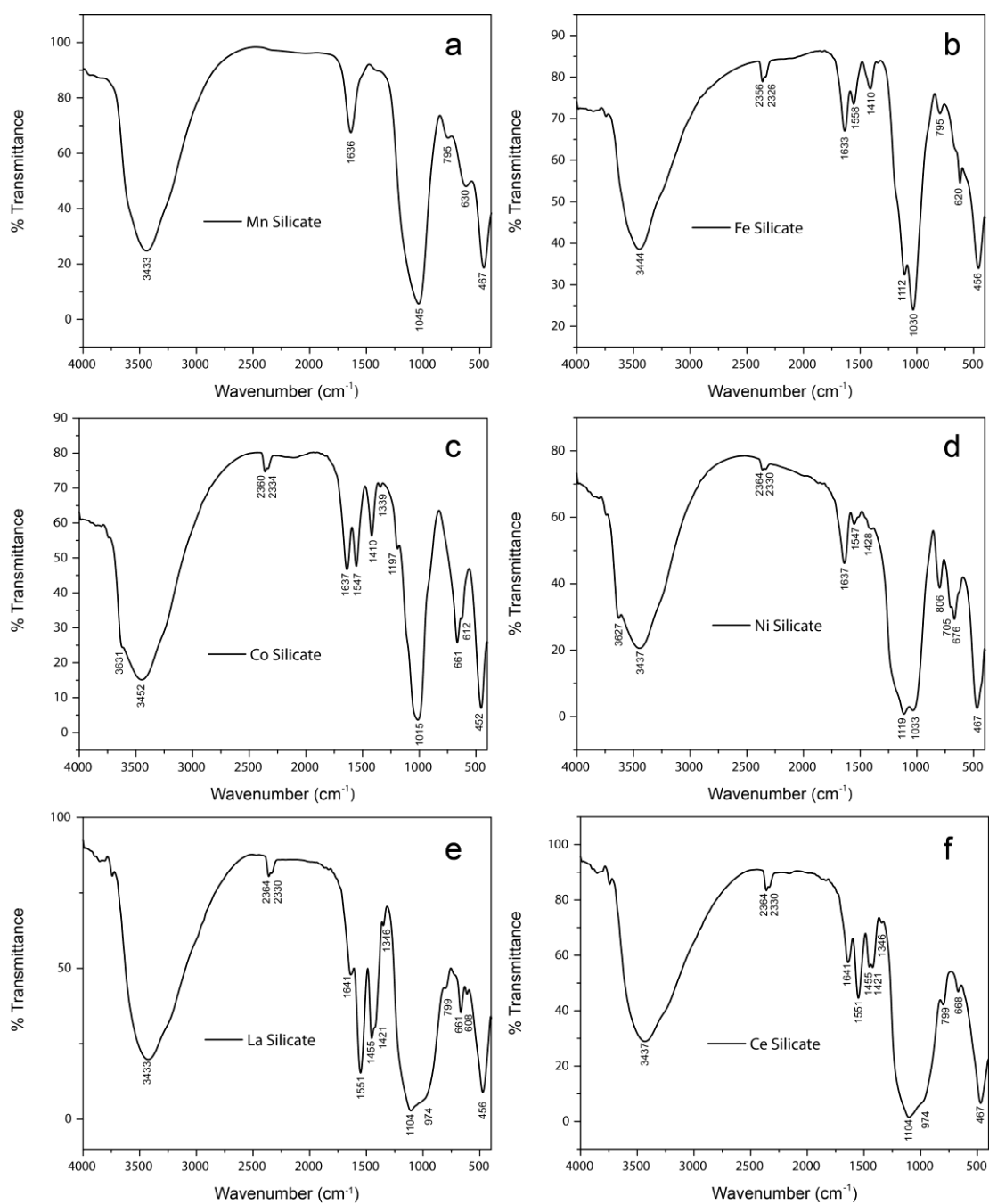
Chemical equilibrium equation:

$[M(H_2O)_n] + L \rightleftharpoons [M(H_2O)_{n-1}L] + H_2O$, where *M* = metal element, and *L* = carboxylate ligands.

Appendix 4-2D XRD and FTIR of Other Transition-Metal Silicate Hollow Structures

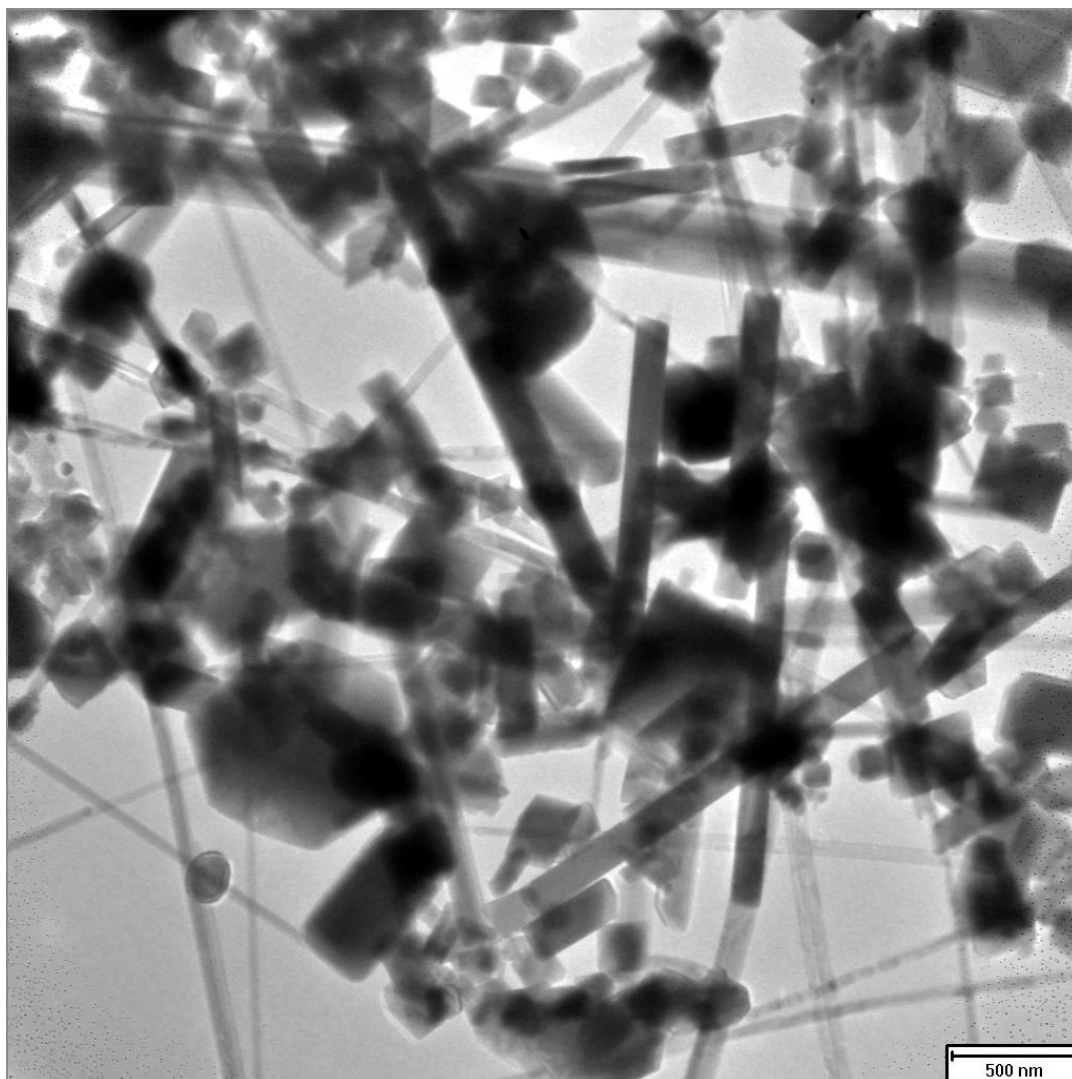


XRD patterns of different hollow spheres of different samples: (a) Fe-silicate, (b) Co-silicate, (c) Ni-silicate, (d) La-silicate, and (e) Ce-silicate. The actual sample morphologies can be seen in Figure 10 of the main text.

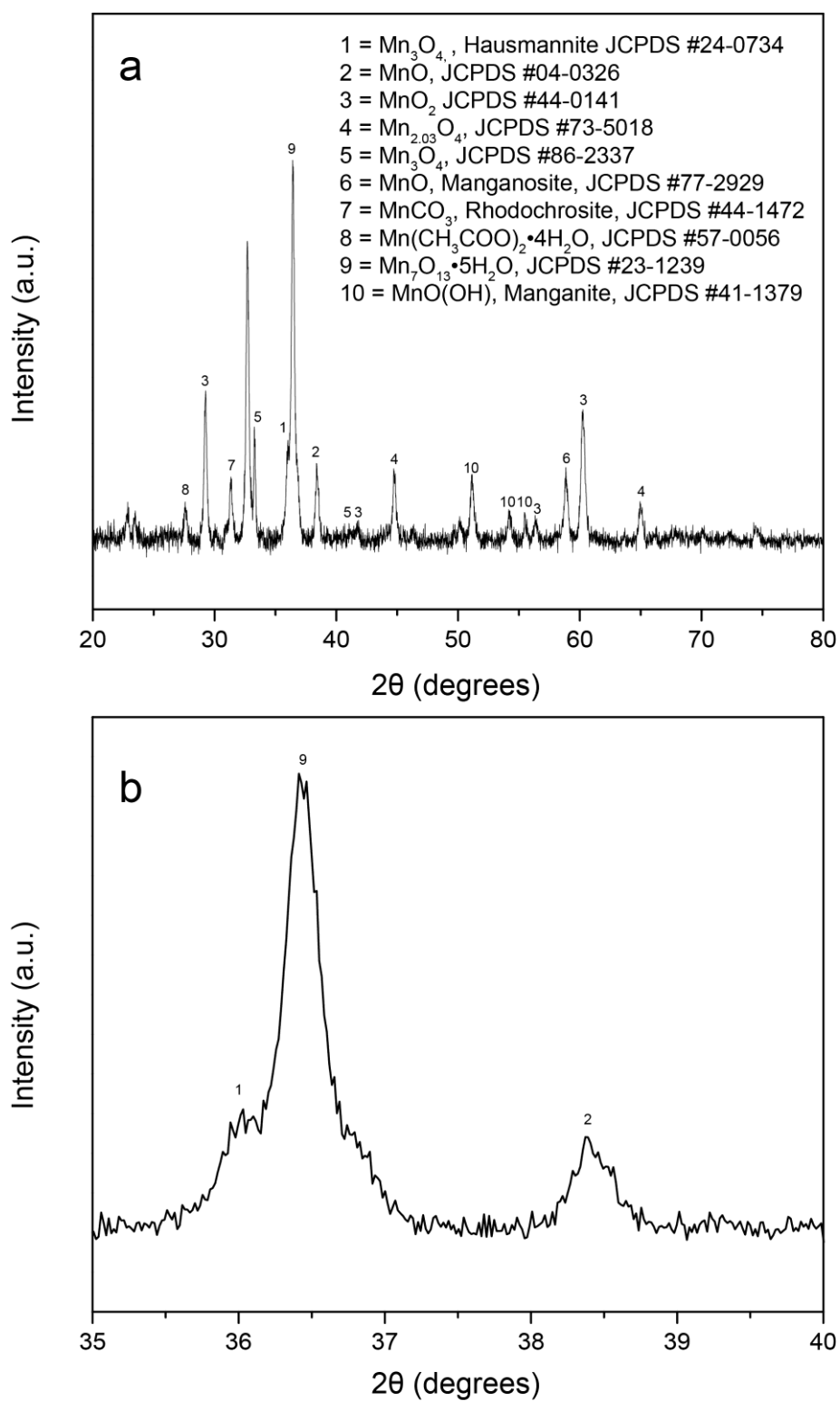


Comparison of IR spectra of different hollow spheres: (a) Mn-silicate, (b) Fe-silicate, (c) Co-silicate, (d) Ni-silicate, (e) La-silicate, and (f) Ce-silicate. The vibration modes of carboxylate RCO_2^- can be observed at $1547\text{--}1558\text{ cm}^{-1}$ (asymmetric stretching) and $1410\text{--}1428\text{ cm}^{-1}$ (symmetric stretching). The two peaks are observed for all the metal-silicate nanostructures except for the case of Mn-silicate (a).

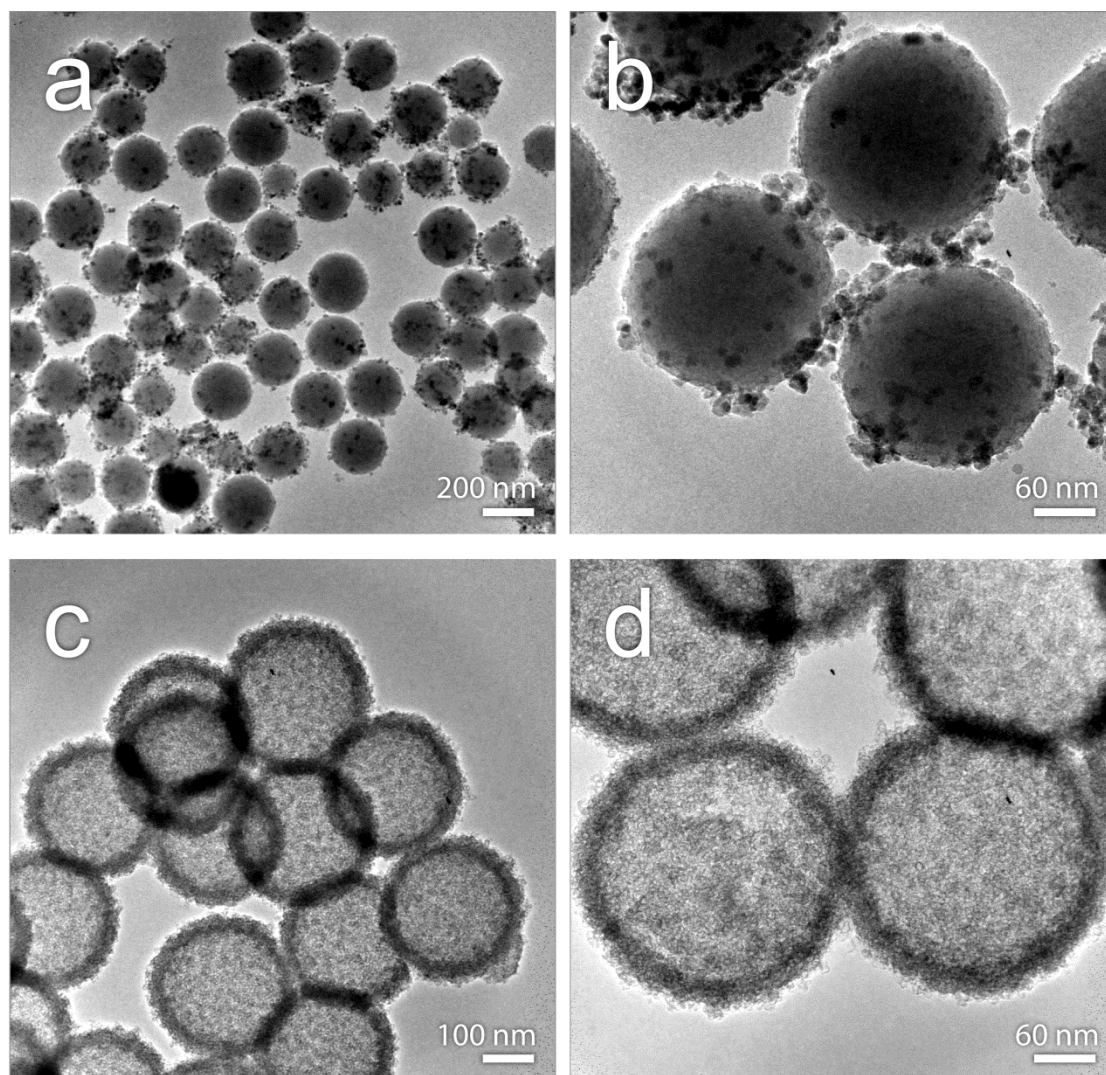
Appendix 4-2E Manganese Oxide Formation under Hydrothermal Conditions



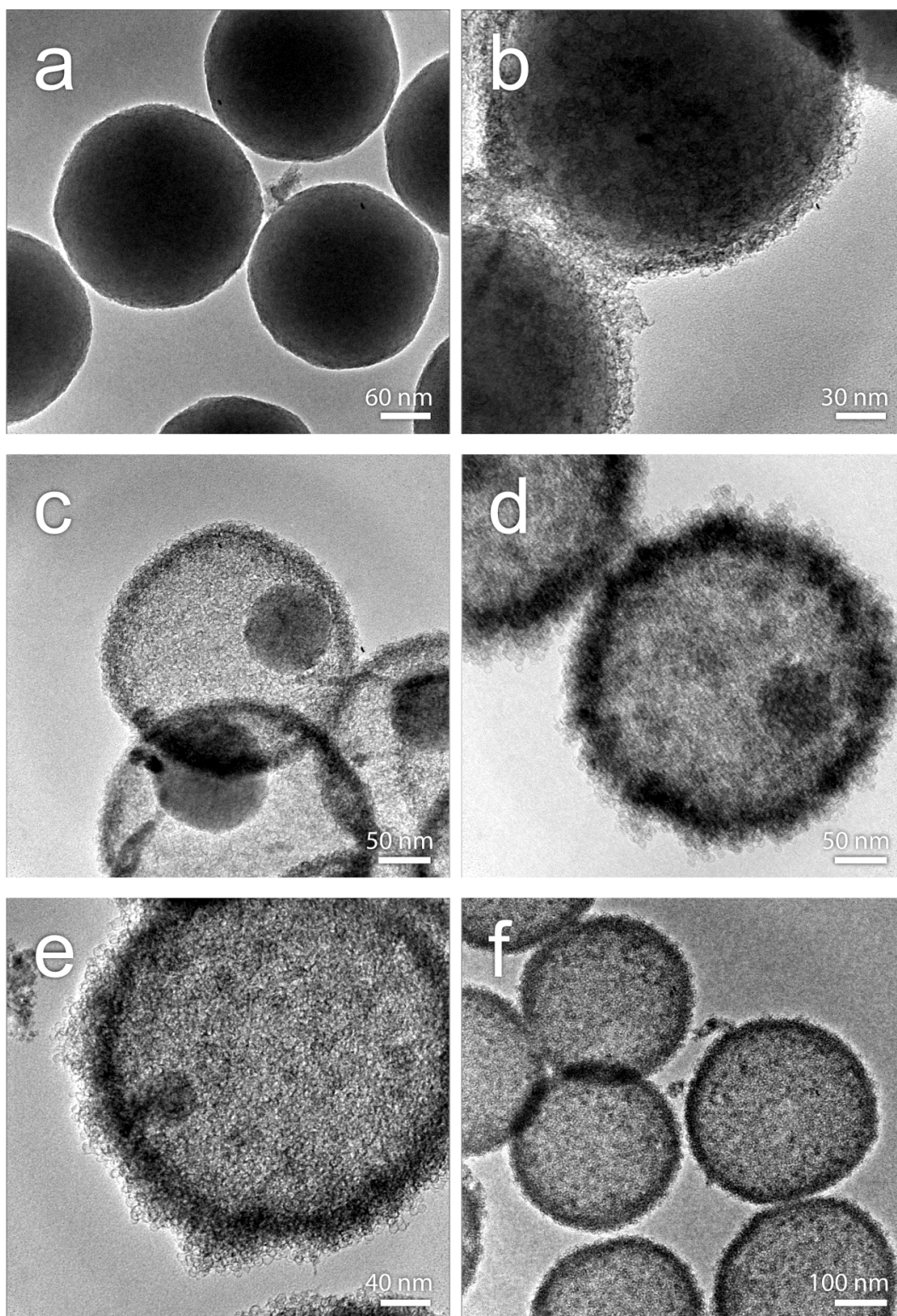
Particles obtained when $\text{Mn}(\text{CH}_3\text{COO})_2$ is hydrothermally treated without SiO_2 templates.



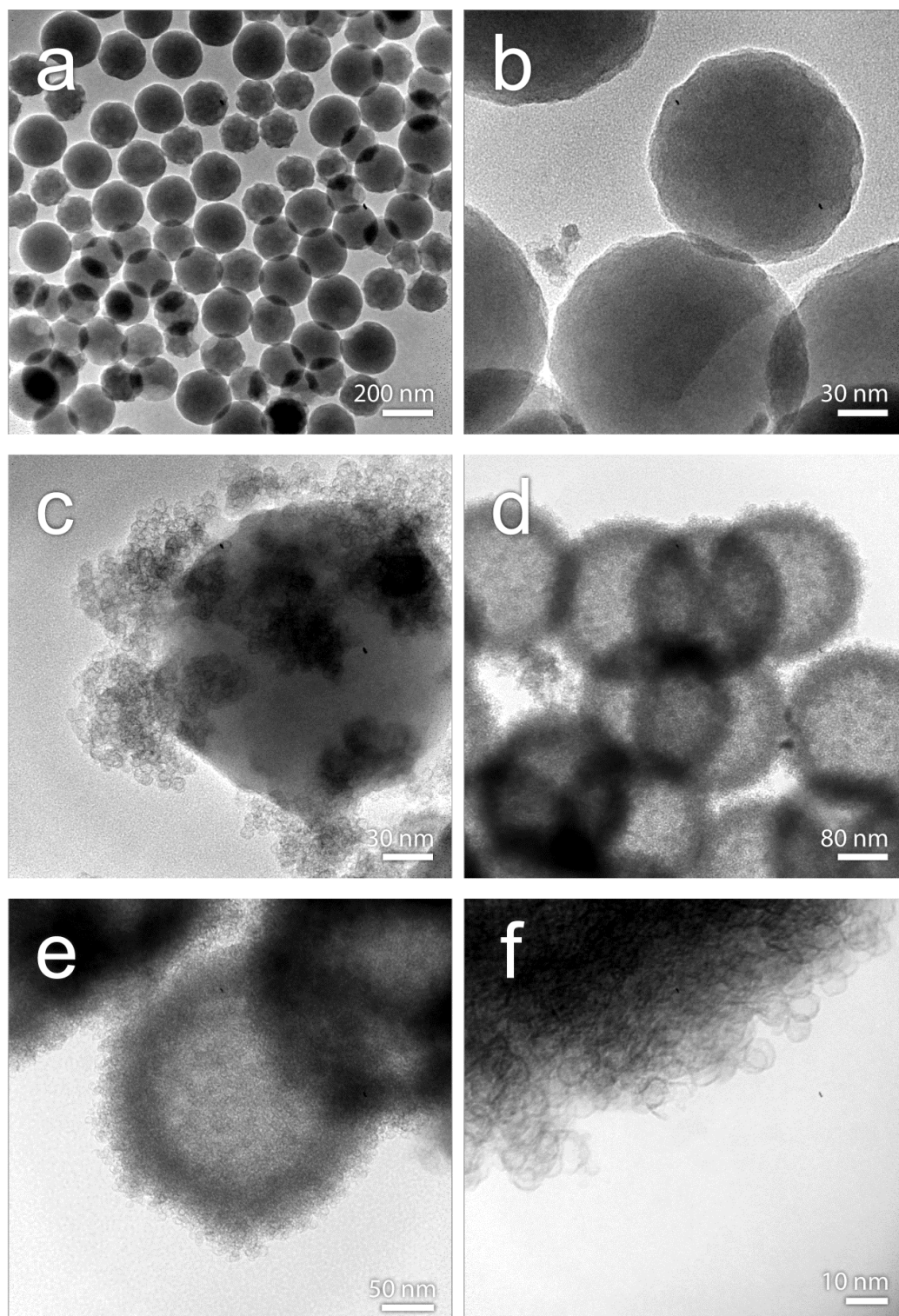
X-ray diffraction patterns for the sample of 28; several manganese compounds are identified (see the numbers indicated): (a) full scale diffraction pattern, and (b) magnified region for 2- θ = 35 to 40 degrees.

Appendix 4-2F Effect of Reaction Pressure

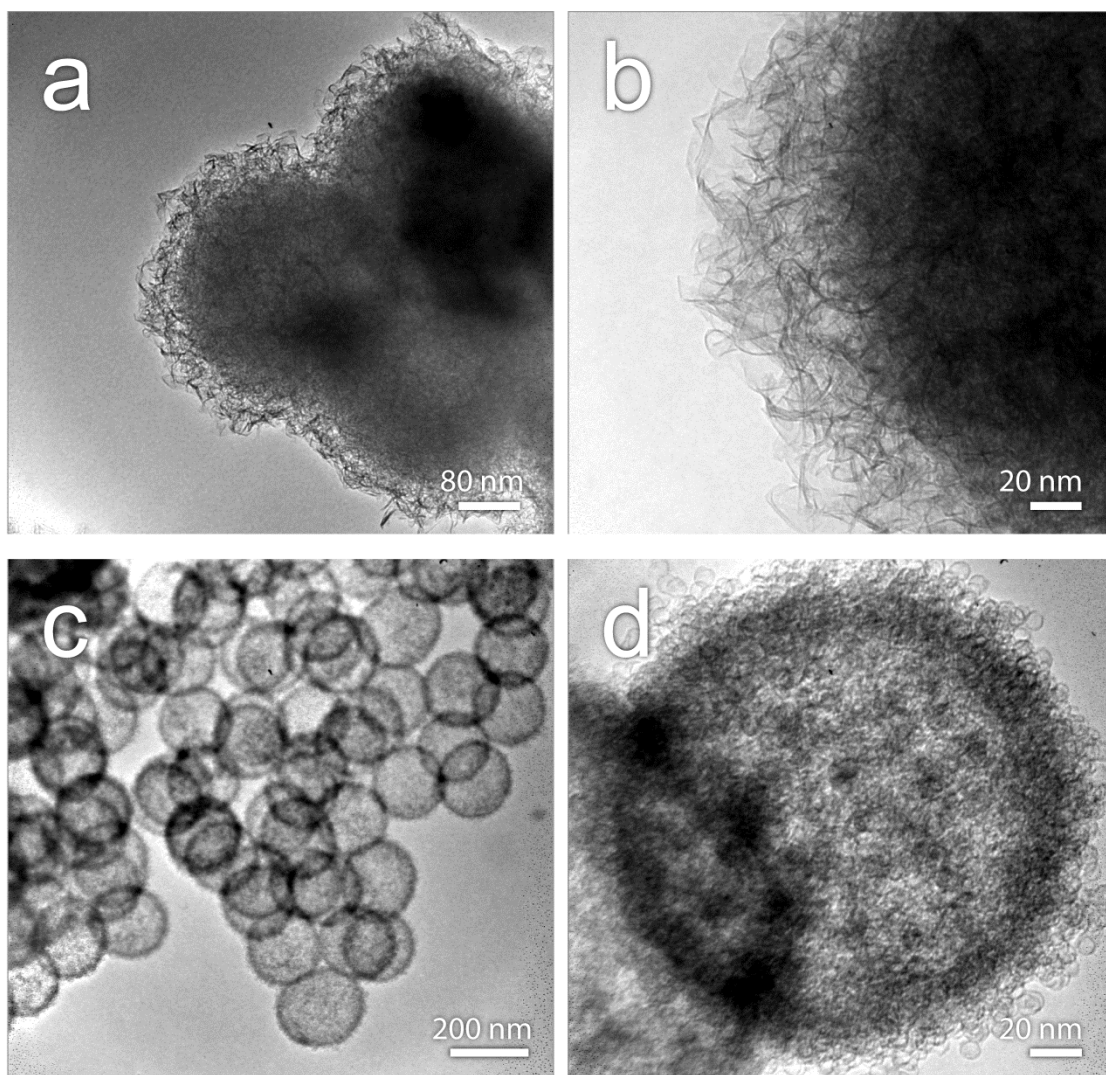
Samples prepared under different reaction conditions: (a-b) reflux method at ambient pressure, and (c-d) hydrothermal method at 180 °C (i.e., at elevated pressure). All reactions were conducted for 12 hours.

Appendix 4-2G Effect of Reaction Time

Samples prepared with different reaction durations: (a) 1, (b) 2, (c) 4, (d) 6, (e) 8, and (f) 12 hours. All reaction solutions were heated under hydrothermal conditions at 180 °C.

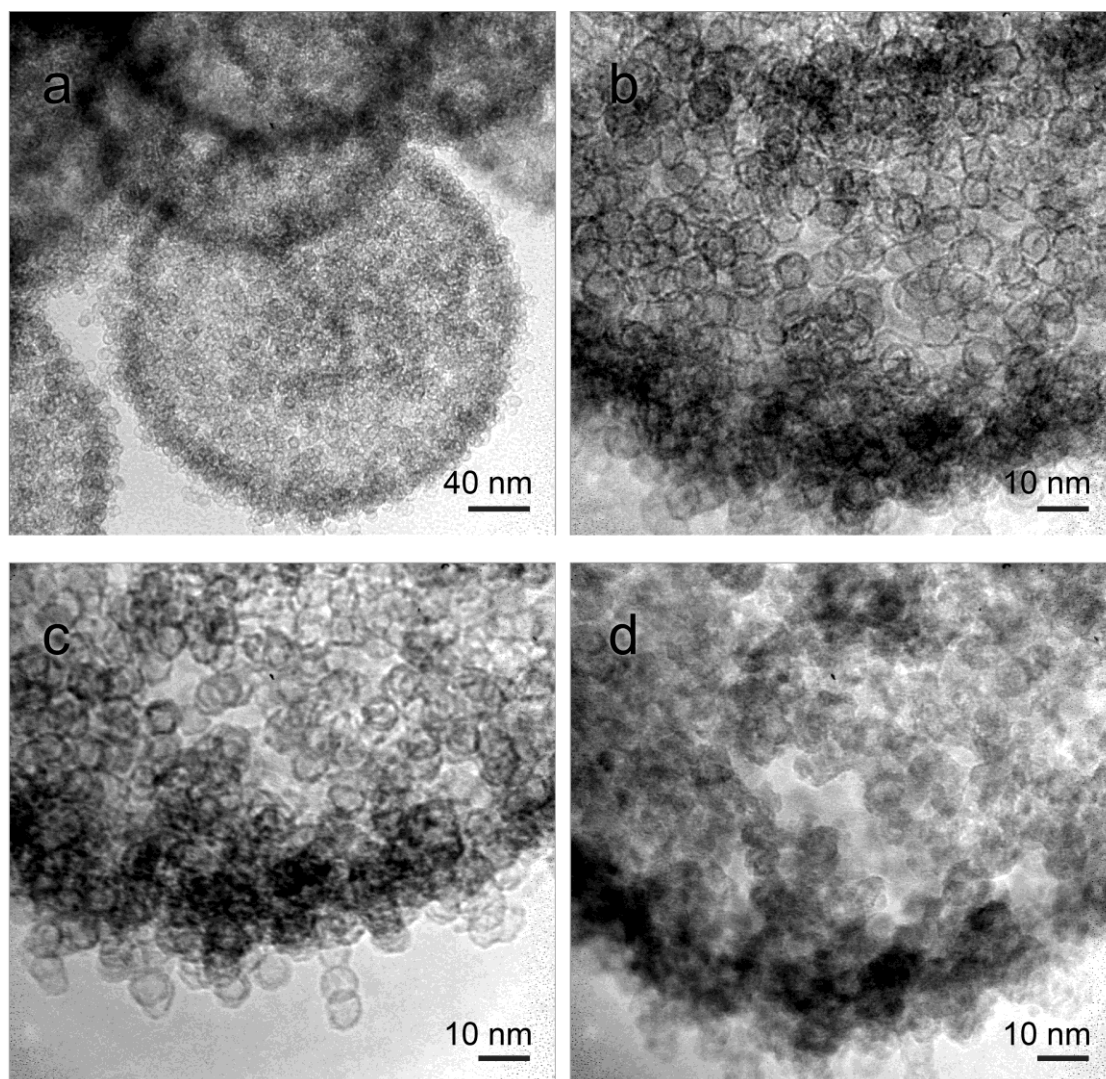
Appendix 4-2H Effect of Solution pH

Samples prepared with different starting pH values: (a) 3.6, (b) 4.7, (c) 4.8, (d) 5.0, and (e-f) 5.4. All reaction solutions were heated under hydrothermal conditions at 180 °C for 12 hours. The pH value was adjusted using acetic acid.

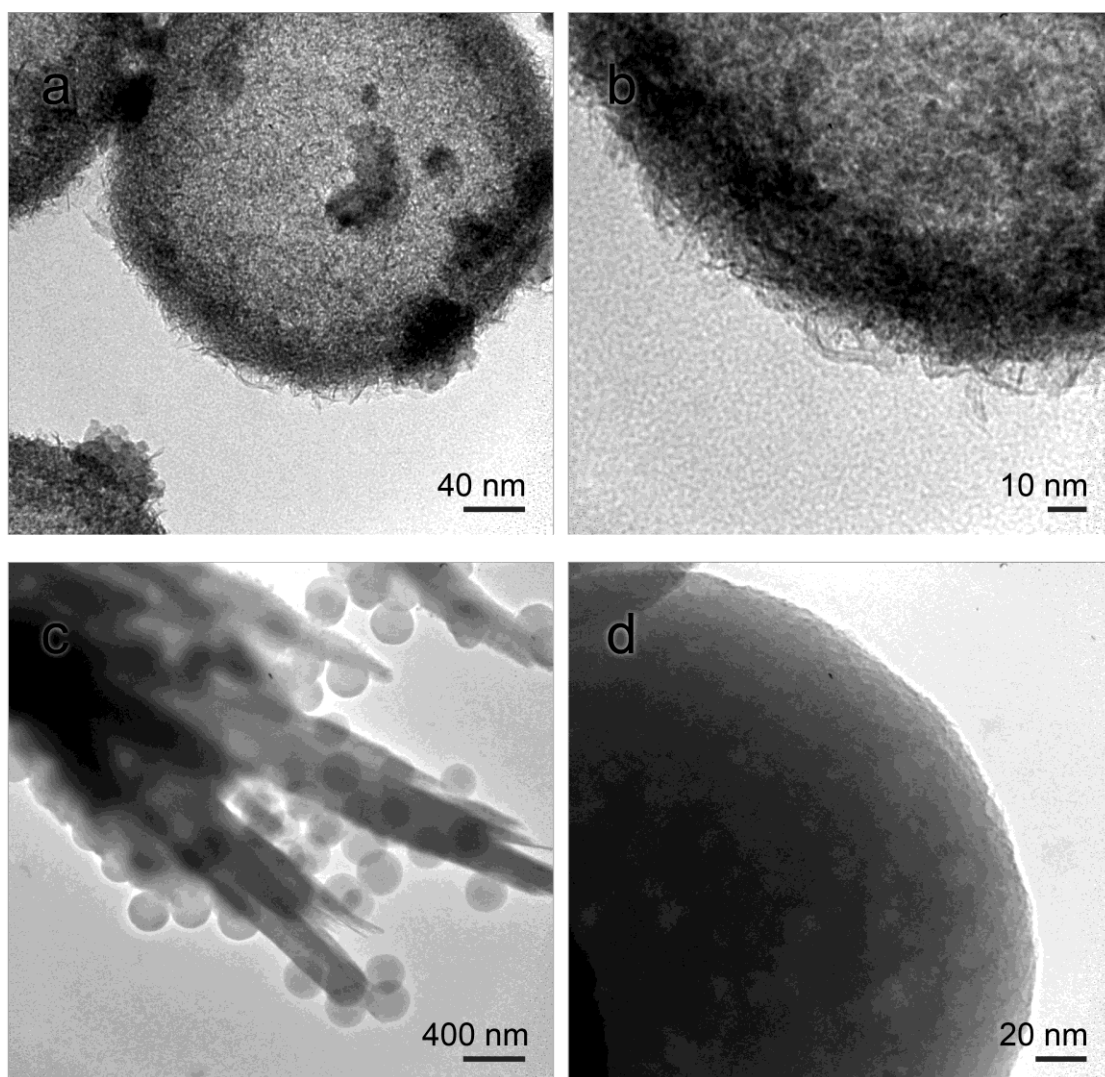
Appendix 4-2I Effect of Precursor Content

Samples prepared with different precursor contents: (a-b) 5 mmol of $\text{Mn}(\text{CH}_3\text{COO})_2$, and (c-d) 5 mmol of MnSO_4 and 1.6 mmol of NaCH_3COO . All reactions were conducted for 12 hours at 180 °C.

Appendix 4-2J Effect of Carbonate and Phosphate on Nanobubble Formation



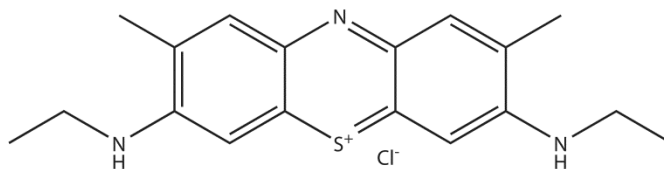
Samples prepared with the reaction of 50 mg SiO_2 sphere with 0.8 mmol MnSO_4 and 0.8 mmol Na_2CO_3 in 20 mL H_2O under hydrothermal conditions (180 °C, 12 hours, pH = 9). (a) Single microsphere nanobubble assembly, (b-c) high magnification image of (a), and (d) prolonged electron beam exposure of (a).



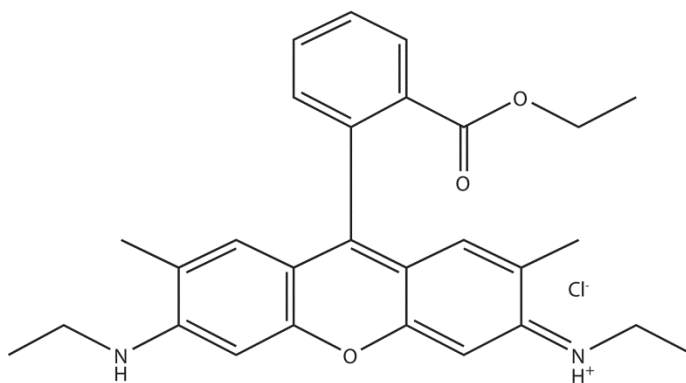
Samples prepared with the reaction of 50 mg SiO_2 sphere with 0.8 mmol MnSO_4 , 0.8 mmol Na_2HPO_4 in 20 mL H_2O under hydrothermal conditions (180 $^\circ\text{C}$, 12 hours) at different pH value. (a) pH = 9, (b) high magnification image of (a), (c) pH = 10 and (d) high magnification of (c).

Appendix 4-3A UV-Vis Spectra of Organic Dyes during Adsorption and AOP

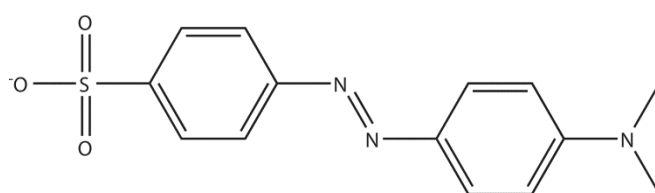
Molecular structures of organic dyes studied in this work:



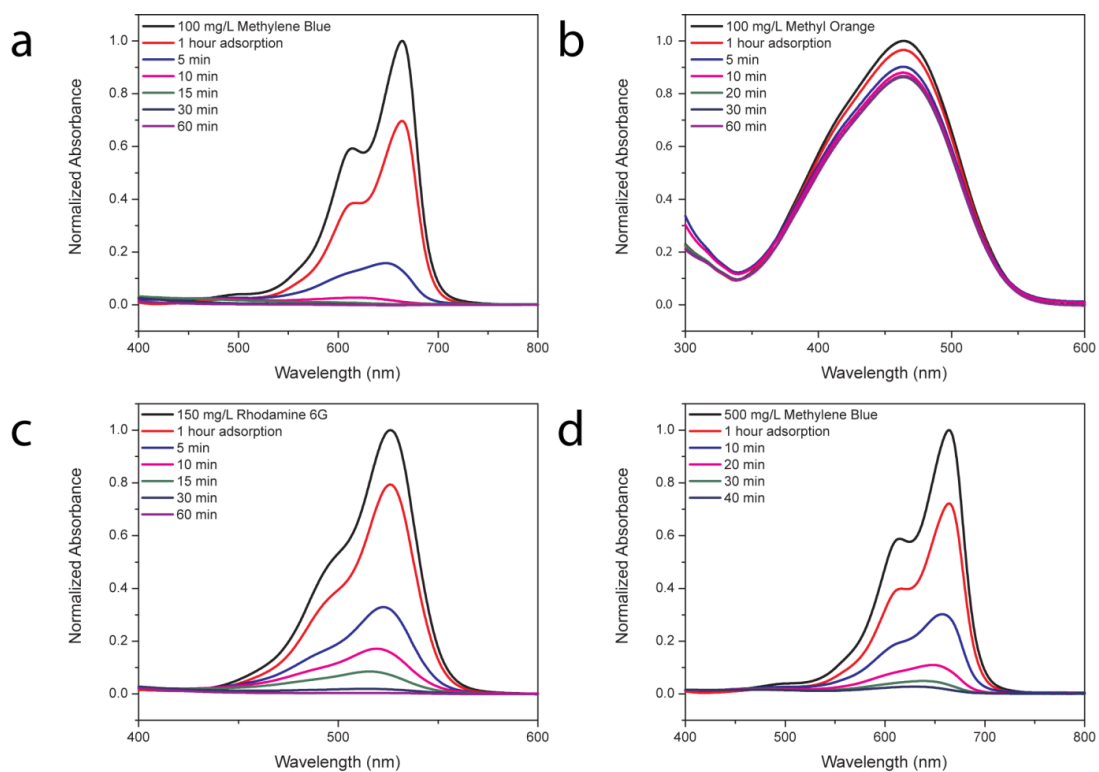
Methylene Blue



Rhodamine 6G

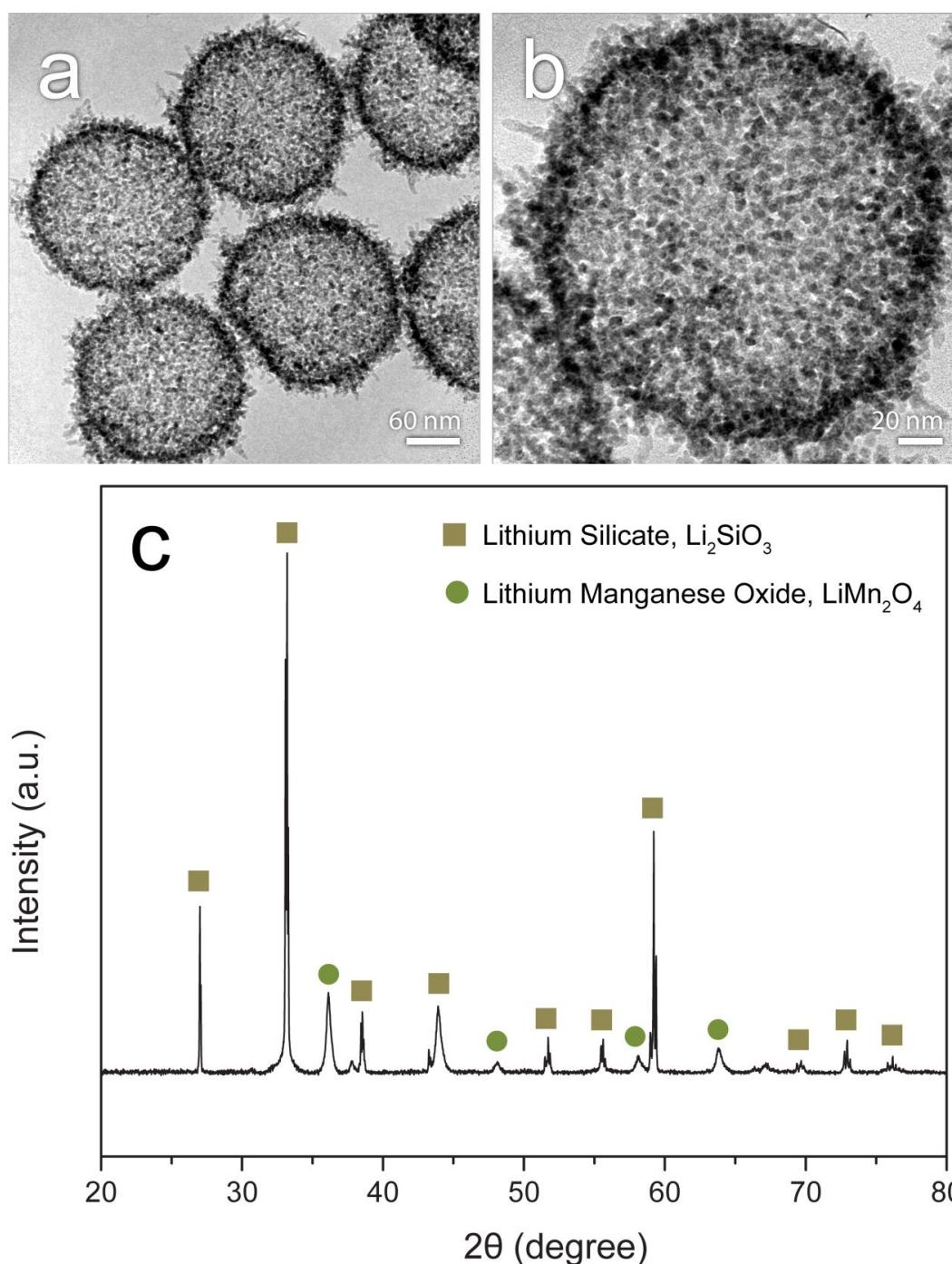


Methyl Orange



UV-Visible spectra of various dye molecules (Appendix 7-1A) during advanced oxidation process (AOP): (a) methylene blue, 100 mg/L; (b) methyl orange, 100 mg/L; (c) rhodamine 6G, 150 mg/L; and (d) methylene blue, 500 mg/L (more concentrated). All the reactions used 100 mL of the dye solution and 20 mg of catalyst (i.e., spherically assembled nanobubbles of manganese silicate) except for the case of (d), in which 50 mg of the catalyst was used.

Appendix 4-3B Lithium Intercalation into Manganese Silicates



Composite hollow spheres of Li_2SiO_3 and LiMn_2O_4 prepared via transforming nanobubbles of manganese silicate (Experimental conditions: 50 mg of Mn-silicate mixed with 1 mmol of LiOH in 20 mL of H_2O ; heated at 180°C for 12 hours under hydrothermal condition). (a-b) TEM images of the composite hollow spheres, and (c) XRD patterns of the composite hollow spheres of (a-b), in which phases of lithium silicate (Li_2SiO_3 , JCPDS card no. 70-0330) and lithium manganese oxide (LiMn_2O_4 , JCPDS card no. 73-5014) can be identified.

Appendix 4-3C Magnetic Separation of Gd-doped Manganese Silicate



Aqueous suspension of Gd-doped manganese silicate separated from the solution through magnetism

Publications Arising from this Thesis

Yec, C.C. and Zeng, H.C., "Band-gap engineering of M@Cu₂O@Zn(OH)₂ (M = Au, Ag, AuAg, and Pd) core-shell structures" (In Preparation)

Yec, C.C. and Zeng, H.C., "Transformative Syntheses of Complex Copper-Based Nanostructures from Precursors with Predesigned Architecture and Reactivity" (In Preparation)

Zhan, G.W., Yec, C.C., and Zeng, H.C., "Mesoporous Bubble-like Manganese Silicate as a Versatile Platform for Design and Synthesis of Nanostructured Catalysts", *Chemistry, A European Journal*, Vol. 21 (2015) pp. xxx-xxx.

Yec, C.C. and Zeng, H.C., "Nanobubbles within a Microbubble: Synthesis of Hollow Manganese Silicate and Its Metal-Doped Derivatives", *ACS Nano*, 2014, 8, pp. 6407-6416

Yec, C.C. and Zeng, H.C., "Synthesis of Complex Nanomaterials via Ostwald Ripening", *Journal of Materials Chemistry A*, 2014, 2, pp. 4843-4851

Yec, C.C. and Zeng, H.C., "Synthetic Architecture of Multiple Core-Shell and Yolk-Shell Structures of (Cu₂O@)_nCu₂O (n = 1-4) with Centricity and Eccentricity", *Chemistry of Materials*, 2012, 24, pp. 1917-1929

